IMPROVING RECONSTRUCTIVE SURGERY THROUGH COMPUTATIONAL MODELING OF SKIN MECHANICS

A Dissertation

Submitted to the Faculty

of

Purdue University

by

Taeksang Lee

In Partial Fulfillment of the

Requirements for the Degree

of

Doctor of Philosophy

August 2020

Purdue University

West Lafayette, Indiana

THE PURDUE UNIVERSITY GRADUATE SCHOOL
STATEMENT OF DISSERTATION APPROVAL

Dr. Adrian Buganza Tepole, Chair

School of Mechanical Engineering

Dr. Thomas Siegmund

School of Mechanical Engineering

Dr. Ilias Bilionis

School of Mechanical Engineering

Dr. Craig Goergen

Weldon School of Biomedical Engineering

Approved by:

Dr. Nicole L. Key

Head of the School Graduate Program

ACKNOWLEDGMENTS

There are a number of people, without whom this dissertation would have been infeasible. First of all, I owe a great deal to my advisor, Adrian Buganza Tepole, for his strong support and patience. He has provided an excellent environment in which I can fully concentrate on my research. Without his insight and intuition that have fed my curiosity and idea, this work may never have matured. Beyond this dissertation, he has been an outstanding mentor, staying always friendly, giving chances to broaden my outlook, and being willing to listen my words.

I would like to thank my committee members, Thomas Siegmund, Ilias Bilionis, and Craig Goergen, for taking the time to give constructive feedback on this dissertation. Special thanks go to Ilias Bilionis, without whom uncertainty analysis in this work would not be timely achieved. I also thank Arun Gosain and Sergey Turin for our fruitful collaboration. Without their invaluable surgical data, patient-specific modeling, which is one of the main building blocks for this dissertation, would not be possible. I am also grateful to Moon Ki Kim, previous advisor for my Master degree, at Sungkyunkwan University in Korea that he supported me for this advanced studies and encouraged me not to hesitate new adventures.

I would like to thank all lab members for producing a sound and joyful work atmosphere. Especially, many thanks go to Vivek Dharmangadan Sree, Tianhong Han, Yifan Guo, Casey Stowers, Marco Pensalfini, and Juan Gustavo Diosa Pena for filling this long journey with their light and friendship. I feel very grateful as well that I got the chance to interact with wonderful people at Purdue. Among all, I thank Dong Young Kim for making me find healthy life and giving me wise advice, Rohit Tripathy for helping me to construct solid understanding on Gaussian process, Wonyeong Jung for letting me know Purdue life at first, Jaesang Hyun for helping me recharge my battery, Hyung-gun Chi for nice trip to Chicago downtown.

Most of all, I thank my family, parents and younger sister Hyemin Lee, for giving me the strength to pursue this work. A few sentences are impossible to express my appreciation for their unconditional love and mental support. This work is dedicated to them with deep gratitude. Last but not the least, I am very thankful to my girl friend, Jieon Kim, for her love and belief to me across the Pacific Ocean. There is no doubt that more brilliant moment is waiting for us.

TABLE OF CONTENTS

Page

Page

Page

Page

Page

LIST OF TABLES

LIST OF FIGURES

Figure Page

Figure Page

Figure Page

ABSTRACT

Lee, Taeksang Ph.D., Purdue University, August 2020. Improving Reconstructive Surgery through Computational Modeling of Skin Mechanics. Major Professor: Adrian Buganza Tepole Professor.

Excessive deformation and stress of skin following reconstructive surgery plays a crucial role in wound healing, often leading to complications. Yet, despite of this concern, surgeries are still planned and executed based on each surgeon's training and experience rather than quantitative engineering tools. The limitations of current treatment planning and execution stem in part from the difficulty in predicting the mechanical behavior of skin, challenges in directly measuring stress in the operating room, and inability to predict the long term adaptation of skin following reconstructive surgery. Computational modeling of soft tissue mechanics has emerged as an ideal candidate to determine stress contours over sizable skin regions in realistic situations. Virtual surgeries with computational mechanics tools will help surgeons explore different surgeries preoperatively, make prediction of stress contours, and eventually aid the surgeon in planning for optimal wound healing. While there has been significant progress on computational modeling of both reconstructive surgery and skin mechanical and mechanobiological behavior, there remain major gaps preventing computational mechanics to be widely used in the clinical setting. At the preoperative stage, better calibration of skin mechanical properties for individual patients based on minimally invasive mechanical tests is still needed. One of the key challenges in this task is that skin is not stress-free *in vivo*. In many applications requiring large skin flaps, skin is further grown with the tissue expansion technique. Thus, better understanding of skin growth and the resulting stress-free state is required. The other most significant challenge is dealing with the inherent variability of

mechanical properties and biological response of biological systems. Skin properties and adaptation to mechanical cues changes with patient demographic, anatomical location, and from one individual to another. Thus, the precise model parameters can never be known exactly, even if some measurements are available. Therefore, rather than expecting to know the exact model describing a patient, a probabilistic approach is needed. To bridge the gaps, this dissertation aims to advance skin biomechanics and computational mechanics tools in order to make virtual surgery for clinical use a reality in the near future. In this spirit, the dissertation constitutes three parts: skin growth and its incompatibility, acquisition of patient-specific geometry and skin mechanical properties, and uncertainty analysis of virtual surgery scenarios.

Skin growth induced by tissue expansion has been widely used to gain extra skin before reconstructive surgery. Within continuum mechanics, growth can be described with the split of the deformation gradient akin to plasticity. We propose a probabilistic framework to do uncertainty analysis of growth and remodeling of skin in tissue expansion. Our approach relies on surrogate modeling through multi-fidelity Gaussian process regression. This work is being used calibrate the computational model against animal model data. Details of the animal model and the type of data obtained are also covered in the thesis. One important aspect of the growth and remodeling process is that it leads to residual stress. It is understood that this stress arises due to the nonhomogeneous growth deformation. In this dissertation we characterize the geometry of incompatibility of the growth field borrowing concepts originally developed in the study of crystal plasticity. We show that growth produces unique incompatibility fields that increase our understanding of the development of residual stress and the stress-free configuration of tissues. We pay particular attention to the case of skin growth in tissue expansion.

Patient-specific geometry and material properties are the focus on the second part of the thesis. Minimally invasive mechanical tests based on suction have been developed which can be used *in vivo*, but these tests offer only limited characterization of an individual's skin mechanics. Current methods have the following limitations:

only isotropic behavior can be measured, the calibration problem is done with inverse finite element methods or simple analytical calculations which are inaccurate, the calibration yields a single deterministic set of parameters, and the process ignores any previous information about the mechanical properties that can be expected for a patient. To overcome these limitations, we recast the calibration problem in a Bayesian framework. To sample from the posterior distribution of the parameters for a patient given a suction test, the method relies on an inexpensive Gaussian process surrogate. For the patient-specific geometry, techniques such as magnetic resonance imaging or computer tomography scans can be used. Such approaches, however, require specialized equipment and set up and are not affordable in many scenarios. We propose to use multi-view stereo (MVS) to capture patient-specific geometry.

The last part of the dissertation focuses on uncertainty analysis of the reconstructive procedure itself. To achieve uncertainty analysis in the clinical setting we propose to create surrogate and reduced order models, especially principal component analysis and Gaussian process regression. We first show the characterization of stress profiles under uncertainty for the three most common flap designs. For these examples we deal with idealized geometries. The probabilistic surrogates enable not only tasks such as fast prediction and uncertainty quantification, but also optimization. Based on a global sensitivity analysis we show that the direction of anisotropy of skin with respect to the flap geometry is the most important parameter controlled by the surgeon, and we show hot to optimize the flap in this idealized setting. We conclude with the application of the probabilistic surrogates to perform uncertainty analysis in patient-specific geometries. In summary, this dissertation focuses on some of the fundamental challenges that needed to be addressed to make virtual surgery models ready for clinical use. We anticipate that our results will continue to shape the way computational models continue to be incorporated in reconstructive surgery plans.

1. INTRODUCTION

Optimal wound healing outcomes following reconstructive surgery, scarless healing being the ultimate goal, remain out of reach. Among the known critical factors implicated in wound healing, mechanical cues are crucial but there is still a gap in our fundamental understanding of how stress and deformations lead to poor healing outcomes (Fig. 1.1). This gap in our knowledge further hinders our ability to anticipate complications and plan for the optimal procedure [1]. Based on *in vitro* an animal experiments, as well as clinical experience, we know that mechanical stress following reconstructive surgery can lead to wound healing delay, hypertrophic scars, wound dehiscence, and skin necrosis [2–5]. Yet, despite of this knowledge, surgeries are still planned and executed based on each surgeon's training and experience rather than quantitative engineering tools. This limitations of current clinical practice stem in part from the difficulty in directly measuring stress in the operating room. Measuring stress and deformation during surgery is not practically feasible beyond very controlled settings and ideal clinical cases [6]. Besides, each patient requires a unique procedure [7], has individual skin mechanical properties and healing response, and stress distributions in complex surgeries are not intuitive. Surgical reconstruction of large skin lesions such as burn injuries and giant birth defects, in particular, lead to intricate tissue rearrangement procedures [8].

An important challenge in predicting stress to plan for optimal treatment is the fact that biological systems are inherently stochastic and there is significant variation in mechanical and biological response across individuals. For instance, tissues *in vivo* are not stress-free [9]. For example, skin *in vivo* is under a state of prestrain due to its natural growth history during development [10]. In clinical techniques such as skin expansion, the skin is stretched and induced to grow, changing its stress-free configuration [7]. Being able to deal with uncertainty in the stress-free configuration

is a basic step to correctly calculate stress due to reconstructive surgery [11, 12]. In addition to the amount of *in vivo* prestrain, the mechanical response of the tissue also shows uncertainty. Since the mechanical behavior of collagenous tissues like skin is highly nonlinear, uncertainty analysis of reconstructive procedures is not trivial but needed. Lastly, the biological response governing skin growth and wound healing is also uncertain. Thus, predictions of healing outcomes have to incorporate this variability in order to make the best possible decisions with the information available.

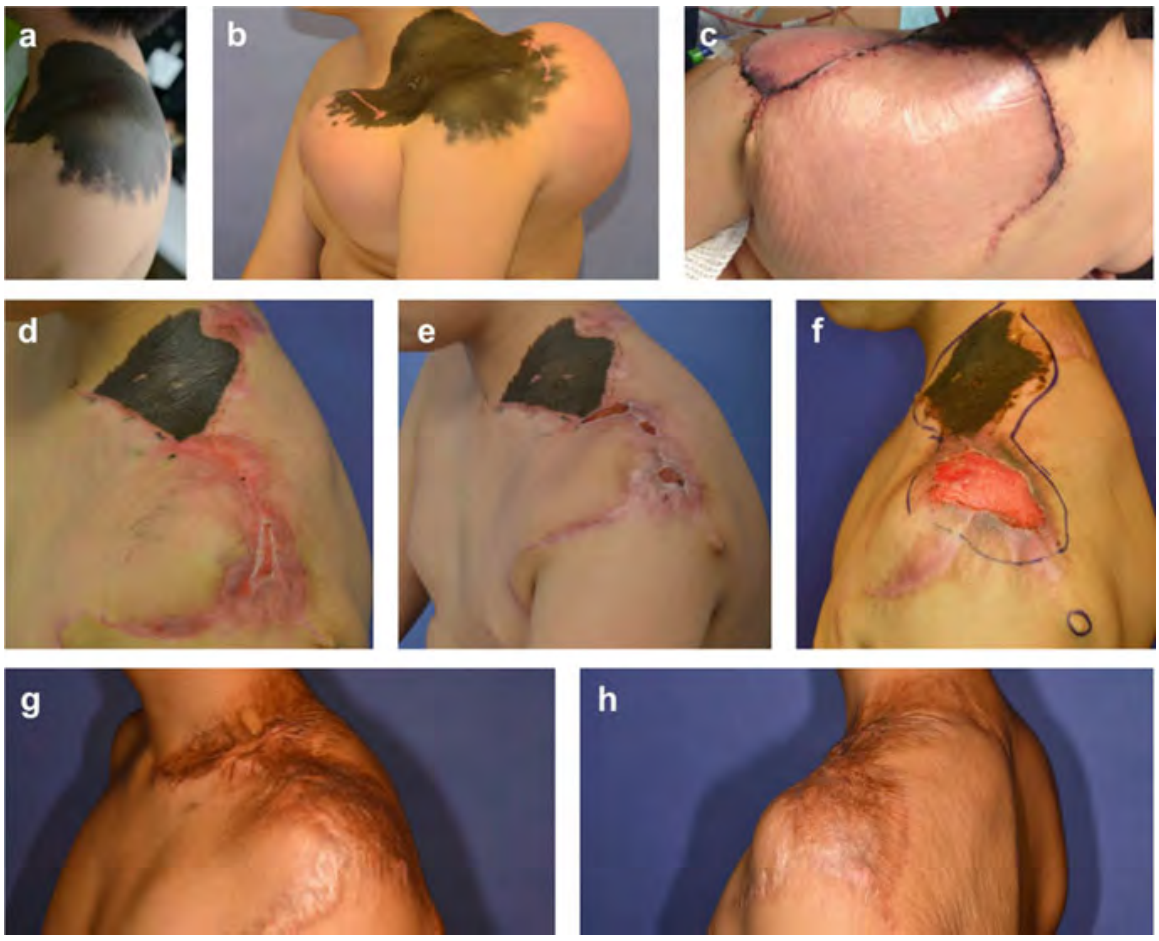

Fig. 1.1.: Wound complications after tissue expansion and subsequent reconstructive surgery. (**a**) 11-year-old patient with giant nevus. (**b**) Tissue expanders were utilized to grow skin by chronic overstretch. (**c**) Gained extra skin was advanced to correct the defect. (**d-f**) Excessive tension due to insufficient skin growth led to a chronic wound. (**g**, **h**) After full thickness graft, there was scarring and contracture at the neck and shoulder. Reprinted by permission from [13], Springer Nature, Copyright 2019.

Computational modeling of soft tissue mechanics has emerged as a powerful tool to determine stress contours over sizable skin regions in realistic situations [14, 15]. While it remains a technology uncommon to clinicians, the finite element method (FEM), for example, is a natural engineering technology that can be used to analyze the biomechanics of surgery and, thus, used to optimize flap designs [16–19]. Virtual surgeries with computational mechanics tools will enable surgeons to explore different surgeries preoperatively, make prediction of stress contours, and eventually aid the surgeon in planning for optimal wound healing. The central objective of this dissertation is to advance skin biomechanics and computational mechanics tools in order to make virtual surgery for clinical use a reality in the near future.

In order to achieve the overall goal, advances in several areas of computational biomechanics are needed. First of all, characterization of incompatibility, residual stresses, and the stress-free configuration of skin affected by growth is of importance to predict the correct stresses in reconstructive surgery scenarios of interest. Basically biological tissues undergo nonhomogeneous growth naturally and in tissue expansion. The growth field is generally complex. A better understanding on the incompatibility and residual stress in soft tissue can improve methods to determine the stress-free state of skin with minimally invasive tools. Importantly, poor understanding on stress-free configuration directly weakens the confidence on the results of FEM for virtual surgery simulations.

Computational models of soft tissues need patient-specific geometries and material properties. Much progress has been done in this area, but some key gaps remain. As mentioned before, tissues show stochasticity and variability. Because the biological and mechanical response is highly nonlinear, the effect of this uncertainty on the resulting stress contour and healing response has not been characterized but is key to make correct predictions. Even with better non-invasive mechanical tests, it may not be even possible to know exactly these parameters for a patient before the surgery. Questions that are currently out of each include: given prior information from similar patients, what is the best outcome possible? What is the probability of achieving a

desired stress profile given this uncertainty? given some partial measurements, what is the best guess for the material properties of an individual? These are questions that we enable through the research presented here.

Extensive mechanical characterization of skin samples with uniaxial [20], biaxial [21,22], bulge [23], torsion [24], indentation [25,26], suction tests [27,28], and with custom robotic manipulators [29] has resulted in a large dataset on mechanical behavior of skin. However, most of these tests are done *ex vivo*, and with a limited number of subjects given the variability that has been found across different studies [30]. Mechanical characterization of *in vivo* skin is much more relevant to patient-specific simulations. Suction devices have emerged as a tool for this need. However, suction tests provide even less information than the *ex vivo* tests. Moreover, for both *in vivo* and *ex vivo* tests, material parameters are obtained by classical inverse methods or analytical approximations which are often inaccurate, ignore previous information, and yield a single set of parameters for what in reality may be an ill-posed problem with multiple valid solutions. This gap is tackled in this thesis. We create fast, accurate, and automated parameter identification of individuals *in vivo* in a Bayesian framework using machine learning surrogates.

Another key challenge is to easily obtain patient-specific geometries. Shape and size of skin lesions are very different across clinical cases, and there are anatomical regions that pose more difficult challenges than others. The face, head and neck region is particularly complex. The geometry of this anatomical area is full of detail and constraints for the surgeon. Planning surgeries in this area can particularly benefit from an accurate geometry in individual cases [31]. Computational simulations using idealized and generic cases enable us to guide and optimize flap designs in general, but every patient requires an individualized treatment in the end [7,32]. Medical imaging has progressed enormously in recent decades, and there are many alternatives to obtain patient-specific geometries such as magnetic resonance imaging (MRI) [33] or computer tomography (CT) scans [34]. Still, these methods suffer from the same limitations: they are expensive and require specialized equipment. Skin has the

advantage of being easily accessible for imaging with more flexible and affordable methods. Three-dimensional (3D) scanners are one alternative to obtain patient geometries. 3D cameras are also on the rise. These methods are still out of reach for hospital with more limited resources. Additionally, with the rise of telemedicine, there is an increasing need for more flexible and inexpensive imaging modalities. Therefore a key gap addressed here is to obtain patient-specific geometries with inexpensive yet accurate methods such as multi-view stereo (MVS).

Virtual surgery based on patient-specific geometry and material parameters would lead to accurate prediction of stress profiles following surgery. Yet, this is not enough to improve outcomes. In the end, the connection between an individual's stress map from the surgical procedures has to be matched to the same patient's healing process in order to dissect the exact relationship between mechanical cues and wound healing. Animal and *in vitro* studies have demonstrated that excessive stress leads to wound complications [35, 36], and very recent clinical cases with stress shielding devices have observed for the first time that reducing the stress at a suture leads to quantitatively less scarring [3]. This progress is currently limited to simple excision and suturing patterns in which the stress contours are intuitive and reduction of stress with a prestretched membrane is straightforward. At the same time, we have a very comprehensive knowledge of the wound healing process, and of the biological process at play in the fibrotic response due to excessive stress. Therefore, we should be able to connect arbitrary stress contours from complicated procedures to the final healing outcome in terms of scar properties and geometry. While this last step is not covered in this thesis, it clearly is the next step. In this thesis, we get to the point of creating patient-specific models of reconstructive surgery and following up on the patients in order to establish, for the first time, a dataset that connects stress contours to wound healing outcomes. This knowledge is the indispensable foundation for the development of computational models of the biological process of wound healing, and, on its own, will aid in the creation of probabilistic models that can anticipate situations prone to complications and recognize best practices.

An underlying thread of the gaps just outlined is the fact that any computational model for virtual surgery will necessarily involve uncertainty in the calibration of the model and in the prediction. For example, the high variability of skin properties between individuals needs to be taken into account, both during the material parameter estimation task and then in the surgical planning. While the geometry of a patient can be captured accurately, identifying optimal surgical plans for general guidelines, or calibrating a model to become patient-specific, can only be done efficiently if there is an underlying understanding of how geometry variations influence the stresses profiles from surgery. Clearly, the biological response is also highly variable across individuals, not to mention other factors, other than mechanical cues, that ultimately determine the healing outcome. In conclusion, uncertainty quantification and propagation is one common theme across the different specific gaps addressed in this thesis. The different components of the thesis thus come together to address the goal of improving the overall pipeline of reconstructive surgery planning and execution through computational mechanics with a data-driven focus.

1.1 Overview of skin anatomy

Skin is a complex multi-layered tissue that protects us from harm and connects us to the outside environment (Fig. 1.2). The detailed structure and fascinating characteristics of this tissue, across multiple scales, are such that it enables its proper function. [37]. Indeed, the epidermis, the outermost layer of the skin, is a stratified, highly cellular tissue, and it exists in a constant state of self-renewal [38]. The basal keratinocytes cells are at the bottom of the epidermis, and are the only cells in the epidermis that can proliferate. As these cells divide, they get pushed up toward the surface and differentiate along the process [39]. At the top of the epidermis there are only dead, flat cells forming a thin shell called the stratum corneum, and these dead cells get released to the environment continuously. The constant renewal of the epidermis makes this layer of the skin particularly suitable to protect us against

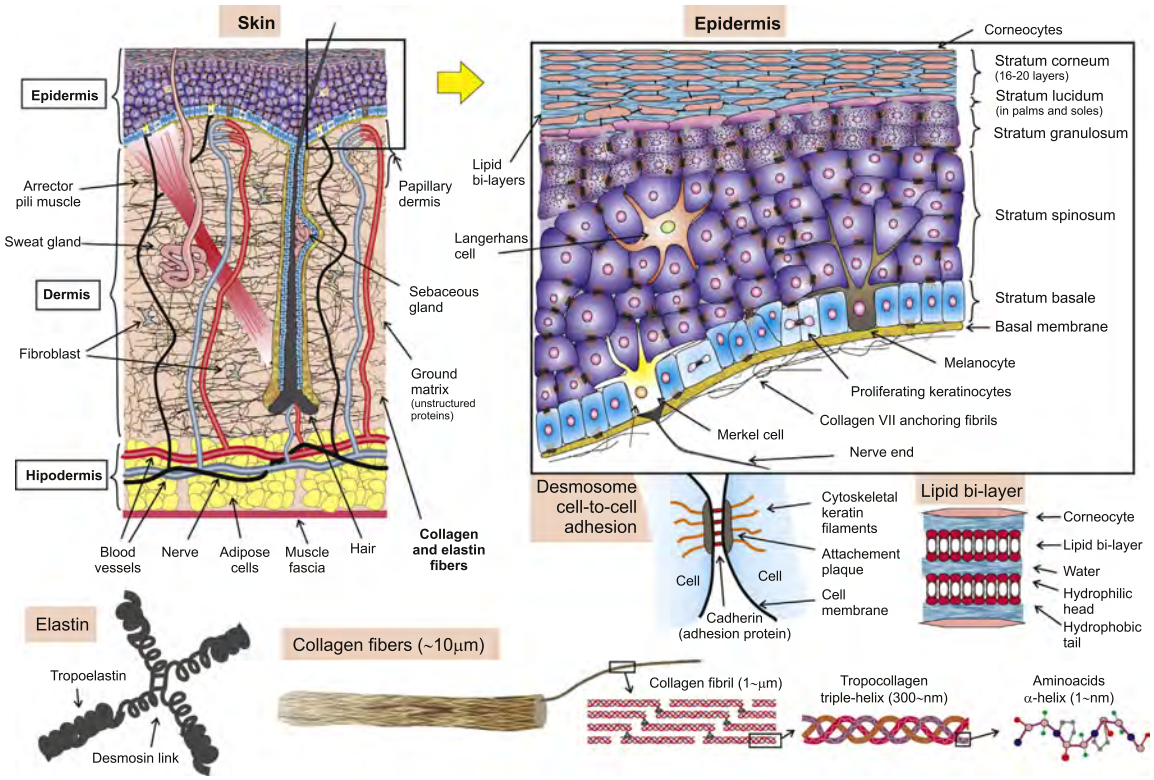

Fig. 1.2.: Structure of skin showing a complex multi-layered tissue and multi-scale components. Skin is largely divided into three layers, epidermis, dermis, and hipodermis, from outer to inner layer. Each layer is characterized by different cells and structures. Reprinted from [37], Copyright 2017, with permission from Elsevier.

abrasion and other superficial harms. This layer is also a primary regulator of heat and fluid exchange between the interior of our bodies and the external environment. Our tactile sense, is also highly dependent on the epidermis healthy functioning. The color of our skin and protection from UV radiation are additional tasks for this layer of the skin [40, 41].

Below the epidermis there is the dermis, which is the most important layer of the skin when it comes to load-bearing tasks. The dermis is a connective soft tissue, and, like other connective soft tissues of the human body, is primarily made out of an interwoven collagen fiber network. Elastin is another important constituent, especially for the mechanical behavior of skin at lower strains. The dermis is further classified into uppermost and thinner layer of papillary dermis and a lower layer called retic-

ular dermis [39]. The mechanical behavior of skin under tension is highly nonlinear and anisotropic, and this is a direct consequence of the tissue microstructure. The collagen fiber network in the dermis shows a preferred orientation, and the fibers have different degree of waviness or slack [42]. As external forces are applied, the macroscopic deformation of skin leads to alignment and stretching of collagen fibers at the microscale, and this causes the tissue to show a characteristic J-shape stress-strain curve [43–45]. Therefore, the interplay of elastin and collagen fibers enable us to have a stretchable but highly resistant tissue that protects us from mechanical insult but at the same time enables us to move freely and effortlessly.

Underlying dermis is the hypodermis, which mainly consists of fat cell called adipocytes. The hypodermis performs energy storage functions, provides thermal insulation [37], and serves also as a mechanical shock absorber [46–48].

Even though skin tissues show common characteristics across individuals, and even across different species of mammals, there is also a relatively wide variability in the structure and mechanical behavior. For instance, mechanical properties of skin vary with age, anatomical location, and from person to person [49,50]. As can be expected, this variability in tissue-level behavior is connected to a variation in the underlying microstructure [51–54]. Changes in skin structure occur not only through aging, but also in response to disease of injury. In this work we are particularly concerned with the changes in skin mechanical properties after wound healing. Unfortunately, the wound healing process leads to scar tissue rather than healthy skin. As a consequence, this tissue is less apt to the mechanical functions it is required to do, and this can have a high cost to the health of an individual. Pathological scarring, such as after burns or aggressive reconstructive procedures, can lead to lack of joint mobility, or disfigurement. We are therefore interested in the mechanics of healthy skin, including its variability, but also of scars.

1.2 Review of the state-of-the-art modeling of skin

The most noticeable features of skin in terms of its mechanical form and function are its nonlinear and anisotropic behavior. To model this, a common framework has been to consider skin as a hyperelastic material. the assumption of near incompressibility has also been deemed appropriate since the tissue is mostly composed of water which, in a relatively short time frame, is not movable within the tissue.

Based on the aforementioned manifest features, modeling the mechanical behavior of skin has been based on the construction of a suitable strain energy density function. Extensive research on the constitutive model of skin can be roughly be summarized into a classification of the different approaches down to three main classifications: phenomenological, structural, and structurally-based phenomenological models [55]. Phenomenological model takes into account macroscopic behavior of skin with assumption that skin is homogeneous material [56]. On the other hand, structural model of skin focuses on microstructural components such as collagen fiber orientation and dispersion. Here, there is argue that structural model is also phenomenological model because only matter is scale [55]. Structurally based phenomenological model is a result to combine structural model with phenomenological model such that macroscopic constitutive equation is integrated with microstructural features [55]. For example, Gasser-Ogden-Holzapfel (GOH) constitutive model [57], which generalizes previous models [58, 59] with dispersion of collagen fiber about preferred fiber orientation, is one of structurally based phenomenological models. Originally GOH model is developed to account for behavior of artery, but it also fits skin well [60].

In reality, the behavior of skin is not entirely described with a hyperelastic framework. Indeed, another noticeable characteristic of skin is viscoelasticity that means both viscous and elastic features occur under deformation [61]. That is, mechanical behavior of skin is time-dependent. This is because 64% of skin weight is water, and while some fraction of this water is tightly bound to some of the structural proteins, a major fraction is highly movable on slow-enough time scales [62]. To describe such

viscoelastic nature of skin, Lanir [63], Shoemaker et al. [64], and Bischoff et al. [65] and so on have developed viscoelastic constitutive model of skin [61]. In this thesis, however, we will focus only on the mechanical response of skin in short time scales for which a hyperelastic description is suitable.

1.3 Review of the state-of-the-art measuring skin mechanical behavior

Following the understanding on skin's mechanical behavior, knowing skin property is of practical importance in reconstructive surgery [66], dermatology [67, 68], and cosmetic field [69] because surgery scheme and medical therapy can be personalized to optimize outcome. Like common mechanical materials, skin as a deformable material can be tested using conventional mechanical test. As the aforementioned, a lot of test methods have been developed to measure mechanical property of skin such as suction, uniaxial or biaxial, torsion, and indentation tests and so forth [45]. Unlike common mechanical materials, on the other hand, skin as a living material contains high variation in terms of material properties. Even for same subject, different mechanical properties are observed with respect to body region [70]. In addition, skin is sensitive to experimental condition such as hydration and temperature [71]. During test, therefore, experimental condition should be well controlled to obtain consistent experimental result.

More sophisticated approach has been carried out to investigate each skin layer of statum corneum [71], epidermis [72], dermis [73], and hypodermis [74], respectively. FEM has also been utilized to inversely derive coefficients in constitutive model which not only depicts experimental results but also results in outcome of finite element analysis. Suction [75] and indentation test [76] are incorporated with FEM to fit experimental result with FEM result.

1.4 Review of surgical simulators

Extension of computational mechanics to biology and medicine has been well achieved since several decades. Through the continuum scale, traditional approach is FEM, and which has elucidated physical phenomenon in biological system. For example, most biological systems entail complex geometry and boundary condition (artery [77], brain [78], heart [79], skin [80]), multi-physics governing equations [81–83], and intrinsic *in vivo* state [84], but those difficulties have been resolved with acceptable accuracy as well as solid explanation. Beyond the fundamental understanding on the behavior of biological system, demands on clinical application also arise to benefit from the FEM in order to yield optimal outcome of surgery. Surgical procedure is individually investigated and outcomes from FEM at each surgical stage help a surgeon design a better surgical plan or anticipate suboptimal outcome. In this response, surgical simulation ideally aims for being real-time and realistic visual with haptic feedback as well as accurate enough. To do so, computational as well as mechanical point of view should be delivered over clinical and biological aspect.

First of all, soft tissue specifically shows complicated behavior to the external force. Unlike classic materials like steel, soft tissue characterizes nonlinear behavior such as J-shaped stress-strain response or time-dependent relaxation, which is generally described as hyperelastic or hyper-viscoelastic models, respectively [85]. The initial approach, on the other hand, has started with linear constitutive model such that behavior of tissue is assumed as infinitesimal deformation and linear response in order to reduce computational work [86–88]. But more advances have been achieved with hyperelastic or hyper-viscoelastic constitutive models and finite deformation, e.g., reconstructive surgery [14, 89–91].

When we also consider an individualized treatment for every patient [32], another requirement to improve surgical simulation is to acquire the accurate geometry like patient-specific approach [31] rather than the simplified model [92]. Taking advantage of graphical technology such as MRI [33] or CT scan [34], patient-specific geometry

can be achieved to implement FEM. However, the complexity of geometry causes non-trivial effort to create hexahedral dominant mesh [93]. To circumvent this hardship, most commonly used approach is to increase the density of mesh using tetrahedral mesh [94] or technically more elegant method is to employ meshless Total Lagrangian explicit dynamics algorithm when accuracy of individual displacements or forces is of less importance than that of overall reaction displacements or forces [95]. High computational cost, however, is inevitable for more accurate geometry. In this regard, nonlinear FEM has been implemented with graphics processing unit (GPU) to reduce computation time and make surgical simulation possible in terms of real-time utilization [96].

1.5 Overview of the dissertation

The main motivation behind this dissertation is to improve reconstructive surgery based on computational modeling of skin mechanics. As shown in Fig. 1.3, each stage of surgery has basic scientific gaps regarding the role of mechanics. Chapter

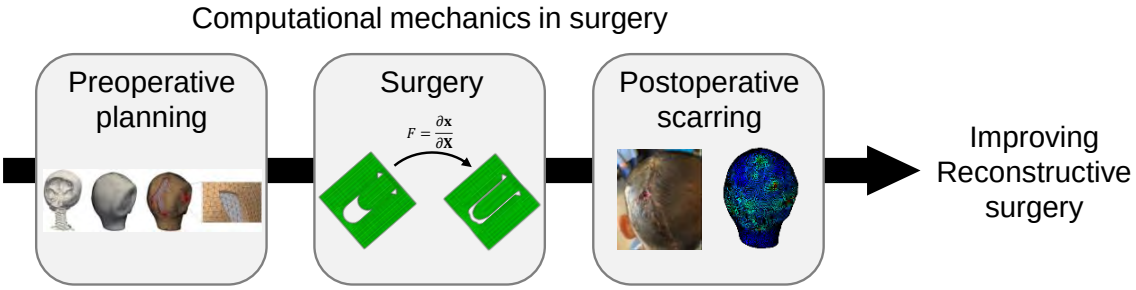

Fig. 1.3.: Pipeline on how to improve reconstructive surgery through computational mechanics framework from preoperative planning to postoperative scarring: The schematic accounts for main stream of this dissertation. At preoperative stage, virtual surgery simulation requires patient-specific geometry and skin property to obtain reliable stress contour. During surgery, possible any uncertainty factors are thoroughly considered, and corresponding calculation of strain and stress guides more robust choice on reconstructive surgery in terms of size of defect, age and gender, and fiber orientation. At postoperative step, individualized stress map is projected to the corresponding patient's surgery region to take into consideration correlation between stress and wound healing process.

2 aims for improving skin expansion protocol based on quantitative study of skin growth using porcine experiment and its kinematics analysis. Chapter 2 has been published in Journal of the Mechanical Behavior of Biomedical Materials. Reprinted from [97], Copyright 2018, with permission from Elsevier. This study demonstrates that skin *in vivo* is not stress free, and precisely quantifies how this stress-free state changes in tissue expansion. Chapter 3 is also focused on tissue expansion. Based on the quantification of the growth and pre-strain fields of skin seen in the animal model and the knowledge that the observed variablity is also a feature of tissue expansion in humans, Chapter 3 presents a novel methodology to account for uncertainty of mechanical and biological responses in tissue expansion. Chapter 3 has been published as a journal paper in Computer Methods in Applied Mechanics and Engineering. Reprinted from [98], Copyright 2020, with permission from Elsevier. Chapter 4 investigates the characteristics of incompatibility of growing tissues and the connection to residual stress. Representative growth scenarios as well as actual biomedical applications are scrutinized in order to connect incompatibility and its residual stress, which constitute a foundation to understand stress-free configuration in biological tissues indispensable for accurate prediction of stress contours upon reconstructive surgery. Chapter 4 has been submitted and in revision. In Chapter 5, we move away from skin growth and the question of the stress-free configuration, and we focus on the inverse problem to obtain mechanical properties of skin from *in vivo* suction measurements. The computational modeling of suction tests takes into account anisotropic nature of skin, as well as its nonlinear hyperelastic response. The solution of the inverse problem is built through a Bayesian framework, which can provide us with an insight on epistemic as well as aleatory uncertainty. The other ingredient for the preoperative planning simulations is to be easily able to create accurate patient-specific models. Chapter 6 thus focuses on the use of computer vision technologies to enable inexpensive geometry acquisition to feed into a personalized finite element model. Chapter 6 has been published in Journal of Biomechanics. Reprinted from [99], Copyright 2018, with permission from Elsevier. Chapter 7 also

deals with patient-specific models of reconstructive surgery. In Chapter 7, we investigate rotation flaps in the scalp. Chapter 7 has been submitted and in revision. Chapter 8 then focuses on the inherent challenge of creating virtual surgery models that can account for uncertainty in the material parameters. The propagation of uncertainty in nonlinear, computationally expensive physics-based models, such as the ones needed for preoperative planning, requires the development of reduced order and surrogate models for these applications. Chapter 8 has been published as a journal paper in Biomechanics and Modeling in Mechanobiology. Reprinted by permission from [100], Springer Nature, Copyright 2018. In Chapter 9, we take a step back from the patient-specific cases and we instead tackle a general investigation of the stress signatures of the most common flap designs. Continuing the theme from the previous chapter, in Chapter 9, we use reduced order and surrogate models to understand how different lesion sizes and changing mechanical properties dictate the corresponding stress contour on the skin. Chapter 9 has been published in Journal of the Mechanics and Physics of Solids. Reprinted from [101], Copyright 2019, with permission from Elsevier. Finally, in Chapter 10, we focus on optimization of each local flap design discussed in the previous chapter. Chapter 10 has been submitted for publication.

2. IMPROVING TISSUE EXPANSION PROTOCOLS THROUGH COMPUTATIONAL MODELING

Abstract: Tissue expansion is a common technique in reconstructive surgery used to grow skin *in vivo* for correction of large defects. Despite its popularity, there is a lack of quantitative understanding of how stretch leads to growth of new skin. This has resulted in several arbitrary expansion protocols that rely on the surgeon's personal training and experience rather than on accurate predictive models. For example, choosing between slow or rapid expansion, or small or large inflation volumes remains controversial. Here we explore four tissue expansion protocols by systematically varying the inflation volume and the protocol duration in a porcine model. The quantitative analysis combines three-dimensional photography, isogeometric kinematics, and finite growth theory. Strikingly, all four protocols generate similar peak stretches, but different growth patterns: Smaller filling volumes of 30 ml per inflation did not result in notable expander-induced growth neither for the short nor for the long protocol; larger filling volumes of 60 ml per inflation trigger skin adaptation, with larger expander-induced growth in regions of larger stretch, and more expander-induced growth for the 14-day compared to the 10-day expansion protocol. Our results suggest that expander-induced growth is not triggered by the local stretch alone. While stretch is clearly a driver for growth, the local stretch at a given point is not enough to predict the expander-induced growth at that location. From a clinical perspective, our study suggests that longer expansion protocols are needed to ensure sufficient growth of sizable skin patches.

2.1 Motivation

Tissue expansion is a popular technique in reconstructive surgery to grow skin *in vivo* in order to correct large cutaneous defects [102]. This technique was introduced in 1957 by Neumann [103] and has since become ubiquitous to reconstruct breasts after mastectomy, to resurface giant nevi, and to treat burn wounds [104–106]. Tissue expansion relies on the unique capacity of living tissue to adapt to mechanical loading through growth and remodeling [107, 108]. Yet, despite the popularity of this procedure, we lack a quantitative understanding of how exactly deformation leads to the growth of new tissue. Not surprisingly, numerous arbitrary protocols have been proposed, depending on the surgeon's experience, training, and personal preference.

In tissue expansion, the surgeon subcutaneously inserts a medical device resembling a balloon called the tissue expander. The device is filled with saline solution at different time points over the course of several weeks. At the end of the inflation process, the expanders are removed and the skin stays as a dome-like structure revealing growth or, equivalently, permanent area changes. In the clinical setting, the surgeon has two main variables to control the tissue expansion process: inflation timing and inflation volume. The optimal design of a skin expansion protocol remains controversial, while some physicians advocate for rapid expansion others favor a longer protocol; some propose to inflate the expander to a larger volume while others prefer smaller amounts of fluid at each inflation step [7, 104, 109, 110]. Here we explore four different protocols of expansion in a porcine model to compare the effect of short or long protocol times, and small or large inflation volumes on skin growth and remodeling.

Another important question when new skin is created in response to stretch is whether or not there are changes in the tissue microstructure that accompany the growth process. While it is apparent that the new tissue looks and feels very similar to the original skin, some remodeling trends have been reported at the microscopic scale [111]. The epidermis, the top layer of skin that is mainly composed of keratinocytes,

generally becomes thicker following tissue expansion [112]. In the dermis, the bottom layer of skin that is primarily made up of collagen, the fiber morphology becomes more disorganized [113]. Here we explore the effect of the four different expansion protocols on the skin microstructure by analyzing histological images.

Characterizing the mechanics of tissue expansion has the advantage that skin is a thin membrane exposed to the outside environment. Thus, imaging systems can be developed to study skin mechanics non-invasively *in vivo* over long periods of time. Here we use three-dimensional photography to capture the geometry of skin in the operating room. Three-dimensional photography based on stereo vision has made significant progress in the last decade. It is now possible to use handheld cameras to capture three-dimensional surfaces with a minimal experimental setup and high accuracy [114]. The advantage of such system is that noninvasive measurements can easily be performed in clinical settings such as the operating room, either for an animal model as we show here, or for translation of this protocol to human patients, which we intend to do in the near future. The work presented here closely follows our previous work on skin expansion biomechanics [115–117]. In our previous studies, we used multi-view stereo to capture three-dimensional geometries. Here we use three-dimensional photography instead of multi-view stereo, but continue to use the same methodology for the mechanical analysis as before. Our approach combines isogeometric kinematics and the continuum theory of finite growth. In addition to our previous methodology, here we collect punch biopsies at the end of the protocol for further histological analysis. The topology of the collagen network and the geometry of the epidermis are crucial for skin mechanical and frictional behavior [55, 118–120]. This auxiliary analysis allows us to study, for the first time, how growth of skin at the tissue scale is related to microstructure changes.

Isogeometric analysis relies on B-spline parameterizations of the geometry [121]. Isogeometric analysis is extremely well-suited for studying skin mechanics since B-spline basis functions can be constructed with high continuity, enabling thin shell descriptions [122] and a smooth representation of the geometry with a relatively coarse

mesh [116]. Furthermore, we express all surfaces in terms of the same parameter domain, such that computation of the deformation gradient between any two configurations is easily achieved with curvilinear coordinates [115]. To estimate the amount of total growth, we assume that the total deformation is a combination of prestrain, elastic deformation, and total growth, through a multiplicative split of the deformation gradient [123]. The underlying finite growth theory has become a well-established framework to describe the mechanical adaptation of biological tissues [124].

The work presented here sheds new light on the impact of inflation volume and protocol duration on the resulting skin deformation and growth patterns and further establishes new technologies that allow us to quantify skin growth and remodeling in an *in vivo* animal model over long periods of time.

2.2 Methods

2.2.1 Porcine model of skin expansion

Four different models of expansion are illustrated in Fig. 2.1. The protocols mimic different clinical expansion strategies. The effect of small versus large inflation volumes is studied by injecting either 30 ml or 60 ml at each inflation step. For the long expansion protocol, the total duration of the experiment is 14 days, with two inflation steps 7 days apart, for the shorter expansion protocol, the second inflation step is only 4 days prior to the end of the experiment resulting in a 10-day protocol.

The experimental methodology used in this study closely follows our prior work with the exception of using three-dimensional photography instead of multi-view stereo, and the additional collection of punch biopsies for histology at the end of the process [115–117]. Briefly, animals are provided with food and water *ad libitum* per veterinary recommendations throughout the study. All animals undergo grid tattooing procedure at age 6-7 weeks, with tissue expander placement surgery performed 1 week after the tattooing procedure. Four square grids are tattooed on the back of an animal. For either the front or the back grids, one side is used for expansion while

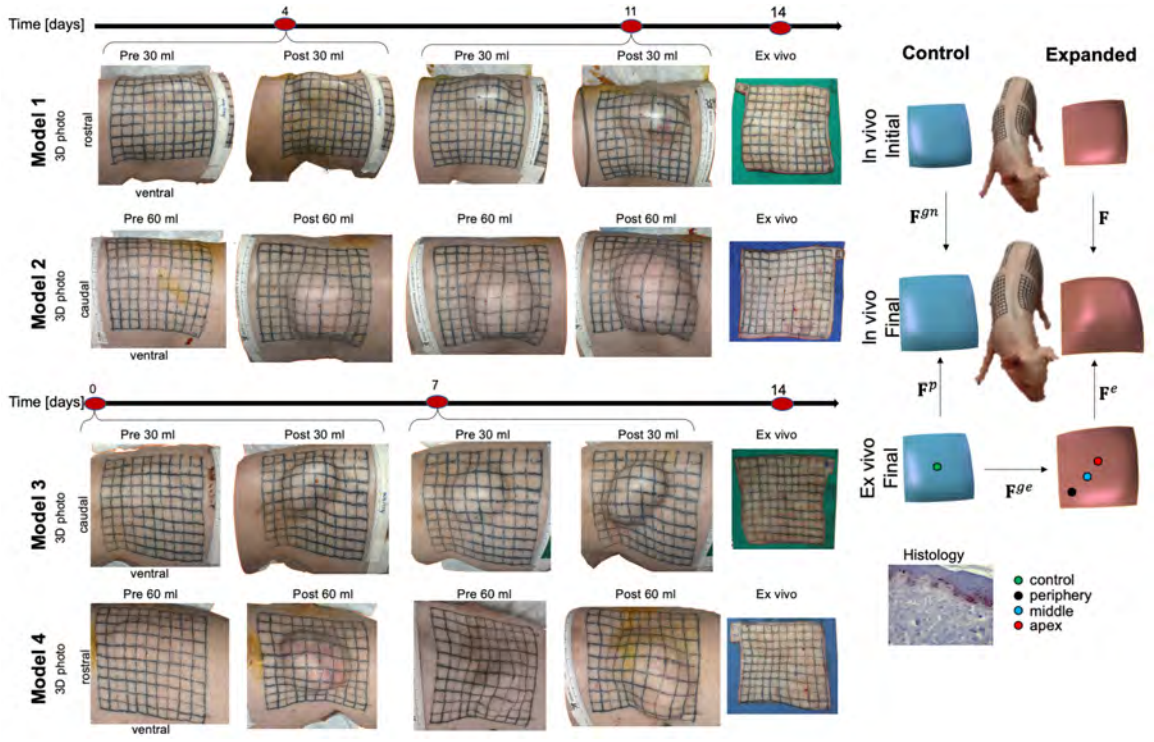

Fig. 2.1.: The four different experimental protocols for porcine models of skin expansion. Model 1 is 10-day expansion with small inflation volumes, model 2 is 10-day expansion with large volumes, model 3 is 14-day expansion with small volumes, and model 4 is 14-day protocol with large volumes. A tattooed grid defines the area of interest and allows for deformation tracking. Three-dimensional photos are taken at every inflation step, before and after inflation. At the end of the protocol, animals are sacrificed and grids excised. The deformations are analyzed using isogeometric analysis within the finite growth framework in which the deformation is a composition of prestrain $\mathbf{F}^p$, deformation induced by expansion $\mathbf{F}$, elastic deformation after expansion $\mathbf{F}^e$, and total growth $\mathbf{F}^g$. Additionally, natural growth $\mathbf{F}^{gn}$ is measured in the control patches in order to isolate the expander-induced growth. Punch biopsies are collected for the control and expanded grids to quantify changes in microstructure by analyzing histological slides.

the contralateral side serves as control. To study the four different protocols, we used two animals, one for the small and one for the large volume protocols.

On the expander side, a two-stage rectangular tissue expander with 120 ml filling capacity (PMT Corporation, catalogue number #3610-06-02, Chanhassen, MN) is inserted subcutaneously underneath the grid and the incisions are sutured and left to heal. The tissue expanders are placed in the plane immediately superficial to the

overlying muscle fascia, i.e., between muscle fascia and subcutaneous fat. This is the same plane in which tissue expanders are inserted clinically in humans. Once the animal has fully recovered from the expander placement surgery, the inflation protocol begins. At each inflation step, we use a syringe to inject the desired amount of saline solution into the expander through a remote inflation port.

To capture the geometry, we take three-dimensional photos immediately before and after each inflation step. We use a handheld commercial system (Vectra H1, Canfield, New Jersey). At the end of the tissue expansion protocol, the animals are sacrificed. Three-dimensional photos of the grids are taken on that day, first *in vivo* and then *ex vivo*, after the entire patch has been excised. Following three-dimensional photo acquisition *ex vivo*, punch biopsies are collected. For the control side a single biopsy is needed, while for the expanded size we harvest three samples, one at the apex of the expander, one at the periphery of the expander, and one at an intermediate location between the apex and the periphery as illustrated in Fig. 2.1. Model 1 is the 10-day expansion protocol with small inflation volumes, model 2 is 10-day expansion with large volumes, model 3 is the long, 14-day expansion with small volumes, and model 4 is the short expansion with large volumes.

2.2.2 Isogeometric analysis and finite growth theory

Isogeometric analysis relies on B-spline surface reconstruction [125]. We start with the same tattooed grid for all the skin patches and assign the same initial parameter space, i.e., same mesh, to every patch at all time points. B-splines can easily reconstruct smooth surfaces due to the availability of high order basis functions, even with a coarse set of control points [122]. In our case, the grids provide a set of 121 material points that are fitted with quadratic B-splines using open source spline libraries (SINTEF, Norway). The parameter space is chosen to be $(\xi, \eta) \in [0, 10] \times [0, 10]$. Hence, for a given grid at a specific point in time, the surface $\mathcal{S}(\xi, \eta)$ is a mapping from the parameter space to the physical $\mathbb{R}^3$ space. Given a pair of

surfaces, we compute the deformation gradient using the corresponding metric tensors associated with the surface embeddings. For example, given $\mathcal{S}^o$ as reference and $\mathcal{S}^f$ as the current surface, respectively, we construct the covariant base vectors

$$\mathbf{G}_1^o = \frac{\partial \mathcal{S}^o}{\partial \xi} \quad \text{and} \quad \mathbf{G}_2^o = \frac{\partial \mathcal{S}^o}{\partial \eta}, \tag{2.1}$$

for the reference surface, and

$$\mathbf{G}_1^f = \frac{\partial \mathcal{S}^f}{\partial \xi} \quad \text{and} \quad \mathbf{G}_2^f = \frac{\partial \mathcal{S}^f}{\partial \eta}, \tag{2.2}$$

for the current surface. Such base vectors span only the surface tangent space and we complement them with the surface normals

$$\mathbf{G}_3^o = \frac{\mathbf{G}_1^o \times \mathbf{G}_2^o}{||\mathbf{G}_1^o \times \mathbf{G}_2^o||} \quad \text{and} \quad \mathbf{G}_3^f = \frac{\mathbf{G}_1^f \times \mathbf{G}_2^f}{||\mathbf{G}_1^f \times \mathbf{G}_2^f||}. \tag{2.3}$$

The contravariant base vectors are defined via the identity $\mathbf{G}_i \cdot \mathbf{G}^j = \delta_i^j$. The deformation gradient is

$$\mathbf{F} = \mathbf{G}_i^o \otimes \mathbf{G}^{fj}, \tag{2.4}$$

where the summation convention was used.

To account for finite volumetric growth, we multiplicatively splits the deformation gradient into total growth and elastic contributions, $\mathbf{F}^g$ and $\mathbf{F}^e$ [126]. Here, the total deformation gradient of the skin surface captures both, the *in vivo* expansion process $\mathbf{F}$ and the amount of prestrain $\mathbf{F}^p$ [127]. The determinant of the deformation gradient obeys the same split. In our case, the determinant of the deformation gradient is equivalent to the area change ϑ,

$$\mathbf{F}\mathbf{F}^p = \mathbf{F}^e\mathbf{F}^g \quad \text{and} \quad \vartheta\vartheta^p = \vartheta^e\vartheta^g. \tag{2.5}$$

The tensors $\mathbf{F}$ and $\mathbf{F}^e$ are obtained from the expanded patch whereas $\mathbf{F}^p$ is calculated from the control patch by mapping the *ex vivo* control surface to the *in vivo* control surface. We can then calculate the total growth tensor, $\mathbf{F}^g = \mathbf{F}^{e-1}\mathbf{F}\mathbf{F}^p$. The total growth tensor can further be decomposed into two contributions, naturally-induced growth $\mathbf{F}^{gn}$ and expansion-induced growth $\mathbf{F}^{ge}$,

$$\mathbf{F}^g = \mathbf{F}^{ge}\mathbf{F}^{gn} \quad \text{and} \quad \vartheta^g = \vartheta^{ge}\vartheta^{gn}\,. \tag{2.6}$$

In addition to changes in area, we compute changes in length along the two directions of interest. For any of the skin patches at day 0, the vector $\mathbf{G}_1$ corresponds to the longitudinal axis of the animal, while the vector $\mathbf{G}_2$ is aligned with the transverse direction. These vectors, however, are not necessarily of unit length. We then define the unit vectors

$$\mathbf{E}_1 = \frac{\mathbf{G}_1}{||\mathbf{G}_1||} \quad \text{and} \quad \mathbf{E}_2 = \frac{\mathbf{G}_2}{||\mathbf{G}_2||}\,. \tag{2.7}$$

The deformations due to the expansion process along the two directions of interest are the stretches

$$\lambda_1 = \sqrt{\mathbf{E}_1^\top \mathbf{C}\mathbf{E}_1} \quad \text{and} \quad \lambda_2 = \sqrt{\mathbf{E}_2^\top \mathbf{C}\mathbf{E}_2}\,, \tag{2.8}$$

where $\mathbf{C} = \mathbf{F}^\top\mathbf{F}$ is the right Cauchy-Green deformation tensor. We further assume that prestrain and total growth leave the two directions unchanged,

$$\begin{aligned} \mathbf{F}^p &= \lambda_1^p\,\mathbf{E}_1 \otimes \mathbf{E}^1 + \lambda_2^p\,\mathbf{E}_2 \otimes \mathbf{E}^2 \\ \mathbf{F}^g &= \lambda_1^g\,\mathbf{E}_1 \otimes \mathbf{E}^1 + \lambda_2^g\,\mathbf{E}_2 \otimes \mathbf{E}^2\,, \end{aligned} \tag{2.9}$$

such that a multiplicative split analogous to Eq. (2.5) is possible for the longitudinal and transverse deformations.

2.2.3 Histology analysis

Following excision of the skin patches, we collect punch biopsies at different locations as indicated in Fig. 2.1. For the control patch, only one sample is collected whereas for the expanded grids, three points are marked with different colors before excision and biopsies are taken *ex vivo*: at the apex (red), at an intermediate point (blue), and at the periphery of the expanded area (black). We use pentachrome staining to visualize the different constituents of skin. In this study we are interested in the thickness of the epidermis and the collagen network morphology. Histological slides are processed with the OrientationJ plugin in imageJ [128] to quantify collagen orientation in the dermis [129]. For a given histological slide, we compute a coherency image which contains local alignment information normalized between 0 and 1. Briefly, for a given image $I(x, y)$, we compute the gradients $I_x = \partial I/\partial x$ and $I_y = \partial I/\partial y$ [129]. From these vector fields, we compute the tensor field $\mathbf{J}$,

$$\mathbf{J} = \begin{pmatrix} \langle I_x, I_x \rangle_w & \langle I_x, I_y \rangle_w \\ \langle I_y, I_x \rangle_w & \langle I_y, Y_y \rangle_w \end{pmatrix}, \tag{2.10}$$

where $\langle f, g \rangle_w = \int_w f \cdot g \, \mathrm{d}A$ denotes the inner product and $w(x, y)$ is a Gaussian weighting function such that the inner product $\langle f, g \rangle_w$ serves as a smoothing filter with a kernel w. Coherency is then defined as

$$C(x, y) = \frac{\lambda_{\max} - \lambda_{\min}}{\lambda_{\max} + \lambda_{\min}}, \tag{2.11}$$

with λ_{max} and λ_{min} the largest and smallest eigenvalues of $\mathbf{J}$. We report the average of the coherency image. OrientationJ also outputs a distribution of the orientations over the entire image. We fit a Gaussian to the fiber distribution and define the standard deviation of such distribution as dispersion. Finally, we measure the thickness of the epidermis using imageJ with a novel tool proposed recently by our groups and described in detail in a separate publication [130].

2.3 Results

2.3.1 Total deformation

Fig. 2.1 shows the three-dimensional photographs obtained at each inflation step and Fig. 2.2 depicts the contour plots of the area change ϑ over the expanded three-dimensional geometries. As expected and in agreement with our previous studies [116, 131], strains are greater at the apex of the expander compared to the periphery. This can be appreciated also in Fig. 2.2, last column, which shows the deformation for specific points of the expanded patch. The red, blue, and black curves correspond to points at the apex, the middle, and the periphery respectively. The same expander was used in all models, however, when the expanders are not yet filled to their capacity, their shape can show some variation as seen in Fig. 2.1. Additionally, two of the expanders moved during the protocol. In model 1, the expander migrated anteriorly by approximately 2 cm. In model 4, the expander migrated posteriorly 1 cm, and ventrally 2 cm. Despite these displacements, the expanders all remained within the tattoo grid at sacrifice. Over the two weeks of the experiment, the overall trend is an increase in deformation at all points. Not all deformation is expander-induced strain. Some deformation is related to the natural growth of the animal measured on the control patches, see Tables 2.1 and 2.2. Greater deformation is consistently seen for the apex point (red) in all expansion models. Surprisingly, the large volume protocols result in similar peak strain as the small volume protocols, see Table 2.2, first column. However, in the large volume models, the blue and black points show progressively less deformation, with $\vartheta \in [1.1, 2]$ at the end time point, whereas in the small volume protocols the deformation is similar for the three points of interest, $\vartheta \in [1.5, 2]$.

Fig. 2.3 shows the stretches $\lambda_1 = ||\mathbf{F}\mathbf{E}_1||_2$ and $\lambda_2 = ||\mathbf{F}\mathbf{E}_2||_2$ in the directions of interest. Recall that $\mathbf{E}_1$ is aligned with the longitudinal axis of the animal at the beginning of the protocol and $\mathbf{E}_2$ is a unit vector field in the transverse orientation. Similarly to what is seen in the total area plots, the stretches for the two principal directions show greater deformation in the apex and less in the periphery

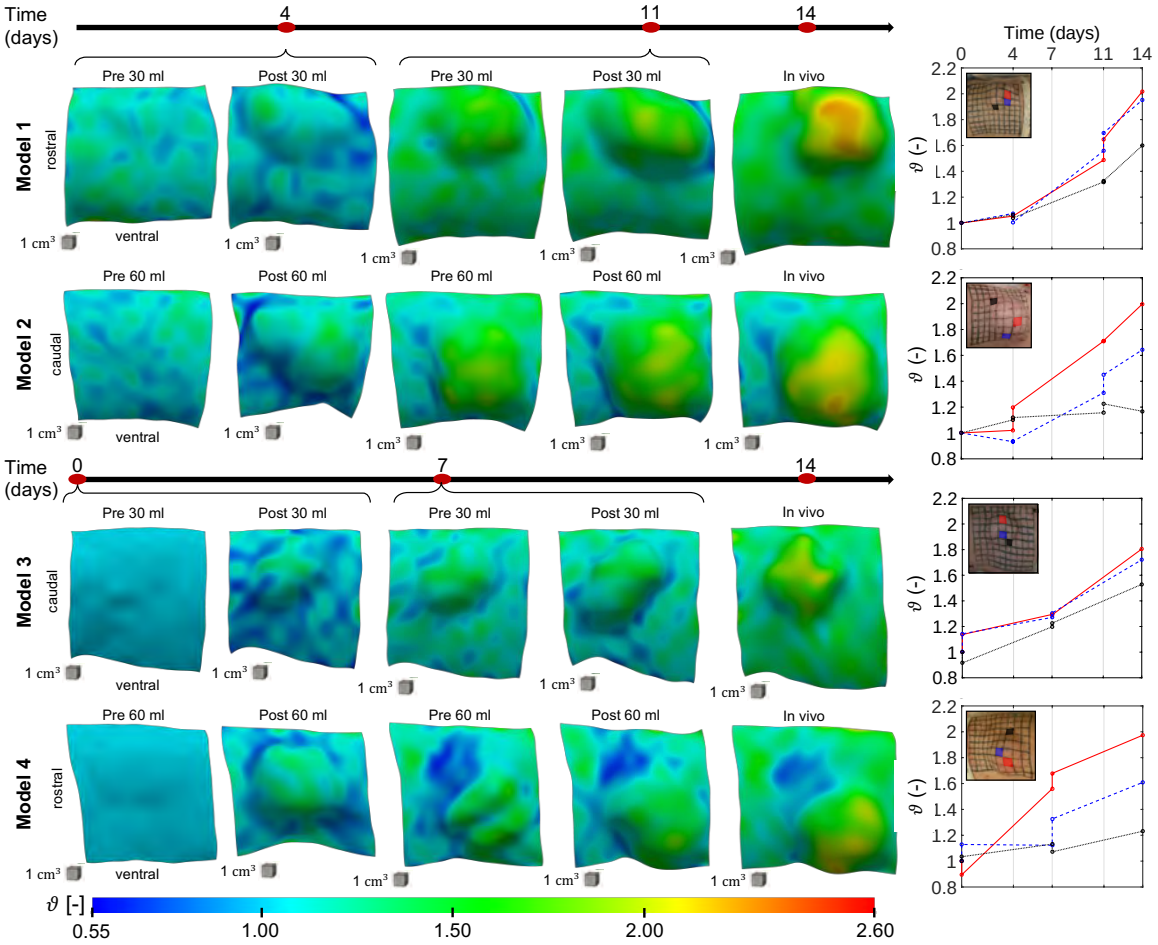

Fig. 2.2.: Area change for the total deformation $\vartheta = \det(\mathbf{F})$ is calculated with respect to the initial *in vivo* state. The rows show the different inflation protocols: The last column shows the deformation for specific points of interest: The red curve corresponds to a point at the apex of the expander, the black curve is a point at the periphery, and the blue curve is an intermediate point. The overall trend is an increase in deformation, with the apex point (red) showing the greatest deformation followed by the intermediate (blue) and the periphery (black) points. Peak stretches are similar across all protocols.

of the expanded area. Another trend that we have consistently observed in our previous studies is that stretches in the longitudinal axis are greater than transverse deformations [115].

Table 2.1.: Average values and standard deviations for total deformation ϑ, elastic deformation ϑ^e, prestrain ϑ^p, total growth ϑ^g, and natural growth ϑ^{gn} calculated over the entire grid for each of the inflation models. Standard deviation over a skin patch is large for the components of the deformation directly affected by the expansion process. Natural growth, measured on the control patches, is a more homogeneous field for all models and hence shows lower standard deviation.

Model	**Timing**	**Volume**	ϑ [-]		ϑ^e [-]		ϑ^p [-]		ϑ^g [-]		ϑ^{gn} [-]	
			avg	std	avg	std	avg	std	avg	std	avg	std
Model 1	Short	Small	1.47	0.23	1.20	0.19	1.22	0.17	1.49	0.20	1.38	0.10
Model 2	Short	Large	1.35	0.30	1.24	0.21	1.15	0.11	1.24	0.17	1.28	0.13
Model 3	Long	Small	1.36	0.18	1.18	0.22	1.30	0.17	1.39	0.19	1.37	0.11
Model 4	Long	Large	1.31	0.28	1.16	0.15	1.10	0.11	1.23	0.21	1.29	0.13

Table 2.2.: Total deformation ϑ, elastic deformation ϑ^e, prestrain ϑ^p, total growth ϑ^g, and natural growth ϑ^{gn} are calculated for the three points of interest. Red (apex of the expander), Blue (intermediate point between the apex and the periphery), Black (periphery of the expander). The red point was consistently deformed the greatest in all models and the peak value was close for all cases (first column). Total growth in the small volume cases was lower at the apex compared to the large volume protocols regardless of whether the inflation was over 10 or 14 days. In contrast, total growth was higher in the blue and black points in the small volume models compared to the larger volumes.

Model	**Points**	ϑ [-]	ϑ^e [-]	ϑ^p [-]	ϑ^g [-]	ϑ^{gn} [-]
Model 1	Red	2.02	1.64	1.17	1.45	1.34
	Blue	1.95	1.47	1.19	1.58	1.36
	Black	1.60	1.22	1.06	1.39	1.30
Model 2	Red	1.99	1.65	1.27	1.54	1.27
	Blue	1.64	1.58	1.19	1.23	1.23
	Black	1.17	1.16	1.17	1.19	1.39
Model 3	Red	1.80	1.60	1.18	1.32	1.30
	Blue	1.72	1.60	1.16	1.25	1.33
	Black	1.53	1.31	1.31	1.53	1.44
Model 4	Red	1.97	1.45	1.00	1.36	1.07
	Blue	1.61	1.26	1.05	1.34	1.21
	Black	1.23	1.06	1.04	1.22	1.47

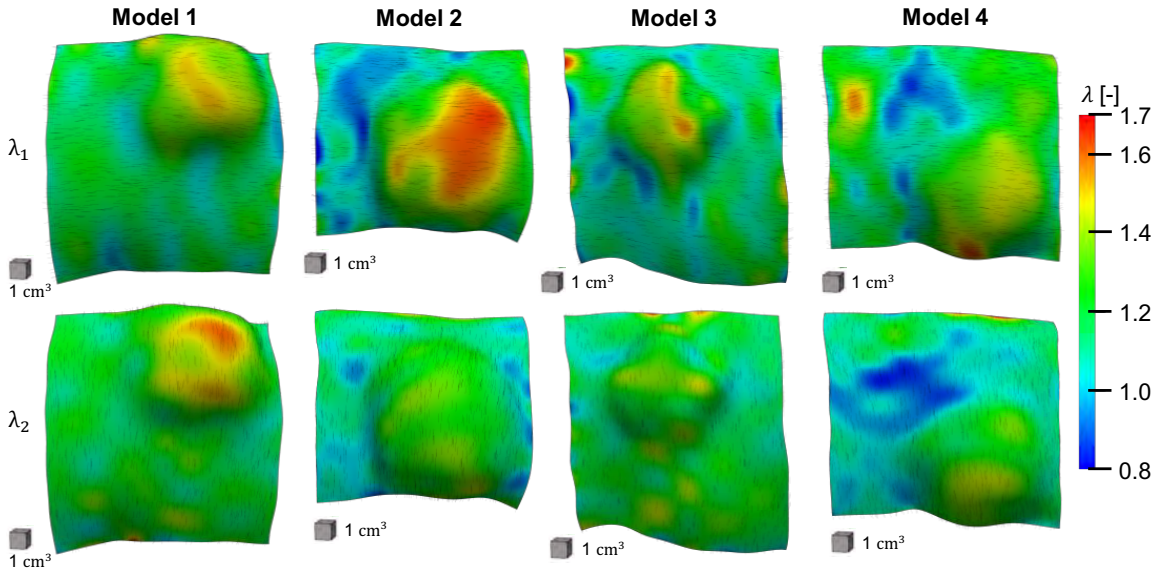

Fig. 2.3.: Total stretch along the two directions of interest. λ_1 is the stretch in the longitudinal axis $\mathbf{E}_1$ of the animal, while λ_2 is the stretch in the transverse direction $\mathbf{E}_2$. The columns show the contours of λ_1 and λ_2 for the different inflation protocols. The vector fields associated to the current configuration, $\mathbf{FE}_1$ and $\mathbf{FE}_2$ where $\mathbf{F}$ is deformation gradient tensor, are also shown.

2.3.2 Elastic deformation, prestrain, and growth

At the end of the expansion protocol, excision of the expanded patch reveals the elastic deformation $\mathbf{F}^e$ while excision of the control patch allows quantification of the prestrain $\mathbf{F}^p$. Then, using $\mathbf{F}$ from the previous section and employing Eq. (2.5) we calculate the total growth $\mathbf{F}^g$. We further use the control patch to measure the natural growth $\mathbf{F}^{gn}$. Fig. 2.4 shows the individual components of the area change for the different experimental models. The elastic area change ϑ^e follows the pattern of the total area change ϑ: Upon excision, the skin retracts the most in regions of highest *in vivo* area change. Prestrain fields ϑ^p are measured in the control patches, thus, they are not directly affected by the expansion procedure and have a less defined spatial pattern. There is some variation between the different animals. For model 1 and model 3, the prestrain is greater towards the ventral side of the animal whereas for models 2 and 4, the prestrain is overall lower and more uniform, see Table 2.1.

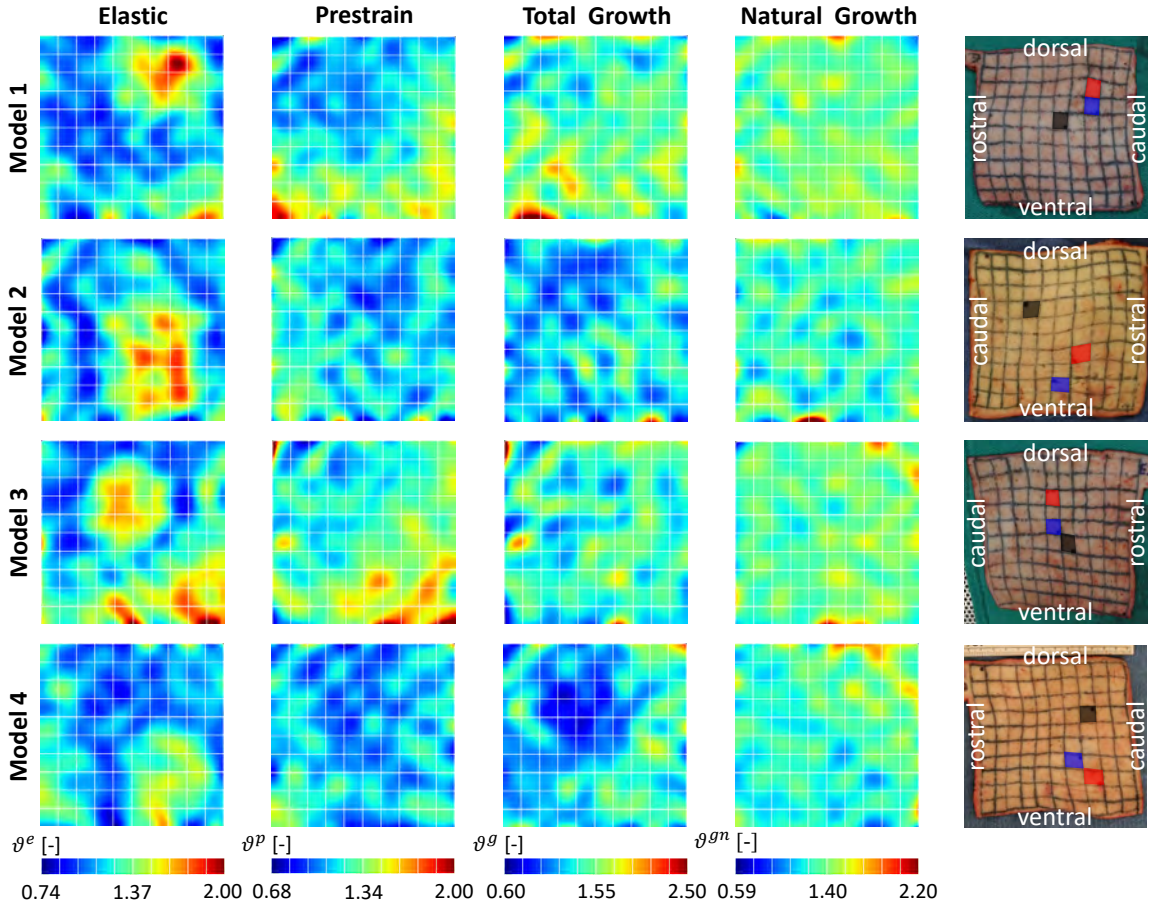

Fig. 2.4.: Contour plots over the parameter space for elastic deformation ϑ^e, prestrain ϑ^p, total growth ϑ^g, and natural growth ϑ^{gn}. The elastic deformation reflects the pattern of the total deformation. Prestrain fields are calculated based on the control patch and not affected by the expansion process, nonetheless some spatial variation is observed as well as inter-specimen variability. Total growth is a combination of natural and expander induced growth. The natural growth fields are uniform in all cases.

The total growth for model 1 and model 3 is larger compared to models 2 and 4. For all protocols, the natural growth fields, measured on the control patches, have the lowest spatial variation among all the components of the deformation. This is also captured in the standard deviation values summarized in Table 2.1.

Growth attributed to the expansion process alone is the key component of deformation for this study. This deformation field, $\mathbf{F}^{ge}$, can be computed using Eq. (2.6) based on the total growth and natural growth fields. Since the natural growth

fields have the lowest spatial variation, the heterogenous patterns of the total growth fields are due to the expansion-induced growth. However, most of the total growth can be attributed to the natural growth of the animals. In other words, the total growth fields, measured in the expanded patches, have to be normalized by the natural growth seen in the control patches. The total growth field is always greater than 1, indicating that skin increases its area for all expansion protocols. However, as seen in the control patches, some growth would occur naturally even in the absence of an expander. The expander-induced growth field then captures the area changes with respect to the naturally grown skin, isolating the contribution of the expansion process. The contours corresponding to the expander-induced growth show that for the larger filling volumes, in model 2 and model 4, zones under larger deformation show larger growth, whereas for the small volume models there is no clear spatial pattern with relation to the expander placement, see Fig. 2.5.

For model 1 and model 3, which were inflated with 30 ml at each inflation step, the expander-induced growth at the points of maximum deformation (red curves in Fig. 2.2) is only 8% and 2%, respectively, see Table 2.3. In contrast, for model 2 and model 4, with 60 ml inflation steps, the apex point reaches a similar deformation as seen in model 1 and model 3, but in this case, expander-induced growth was as large as 22% and 27%. For the small volume protocols, models 1 and 3, for which the intermediate and periphery points show similar deformation history compared to the apical point, the expander-induced growth is also within a narrow range. For the large volume protocols, models 2 and 4, where the three points of interest show markedly different deformation history, the expander-induced growth also shows notable variation. As just reported, the apical point showed the greatest *in vivo* deformation and greatest expander-induced growth in models 2 and 4. The points between the apex and the periphery show intermediate values of deformation and also modest expander-induced growth. The periphery points were deformed the least in model 2 and model 4, and show negative expander-induced growth ($\vartheta^{ge} < 1$), i.e., the skin at these locations shrinks compared to the naturally grown skin. Calculating the components of the

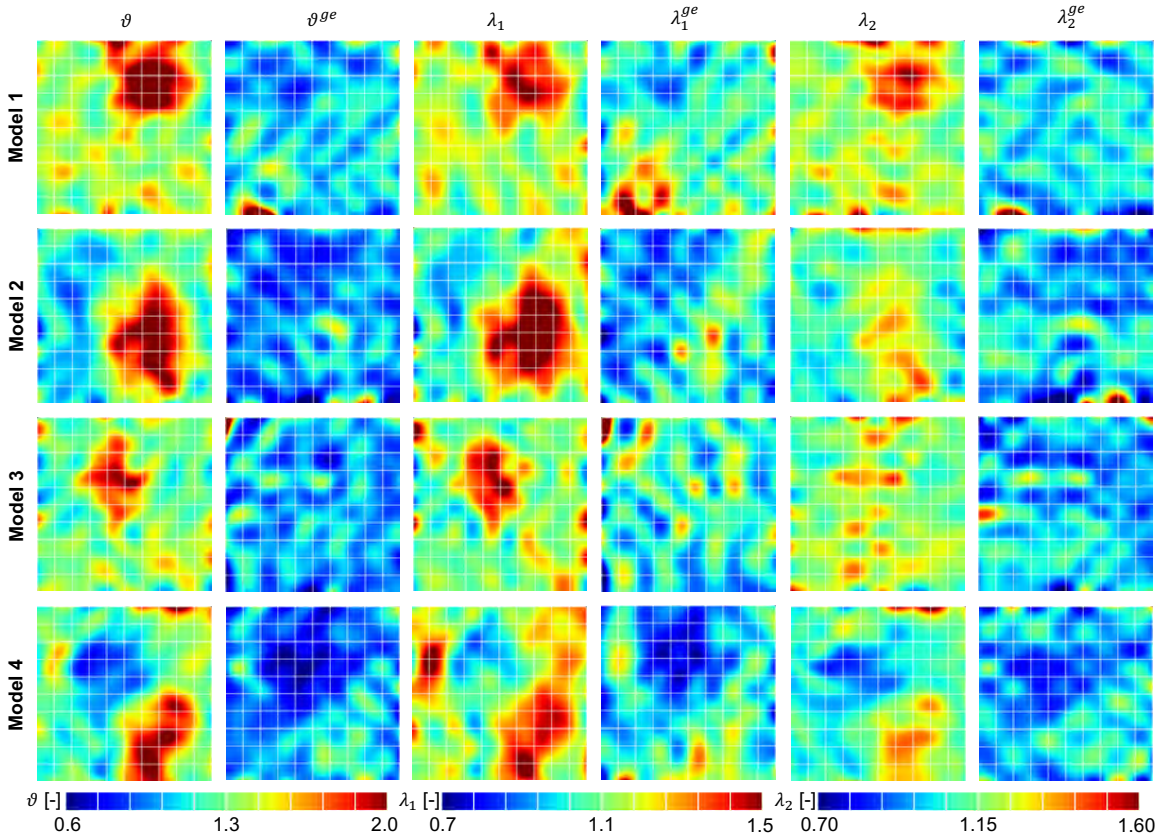

Fig. 2.5.: Contour plots over the parameter space for total *in vivo* deformation $\vartheta = \det(\mathbf{F})$, and expander-induced area growth $\vartheta^{ge} = \det(\mathbf{F}^{ge})$, as well as the split in the two directions of interest, $\lambda_1 = ||\mathbf{F}\mathbf{E}_1||_2$ and $\lambda_2 = ||\mathbf{F}\mathbf{E}_2||_2$ for the total deformation, and $\lambda_1^{ge} = ||\mathbf{F}^{ge}\mathbf{E}_1||_2$ and $\lambda_2^{ge} = ||\mathbf{F}^{ge}\mathbf{E}_2||_2$ for the expander-induced growth. The large volume protocols (models 2 and 4) show greater expander-induced growth at the apex of the expander which corresponds to the regions of higher total deformation. The small volume models do not show a well-defined spatial trend. Calculating the components of this growth field on the two directions of interest shows that the longitudinal direction $\mathbf{E}_1$ grows more in response to stretch compared to the transverse orientation.

expansion-induced growth λ_1^{ge} and λ_1^{ge} in the two directions of interest reveals a similar trend compared to the area changes. The longitudinal axis of the animal, which experiences greater deformations, also presents higher growth values in that direction.

Table 2.3.: Area growth attributed to the expansion process alone, ϑ^{ge}, and split in the two orientations of interest λ_1^{ge} and λ_2^{ge}. Values are calculated for the three points of interest: Red (apex of the expander), Blue (intermediate point between the apex and the periphery), Black (periphery of the expander). The red point, which was consistently deformed the greatest in all models, shows greater expansion-induced growth for the large volume models but not for the small volume ones. Expander-induced growth occurs primarily in the longitudinal axis of the animal.

Model	**Points**	ϑ^{ge} [-]	λ_1^{ge} [-]	λ_2^{ge} [-]
	Red	1.08	0.99	1.07
Model 1	Blue	1.16	1.10	1.06
	Black	1.07	1.04	1.03
	Red	1.22	1.25	0.99
Model 2	Blue	1.00	1.08	0.94
	Black	0.85	0.90	0.95
	Red	1.02	1.12	0.91
Model 3	Blue	0.94	1.00	0.93
	Black	1.06	1.02	1.06
	Red	1.27	1.19	1.08
Model 4	Blue	1.11	1.06	1.06
	Black	0.83	0.90	0.92

2.3.3 Changes in tissue microstructure

The incision for expander placement was made 2 cm away from the expander grid periphery; therefore, the area of expansion was remote from areas of the skin surgical scar. However, due to the natural foreign body response, a collagen capsule always forms around the tissue expander. This is observed clinically in humans as well. These capsules become firmer and thicker if there is a secondary insult such as radiation or infection. There was no infection in these animals and the peri-prosthetic capsule was soft in all cases. Fig. 2.6 shows sample histological images representative of the expansion models. These images correspond to the apex point which was subjected to the greatest deformation and showed the highest expansion-induced growth. Table 2.4 summarizes the results from the histological analysis. The epidermal thickness increased in the expanded patches compared to the controls, which is evident from looking at the images with the naked eye and then confirmed with the measurements.

Table 2.4.: Analysis of histological slides. Thickness of the epidermis was determined with imageJ with a method proposed by our group [130]. Collagen orientation was done with the ImageJ plugin OrientationJ [129] which outputs coherency and dispersion of the orientation distribution. Coherency is a local metric of alignment normalized between 0 and 1 whereas dispersion relates to the spread of the fiber orientation distribution of an entire image. No clear trend is seen between expanded and control patches regarding the orientation distribution. However, thickness of the epidermis was higher in expanded patches compared to controls.

Model	Epidermis thickness [μm]	Papillary coherency [-]	Reticular coherency [-]	Papillary dispersion [deg]	Reticular dispersion [deg]
Model 1	96.8 (sd 8.9)	0.46 (sd 0.01)	0.41 (sd 0.01)	15.11 (sd 1.08)	25.43 (sd 3.01)
Model 2	60.7 (sd 5.3)	0.57 (sd 0.02)	0.49 (sd 0.02)	13.02 (sd 1.20)	27.06 (sd 1.09)
Model 3	76.7 (sd 6.9)	0.48 (sd 0.02)	0.44 (sd 0.03)	15.25 (sd 1.42)	23.39 (sd 4.00)
Model 4	64.5 (sd 3.5)	0.50 (sd 0.02)	0.43 (sd 0.02)	16.96 (sd 3.82)	23.99 (sd 3.82)
Control 1	58.4 (sd 10.4)	0.55 (sd 0.02)	0.46 (sd 0.01)	9.85 (sd 1.96)	25.15 (sd 2.22)
Control 2	43.0 (sd 1.4)	0.55 (sd 0.01)	0.50 (sd 0.02)	15.02 (sd 0.95)	25.83 (sd 1.95)
Control 3	53.0 (sd 1.7)	0.45 (sd 0.02)	0.43 (sd 0.01)	16.32 (sd 0.67)	38.95 (sd 11.96)
Control 4	48.4 (sd 8.7)	0.50 (sd 0.03)	0.44 (sd 0.05)	14.40 (sd 0.32)	16.63 (sd 2.88)

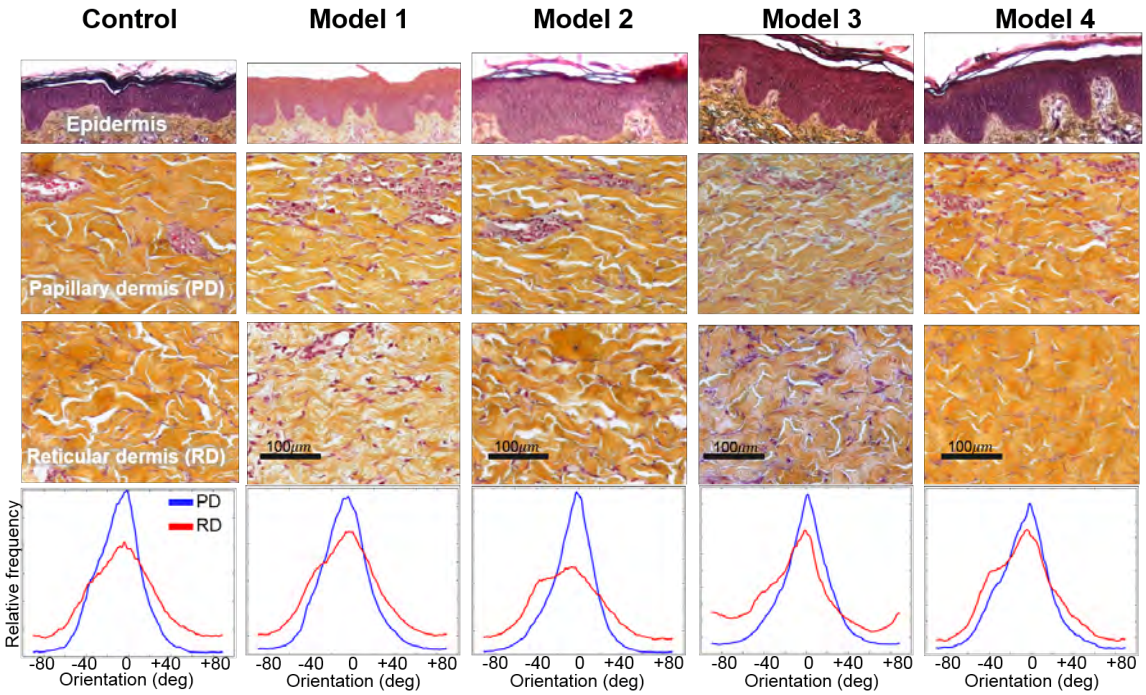

Fig. 2.6.: Pentachrome-stained histological slides corresponding to the apex point of the different models as well as a representative control. Collagen is visible in orange while cells are stained in purple. As expected, the epidermis, the top layer of the skin primarily made out of keratinocyte cells, thickens upon expansion (see also Table 2.4). The dermis is divided into two sublayers, the papillary dermis is immediately below the epidermis and the reticular dermis is underneath the papillary layer. Collagen bundles in the control skin appear thicker compared to the expansion protocols but no trend could be identified (see Table 2.4).

Results from the OrientationJ plugin did not show clear differences between expanded skin and controls. While in some cases the collagen network in the control case is thicker and more organized than the expanded patches, this is not true for all the models. In Fig. 2.6, the dermis is split into two sublayers. The papillary dermis is the top sublayer, just below the epidermis. The reticular dermis is the bottom sublayer. For the papillary dermis, coherency values are similar across all models and controls. The reticular coherency is slightly higher in the control cases, particularly in the 10-day expansion of model 1 and model 2. Interestingly, the papillary coherency is greater than the reticular coherency for both expanded skin and controls. The

dispersion of the fiber orientation does not provide any clear difference between the expansion protocols and the controls. Nonetheless, it is clear that the papillary dermis is more organized, and thus has a lower dispersion of the fiber orientation, compared to the reticular dermis in both expanded skin and controls.

2.4 Discussion

Tissue expansion is a popular technique to grow skin *in situ*; yet, the parameters that drive this procedure remain poorly understood. This study was particularly motivated by the lack of consensus regarding the optimal volume and timing of inflation [104, 132, 133]. Quantitative tools to predict the effects of the different process parameters is an important step towards improving efficiency and making the technology more applicable. Equipped with an innovative experimental design, we are able to characterize the mechanics of small or large inflation volumes for short or long inflation protocols. Our method is based on three-dimensional photography, isogeometric kinematics, and finite growth theory.

Our results confirmed previous experimental and computational results with greater deformation at the apex of the expander compared to the periphery [115, 116]. Interestingly, the maximum deformation was similar in response to all four protocols regardless of the amount of fluid in each inflation step. There are several possible explanations for this non-intuitive observation. The total *in vivo* deformation is a combination of elastic deformation, natural growth, and expander-induced growth. Natural growth is measured in the control skin and not directly affected by the expansion process; however, it does vary from one animal to another. Therefore, comparing the total *in vivo* deformation between animals ignores this source of variation. In fact, in the small volume experiments, the animals showed greater natural growth, which could help explain why the peak values of deformation were similar across all protocols. It is also possible that the supraphysiological growth at the expanded sites could lead to systemic changes affecting natural growth on the rest of the animal, including

skin in the control patches. Our previous work [115, 116] together with this study confirms that natural growth of the animals is on the order of 1 to 2% per day. While our previous protocols consisted of different inflation volumes and time points of inflation, we previously reported that the deformation at day 15, at a volume of 150 ml, was 1.43, similar to the values reported here. Prestrain is also measured in the control patches and, thus, not directly affected by the expansion process. However, there is also some variability in prestrain between animals independently of the expansion protocols. In the experiments reported here, average values of prestrain for model 1 and model 3 are within the previously reported ranges from 1.24 to 1.44. Prestrains for model 2 and model 4, however, are lower in this study, 1.10 and 1.15. Even in the presence of some variability, our data aligns with our previous observations.

For all four models, the average value of expander-induced growth was close to one, indicating little to no growth with respect to the natural growth field. This finding is not entirely surprising based on our previous work. We have reported expansion-induced growth of 1.54 for a 37-day expansion protocol [115] and 1.17 and 1.10 for two different 21-day protocols [116]. It is possible that 14 days is not long enough to capture significant amount of expander-induced growth over entire skin patches. However, our local contours reveal that some regions do indeed grow. Focusing on the apex, which was subjected to the largest deformation, we observe that for the small volume model 1 and model 3, the expander-induced growth was smaller compared to the large volume model 2 and model 4. This is important because for the apical points the elastic and total deformations were similar, suggesting that expander-induced growth may not just be a local effect. On the other hand, the intermediate and periphery points in the small volume experiments showed similar values of total deformation as the apex, and similar values of expander-induced growth. For the large volume experiments, the intermediate and periphery points showed progressively less deformation compared to the apex, and also less expander-induced growth. These findings support that the deformation pattern for a given patch is indeed related to the expander-induced growth field. One possibility is that the dif-

ference in the expander-induced growth fields between the small and large volume experiments is only attributed to animal variability. However, in light of our previous work [115,116], and also current understanding of skin mechanobiology [134–136], we hypothesize that the expander-induced growth field is a function of the spatial pattern of deformation but not just the deformation at a local point. In other words, knowing the total deformation at a single location is not enough to anticipate the growth at that location. The data presented here are only a macroscopic mechanics description and further experiments are needed at the cellular scale to clarify the biological pathways involved in the growth process. Nevertheless, this non-locality hypothesis is also supported by our previous studies that found an expander-induced growth field which was not perfectly aligned with the expansion-induced deformation, but rather seemed to be a smoothed version of this deformation field [115, 116]. The literature on skin mechanobiology also points towards the coupling of non-local signals, mainly, the production of growth factors that diffuse and trigger growth beyond points of maximum deformation [136–138]. These secondary mechanotransduction pathways include transforming growth factors $\beta 1$ and α (TGF-$\beta 1$, TGF-α) [139, 140]. Growth factors inherently require consideration of diffusion and could help explain the mismatch between total deformation and expander-induced growth . We also remark that the expanders in models 1 and 4 moved approximately 2 cm from their initial location in the grid. This could add an extra variation to the final expander-induced growth pattern. Nonetheless, despite this movement, the expander-induced growth field in model 4, one of the large volume protocols, did resemble the total deformation field, similar to the other large volume case, model 2. Both small volume models show expander-induced growth patterns that do not resemble the total deformation, even though only the expander in model 1 moved.

A closer look at the microstructure reveals a change in epidermal thickness in the expanded patches consistent with previous reports [141–143]. Epidermal thickness at the apex increased in all expansion protocols. Interestingly, thickness increased more on the small volume model 1 and model 3 compared to the large volume models

2 and 4. This is the opposite trend with respecto to expander-induced growth at this location. We remark that expansion-induced growth corresponds to area changes normalized by the amount of naturally grown skin. Therefore, total growth may offer a better understanding of epidermal thickening. Total growth at the apex was similar between small and large volume protocols. This is because the natural growth in the small volume modes was larger compared to the large volume cases. Nevertheless, total growth at the apex was still higher in the large volume protocols. Further work is needed to clarify this result. Our next step is to directly quantify proliferation rates of keratinocytes rather than thickness values alone. Trends in the morphology of the collagen network are not unique. Since we analyze thin histological slides, the handling of these slides could potentially alter the tissue microstructure. Furthermore, the slides are taken transversely to the skin surface and some of the network morphologies are not captured within this plane. A more reliable measurement would be a volumetric imaging approach such as second-harmonic generation [144], which we intend to do in the near future. Nonetheless, even with the limitations of our current approach, some trends emerge: Our analysis suggests that the papillary dermis, the top sublayer of the dermis, is not affected by the expansion protocol. In the reticular dermis, the bottom sublayer, coherency decreases in the expanded skin. A more careful investigation is needed to fully characterize the change in collagen microstructure over time as a result of applied stretch. Another area of future investigation is measuring the change in mechanical properties during skin growth with noninvasive tools [27].

This study is not without its limitations, some of which have already been acknowledged. The three-dimensional photography system was compared to geometries generated with multi-view stereo, and we verified that both methods produced the same results. We have shown that the multi-view stereo reconstruction has errors that are on average 2% but can reach 10% in a small number of cases [115]. We thus expect a similar measurement error in the results presented here. Another limitation is the small number of animals used in the experiments. Nonetheless, the results

shown here align with our previous reports. Furthermore, even though the number of animals is small, each grid offers 121 data points. The challenge we face is that each of these points undergoes a different growth trajectory, and a direct comparison of the different deformation components is not possible. To address this, we need to parameterize the growth rate as a function of deformation and solve an inverse problem to identify the best parameters that describe the data. Such approach would then allow a proper statistical analysis based on the growth trajectories of all 121 points per patch. This inverse problem is one of our next goals. Finally, the methodology still lacks a more comprehensive analysis of the cell scale. This work shows an important step in that direction. Before, we only measured tissue scale information. Here, we have introduced the histological analysis to better understand the remodeling of skin during tissue expansion. Still, more work in this direction is needed in order to identify the cellular mechanisms governing the observed histological changes.

2.5 Conclusion

This study establishes a methodology to study skin deformations and growth in a porcine model. Traditionally, *in vitro* systems have been used to characterize skin mechanotransduction. However, such experiments are unable to capture the complex biological response *in vivo*. Three-dimensional photography and isogeometric kinematic analysis enables tracking deformations of sizable skin patches, non-invasively, *in vivo*, and over long periods of time. Using the multiplicative split of the deformation gradient into elastic and growth contributions and accounting for prestrain and natural growth allows us to precisely quantify the differences of tissue expansion protocols for varying inflation timing and inflation volume. We found that larger volumes induce a heterogeneous deformation pattern characterized by large deformation at the apex and progressively less deformation toward the periphery of the expanded area. The expander-induced growth field for the large inflation volumes aligned with the total deformation patterns. For the small inflation volumes, the total deforma-

tion and expander-induced growth fields were more homogeneous. Overall, the apical points in the large volume models showed the greatest amount of expansion-induced growth. Further work is needed to elucidate the biological mechanisms that link the observed macroscopic effects to the underlying cellular mechanisms. Our histological analysis is a first step in this direction. It confirms previous observations that the epidermis becomes thicker upon tissue expansion. The exact mechanisms of skin growth and remodeling remain a topic of further investigation.

3. PROPAGATION OF UNCERTAINTY IN THE MECHANICAL AND BIOLOGICAL RESPONSE OF GROWING TISSUES

Abstract: A key feature of living tissues is their capacity to remodel and grow in response to environmental cues. Within continuum mechanics, this process can be captured with the multiplicative split of the deformation gradient into growth and elastic contributions. The mechanical and biological response during tissue adaptation is characterized by inherent variability. Accounting for this uncertainty is critical to better understand tissue mechanobiology, and, moreover, it is of practical importance if we aim to develop predictive models for clinical use. However, the current gold standard in computational models of growth and remodeling remains the use of deterministic finite element (FE) simulations. Here we focus on tissue expansion, a popular technique in which skin is stretched by a balloon-like device inducing its growth. We construct FE models of tissue expansion with various levels of detail, and show that a sufficiently broad set of FE simulations from these models can be used to train an accurate and efficient multi-fidelity Gaussian process (GP) surrogate. The approach is not limited to simulation data, rather, it can fuse different kinds of data, including from experiments. The main appeal of the framework relies on the common experience that highly detailed models (or experiments) are more accurate but also more costly, while simpler models (or experiments) can be easily evaluated but are bound to have some error. In these situations, doing uncertainty analysis tasks with the high fidelity models alone is not feasible and, conversely, relying solely on low fidelity approximations is also undesirable. We show that a multi-fidelity GP outperforms the high fidelity GP and low fidelity GP when tested against the most detailed FE model. In turn, having trained the multi-fidelity GP model, we showcase the propagation of uncertainty from the mechanical and biological response

parameters to the spatio-temporal growth outcomes. We expect that the methods and applications in this paper will enable future research in parameter calibration under uncertainty and uncertainty propagation in real clinical scenarios involving tissue growth and remodeling.

3.1 Motivation

Living tissues remodel and grow in response to mechanical cues. This response can be detrimental, which is common in diseases such as heart fibrosis and dilation following infarct [145,146], but it can also be leveraged for medical treatment. A prime example is tissue expansion [7,115]. In this technique, a balloon-like device is inserted subcutaneously and inflated gradually, stretching the skin and inducing its growth [116]. Newly grown skin created with this method is used to design flaps to resurface large defects [106]. Even though the tissue expansion process has gained popularity in reconstructive surgery for its unique capacity to create new skin that is equally functional to native tissue, we still lack predictive capability of how skin adapts to mechanical cues [97]. As a consequence, treatment plans for tissue expansion still heavily rely on surgeon's training and experience rather than aided by predictive models.

Our need for quantitative knowledge of skin's response to stretch is part of a broader quest to fundamentally understand the mechanical adaptation of soft tissues [147]. In response to this need, computational modeling of growth and remodeling of living matter has advanced tremendously in the last two decades [108, 148]. One common approach is to describe growth within a continuum mechanics framework through the multiplicative split of the deformation gradient [123]. The split into growth and elastic contributions isolates the two processes kinematically. The evolution of the growth tensor is prescribed with phenomenological equations that aim at capturing essential features of the underlying biological process [149]. The elastic tensor, on the other hand, dictates the stress field through an appropriate

constitutive equation describing the tissue mechanical behavior. This approach has been used for a plethora of examples, including the skin, but also valve leaflets, the heart, arteries, and the brain, to name a few applications [150–153]. The theoretical framework has been extremely successful in isolating key features of the growth and remodeling process. At the same time, the maturation of this methodology to the point at which it can guide medical treatment still requires overcoming some longstanding challenges. One open question is to incorporate the role of inherent variability in biological response and tissue mechanical properties on the corresponding probability of the spatio-temporal growth and remodeling outcome [101]. The current paradigm relies on detailed finite element (FE) models with deterministic parameters adjusted based on some combination of experimentation and parameter sensitivity analyses [154]. This is not enough for decision making in the clinic. At the other end of the spectrum, fully personalized FE methods, such as [147], are also impractical if not unfeasible at scale.

A recent explosion of data-science and machine learning methods has started to permeate into the tissue biomechanics community [155–160]. For example, we have recently tackled the propagation of material behavior uncertainty through reduced order models and Gaussian process (GP) surrogates in the context of reconstructive surgery [100, 101]. Our methodology relies on simulation of many reconstructive surgery procedures spanning a range of inputs, namely, tissue mechanical properties and flap design parameters. The Bayesian surrogate is computationally inexpensive and enables tasks such as parameter calibration, uncertainty propagation, and design optimization. Other examples of how data science is impacting biomechanics include data-driven constitutive modeling, multiscale homogenization, and Bayesian model selection [161–164].

Here we present the use of Bayesian surrogates to enable uncertainty analysis of tissue growth and remodeling. We focus on tissue expansion. Unlike our previous work which dealt with uncertainty in variables that impact the state of deformation and stress at a single instant in time, the growth and remodeling process entails incor-

porating uncertainty in biological parameters which propagates through time coupled with the mechanical equilibrium problem (see Figures 3.1 and 3.2). In turn, the corresponding computational models are also more expensive to evaluate compared to mechanical equilibrium at a single time instant. To deal with this challenge, we propose to use multi-fidelity machine learning techniques [165]. While in this study we rely solely on simulation data, an added benefit of the multi-fidelity framework is that it enables combination of different kinds of data, including from experiments [166].

In essence, multi-fidelity approaches imply combining data with different levels of resolution or accuracy. For example, there might be some data which is very reliable, such as measurements or simulations with very detailed spatial or temporal resolution and with high accuracy. Usually, these data are difficult to obtain, either because the simulation is computationally expensive, because the parameter input space is very large, or because the experiments are costly or time consuming [167, 168]. Usually there are other, less expensive (financially and computationally) means of acquiring data, such as changing the model to a simplified one or doing experiments with less specialized equipment [169,170]. In a multi-fidelity framework, these different sources of information are combined to create a new model that outperforms the predictions done with a single type of data [171].

The multi-fidelity approach is particularly appealing for creating predictive models of biological tissue adaptation. As mentioned previously, biological systems are characterized by inherent uncertainty in mechanical properties and biological response [172–174]. Computational models with different level of detail can be constructed to compute the growth and remodeling response over time for a wide parameter range. Here we only employ simulation data to train the surrogate, but the problem can be extended to capture our previous experimental work [115]. Furthermore, we specifically use multi-fidelity GP regression. This allows us to not only make predictions of the tissue response for a new set of inputs, but it also gives us the confidence in the prediction based on the observed data. We are hopeful that constructing this kind of data-driven model for tissue growth and remodeling will

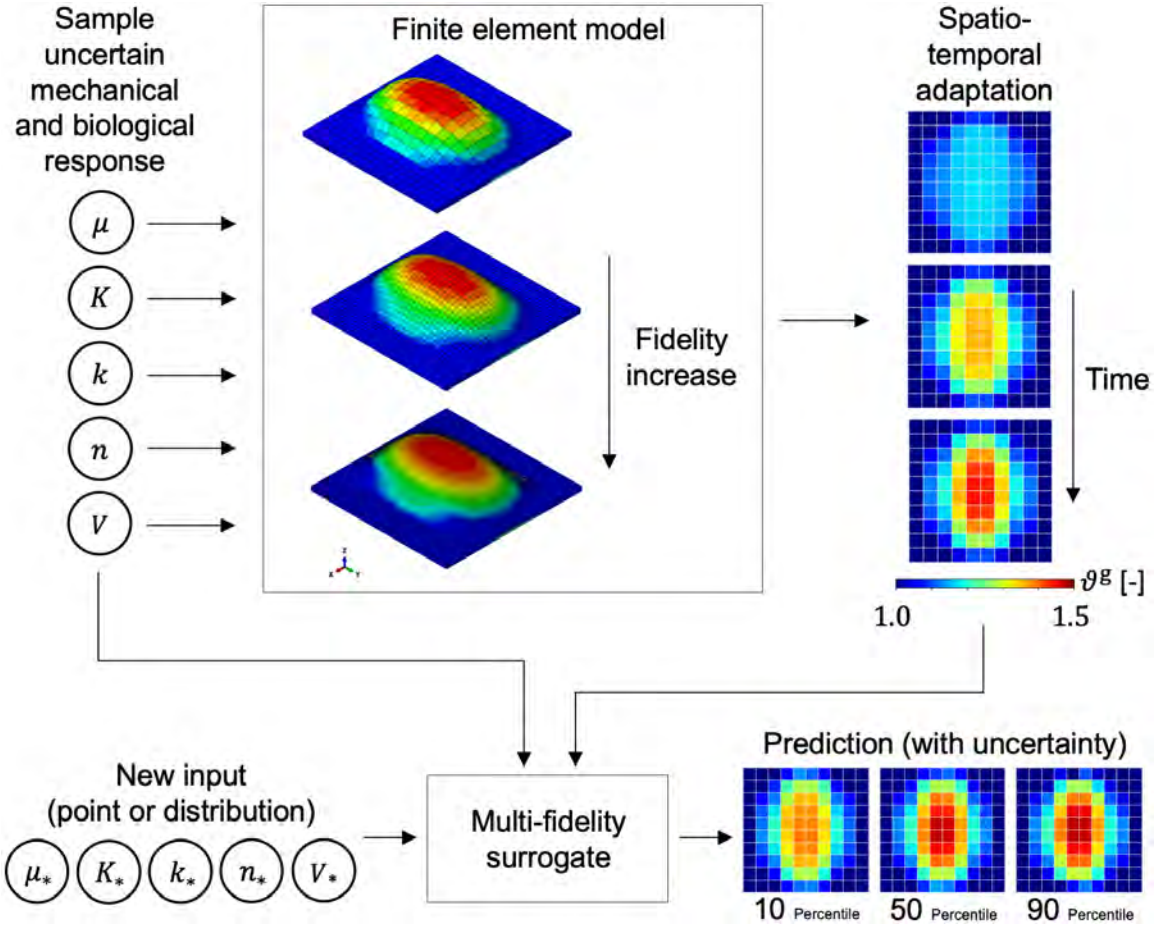

Fig. 3.1.: Multi-fidelity surrogate for skin growth. The uncertain input space consists of the mechanical and biological response parameters as well as the volume of the expander: $[\mu, k, K, n, \mathrm{V}]$ where μ is the shear modulus, and k, K, and n are coefficients of a Hill function controlling the growth rate. Samples of this space are used in finite element simulations with different level of detail or fidelity. The corresponding output is the growth field ϑ^g, which varies in space and time. The the full output is transformed into pairs of input-output data from the different fidelity models which are used to train a multi-fidelity Gaussian process surrogate. The surrogate predicts the mean and confidence interval of the growth variable over space and time at a new input $[\mu_*, k_*, K_*, n_*, \mathrm{V}_*]$.

impact the clinical setting in the near future by enabling uncertainty analysis, model calibration, and treatment optimization.

3.2 Methods

3.2.1 Tissue growth through the multiplicative split of the deformation gradient

We start by introducing some standard notation. Let $\mathbf{X} \in \mathcal{B}_0 \subset \mathbb{R}^3$ be the reference configuration and $\mathbf{x} \in \mathcal{B} \subset \mathbb{R}^3$ the current configuration of the tissue. The local deformation is captured by the gradient $\mathbf{F} = \nabla_{\mathbf{X}}\mathbf{x}$, whose determinant is the volume change $J = \det(\mathbf{F})$. For skin, since it is a membrane, we define the normal field $\mathbf{N}$. This vector field, in turn, allows us to define the area deformation field induced by $\mathbf{F}$, which we refer to as $\vartheta = ||\mathrm{cof}(\mathbf{F}) \cdot \mathbf{N}||$.

Growth in biological materials can be done via the multiplicative split of the deformation gradient into growth and elastic components [123]

$$\mathbf{F} = \mathbf{F}^e\mathbf{F}^g \,. \tag{3.1}$$

The growth tensor $\mathbf{F}^g$ captures the biological response and requires further definition of its form, which is both a constitutive and kinematic assumption. For skin, since it is a thin membrane, we consider only in plane area growth

$$\mathbf{F}^g = \sqrt{\vartheta^g}\mathbf{I}_s + \mathbf{N} \otimes \mathbf{N}, \tag{3.2}$$

where ϑ^g is the area growth, and $\mathbf{I}_s = \mathbf{I} - \mathbf{N} \otimes \mathbf{N}$ is the surface identity defined in terms of the second-order identity tensor $\mathbf{I}$ in the reference configuration and the surface normal $\mathbf{N}$. The split Eq. (3.1) further implies the split of the area change into elastic and growth components

$$\vartheta = \vartheta^e\vartheta^g \,. \tag{3.3}$$

The elastic deformation $\mathbf{F}^e$ in Eq. (3.1), encapsulates the mechanical response of the tissue. We consider skin as a hyperelastic material [76, 118]. The mechanical equilibrium of the tissue depends on the definition of a strain energy function in terms

of the elastic component of the deformation only, $\Psi(\mathbf{F}^e)$ [175]. A thought experiment that may bring clarity to the split of the deformation gradient consists of imagining that we cut the current configuration of the tissue, $\mathcal{B}$, into small pieces while removing all external forces and constraints. All these small portions of material would then achieve mechanical equilibrium. Each piece is allowed to have its own equilibrium state, such that the field $\mathbf{F}^e$ is not necessarily the gradient of a deformation field. This is why the multiplicative split is also said to introduce an intermediate incompatible configuration [116]. The total energy released in the thought experiment depends only on the field $\mathbf{F}^e$, hence $\Psi(\mathbf{F}^e)$. On the other hand, the equilibrium configuration of each piece of material depends on its growth history $\mathbf{F}^g$. The stress in the current configuration is

$$\sigma = \mathbf{B}^e \frac{\partial \Psi}{\partial \mathbf{B}^e}, \tag{3.4}$$

with $\mathbf{B}^e = \mathbf{F}^e \mathbf{F}^{e\top}$ the left Cauchy-Green elastic deformation tensor. Alternatively, the stress can be expressed in the intermediate configuration or in the reference configuration, as reviewed in [176]. The overall stress field has to satisfy balance of linear momentum in the standard form

$$\nabla \cdot \sigma = \mathbf{0}. \tag{3.5}$$

The simulation of the growth process with the FE method requires the derivation of the consistent tangent. We postpone the discussion of the numerical implementation until after we have introduced the corresponding constitutive equations for the biological and mechanical behavior of skin.

3.2.2 Constitutive modeling of growth

We already introduced the assumption that growth of skin occurs only in the plane, which is motivated by our current understanding of skin growth in tissue expansion

[136, 177]. Next, we need to prescribe the evolution of the growth variable. Growth is a dynamic process and a constitutive model entails specifying the rate of change of growth in response to the mechanical cues. Following our current understanding of skin mechanobiology, we pose that the growth rate is proportional to stretch in a nonlinear fashion [97]. We depart from previous forms of the growth rate [175]. In the spirit of a systems biology approach, we assume that the elastic deformation generates a chemical signal that is interpreted by the cells, showing saturation as the input increases. Hence, we use a Hill function

$$\dot{\vartheta}^g = H(\vartheta^e) = \frac{k(\vartheta^e - \vartheta^{\text{cr}})^n}{K^n + (\vartheta^e - \vartheta^{\text{cr}})^n}, \tag{3.6}$$

which is parameterized by $k, K, \vartheta^{\text{cr}}$ and n. In the uncertainty analysis presented here we consider the parameters k, K and n as sources of biological uncertainty. We do not consider variation in ϑ^{cr} and instead fix this parameter to 1.1. The reason for this choice is that ϑ^{cr} controls the homeostatic state. Changing this parameter would require an additional equilibration step prior to the tissue expansion procedure, which we avoid here.

3.2.3 Constitutive modeling of skin mechanics

Skin is a complex tissue, comprised of three layers with distinct structure and mechanical behavior in just $1 - 3$ mm across the thickness [37]. The mechanical response under tension is primarily driven by the dermis, which is the intermediate layer of the skin [45]. The dermis is a connective tissue, and it is primarily made out of collagen. At moderate deformations, the stress-strain curve is only slightly nonlinear. Subjected to progressively larger strains, the skin exhibits rapid stiffening, resulting in a J-shaped stress-strain curve, characteristic of other connective tissues [178]. The collagen fiber network in the skin is a source of anisotropy [51, 179], although the fiber dispersion seen in the dermis is relatively large [180]. Extensive efforts in constitutive modeling of skin mechanics has resulted in a variety of strain energy functions [118].

In the work shown here we restrict our attention to a neo-Hookean strain energy function

$$\Psi = \frac{\mu}{2}(I_1 - 3 - 2\ln(J^e)) + \frac{\lambda}{2}\ln^2(J^e), \tag{3.7}$$

where $I_1 = \mathbf{B}^e : \mathbf{I}$ is the first invariant of the left Cauchy-Green elastic deformation tensor, $J^e = \det(\mathbf{F}^e)$ is the elastic volume change, μ is the shear modulus, and λ is the bulk modulus.

Like most biological materials, skin shows inherent variability in mechanical properties. For instance, it is clear to anyone that the skin varies from one anatomical region to another [23, 181]. In addition, there are changes in skin mechanics with gender, age, sun exposure, nutrition, to name a few factors [67, 182, 183]. Even individuals from similar demographics can have distinct skin mechanical behavior. With non-invasive mechanical testing through suction devices, the properties of skin under suction have been measured for a large population [184,185]. In this paper we consider the variability in mechanical properties through the uncertainty in the parameter μ.

The stress can be calculated explicitly based on Eq. (3.4) and Eq. (3.7),

$$\sigma = \frac{1}{J^e}(\lambda \ln(J^e) - \mu)\mathbf{I} + \frac{\mu}{J^e}\mathbf{B}^e\,. \tag{3.8}$$

3.2.4 Finite element implementation

We solve the coupled problem of growth under evolving mechanical equilibrium with a user subroutine in the nonlinear FE package Abaqus (Dassault Systems, Waltham, MA). Our implementation follows closely that of [175]. We create a square domain of dimensions $10 \times 10 \times 0.3$ cm and discretize it with either 800, 3,200, or 20,000 trilinear brick elements. As it will become clearer later on, the different mesh refinement leads to a multiple levels of fidelity in the data. A rectangular expander of dimensions 4.5×8 cm is placed underneath the skin. We use the fluid cavity feature in Abaqus. We start the simulation with the initial conditions $\mathbf{F}(t = 0) = \mathbf{F}^e = \mathbf{I}$,

$\vartheta^g(0) = 1$, and an empty expander. The expander is then inflated to a given volume V by implementing a PID controller in an additional user subroutine. The degrees of freedom are the displacement vectors at the nodes, $\mathbf{u}_{\text{ni}}$, and the growth field, which is discretized at the integration points ϑ^g_{ip}. The mechanical equilibrium problem is nonlinear and has to be solved iteratively. Given a guess for the displacements $\mathbf{u}_{\text{ni}}$, the deformation gradient tensor $\mathbf{F}$ is available at the integration points. In the integration point subroutine the growth tensor is then updated by solving the following backward Euler problem

$$\vartheta^g_{t+\Delta t} - \vartheta^g_t - \Delta t H(\vartheta^e_{t+\Delta t}) = 0\,, \tag{3.9}$$

where ϑ^g_t is the growth variable from the previous converged step, $\vartheta^g_{t+\Delta t}$ is the new guess for the growth variable for the current time step $t + \Delta t$, and $\vartheta^e_{t+\Delta t} = \vartheta / \vartheta^g_{t+\Delta t}$ is the current guess for the elastic deformation component of the area change. Solving this local problem, the new $\mathbf{F}^g$ is constructed, which, together with the current guess for $\mathbf{F}$ yields $\mathbf{F}^e$. The stress is calculated according to Eq. (3.8). Finally, to drive the global Newton-Raphson iterations, we introduce the Eulerian tangent moduli

$$\mathbf{c} = 4\mathbf{B}^e \frac{\partial^2 \Psi}{\partial \mathbf{B}^e \partial \mathbf{B}^e} \mathbf{B}^e = \mathbf{c}^e + \mathbf{c}^g\,. \tag{3.10}$$

The elastic moduli has also an elastic and a growth component. The elastic part is

$$\mathbf{c}^e = \lambda \mathbf{i} \otimes \mathbf{i} + (\mu - \lambda \ln(J^e))(\mathbf{i}\overline{\otimes}\mathbf{i} + \mathbf{i}\underline{\otimes}\mathbf{i})\,, \tag{3.11}$$

with $\{\bullet\overline{\otimes}\circ\} + ijkl = \{\bullet\}_{ik}\{\circ\}_{jl}$, $\{\bullet\underline{\otimes}\circ\} + ijkl = \{\bullet\}_{il}\{\circ\}_{jk}$, and $\mathbf{i}$ the second-order identity tensor in the current configuration. The second part of the Eulerian tangent moduli is defined as

$$\mathbf{c}^g = -\frac{\Delta t}{K^\vartheta \vartheta \vartheta^g} \frac{\partial \dot{\vartheta}^g}{\partial \vartheta^g} (\lambda \vartheta^g \mathbf{i} + \mu(\mathbf{B} - \mathbf{n} \otimes \mathbf{n})) \otimes (\vartheta \mathbf{i} - J^2 \vartheta^{-1} (\mathbf{F}^{-\top}\mathbf{N}) \otimes (\mathbf{F}^{-\top}\mathbf{N}))\,, \tag{3.12}$$

where $\mathbf{B} = \mathbf{F}\mathbf{F}^\top$ the left Cauchy-Green deformation tensor, $K^\vartheta = 1 - \frac{\partial \dot{\vartheta}^g}{\partial \vartheta^g}\Delta t$, which is calculated based on the derivative of the residual Eq. (3.9) with respect to ϑ^g, and $\mathbf{n}$ is the surface normal vector in the current configuration. In Abaqus, the tangent moduli used is that corresponding to the Jaumann stress rate. Thus, Eq. (3.10) is further transformed to the desired tangent as shown in [152, 186].

3.2.5 Multi-fidelity Gaussian process regression

A GP is a probability measure over functions such that the function values at any set of input points have a joint Gaussian distribution [187]. This property, and the fact that for any set of observations with joint Gaussian distribution, the distribution of a subset conditioned on the rest is also Gaussian, enables making predictions at an unknown point based on previous observations. In other words, the GP regression can be interpreted in terms of Bayes' rule as representing the posterior state of one's knowledge about an unknown function conditional on observed data. Additionally, since the posterior is also a GP, both the expected value and covariance of any collection of new points are analytically available.

We are interested in learning a latent function $f(\mathbf{x})$ from input-output observations. Assume that we have collected M observations with inputs $\mathbf{x}_m$ in $\mathbb{R}^d$ and outputs $y_m = f(\mathbf{x}_m) + \epsilon_m$ in $\mathbb{R}$, where ϵ_m are independent identically distributed zero mean Gaussian random variables with unknown variance σ_G^2, to be determined. Generally, it is a good idea to include a noise term even if the measurement process noiseless, because it improves the numerical stability of the algorithm [188].

We are collectively denoting this dataset by $\mathcal{D} = (\mathbf{X}, \mathbf{y})$, where $\mathbf{X} \subset \mathbb{R}^{M \times d}$ is the collection of M total inputs, while $\mathbf{y}$ is the vector with all outputs. We posit that out prior state of knowledge about f can be described by a GP with the mean and covariance functions, $m(\cdot; \boldsymbol{\theta})$ and $k(\cdot, \cdot; \boldsymbol{\theta})$, i.e.,

$$f(\cdot)|\boldsymbol{\theta} \sim \mathcal{GP}\left(m(\cdot; \boldsymbol{\theta}), k(\cdot, \cdot; \boldsymbol{\theta})\right), \tag{3.13}$$

where $\boldsymbol{\theta}$ includes all hyperparameters that affect the mean and covariance functions. To keep the notation simple, assume also that $\sigma_G^2 \in \boldsymbol{\theta}$ even though the mean and covariance functions do not depend on it. Assuming no particular knowledge about the trend of the function, we pick a zero mean function. The choice of the covariance function models our prior beliefs about the regularity of the function (there is a one-to-one correspondence between the differentiability of the covariance function and samples from the GP probability measure [189]). Assuming that f is infinitely differentiable, we choose the squared exponential covariance function:

$$k(\mathbf{x}, \mathbf{x}'; \boldsymbol{\theta}) = v \exp\left\{-\sum_{i=1}^{d} \frac{\left(x_i - x_i'\right)^2}{2\ell_i^2}\right\}, \tag{3.14}$$

where the positive hyperparameters $\{v, \ell_1, \ldots, \ell_d\} \in \boldsymbol{\theta}$ model the variance of the process and the length scales of each input dimension, respectively. Note that the GP regression avoids the explicit parameterization of f and instead it *let the data speak for themselves*, with the only exception of these hyperparameters.

To fit the hyperparameters, we look for the $\boldsymbol{\theta}$ that maximizes the log-marginal likelihood

$$\log p(\mathbf{y}|\mathbf{X}, \boldsymbol{\theta}) = -\frac{1}{2}\mathbf{y}^\top(\mathbf{K} + \sigma_G^2\mathbf{I})^{-1}\mathbf{y} - \frac{1}{2}\log|\mathbf{K} + \sigma_G^2\mathbf{I}| - \frac{M}{2}\log 2\pi \tag{3.15}$$

where $\mathbf{K}$ is the $M \times M$ symmetric and positive definite matrix $\mathrm{K}_{ij} = k(\mathbf{x}_i, \mathbf{x}_j; \boldsymbol{\theta})$, which stores the covariance between every pair of inputs in $\mathbf{x}$. As stated at the beginning of this section, the fact that any set of function values is jointly Gaussian means that the prior of the observed data $\mathcal{D}$ together with a test pair $(\mathbf{x}_*, f_*)$ satisfy

$$\begin{bmatrix} \mathbf{y} \\ f_* \end{bmatrix} \sim \mathcal{N}\left(\begin{bmatrix} \mathbf{0} \\ 0 \end{bmatrix}, \begin{bmatrix} \mathbf{K} + \sigma_G^2\mathbf{I} & \mathbf{k}(\mathbf{X}, \mathbf{x}_*; \boldsymbol{\theta}) \\ \mathbf{k}(\mathbf{x}_*, \mathbf{X}; \boldsymbol{\theta}) & k(\mathbf{x}_*, \mathbf{x}_*; \boldsymbol{\theta}) \end{bmatrix}\right), \tag{3.16}$$

where $\mathbf{k}(\mathbf{x}_*, \mathbf{X}; \boldsymbol{\theta}) = (k(\mathbf{x}_*, \mathbf{x}_1; \boldsymbol{\theta}), \cdots, k(\mathbf{x}_*, \mathbf{x}_M; \boldsymbol{\theta}))^\top$ is the cross covariance between $\mathbf{x}_*$ and $\mathbf{X}$ and f_* is the value of the function at the unknown input $\mathbf{x}_*$. Using Bayes' rule:

$$f_* | \mathcal{D}, \mathbf{x}_*, \boldsymbol{\theta} \sim \mathcal{N}\left(\mu_*(\mathbf{x}_*; \boldsymbol{\theta}), \sigma_*^2(\mathbf{x}_*; \boldsymbol{\theta})\right), \tag{3.17}$$

where

$$\mu_{f_*}(\mathbf{x}_*; \boldsymbol{\theta}) = \mathbf{k}^\top(\mathbf{x}_*, \mathbf{X}; \boldsymbol{\theta})(\mathbf{K} + \sigma_G^2 \mathbf{I})^{-1}\mathbf{y} \tag{3.18}$$

and

$$\sigma_*^2(\mathbf{x}_*; \boldsymbol{\theta}) = k(\mathbf{x}_*, \mathbf{x}_*; \boldsymbol{\theta}) - \mathbf{k}^\top(\mathbf{x}_*, \mathbf{x}; \boldsymbol{\theta})(\mathbf{K} + \sigma_G^2 \mathbf{I})^{-1}\mathbf{k}(\mathbf{x}, \mathbf{x}_*; \boldsymbol{\theta}) \tag{3.19}$$

are the predictive mean and variance, respectively.

Up to this point, the GP regression is considered for a single information source. We now extend the concept to exploit the availability of data sources of different fidelity. To be specific, different levels of mesh refinement in the FE model indicate the level of fidelity in this study, e.g., a very fine mesh corresponds to the high fidelity simulation, while a coarser mesh is associated with a lower fidelity simulation. More generally, assume that there are S levels of increasing fidelity each corresponding to an unknown function f_t with $t = 1, \ldots, S$. Even though these functions can be quite different, the assumption that they describe the same physical phenomenon makes it more likely that they exhibit similar trends. If this assumption is true, then one may learn the high fidelity function f_S from a large amount of low fidelity examples and a small number of high fidelity ones. Let $\mathcal{D}_t := (\mathbf{X}_t, \mathbf{y}_t)$ with $t = 1, \ldots, S$ be data sets at the fidelity levels $t = 1, \ldots, S$. Hence, $\mathbf{y}_1$ represents the less accurate but inexpensive output data obtained from the lowest fidelity, while $\mathbf{y}_S$ is the most accurate but expensive data which comes from the highest fidelity. One way to combine such multi-fidelity information is through the autoregressive approach of [190]. In this approach, one starts by assigning a GP prior on the lowest fidelity, i.e.,

$$f_1(\cdot) | \boldsymbol{\theta}_1 \sim \mathcal{GP}\left(m_1(\cdot; \boldsymbol{\theta}_1), k(\cdot, \cdot; \boldsymbol{\theta}_1)\right), \tag{3.20}$$

and then modeling the next level of fidelity according to

$$f_t(\mathbf{x}) = \rho_{t-1} f_{t-1}(\mathbf{x}) + \delta_t(\mathbf{x}), \tag{3.21}$$

for $t = 2, \ldots, S$, where ρ_{t-1} is a scaling factor that quantifies the correlation between output data at fidelity levels $t-1$ and t, and $\delta_t(\mathbf{x})$ is a correction term with prior modeled as a GP, i.e., $\delta_t(\cdot) \sim \mathcal{GP}(\mu_t(\cdot), k_t(\cdot,\cdot;\boldsymbol{\theta}))$, with $\mu_t(\cdot)$ and $k_t(\cdot,\cdot;\boldsymbol{\theta})$ the mean and covariance functions. Although the autoregressive approach from Eq. (3.21) could lead to the combination of multi-fidelity information, the implementation is hindered by computational cost. The computation of the full covariance for the original autoregressive approach is unfeasible when the number of fidelity levels or the input dataset is large [190].

To overcome this barrier, the autoregressive formulation has been advanced by replacing the f_{t-1} prior with its posterior, denoted f_{*t-1}. This change leads to a more numerically efficient algorithm [191]. In practical terms, the proposed switch implies that the information from different fidelity levels is decoupled and one can compute separate covariance matrices at each fidelity level recursively rather than computing the full covariance matrix for all S levels at once. The operation count to compute the inverse of the covariance by Cholesky decomposition is $O(n_t^3)$ for each fidelity level, and the total operation count becomes $\sum_{t=1}^{S} O(n_t^3)$, instead of $O((\sum_{t=1}^{S} n_t)^3)$ that would be needed for the full covariance of all fidelity levels. We also remark that the dataset for each fidelity has nested training inputs, $\mathbf{X}_t \subseteq \mathbf{X}_{t-1}$, which is not necessary but enables a closed form expression for the parameters in the multi-fidelity GP regression. Finally, we note that in [191], a constant value of ρ_{t-1} was used, which captures linear correlations between different fidelity models. Of course, ρ_{t-1} can also be a function of the input $\rho_{t-1}(\mathbf{x})$, to allow for nonlinear correlations. Recently, the authors of [166] have proposed a new approach which not only maintains the same philosophy of [191] but also captures nonlinear correlations between different levels of fidelity.

The approach of [166] is a kind of *deep GP* in which the GP posterior from a previous inference level is used as one more dimension in the training input dataset of next level of fidelity. Hence, the training input dataset ends up having $d + 1$ dimensionality for all except the lowest level of fidelity. This approach thus replaces Eq. (3.21) with the nested model

$$f_t(\mathbf{x}) = g_t(\mathbf{x}, f_{*t-1}(\mathbf{x})), \tag{3.22}$$

where $g_t \sim \mathcal{GP}(\mathbf{f}_t|\mathbf{0}, k_{g_t}((\mathbf{x}, f_{*t-1}(\mathbf{x})), (\mathbf{x}', f_{*t-1}(\mathbf{x}')); \boldsymbol{\theta}_t))$ [166] . We also assume that the input data points are nested, similar to the autoregressive scheme before. A covariance function yielding function samples of the form of Eq. (3.22), see [166], is:

$$k_{g_t}(\mathbf{x}, \mathbf{x}'; \boldsymbol{\theta}_{g_t}) = k_{\rho_t}(\mathbf{x}, \mathbf{x}'; \boldsymbol{\theta}_{\rho_t}) k_{f_t}(f_{*t-1}(\mathbf{x}), f_{*t-1}(\mathbf{x}'); \boldsymbol{\theta}_{f_t}) + k_{\delta_t}(\mathbf{x}, \mathbf{x}'; \boldsymbol{\theta}_{\delta_t}), \tag{3.23}$$

where k_{ρ_t}, k_{f_t}, and k_{δ_t} denote covariance functions with hyperparameters $\boldsymbol{\theta}_{\rho_t}$, $\boldsymbol{\theta}_{f_t}$, and $\boldsymbol{\theta}_{\delta_t}$, respectively. Note that k_{f_t} makes use of the function value at the $t-1$ level of fidelity, and not the input point at the t level of fidelity. In [166], the squared exponential kernel, Eq. (3.14), was employed, and we do the same in this paper.

Except for the lowest level of fidelity, which is a standard GP model and has a Gaussian as posterior, the posterior distribution of $f_{*t-1}(\mathbf{x}_*)$ with $t \geq 3$ is no longer Gaussian since the GP of a GP is not a GP anymore. We use Monte Carlo integration to calculate the predictive mean and the corresponding variance of the posterior distribution, except at the lowest level of fidelity.

The multi-fidelity GP regression in Eq. (3.22) can be applied to various applications in which it is desirable to combine information obtained with different fidelity. For example, combining data from finite element models with different degree of mesh refinement [192], linearization of nonlinear mathematical expressions [193], and reduction of model dimension such as the approximation of a 3-D physical system with a 1-D formulation [194], are a few examples in which one can get different fidelity of data for the same system of interest. In addition, experimental data might also be

used as one level of fidelity. In this study, we deal only with simulation data. Three different levels of fidelity are considered, each corresponding to a different discretization scheme in the FE model (see Fig. 3.2**a**). Note that the lowest fidelity level is expected to be inaccurate yet really inexpensive to evaluate (approximately 10 minutes on 1 CPU). In contrast, the highest fidelity model is much more accurate but computationally expensive (approximately 6 hours on 1 CPU). For the GP regression in this study we used the open source library GPy [195], and the multi-fidelity GP regression code from [166].

3.2.6 Propagation of uncertainty in the biological and mechanical response of growing skin

As discussed in the previous section, we build multi-fidelity surrogates to predict the deformation and growth of skin resulting from tissue expansion. The tissue expansion protocol is determined by the inflation volume V, and the inflation timing, i.e., the time that the surgeon waits before the next inflation step. We do not consider uncertainty in these variables. Rather, we fix the volume to $V = 40$, 50, or 60 cm^3 (cc), common in clinical practice [7, 97], and a time period of $t = 7$ days, also a common time window between consecutive inflation steps [7, 97]. We remark that in the majority of the results we show the output from three different GPs, each for a different volume. However, the volume can be considered as an input parameter for the regression, as we show towards the end of the Results section 3.3. The uncertainty in the response is due to either the mechanical or the biological response of the tissue. The shear modulus μ is considered as the only source of uncertainty for the mechanical response, and the parameters k, K, and n are the sources of biological uncertainty. The possible ranges for these parameters are summarized in Table 3.1. These ranges have been determined based on the literature [184,185] and our previous work on a porcine model of tissue expansion [97, 115].

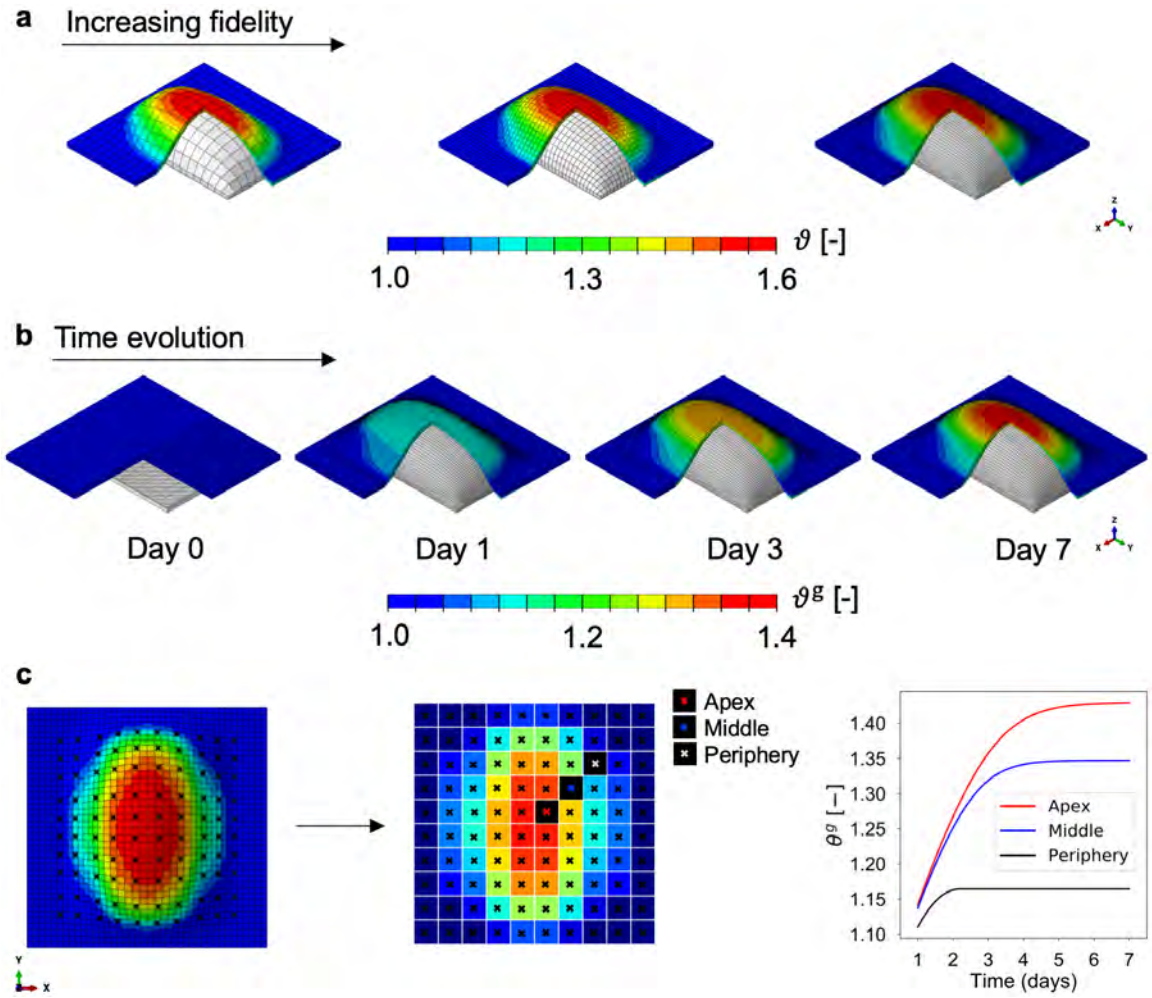

Fig. 3.2.: Multi-fidelity data used to construct the Bayesian surrogate of skin expansion. **a**) Finite element models of tissue expansion with different mesh refinement. Models are discretized with 800, 3,200, and 20,000 trilinear brick elements. A rectangular expander is inflated below the skin, causing total area change ϑ, characterized by greater deformation at the apex of the expander compared to the periphery. **b**) Time evolution of the output of interest, the growth area change ϑ^g, over the domain discretized with the finest mesh. The expander is inflated to either 40, 50, or 60 cc on day 1, and the volume is held constant over 7 days. Growth increases over time, and shows spatial variation with greater growth at the apex. **c**) The field ϑ^g is defined over the entire domain, but we reduce the output to a 10×10 grid that we use to train the surrogate. We remark that both spatial and temporal information is used. Accordingly, the bottom right panel illustrates that for each grid point we have the time history of ϑ^g.

Table 3.1.: Mechanical and biological parameter ranges for input space

Parameter	Range
μ [MPa]	[0.10,1.00]
K [-]	[0.02,0.06]
k [-]	[0.10,1.00]
n [-]	[0.80,1.20]

We note that the FE simulation leads to a deformation and a growth field over the domain. In the past we have used principal component analysis to extract the main features of the deformation and stress fields [100]. Here, we instead opt to keep the spatial analysis consistent with our animal protocol [97], and create independent surrogates for each region from a 10 $\times$ 10 grid. The outputs for the surrogates for each of these regions are the total deformation ϑ (Fig. 3.2**a**) and the growth variable ϑ^g over time (see Fig. 3.2**b** and **c**).

3.3 Results

3.3.1 Creation of Gaussian process surrogates

The input parameters for mechanical and biological response and their corresponding range are shown in Table 3.1. For the low fidelity data we sample 100 points from the space $[\mu, K, k, n]$ using Latin hypercube sampling (LHS), and we extend these points to a 5-dimensional input space by including time as the additional input. These input points are denoted $\tilde{\mathbf{X}}_1$. Likewise, we generate the input datasets $\tilde{\mathbf{X}}_2$ and $\mathbf{X}_3$ by sampling additional 50 and 10 input points from $[\mu, K, k, n]$, respectively. In order to satisfy the requirement of nested input datasets, we run low fidelity simulations for all input points $\mathbf{X}_1 = \tilde{\mathbf{X}}_1 \cup \tilde{\mathbf{X}}_2 \cup \mathbf{X}_3$, the medium fidelity model is evaluated at $\mathbf{X}_2 = \tilde{\mathbf{X}}_2 \cup \mathbf{X}_3$, and the high fidelity model is only run for $\mathbf{X}_3$. This strategy not only satisfies nested inputs for increasing fidelity, but also preserves the LHS features of evenly and randomly distributed points over the input space. The FE models with increasing fidelity are depicted in Fig. 3.2**a**. For each simulation, we inflate the ex-

pander to the volume V = 40, 50, or 60 cc at day 1 and keep the volume constant over 7 days. Note that in the majority of this section we create separate multi-fidelity GP surrogates for each volume, but we also show that the volume can be used as an additional input during regression as depicted in Fig. 3.10. Note that the output of the simulations is the growth field ϑ^g over the domain and across time (see Fig. 3.2**b**). As noted, time is used as an input in the regression, and the spatial variation is captured by creating surrogates independently for the 10×10 grid illustrated in Fig. 3.2**c**.

The simulation in Fig. 3.2**b** shows the growth field over time for a single input point corresponding to the mean value of the parameter range in Table 3.1. Yet, even for a single input point, we note that the simulation shows the expected trends associated with skin growth in tissue expansion: the growth field is greatest at the apex of the expander and less toward the periphery, and the response is nonlinear [196].

The data from the 230 simulations are used to build the surrogates according to the Materials and Methods section 3.2.

3.3.2 Validation of the Gaussian process surrogates

We create a validation dataset by sampling 30 additional points from the $[\mu, K, k, n]$ space using LHS. For these points we only run the highest fidelity model which we consider as the true response in this paper. Fig. 3.3**a** shows the average error of the surrogates compared to the validation set for each of the 10×10 grid points. Each row in the figure corresponds to a different volume. In addition to showing the error in the prediction using the multi-fidelity GP regression, we also show the error for two alternative surrogates, the high fidelity GP regression and the low fidelity GP regression. As the name implies, the high fidelity surrogate is built with data from the most detailed FE model only, while the low fidelity GP uses only the results from the coarsest mesh. As desired, the multi-fidelity scheme outperforms the single fidelity

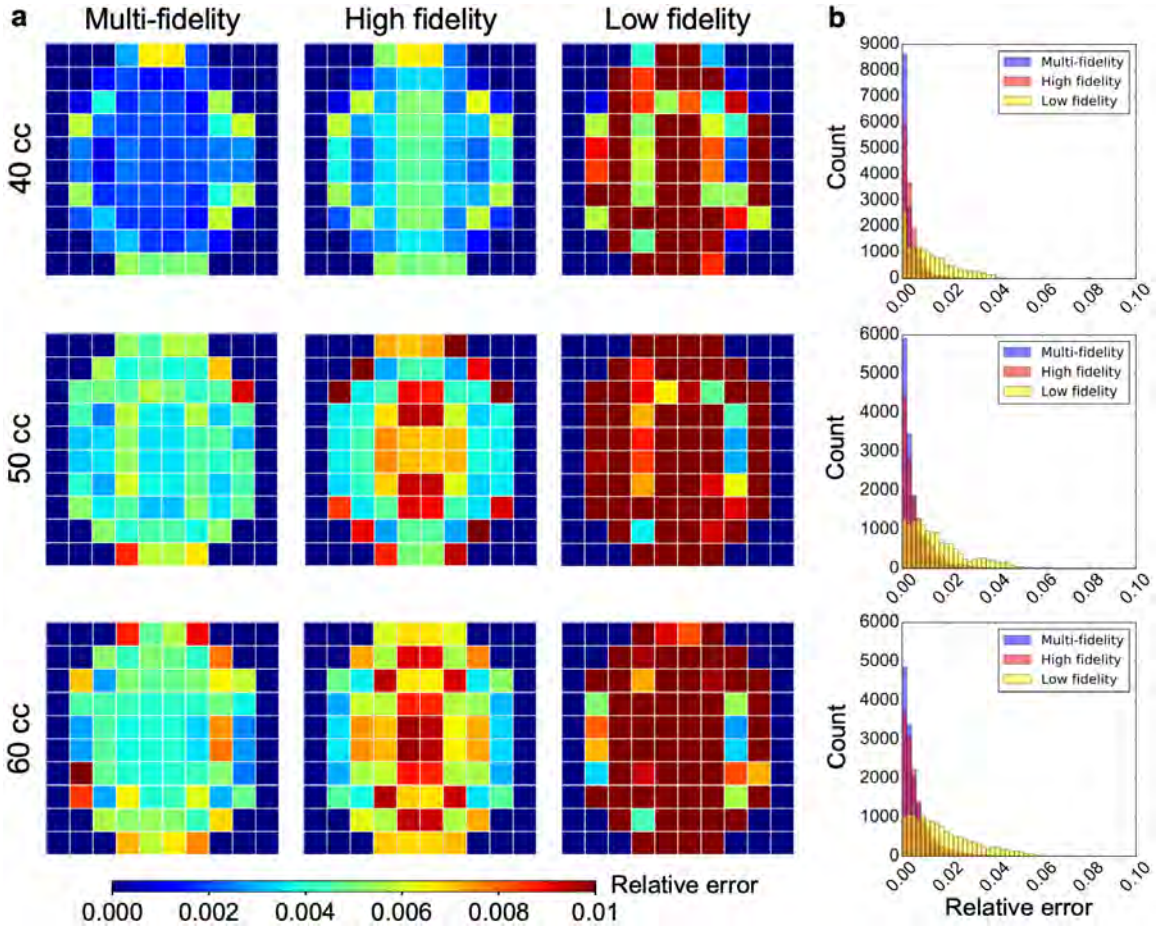

Fig. 3.3.: Validation of the surrogates against high fidelity simulations that were not used in the training. **a**) Average of relative error for the validation dataset composed of 30 input parameters $\times 7$ time points for each of the 10×10 grid points. The multi-fidelity scheme is compared against single fidelity Gaussian process (GP) surrogates, i.e., surrogates trained with either only high or low fidelity data. The multi-fidelity GP surrogate outperforms the alternatives. **b**) Histograms of the error used to create the contours in **a**.

surrogates. Fig. 3.3**b** shows the histograms of the relative error for all the validation points (30 input parameters $\times 7$ days $\times 100$ locations), further illustrating the quality of the multi-fidelity GP surrogate.

Given that the output data varies not only in space but also in time, Fig. 3.4 focuses on the temporal variation. Once again, we are interested in the performance of the multi-fidelity scheme against single fidelity approaches. Fig. 3.4 shows the

temporal variation of ϑ^g for the three volumes of interest and three points of interest: the apex, a middle point, and a point at the periphery of the expanded region (see also Fig. 3.2**c**). The input point for the plots in Fig. 3.4 is the mean value of the parameter ranges in Table 3.1. Alongside the predictions from the surrogates, we show the results from the high fidelity simulations at the same input. Crucially, Fig. 3.4 also shows the confidence intervals predicted by the surrogates based on the observed data. Undoubtedly, being able to show the uncertainty in the prediction is one of the main appeals of GP surrogates. To further analyze the difference between the surrogates, Fig. 3.5 shows scatter plots of the standardized residual for the three volumes of interest and for all grid points. The standardized residual is the ratio of error between the true and the predicted values divided by the standard deviation of the prediction. If the GP surrogate is well calibrated, we expect to see the values of the standardized residual to be contained in the $[-3, 3]$ confidence interval. Moreover, packing of the scatter plot around 0 is reflective of smaller errors in the prediction. Therefore, from Fig. 3.5 we see that the multi-fidelity scheme shows standardized residuals well within the $[-3, 3]$ range and mostly around 0, as desired. The principal observation from Fig. 3.4 and 3.5 is that the low fidelity surrogate evidently performs poorly compared to the two other alternatives.

Our last validation experiment is to show the trade-off between the number of high fidelity evaluations for training and the quality of the multi-fidelity surrogate compared to the high fidelity GP. It is reasonable to expect that as the number of high fidelity training points increases, the single fidelity GP built with the high fidelity data alone might outperform the multi-fidelity approach. For the data shown in Figures 3.3 to 3.5, a total of 230 simulations were used for training, out of which $M_h = 10$ simulations were done with the most detailed finite element model. Fig. 3.6 shows the results when there are either $M_h = 5$ or $M_h = 20$ high fidelity function evaluations available for training of the surrogates. With $M_h = 5$, both the single and multi-fidelity schemes perform poorly in terms of average relative error over the validation set, while for $M_h = 20$ the multi-fidelity approach continues to outperform

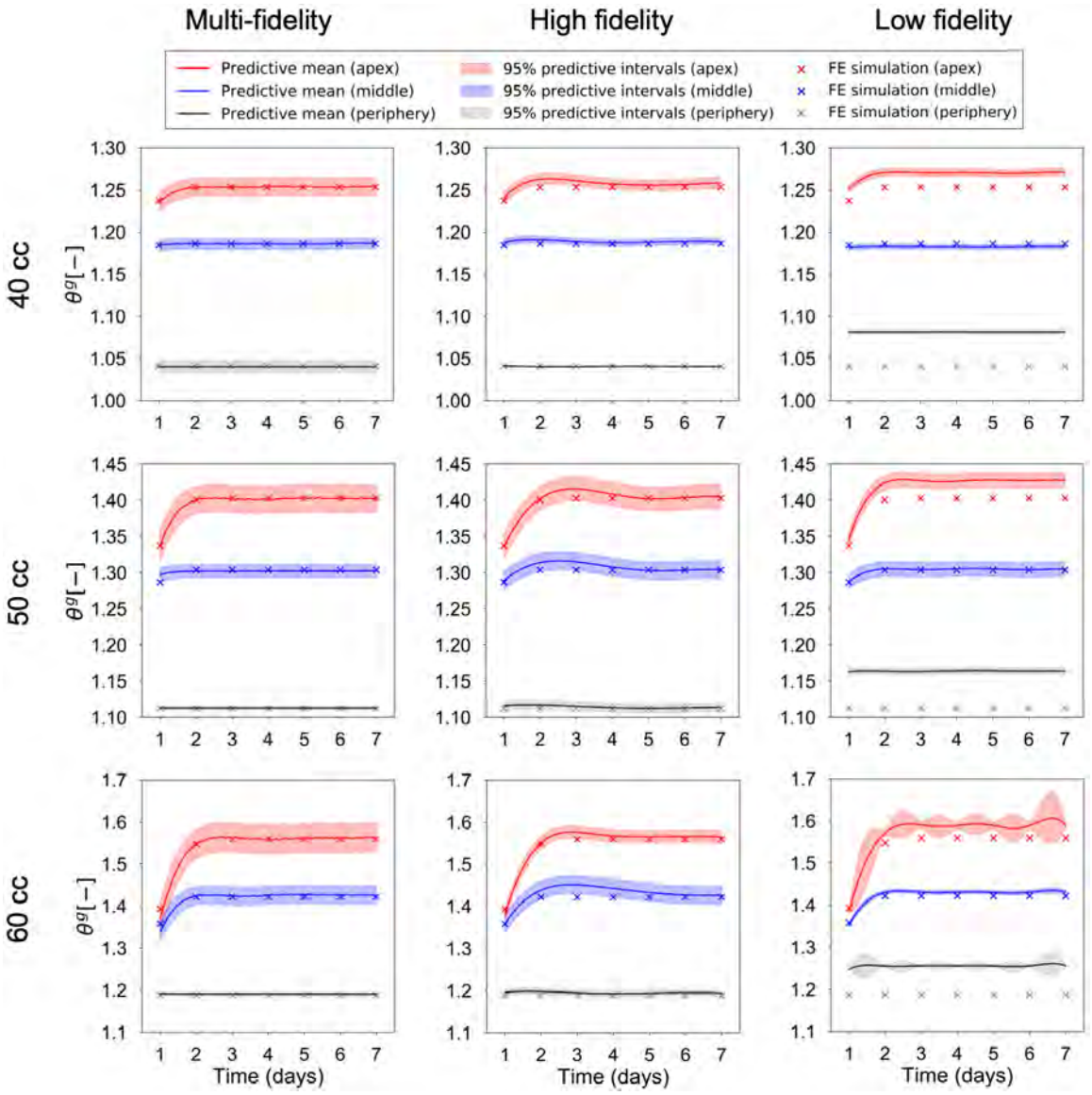

Fig. 3.4.: Validation of the temporal response predicted by the surrogates against the corresponding high fidelity simulation. Plots of the growth variable ϑ^g are predicted for 3 points of interest: the point in apex, middle, and the periphery of the expanded area. The test input for the surrogates is the mean of the parameters in Table 3.1. The output of the corresponding high fidelity simulation is shown for validation. The evaluation of the Gaussian processes (GPs) results in the prediction of a mean value and the corresponding variance, a key feature of Bayesian surrogates. The low fidelity surrogate is completely inaccurate, while the multi-fidelity and high fidelity GPs have good agreement with the true response in all three volumes.

the high fidelity GP (Fig. 3.6). This trend is clearer when looking at the histograms of the relative error shown in Fig. 3.6.

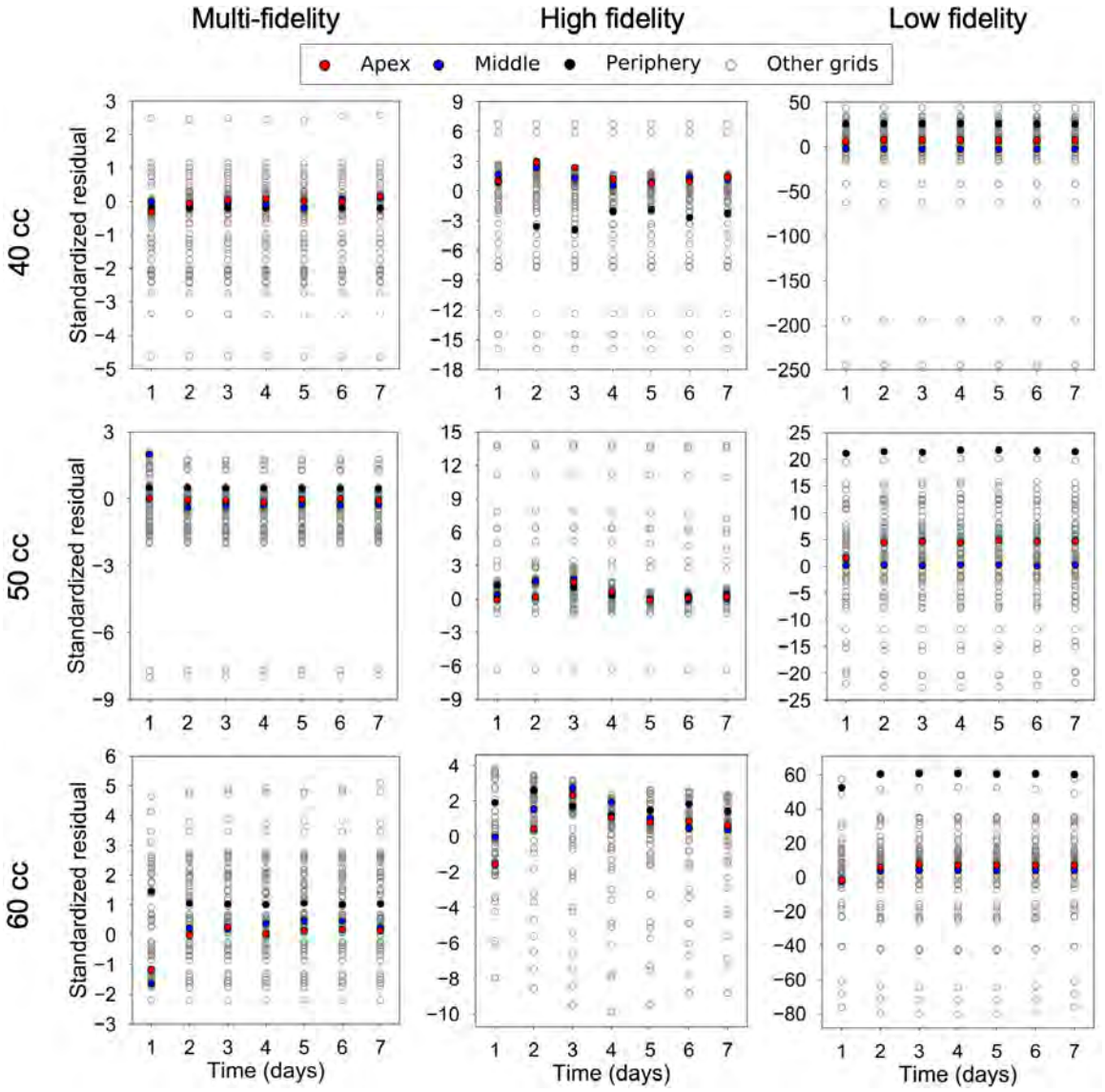

Fig. 3.5.: Validation of the temporal response predicted by the surrogates against the corresponding high fidelity simulation. The test input is the mean of the parameters in Table 3.1. The standardized residuals are shown for the 100 grid points for three volumes of interest, V = 40, 50, and 60 cc. If the surrogates are trained properly, the standardized residuals should fall within the $[-3, 3]$ confidence intervals as can be observed for the multi-fidelity Gaussian process regression.

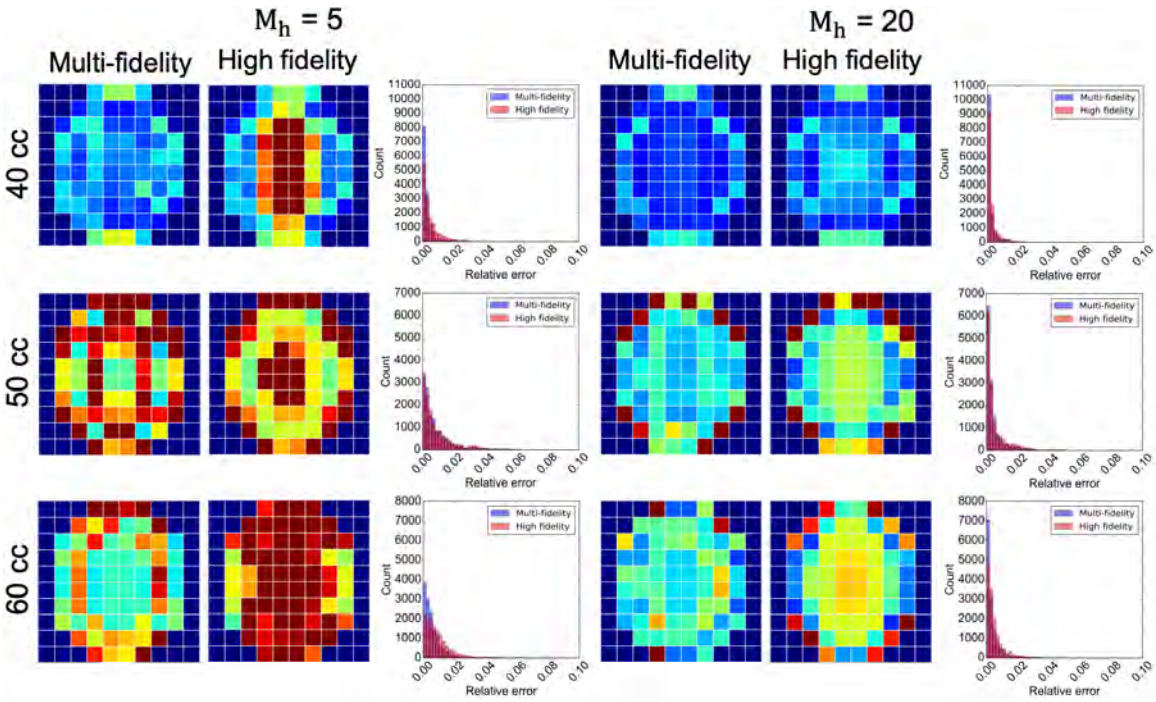

Fig. 3.6.: Effect of changing the number of high fidelity function evaluations on the performance of the multi-fidelity and high fidelity Gaussian process (GP) surrogates for inflation volumes V = 40, 50, and 60 cc. Average error over the 10×10 grid and histograms of the error are shown for the case when there are either $M_h = 5$ or $M_h = 20$ high fidelity function evaluations available for training. For $M_h = 5$ both surrogates perform poorly, while for $M_h = 20$ the multi-fidelity GP surrogate outperforms the single fidelity approach

We then focus on the performance of the surrogates over the temporal domain. Fig. 3.7 shows the validation results for V = 50 cc only. Results for other volumes are shown in the Supplementary materials. The trends are similar between the different volumes: the multi-fidelity surrogates outperform high fidelity models for both $M_h = 5$ and $M_h = 20$. More quantitative comparison is represented in Fig. 3.7**b** in terms of the standardized residual for all 100 grid points for all the validation simulations. Not surprisingly, $M_h = 20$ leads to better performance than $M_h = 5$ for all volumes. Once again, the standardized residuals confirm that the multi-fidelity scheme outperforms the single fidelity schemes. However, these results also underscore the importance of choosing a suitable number of high fidelity evaluations. If

there are too few high fidelity evaluations, here $M_h = 5$, the multi-fidelity GP surrogate itself cannot recreate an accurate GP surrogate model. On the other hand, if the number of high fidelity evaluations is high enough, $M_h = 20$ here, the high fidelity GP regression itself is already accurate enough and there is no more need to incorporate low fidelity information to improve the prediction.

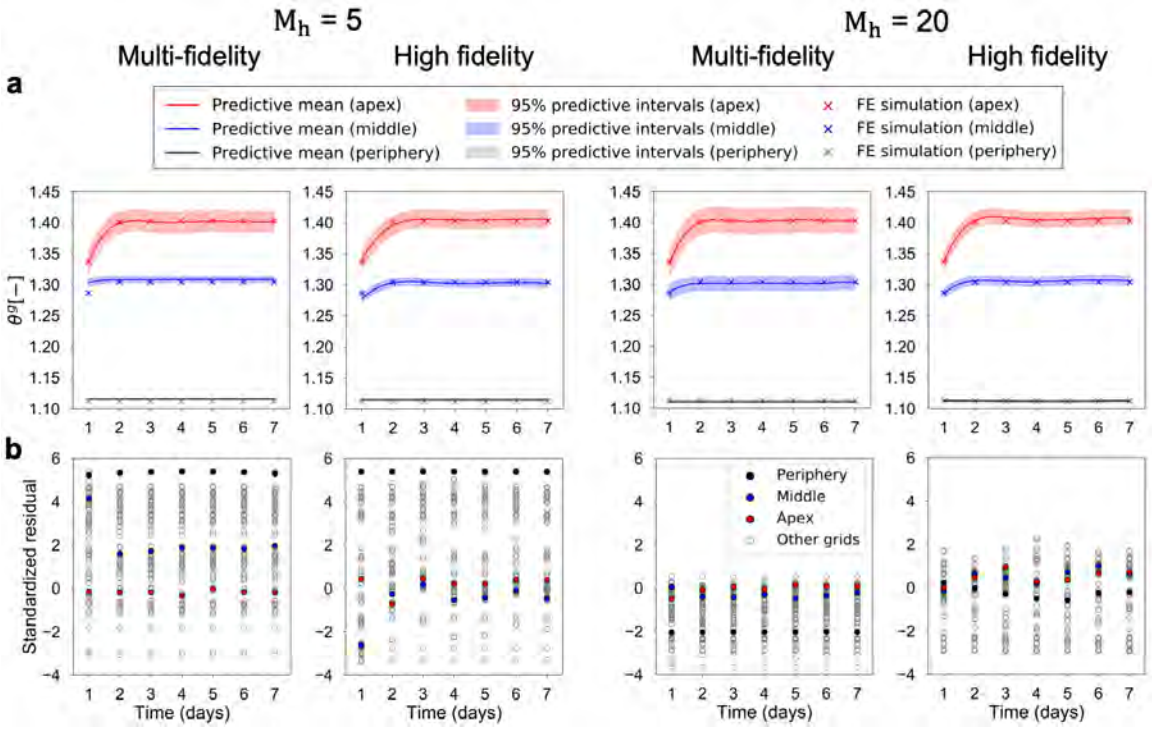

Fig. 3.7.: Effect of changing the number of high fidelity function evaluations on the performance of the multi-fidelity and high fidelity Gaussian process regression for $V = 50$ cc. The test input for the surrogates is the mean of the parameters in Table 3.1. Results are shown for the cases in which either $M_h = 5$ or $M_h = 20$ high fidelity function evaluations are available for training. (**a**) Prediction of the temporal evolution of the growth variable ϑ^g for three points of interest: apex, middle, and periphery of the expander. Plots show the predictive mean and confidence intervals alongside the truth (corresponding high fidelity finite element simulation). (**b**) Standardized residuals for all 100 grid points and 7 time points.

3.3.3 Uncertainty propagation: skin material properties and biological response

We use the validated surrogate to investigate the effect of uncertain mechanical and biological response on the resulting tissue growth. We first set the biological parameters $[K, k, n]$ to their mean value and focus on the variation of the material parameter μ. We remark that the range for the biological parameters is based on our previous experience with the porcine model of tissue expansion [97, 196]. However, without any additional detailed knowledge about the distribution of the biological parameters, we assume the mean of the range to be a meaningful choice. For the mechanical response, on the other hand, we know that skin mechanical properties change with patient demographics. Here we focus on the effect of aging [67, 183]. Testing of skin *in vivo* with suction devices has enabled determination of mechanical function parameters for a wide patient population [184, 185]. In particular, in [185], the vertical displacement of skin under suction (with the same value of negative pressure used for the entire patient population) is reported as a function of age. Based on this report, we estimate that older skin (60 to 80-year-old demographic) is 2.5 times stiffer compared to younger skin (20 to 40-year-old demographic). From their data, it is also clear that there is some variance of mechanical properties for each age group [185]. Hence, we consider two normal distributions of μ to capture the variation in mechanical properties reported in [185]. For the younger group we assume that μ follows a normal distribution with mean $\mu_y = 0.3$ and standard deviation 0.051, which results in a 95% confidential interval $[0.2, 0.4]$ for μ_y. For the older individuals we consider also a normal distribution, with mean $\mu_o = 0.75$ and standard deviation 0.026, resulting in $[0.7, 0.8]$ as the 95% confidential interval of μ_o. We propagate this uncertainty through the surrogate. To do so, we sample 100 points from the distribution of μ for each of the age groups, and evaluate the surrogate. Then, collecting the 100 surrogate evaluations, we determine their mean and confidence interval with Monte Carlo integration [166].

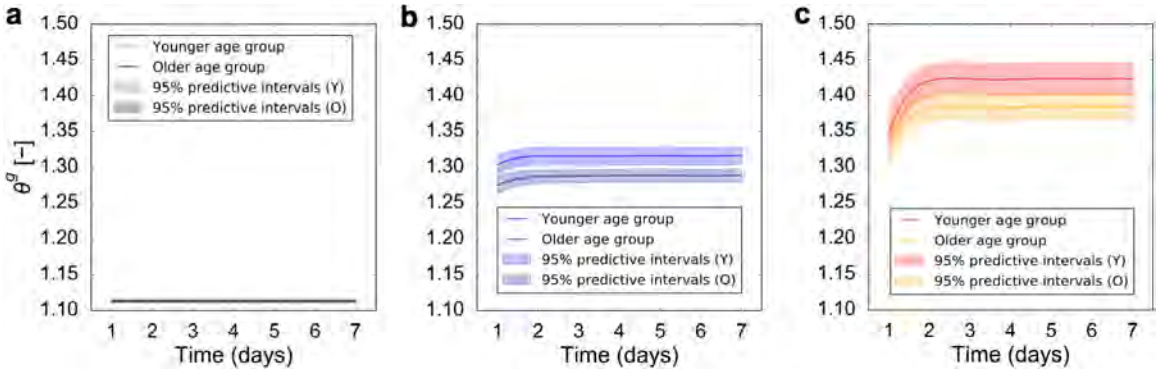

Fig. 3.8.: Propagation of mechanical response uncertainty on the resulting tissue growth at periphery (**a**), middle (**b**), and apex (**c**) for $V = 50$ cc. We consider two age groups with different distribution for the shear modulus, μ. For the younger group, the tissue parameter is normally distributed with mean $\mu_y = 0.3$ and standard deviation 0.051. For the older group, the mean is $\mu_o = 0.75$ and the standard deviation is 0.026. We sample these distributions and use the surrogate to predict the resulting area growth, ϑ^g, at three locations of interest. The younger group shows greater growth compared to the older group at the middle (**b**) and apex (**c**) points, while the periphery (**a**) point shows little difference between age groups.

In Fig. 3.8, we show the results for the three points of interest (apex, middle, and periphery) for $V = 50$ cc, while results for other volumes is available in the Supplementary materials. The younger group tissue properties lead to a higher growth, especially at the apex compared to the older group (Fig. 3.8). The mean value of the response has similar trends in both groups, with growth reaching equilibrium by day 3. The uncertainty in the growth for the younger group is greater compared to the older group, which is expected since the uncertainty in the material properties for the younger group is much larger compared to that of the older group.

The second part of the uncertainty propagation analysis is to investigate the effect of uncertainty in the biological response. Lacking specific knowledge of how these parameters vary with different demographics, we focus on the effect of choosing these parameters to be either their 10 percentile or 90 percentile. We still consider the two age groups, but present only the results for $V = 50$ cc in Fig. 3.9. For each age group, we keep two of the three biological parameters at their mean, and vary the remaining parameter. We show the transient response for the three locations

of interest, as well as the contour of growth (the 50 percentile of the predicted ϑ^g distributions) at day 7. It is immediately clear that the response at day 7 is only mildly affected by the biological parameters. In other words, while the material response leads to a clear difference at day 7 between age groups, the effect of the biological parameters is mostly seen in the transient response. The parameter K in the Hill function describing growth is related to the saturation of the growth rate with respect to the elastic stretch. Consequently, a smaller value of this parameter leads to a greater sensitivity of the growth rate and to an apparent underdamped response. The larger the K, the greater the deformation that is needed for saturation of the growth rate, resulting in curves with greater damping. The parameter k is associated with the time scale of adaptation. A smaller value of k leads to a slower response. When k is set to the 10 percentile value, the growth extends up to day 5. Lastly, the parameter n controls the nonlinearity of the growth rate in response to applied stretch. When n is set to the 10 percentile, the response is underdamped. When n is set to the 90 percentile, the growth curves achieve equilibrium quickly and without oscillations for both age groups.

3.3.4 Effect of expansion volume on tissue growth under uncertainty

Our second analysis is to include the inflation volume V as an input dimension for regression. Therefore, the input training dataset becomes $[\mu, K, k, n, V]$ with $V =$ 30, 40, 50, and 60 cc. For this analysis, we only use ϑ^g at day 7, i.e., we ignore the temporal response in this case. Nonetheless, a full regression including the evolution of ϑ^g over time is also possible. After we build the multi-fidelity GPs, we propagate the uncertainty in the mechanical response corresponding to the two age groups as before. The results are shown in Fig. 3.10. Because the underlying assumption of tissue adaptation is stretch-driven growth, the value of ϑ^g reflects the total area stretch ϑ, which, in turn, is determined by the volume of the expander. Higher volumes lead to increasingly more stretch and consequently more growth. However,

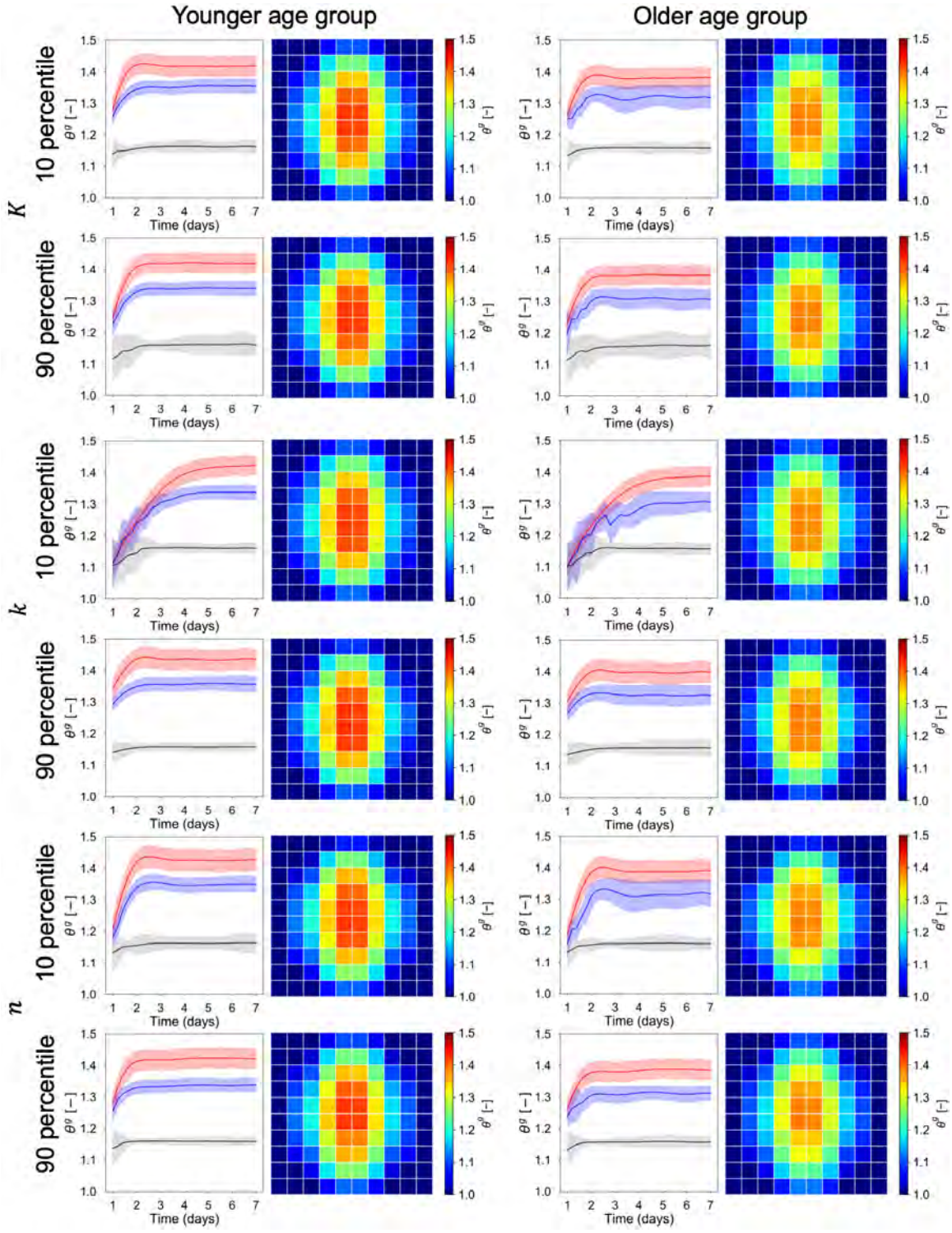

Fig. 3.9.: Continued on the following page.

The effect of biological response uncertainty coupled with the uncertainty in the mechanical behavior for the two age groups. The two age groups are differentiated by the mechanical response μ. For the young group the mean value of the shear modulus is $\mu_y = 0.3$, with standard deviation 0.051. For the old group, the mean value of the shear modulus is $\mu_o = 0.75$, and the standard deviation is 0.026. The contours of the growth field ϑ^g show distinct trends between the two age groups, but little variation as the biological parameter $[K, k, n]$ are varied. At day 7, the young group has an average growth greater compared to the older group. The biological parameters mostly influence the transient response. The parameter K controls the saturation of the growth rate in response to elastic stretch, leading to either underdamped or overdamped curves for the three points of interest: apex (red), middle (blue) and periphery (black). The parameter k controls the speed of the adaptation. The parameter n influences the nonlinearity of the growth rate function, leading to underdamped or overdamped responses.

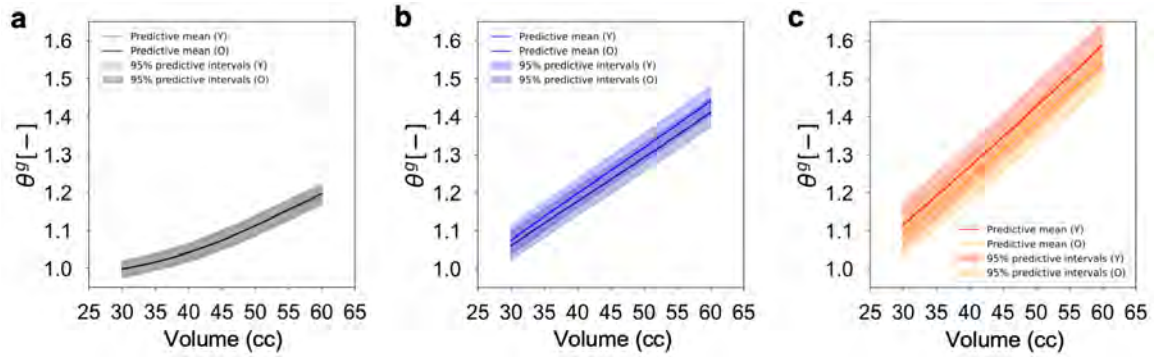

Fig. 3.10.: Prediction of area growth, ϑ^g, using Gaussian process surrogates trained using the inflation volume V as an input during the regression. With respect to temporal variation, only growth at day 7 is considered. Regarding spatial variation, growth at the three points of interest: periphery (**a**), middle (**b**), and apex (**c**), is shown with respect to the change of V. Uncertainty in material properties for two age groups is also considered, as described in the main text.

there is spatial variation, with the apex point showing the more pronounced increase in growth with increasing volume compared to the middle and periphery points. This result underscores the importance of accounting for spatial heterogeneity in designing tissue expansion protocols.

It should also be noted that the uncertainty in the mechanical properties of the tissue leads to a fairly constant variance in the prediction for different volumes. In other words, the uncertainty in the prediction of skin growth accounting for the variation in the mechanical response is not sensitive to the volume change. In fact, this observation then prompts the sensitivity analysis presented in the next subsection.

3.3.5 Sensitivity analysis

The last subsection of the results focuses on a global sensitivity analysis. We follow the Sobol sensitivity analysis [197] using the SALib Python library [198]. The main idea of the Sobol sensitivity analysis is to decompose the variance of the model output into the contributions attributed to individual inputs. For example, an input component is fixed while the other components are varied. If the resulting variance

in the predictions is large, the fixed component of the input is less influential on the output, and vice versa. After accounting for the total variance and normalization using the conditional distribution, the first-order sensitivity index can be calculated. This concept can be extended to higher order sensitivity indices that take into account correlations between different components of the input, e.g., the second-order sensitivity index measures the contribution of pairs of input components. When the dimension of the input, d, increases, the correlation between input components increases as $2^d - 1$. The total-order sensitivity index for one specific component of the input can be deduced in a reverse manner, i.e., the expectation of the variance of the model output is calculated when the set of evaluation points does not have any correlation with the component of interest [199].

We generate a total of 12,000 evaluations of the surrogate, decided from $N\times(2d+2)$, where $N = 1,000$ is the number of samples, and $d = 5$ is the dimension of the input space. We use Saltelli′s sampling scheme [200]. The output dataset is retrieved, and then processed to get the total-order sensitivity index for the apex, middle, and periphery spatial locations of interest, and for three different volumes (Fig. 3.11). We remark that the calculation of the Sobol indices was done via Monte Carlo integration. Therefore, the values reported in Fig. 3.11 are bound to have some noise. Accordingly, we report the uncertainty in the indices. Because each panel (Fig. 3.11**a** to **c**) is derived independently, it should be interpreted individually even though the volume change could also be treated as an input. In fact, it should be noted that the volume consistently influences the variance of the output.

For the apex and middle points, n and K in the Hill function have less impact on ϑ^g for all three volumes. In contrast, μ, k, and time are influential on ϑ^g, but their importance changes for the different volumes. As volume increases, the mechanical parameter, μ, has less contribution than k and time. This result follows from the spatial distribution of the strains, and from the fact that $\vartheta^{\text{cr}} = 1.1$. As a consequence, for small volumes, the lower area changes, close to ϑ^{cr}, coupled with the spatial distribution of the strain field plays an important role to determine the amount of growth.

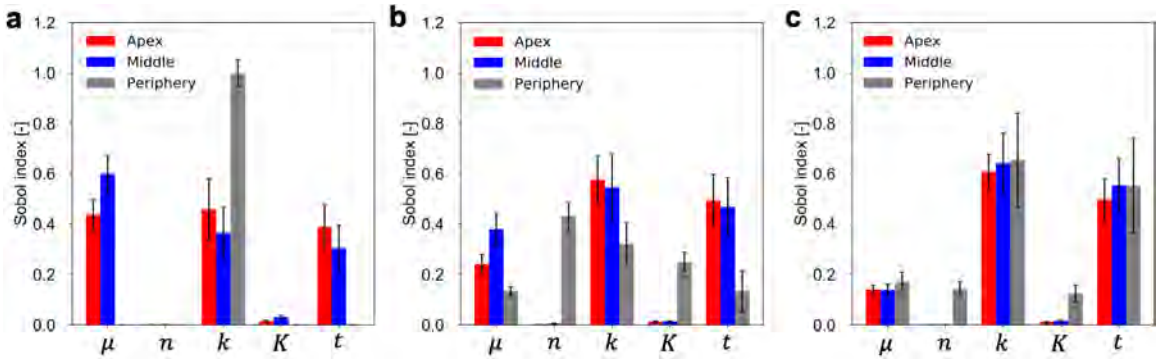

Fig. 3.11.: Sobol sensitivity analysis of area growth, ϑ^g, with respect to individual input dataset, $[\mu, n, k, K, t]$, for volumes V = 40 (**a**), 50 (**b**), and 60 cc (**c**). Here, t indicates day as time. In each panel, three points of interest are considered. Each bar indicates the total-order index. The associated 95% confidential intervals are also shown.

As the volume increases, the strains become more homogeneous independently of μ, and they are always larger than the critical value. Therefore, k and t become more important than μ. These trends are particularly consistent for the middle and apex points. For the periphery point, however, the stretch is always close to the critical value. In the 40 cc case (Fig. 3.11**a**), the stretch in the periphery rarely exceeds ϑ^{cr}, and the growth is negligible at this location for the lowest volume. As the volume increases, the periphery point also shows similar trends compared with the apex and middle points.

3.4 Discussion

In this manuscript we develop a multi-fidelity GP regression surrogate to investigate the effect of uncertain mechanical and biological response of soft tissues on the resulting spatio-temporal growth field. We focus on tissue expansion, but the analysis shown here could be used to study uncertainty in growth and remodeling for other tissues in clinically relevant scenarios [174, 201]. The main motivation for our analysis is the inherent variability in living tissue, both in terms of mechanical properties and also adaptation to environmental cues [202]. While computational models

of growth and remodeling have furthered our understanding of tissue mechanobiology, the role of uncertain parameters in these models remains poorly studied [147]. Machine learning techniques are needed to enable uncertainty analysis of biological systems due to the high computational cost of detailed models, which prevents more traditional analysis such as Monte Carlo sampling [203]. We have shown before that GP surrogates enable uncertainty analysis of stress contours in reconstructive surgery applications [97,101]. Unfortunately, as the complexity and computational cost of the model increases, for example going from a static equilibrium analysis to a model of skin growth in tissue expansion, standard GP regression becomes unattainable. The multi-fidelity strategy used here circumvents this limitation. Instead of relying on a single, very detailed model, we create three models with increasing refinement and use data from all three models to train the surrogate.

Our results confirm that the multi-fidelity GP regression surrogate outperforms the single fidelity GP regression surrogate over the validation set. Interestingly, the low fidelity information is valuable even if the corresponding surrogate shows that the low fidelity model is not an accurate representation of the system. Yet, since all models have correlated trends in the growth field, the low fidelity information can supplement the limited number of high fidelity simulations in the multi-fidelity approach [166]. In contrast, the epistemic error, which results from the limited number of training, cannot be reduced in the high fidelity GP, as evidenced in Figs. 3.3 and 3.4, and in the scatter plots of the standardized residuals in Fig. 3.5.

Design of the training dataset for the multi-fidelity surrogate is a key consideration in the methodology. Evidently, the cost of training the multi-fidelity GP regression depends strongly on the number of high fidelity function evaluations. Too few and the multi-fidelity model will be spoiled by the inaccurate low fidelity data. Similarly, too many high fidelity simulations defeat the purpose of the multi-fidelity scheme. We tested different numbers of high fidelity function evaluations but did find a clear threshold for choosing this number. Our results indicate that the smallest number of high fidelity function evaluations, $M_h = 5$, led to poor performance of the surrogates,

whereas either 10 or 20 high fidelity simulations paired with one order of magnitude more medium and low fidelity simulations led to an accurate surrogate. This trade-off largely depends on the sensitivity of the system to the input parameters. The results in Figs. 3.6 and 3.7 together with the uncertainty propagation analysis indicate that, for the constitutive models we chose and for the range of parameters considered, only a few high fidelity simulations are required. Further work is needed to establish design parameters for the training set of the multi-fidelity surrogates.

As mentioned at the beginning of this section, a key feature of biological tissue that has been often disregarded in the field of tissue mechanobiology is uncertainty in the mechanical and biological response. Moreover, the high nonlinearity of the growth process is one of the main difficulties to accurately investigate correlation of the growth and remodeling fields with varying mechanical and biological parameters. Our study is precisely tailored to tackle this challenge. In turn, this capability is crucial to enable the deployment of computational models of growth and remodeling in relevant clinical settings. For instance, tissue expansion protocols are used for a wide array of patient demographics, from children with large congenital defects [7], to burn wounds in adults [204], breast reconstruction after mastectomy [105], and melanoma surgery in older adults [205]. These different patient populations have distinct skin mechanical properties [67, 181, 184, 185]. In turn, computational models of skin expansion have to account for this kind of variability to guide decision making and treatment planning. Here we focused on the effect of age on the stiffness of skin based on the evidence from the literature. As shown in Fig. 3.8, we are able to make predictions of the resulting growth probability distributions when the mechanical properties of the tissue follow realistic normal distributions that vary with age. A key insight from the analysis is that skin from younger adults is expected to grow more under the same tissue expansion protocol based solely on its mechanical properties, but the uncertainty of this result is larger compared to the older adult population.

Continuing with the two different groups in terms of the mechanical response, we further tested the sensitivity of the growth response to the biological parameters. The

main insight from this investigation is that, for the specific form of the growth law and the range of parameters considered, the variation in the biological parameters affects the transient response, within the first 5 days post-inflation, but has little effect on the growth contours at day 7 (Fig. 3.9). This kind of knowledge can help design safer inflation protocols. A more thorough calibration of the model is of course needed, but our current analysis suggests that waiting 7 days between expansions may be a good decision to ensure that the skin has reached a stable point before the next inflation. As mentioned in the introduction, weekly expansions are indeed common [7], but more aggressive expansion protocols have also been proposed [133].

Our work is not free of limitations. Regarding the construction of the surrogate, we rely on simulation data alone and assume that these data are noiseless [166, 190]. As discussed in [166], introducing noise into the training data set is more representative of the real system, especially if we are to extend our framework to include experimental data. Another limitation of our methodology is that the design of the training data set remains arbitrary and it is thus difficult to anticipate the number of function evaluations needed to train an accurate surrogate. Further work in this area is particularly important since one would like to avoid unnecessary evaluations of the high fidelity model. Thirdly, here we focus on a single inflation step and on a single expander shape, our future work will extend the analysis to different expander shapes and inflation protocols. We will also continue to integrate the computational model with our experimental model of tissue expansion [97]. Lastly, here we used a simple isotropic material model, the neo-Hookean strain energy, to model skin. In reality, skin is an anisotropic material [51, 180]. We have shown in previous simulations that anisotropic material properties lead to anisotropic growth fields [176]. We have also observed this experimentally [115]. Therefore, our future work will also include the effect of anisotropy on growth and remodeling of soft tissues.

3.5 Conclusion

We present a multi-fidelity Gaussian process surrogate to predict the growth of skin in tissue expansion when the mechanical response and the biological response are assumed uncertain. The multi-fidelity Gaussian process surrogate outperforms single fidelity approaches, making it particularly appealing for uncertainty analysis of biological systems, which are highly nonlinear and for which high fidelity finite element models are computationally expensive. We expect that the results shown here will be valuable beyond their application to tissue expansion, for the analysis of other soft tissues that growth and remodel in relevant clinical scenarios.

4. THE GEOMETRY OF INCOMPATIBILITY IN GROWING SOFT TISSUES

Abstract: Tissues *in vivo* are not stress-free. Moreover, as we grow, our tissues adapt to different physiological and disease conditions through growth and remodeling. This adaptation occurs at the microscopic scale, where cells control the microstructure of their immediate extracellular environment to achieve homeostasis. The local and heterogeneous nature of this process is linked to the accumulation of residual stresses. At the macroscopic scale, growth and remodeling can be accurately captured with the finite volume growth framework within continuum mechanics, which is akin to plasticity. The multiplicative split of the deformation gradient into growth and elastic contributions brings forth the notion of incompatibility as a plausible description for the origin of residual stress. Here we define the geometric features that characterize incompatibility in biological materials. We introduce the geometric incompatibility tensor for different growth types, showing that the constraints associated with growth lead to specific patterns of our incompatibility metrics. To numerically investigate the distribution of incompatibility measures we implement the analysis within the finite element framework. Simple, illustrative examples are shown first to explain the main concepts. Then, numerical characterization of incompatibility and residual stress in three biomedical applications are performed: brain atrophy, skin expansion, and cortical folding. Our analysis provides new insights into the role of growth in the development of tissue defects and residual stresses. Thus, we anticipate that our work will further motivate additional research to characterize residual stresses in living tissue and their role in development, disease, and clinical intervention.

4.1 Motivation

It is well known that soft tissues are not in a stress-free configuration in the human body [9]. For instance, skin has been shown to have prestrain [115], as well as the heart and heart valves [127]. Moreover, prestress in arteries actually minimizes the stress distribution during systole [206]. Beyond arteries, it has been hypothesized that the state of prestress of different organs yields specific physiological function [207]. To quantify prestrain fields, several experimental techniques have been proposed. For example, the opening angle experiment of arteries has been adopted as a key measure of residual deformation [208]. Heart valves have been measured *in vivo* and *ex vivo* to quantify the overall prestrain [209]. Thick slices of whole hearts have been dissected and then cut to measure the opening of these slices and, by extension, of the heart [210, 211]. Such approaches have further established the existence of prestrain, but they are incomplete because they reduce the residual strain field to a homogeneous indicator like the scalar opening angle. The true state of residual deformation may be more complex [212]. Indeed, there is evidence that tissues develop heterogeneous patterns of residual deformation during growth [213]. In response to skin expansion, for instance, the residual deformation of skin changes across the entire expanded region [116] and significant variation of opening angle along major arteries has been observed [85]. Thus, although many previous studies have confirmed the existence of prestrain in living tissue, the precise features and origins of this field are still poorly understood. Understanding the basic mechanisms that can drive and determine the development of residual strain in soft tissues has significant implications: it would allow estimation of the true reference configuration, the true mechanical behavior of tissues with respect to a stress-free state, and the way in which residual strain contributes to tissue mechanical function *in vivo* [11, 12].

Among various theoretical frameworks of growth and remodeling, a phenomenological description adopted from the theory of plasticity has been particularly successful [147, 148, 214]. In finite deformation plasticity, the deformation gradient tensor

is multiplicatively split into elastic and inelastic (usually called plastic when rate sensitivity is neglected) deformations [215]. Instead of a plastic deformation, the corresponding tensor in biomechanics is denoted growth deformation [123, 216], and captures addition of mass by changes in volume [217]. The decomposition of the deformation gradient tensor plays a key role in understanding the origin of residual stresses at the macroscopic scale. The multiplicative split in fact introduces a geometric origin to the residual stress [218]. Growth and elastic deformations are in general incompatible fields, which means they do not derive from a displacement field [219]. If the growth deformation is incompatible, then an incompatible elastic deformation is required such the combination of both ensures a compatible total deformation seen *in vivo*. In turn, the necessary incompatibility of the elastic deformation is the source of the residual stress field [220]. In summary, quantifying the incompatibility of growth fields is intimately linked to the understanding of residual strains and how it may originate at the microscopic scale.

The notion of incompatibility arising from the multiplicative split of the deformation gradient is common between plasticity and growth, but the physical mechanisms leading to incompatibility and the following residual stress are different between engineering materials with crystal structure and living organisms. In crystals, it is universally acknowledged that plastic deformation occurs through the movement of a dislocation, which is the most important line defect in crystals [218]. Plastically-induced misfit between adjacent regions in the crystal results in the change of the lattice structure [221, 222]. This incompatibility at the atomic level is captured in the plastic deformation tensor at the macroscopic scale. Defects or imperfections of the lattice accommodated by the dislocation are connected to the storage of additional energy and, hence, residual stress [223–225]. Other types of topological defects in crystals can lead to residual stress, for instance quasi-plastic thermal expansion [222, 226, 227]. In soft tissues, on the other hand, the physical mechanism at the microscale behind the accumulation of residual stress is still unclear [11]. Previous studies have proposed intrinsic differences in mechanical properties between adjacent

structures within the tissue [213], different growth rates leading to unequal material accumulation [10], microstructure reorganization [85,216], surface accretion [228,229], and multiple and evolving natural configurations for different constituents [230]. Even if the precise microscopic origin of the residual stress is still in question, the macroscopic observation captured by the framework of finite volume growth condenses the origin of the residual stress to geometric mismatches in the soft tissue microstructure.

In this manuscript, we quantify the geometric incompatibility that arises during growth of soft tissue within the finite volume growth framework. This geometric characterization is linked to the origin of residual stress at the continuum scale. For our analysis, we rely on some well-established tools from crystal physics, such as re-interpretation of the Burgers vector and the geometric dislocation density tensor [231, 232]. In plasticity, the Burgers vector explains the geometry of the dislocation density [233–235]. Soft tissues do not accumulate dislocations due to growth, but we can still use similar geometric analysis to understand the type of incompatibility possible in growing tissue, and how it may be connected to the accumulation of residual stress. We derive the form of the local Burgers vector density for representative scenarios of growth such as volumetric, area, and fiber growth. Moreover, we also characterize incompatibility and the associated residual stress for relevant biomedical applications such as human brain atrophy and skin expansion. We believe that our results will provide new insights and foster discussion about the geometric incompatibility induced by growth, how it is related to microscale phenomena, and how it is connected to the accumulation of residual stress. Moreover, we anticipate that this work will not only improve our basic understanding of tissue mechanics, but also be useful for medical interventions.

4.2 Methods

4.2.1 Kinematics of growth

Starting from the kinematics of finite deformation, we introduce the functional relation $\mathbf{x} = \varphi(\mathbf{X}, t)$ to describe the motion of a body at time t. Let $\mathbf{X} \in \mathcal{B}_0 \subset \mathbb{R}^3$ be a point in the reference configuration, $\mathcal{B}_0$. Then φ maps $\mathbf{X}$ to a point in the current configuration, $\mathbf{x} \in \mathcal{B} \subset \mathbb{R}^3$. The map φ is continuously differentiable with respect to $\mathbf{X}$. Thus the local deformation is captured by the deformation gradient $\mathbf{F} = \nabla_0 \varphi$, which is a linear transformation of points from the tangent space $\mathcal{T}\mathcal{B}_0$ to $\mathcal{T}\mathcal{B}$. The determinant of the deformation gradient captures the local volume change $J = \det(\mathbf{F})$. Growth in biological tissues can be expressed via the multiplicative split of the deformation gradient tensor $\mathbf{F}$ into growth and elastic components [123],

$$\mathbf{F} = \mathbf{F}^e \mathbf{F}^g \,, \tag{4.1}$$

where $\mathbf{F}^g$ is the growth contribution and $\mathbf{F}^e$ is the elastic deformation. The tensor $\mathbf{F}^g$ captures the biological process of tissue adaptation and requires further constraints. In fact, the form of $\mathbf{F}^g$ is not just a kinematic assumption but also a constitutive one. The split in Eq. (4.1) further implies the split of the local volume change into elastic and growth components

$$J = J^e J^g \tag{4.2}$$

with $J^e = \det(\mathbf{F}^e)$ and $J^g = \det(\mathbf{F}^g)$. In a more general scenario, growth can mean also atrophy or shrinkage and not just addition of mass,

$$\begin{aligned} J^g > 1 &: \text{ growth}\,, \\ J^g < 1 &: \text{ shrinkage}\,. \end{aligned} \tag{4.3}$$

Of course, both J^e and J^g should be positive. At the microscopic level, $J^g > 1$ can be interpreted, for instance, as cell migration into the tissue, cell proliferation,

material deposition, or hyperplasia of cells. On the other hand, $J^g < 1$ can entail cell necrosis or apoptosis, or material degradation [148].

The first requirement is that $\mathbf{F}^g$ should not be singular; then $\mathbf{F}^e$ can be recovered from Eq. (4.1), $\mathbf{F}^e = \mathbf{F}\mathbf{F}^{g-1}$. Other reasonable assumptions include that $\mathbf{F}^g$ should be symmetric [236, 237]. Further restrictions on $\mathbf{F}^g$ are related to particular biological contexts as will be seen in later sections. The split, see Eq. (4.1), implies the presence of an intermediate configuration that is stress-free. However, the intermediate configuration is fictitious and, generally, incompatible. In other words, $\mathbf{F}^g$ cannot be observed in general since the deformation described by this tensor does not originate from the continuous deformation of a body. At the same time, the elastic deformation $\mathbf{F}^e = \mathbf{F}\mathbf{F}^{g-1}$ is, by construction, the necessary incompatible field that renders the total deformation compatible. In turn, the need for $\mathbf{F}^e$ to ensure compatibility even in absence of any external loading is the source of residual stress.

Let's further consider the polar decomposition of $\mathbf{F}^e$ into

$$\mathbf{F}^e = \mathbf{V}^e\mathbf{R}^e = \mathbf{R}^e\mathbf{U}^e, \tag{4.4}$$

where $\mathbf{V}^e$ and $\mathbf{U}^e$ are elastic left and right stretch tensors and $\mathbf{R}^e$ is the elastic rotation tensor. The stress in the current configuration is calculated based on the elastic deformation $\mathbf{F}^e$. To satisfy objectivity, however, the elastic left and right Cauchy-Green tensors are used,

$$\mathbf{B}^e = \mathbf{F}^e\mathbf{F}^{e\top} = \mathbf{V}^e\mathbf{V}^{e\top} \text{ and } \mathbf{C}^e = \mathbf{F}^{e\top}\mathbf{F}^e = \mathbf{U}^{e\top}\mathbf{U}^e. \tag{4.5}$$

The stress in the current configuration can be derived in terms of either $\mathbf{B}^e$ or $\mathbf{C}^e$, which are independent of the rotation $\mathbf{R}^e$. This suggests that the elastic deformation field needed for compatibility does not always induce stress. If the incompatible deformation needed is a pure rotation $\mathbf{F}^e = \mathbf{R}^e$, then the current configuration is still stress-free. In crystal plasticity, this scenario is the stress-free curvature of the crystal lattice [238, 239]. An example of this situation for growing tissue will be covered

in the Results section 4.3. Note also that, if $\mathbf{F}^g$ is actually compatible, then in the absence of any external loading we would recover $\mathbf{F} = \mathbf{F}^g$ and in that case the elastic deformation is the second-order identity tensor $\mathbf{F}^e = \mathbf{I}$. In other words, if the growth field is compatible and no forces are applied at the boundary, then there is no residual stress in the body.

4.2.2 The geometric incompatibility tensor G

As stated above, the deformation gradient tensor is compatible, as it is the gradient of a vector field, while the growth and elastic contributions are not [218]. The condition of compatibility can be expressed via the Curl$(\bullet)$ operator. For any vector field $\mathbf{v}$, it is always the case that $\mathrm{Curl}\,(\mathrm{Grad}\mathbf{v}) = \mathbf{0}$. The notation Grad$(\bullet)$ denotes the same operation as $\nabla(\bullet)$. Similarly, the Curl can also be represented with the notation $\nabla \times (\bullet)$. It is clear that for the total deformation of a body, we have $\mathrm{Curl}\,\mathbf{F} = \mathbf{0}$, while $\mathrm{Curl}\,\mathbf{F}^g$ and $\mathrm{Curl}\,\mathbf{F}^e$ are not necessarily zero. Therefore, $\mathrm{Curl}\,\mathbf{F}^g$ and $\mathrm{Curl}\,\mathbf{F}^e$ are quantitative indicators for the degree of incompatibility induced by growth or shrinking. The Curl of a tensor field $\mathbf{A}$ is another tensor field defined by

$$(\mathrm{Curl}\,\mathbf{A})\mathbf{v} = \mathrm{Curl}(\mathbf{A}^\top \mathbf{v}) \tag{4.6}$$

for all constant vectors $\mathbf{v}$. We use the notation Curl$(\bullet)$ for the operation with respect to the reference configuration, $\mathbf{X}$, compared to curl$(\bullet)$ which is with respect to the current configuration, $\mathbf{x}$ [232]. In index notation, the components of Curl$\mathbf{A}$ are

$$(\mathrm{Curl}\,\mathbf{A})_{ij} = \varepsilon_{irs}\frac{\partial A_{js}}{\partial X_r}, \tag{4.7}$$

where ϵ_{irs} is the permutation symbol. We remark also that our definition of the Curl is sometimes introduced as the transpose of the Curl in other references and the reader should be careful about the definition being used [232, 238]. Next, we introduce the Burgers vector, which measures the gap introduced after deforming a closed circuit

on a reference surface by the tensor field $\mathbf{F}^g$. With the help of Stokes' theorem, the Burgers vector $\mathbf{b}$ can be written in terms of the Curl($\bullet$)

$$\mathbf{b}(\mathcal{S}_0) \coloneqq \int_{C_0} \mathbf{F}^g \, \mathrm{d}\mathbf{X} = \int_{\mathcal{S}_0} (\mathrm{Curl}\, \mathbf{F}^g)^\top \mathbf{n}_0 \, \mathrm{d}A_0 \,, \tag{4.8}$$

where C_0 is the closed circuit on a surface $\mathcal{S}_0(\mathcal{B}_0)$, with normal $\mathbf{n}_0$ in the reference configuration. The differential $\mathbf{n}_0 \mathrm{d}A_0$ is the surface element in the reference configuration. If $\mathrm{Curl}\, \mathbf{F}^g = 0$, the growth deformation is compatible and the Burgers vector $\mathbf{b}$ vanishes. This is the integrability condition for there to exist a unique vector field $\mathbf{v}$ whose gradient is $\mathbf{F}^g$ [225,238]. Failure to satisfy this integrability condition implies the contrary, that there is no $\mathbf{v}$ whose gradient leads to $\mathbf{F}^g$.

The Burgers vector in crystal physics measures the geometry of a dislocation. On the other hand, the Burgers vector in Eq. (4.8) for growing tissues can be interpreted as a mismatch in the geometry between two adjacent surface elements that occurs because growth is non-uniform in general. For example, imagine more material is deposited in one small element compared to an adjacent microscopic volume. Upon growth, the initially closed circuit that traverses these two areas would not be closed anymore. The resulting gap length of the mismatch is uniquely given by the Burgers vector. Note that this picture does not capture the molecular mechanism of the incompatibility. We restrict our incompatibility density measure to the continuum scale.

The Burgers vector defined over the small region $\mathcal{S}_0$ can be localized [232]. In addition, the Burgers vector actually lies in the intermediate configuration, but the variable of integration in Eq. (4.8) is defined in the reference configuration. Using Nanson's formula, we can express the localized Burgers vector completely in terms of quantities in the intermediate configuration

$$(\mathrm{Curl}\, \mathbf{F}^g)^\top \mathbf{n}_0 \, \mathrm{d}A_0 = \frac{1}{J^g} (\mathrm{Curl}\, \mathbf{F}^g)^\top \mathbf{F}^{g^\top} \bar{\mathbf{n}} \, \mathrm{d}\bar{A} \,, \tag{4.9}$$

where $\bar{\mathbf{n}}\,\mathrm{d}\bar{A}$ is the surface element in the intermediate configuration with normal $\bar{\mathbf{n}}$. Therefore, Eq. (4.9) evaluates the incompatibility due to growth or shrinkage on a surface with normal $\bar{\mathbf{n}}$ at a point in the intermediate configuration. To capture the incompatibility in all possible directions, we now introduce the central geometric object in this paper: the geometric incompatibility tensor $\mathbf{G}$ [232],

$$\mathbf{G} = \frac{1}{J^g}\mathbf{F}^g \mathrm{Curl}\,\mathbf{F}^g\,. \tag{4.10}$$

The local Burgers vector density can now be computed for any direction $\bar{\mathbf{n}}$ using $\mathbf{G}$,

$$\mathbf{b} \coloneqq \mathbf{G}^\top \bar{\mathbf{n}}\,. \tag{4.11}$$

Strikingly, it should be possible to quantify the amount of incompatibility without knowing the growth field. Consider the following thought experiment: A body in the current configuration is unloaded and broken up into smaller and smaller pieces. As constraints are released and the body is split into differential volume elements that each approach a stress-free state, we would recover the incompatible elastic deformation field $\mathbf{F}^e$. Knowledge of this field alone should be sufficient to determine the residual stress in the body $\mathcal{B}$. Indeed, $\mathbf{G}$ can be derived from $\mathbf{F}^e$ via [233, 235]

$$\mathbf{G} = J^e \mathbf{F}^{e-1} \mathrm{curl}\,\mathbf{F}^{e-1}\,. \tag{4.12}$$

The equivalence between Eqs. (4.10) and (4.12) can be evaluated using Eqs. (4.1) and (4.2).

4.2.3 Constraints on the growth field determine the geometry of incompatibility

As mentioned before, the specific form of $\mathbf{F}^g$ is both a kinematic and a constitutive assumption. In particular, the restrictions in the tensor $\mathbf{F}^g$ should reflect the connec-

tion between growth and tissue microstructure. Here we focus on three representative growth models: volume, area, and length (or fiber) growth [147]. Additionally, the tensor $\mathbf{F}^g$ can be expressed in terms of scalar fields directly linked to mass sources. The scalar field for growth is denoted by ϑ^g throughout this manuscript. The added structure for $\mathbf{F}^g$ leads to interesting properties of the geometric incompatibility tensor $\mathbf{G}$ which are unique to growing soft tissue.

Isotropic volume growth

The simplest and most natural growth model is isotropic volume growth. This corresponds, for instance, to cell proliferation or deposition of new tissue without any preferred orientation. A common example of this type of growth is tumor growth [240, 241]. We have

$$\mathbf{F}^g := \sqrt[3]{\vartheta^g}\mathbf{I}, \tag{4.13}$$

where ϑ^g is a scalar field that represents local volume change due to growth, and $\mathbf{I}$ is the second-order identity matrix. The evolution of ϑ^g should obey a constitutive equation representing cell mechanobiology. The Curl operation for this tensor leads to

$$(\mathrm{Curl}\,\mathbf{F}^g)_{ij} = \epsilon_{irs}\frac{\partial F^g_{js}}{\partial X_r} = \frac{\partial \sqrt[3]{\vartheta^g}}{\partial X_r}\epsilon_{irs}\delta_{js} = \frac{\partial \sqrt[3]{\vartheta^g}}{\partial X_r}\epsilon_{irj}\,. \tag{4.14}$$

Alternatively, in tensor notation,

$$\mathrm{Curl}\,\mathbf{F}^g = \frac{1}{3\sqrt[3]{\vartheta^{g2}}} \star \nabla\vartheta^g = \frac{1}{3\sqrt[3]{\vartheta^{g2}}}(\nabla\vartheta^g \times \mathbf{e}_i)\otimes\mathbf{e}_i\,, \tag{4.15}$$

with $\star(\bullet)$ denoting the Hodge star operator, and $\mathbf{e}_i$ are the standard orthonormal basis vectors. For isotropic volume growth, using Eq. (4.15) and recalling the definition of the geometric incompatibility tensor in Eq. (4.10), we find that $\mathbf{G}$ is a skew-symmetric

tensor and the matrix form corresponding to the choice of the standard Cartesian basis is

$$\mathbf{G} = \frac{1}{3\sqrt[3]{\vartheta^{g4}}} \begin{bmatrix} 0 & -\vartheta^{g}_{,X_3} & \vartheta^{g}_{,X_2} \\ \vartheta^{g}_{,X_3} & 0 & -\vartheta^{g}_{,X_1} \\ -\vartheta^{g}_{,X_2} & \vartheta^{g}_{,X_1} & 0 \end{bmatrix}, \tag{4.16}$$

where $\vartheta^{g}_{,X_1}$, $\vartheta^{g}_{,X_2}$, and $\vartheta^{g}_{,X_3}$ are the partial derivatives of ϑ^{g} with respect to the reference configuration coordinates.

Considering Eq. (4.11), each local Burgers vector density for the standard basis in 3D Euclidean space is, in matrix form,

$$\begin{aligned} \mathbf{b}_1 &= \mathbf{G}^{\top}\mathbf{e}_1 = \frac{1}{3\sqrt[3]{\vartheta^{g4}}}(0,\, -\vartheta^{g}_{,X_3},\, \vartheta^{g}_{,X_2})^{\top}, \\ \mathbf{b}_2 &= \mathbf{G}^{\top}\mathbf{e}_2 = \frac{1}{3\sqrt[3]{\vartheta^{g4}}}(\vartheta^{g}_{,X_3},\, 0,\, -\vartheta^{g}_{,X_1})^{\top}, \\ \mathbf{b}_3 &= \mathbf{G}^{\top}\mathbf{e}_3 = \frac{1}{3\sqrt[3]{\vartheta^{g4}}}(-\vartheta^{g}_{,X_2},\, \vartheta^{g}_{,X_1},\, 0)^{\top}. \end{aligned} \tag{4.17}$$

Recall that these Burgers vectors $\mathbf{b}_i$ measure the incompatibility on planes defined by the basis vectors $\mathbf{e}_i$. Thus, here we see that for isotropic growth, there is no incompatibility orthogonal to the plane of interest. In other words, for the plane defined by each $\mathbf{e}_i$, the local Burgers vector density is restricted to that plane. Contrast this with crystals, where screw dislocations are possible and entail defects in the direction of the normal vector [242]. Another key insight from analyzing incompatibility in the context of growth and remodeling is that we have a direct connection between the gradients of growth and incompatibility. For instance, if the growth is uniform (that is, if $\vartheta^{g}_{,\mathbf{X}} = 0$) then it is clear that $\mathbf{G}$ vanishes. Another useful example would be growth that only varies in one direction, for instance X_1. In that case, $\mathbf{b}_1$ vanishes completely and there is no incompatibility in planes defined by the growth gradient. We actually explore this example further in the Results section 4.3. We also investigate a brain atrophy model [243] where shrinkage of white and gray matter leads to local growth gradients and, in consequence, residual stresses from incompatibility [244].

Transversely isotropic area growth

Transversely isotropic in-plane area growth is applicable for thin tissues in which there is area growth while the thickness remains unchanged [245]. An important example of area growth is that of skin in tissue expansion [246]. Computational models of skin growth based on the multiplicative split of the deformation gradient have been shown to accurately capture animal experiments and patient-specific scenarios [80, 131]. The growth deformation tensor for area growth takes the form

$$\mathbf{F}^g := \sqrt{\vartheta^g}\mathbf{I} + (1 - \sqrt{\vartheta^g})\mathbf{N}_0 \otimes \mathbf{N}_0\,, \tag{4.18}$$

where $\mathbf{N}_0$ is the tissue normal vector in the reference configuration. Eq. (4.18) inherently restricts volume change to permanent changes in area while keeping thickness deformations purely elastic. The determinant of Eq. (4.18), which is the total volume of new tissue, is also the local area change. The Curl operation in this case can be expressed in tensor notation as

$$\operatorname{Curl}\mathbf{F}^g = \frac{1}{2\sqrt{\vartheta^g}}(\nabla\vartheta^g \times \mathbf{e}_i) \otimes \mathbf{e}_i - \frac{1}{2\sqrt{\vartheta^g}}(\nabla\vartheta^g \times \mathbf{N}_0) \otimes \mathbf{N}_0\,. \tag{4.19}$$

The geometric incompatibility tensor for area growth can be computed from Eqs. (4.19) and (4.10). For completeness, in index notation this tensor takes the form

$$G_{ij} = \left(\frac{1}{\sqrt{\vartheta^g}}\delta_{im} + \left(\frac{1}{\vartheta^g} - \frac{1}{\sqrt{\vartheta^g}}\right)N_{0i}N_{0m}\right)\epsilon_{mrs}\frac{\partial F^g_{js}}{\partial X_r}\,. \tag{4.20}$$

Similar to the isotropic case, incompatibility occurs due to gradients in the permanent area change, as is evident from Eq. (4.19). Having $\mathbf{G}$, we can determine the Burgers vector density in any direction. To that end, the most relevant plane is defined by $\mathbf{N}_0$ or, more rigorously, the normal $\bar{\mathbf{N}}$ in the intermediate configuration.

For this particular type of growth we have $\bar{\mathbf{N}} = \mathbf{N}_0$. The local Burgers vector density $\mathbf{G}^\top\bar{\mathbf{N}}$ becomes

$$\mathbf{b} = \mathbf{G}^\top\bar{\mathbf{N}} = \frac{1}{2\sqrt{\vartheta^{g3}}}(\mathbf{s}_\alpha \otimes (\nabla\vartheta^g \times \mathbf{s}_\alpha))\bar{\mathbf{N}}, \tag{4.21}$$

where the vectors $\mathbf{s}_\alpha$, with $\alpha = \{1, 2\}$, are the local basis for the surface defined by $\bar{\mathbf{N}}$. We observe again that the Burgers vector corresponding to the plane defined by $\bar{\mathbf{N}}$ is restricted to that plane and will have only components along the $\mathbf{s}_\alpha$ directions. Moreover, if the gradient is aligned with any of the surface basis vectors, then the expression can be further simplified. For instance, assume, without loss of generality, that $\nabla\vartheta^g$ is aligned with $\mathbf{s}_2$ and denote $\mathbf{s}_1 = \mathbf{s}$ as the vector orthogonal to the in plane growth gradient. Then,

$$\mathbf{b} = \frac{|\nabla\vartheta^g|}{2\sqrt{\vartheta^{g3}}}\mathbf{s}\,. \tag{4.22}$$

This last expression condenses the key type of incompatibility of area growth. Since the local basis can always be aligned with the direction of the growth gradient, Eq. (4.22) shows that the incompatibility is orthogonal to the growth gradient and its magnitude is proportional to the magnitude of the growth gradient scaled with respect to the amount of growth.

Uniaxial Fiber growth

In tissues such as muscle, growth can occur along the fiber direction [247, 248]. In addition, axons in the white matter of the brain also show lengthwise growth induced by chronic overstretch during development [249]. Cortical folding of the brain is a phenomenon that occurs in part due to mechanical instabilities triggered by this type of growth coupled to biological factors [250]. The heart also has a unique and

well-defined fiber structure along which growth can occur, especially due to volume overload. For growth along the fiber direction, $\mathbf{F}^g$ is defined as

$$\mathbf{F}^g := \mathbf{I} + (\vartheta^g - 1)\mathbf{f}_0 \otimes \mathbf{f}_0\,, \tag{4.23}$$

where $\mathbf{f}_0$ is the fiber direction in the reference configuration. The determinant of Eq. (4.23) explains that the volume change in fiber growth is now related to the irreversible change in length along the fiber direction.

For this specific type of growth tensor, the Curl operator leads to an elegant form

$$\operatorname{Curl}\mathbf{F}^g = (\nabla\vartheta^g \times \mathbf{f}_0) \otimes \mathbf{f}_0. \tag{4.24}$$

The incompatibility tensor can then be computed based on its definition $\mathbf{G} = 1/\vartheta^g \mathbf{F}^g \operatorname{Curl}\mathbf{F}^g$. For completeness, we write it in index notation,

$$G_{ij} = \left(\frac{1}{\vartheta^g}\delta_{im} + (1 - \frac{1}{\vartheta^g}) f_{0i} f_{0m}\right) \epsilon_{mrs} \frac{\partial \vartheta^g}{\partial X_r} f_{0j} f_{0s}\,. \tag{4.25}$$

For fiber growth, fiber direction is unchanged in the intermediate configuration, $\bar{\mathbf{f}} = \mathbf{f}_0$. The local Burgers vector density in the plane defined by the fiber direction $\bar{\mathbf{f}}$ is

$$\mathbf{G}^\top \bar{\mathbf{f}} = \frac{1}{\vartheta^g}\mathbf{f}_0 \otimes (\nabla\vartheta^g \times \mathbf{f}_0)\bar{\mathbf{f}} = \mathbf{0}\,. \tag{4.26}$$

Thus, in the case of fiber growth, there cannot be incompatibility in the direction of the fiber. More interesting are the planes orthogonal to the fiber. Also from Eq. (4.24) it can be seen that if the gradient of growth is aligned with the direction of the fiber there is also no incompatibility. Consider the unit vector in the intermediate configuration $\bar{\mathbf{m}}$, which is locally orthogonal both to the growth gradient and the fiber direction. Then, the local Burgers vector density for the plane defined by $\bar{\mathbf{m}}$ is

$$\mathbf{G}^\top \bar{\mathbf{m}} = \frac{|\nabla\vartheta^g| \sin(\beta)}{\vartheta^g}\mathbf{f}_0\,, \tag{4.27}$$

where β is the angle between the growth gradient and the fiber direction. Therefore, the incompatibility for fiber growth is aligned with the fiber direction, and the magnitude of the Burgers vector is proportional to the magnitude of the growth gradient and inversely proportional to the amount of growth. As stated before, if the growth gradient is aligned with the fiber direction, the Burgers vector vanishes. On the contrary, the Burgers vector will have maximum magnitude when the growth gradient is orthogonal to the fiber direction.

In the Results section 4.3, we present examples for each of the three above-shown cases. First, we illustrate the effect of a specific form of the growth tensor in Eqs. (4.13), (4.18), and (4.23) on the resulting patterns of incompatibility. Second, we characterize incompatibility and residual stresses for the examples of skin growth during tissue expansion, brain atrophy, and cortical folding due to axon fiber growth. Overall, the notion of the geometric incompatibility tensor $\mathbf{G}$ takes on specific features for growing soft tissues described with the finite growth framework. While we limit the present work to this geometric description, the characteristics of $\mathbf{G}$ and the Burgers vector for the different growth cases raises intriguing questions about the possible microscopic and molecular origins of these phenomena.

4.2.4 Balance equations for growing soft tissues

Growth requires considering the thermodynamics of open systems, as carefully outlined in [236]. Under the assumption of a quasi-static process, balance equations for linear momentum akin to plasticity are derived. For completeness, we review the mass specific format of the balance equations in the Lagrangian form, similar to [251].

Balance of mass

Let the density of the mass element in the reference configuration be ρ_0 and its rate of change $\dot{\rho}_0$. We remark that ρ_0 is the current density of the material but pulled back to the reference configuration. Then the local form of balance of mass for open

systems (growing tissues in our setting) implies the possible influx or outflux of mass $\mathbf{R}$ and a possible mass source $\mathcal{R}_0$ term [252],

$$\dot{\rho}_0 = \nabla_0 \cdot \mathbf{R} + \mathcal{R}_0 \,. \tag{4.28}$$

The mass change of growing matter can occur at constant density or constant volume. In the framework of finite volume growth, the density-preserving notion is implied [217]. In consequence, the mass source will be linked to the time evolution of $\mathbf{F}^g$.

Balance of linear momentum

The local form of balance of linear momentum for the open systems is obtained by considering $\dot{\rho}_0$ in the Lagrangian equations of motion such that

$$\dot{\rho}_0 \mathbf{v} + \rho_0 \dot{\mathbf{v}} = \nabla_0 \cdot \mathbf{P} + \rho_0 \mathbf{f} \,, \tag{4.29}$$

where $\mathbf{v}$ is the velocity vector, $\mathbf{P}$ is the first Piola-Kirchhoff stress, and $\mathbf{f}$ is the body force field. Under quasi-static conditions and neglecting the mass flux, $\mathbf{R} = 0$ and $\dot{\mathbf{v}} = 0$, Eq. (4.29) can be simplified considerably,

$$\mathbf{0} = \nabla_0 \cdot \mathbf{P} + \rho_0 \mathbf{f} \,. \tag{4.30}$$

Balance of entropy

Local balance of entropy is enforced through the Clausius-Duhem inequality. For an open system, the local form of the dissipation inequality $\mathcal{D}$ ignoring temperature changes [80] can be stated as

$$\rho_0 \mathcal{D} := \mathbf{S} : \dot{\mathbf{E}} - \rho_0 \dot{\psi} - T \rho_0 S_0 \geq 0 \,, \tag{4.31}$$

where $\mathbf{S} = \mathbf{F}^{-1}\mathbf{P}$ is the second Piola-Kirchhoff stress, $\dot{\mathbf{E}}$ is the rate of the Green-Lagrange strain tensor, $\Psi = \rho_0\psi$ is the volume specific free energy density, T is temperature, and S_0 is an external entropy source [253]. For growing tissues, it is common to assume that added mass does not contribute to additional entropy and $S_0 = 0$. Hence, neglecting any dissipative mechanisms, Eq. (4.31) reduces to the standard definition of the second Piola-Kirchhoff stress as the derivative of the strain energy with respect to its work-conjugate Green-Lagrange strain tensor $\mathbf{E}$,

$$\mathbf{S} = \rho_0 \frac{\partial \psi}{\partial \mathbf{E}} \,. \tag{4.32}$$

To close this section on the balance equations of growth, we establish the relationship between the mass balance Eq. (4.28) and the growth tensor $\mathbf{F}^g$. Considering that the density in the current and intermediate configurations is constant, $\rho^g = \rho = \text{const}$ [236], we have $\rho^g = j^g \rho_0$ with $j^g = J^{g-1}$, then

$$\dot{\rho}^g = \dot{j}^g \rho_0 + j^g \dot{\rho}_0 = 0 \,. \tag{4.33}$$

In addition, recall that we ignore the mass flux term. Then, Eqs. (4.28) and (4.33) yield

$$\dot{\rho}_0 = -\rho_0 J^g \dot{j}^g = -\rho_0 J^g \frac{\partial j^g}{\partial \mathbf{F}^{g-1}} : \dot{\mathbf{F}}^{g-1} = -\rho_0 \mathbf{F}^{g\top} : \dot{\mathbf{F}}^{g-1} \,, \tag{4.34}$$

where we have introduced the growth velocity tensor $\mathbf{L}^g = \dot{\mathbf{F}}^g \mathbf{F}^{g-1}$ [217]. Using $\dot{\mathbf{F}}^g \mathbf{F}^{g-1} = -\mathbf{F}^g \dot{\mathbf{F}}^{g-1}$ we have

$$\rho_0 \mathrm{tr}(\mathbf{L}^g) = \mathcal{R}_0 \,, \tag{4.35}$$

which is the link between the mass source field and the growth tensor field.

4.2.5 Constitutive model for soft tissue mechanics

We consider hyperelastic behavior, which is a common framework for modeling soft tissues. This requires the definition of the volume specific free energy density which depends only on the elastic deformation, $\Psi = \rho_0\hat{\psi}(\mathbf{F}^e, \rho_0) = \Psi(\mathbf{C}^e)$. Moreover, the strain energy can be written in terms of the invariants of $\mathbf{C}^e$, $\Psi = \Psi(I_1^e, I_2^e, I_3^e)$. Two different models are considered. First, we introduce a compressible neo-Hookean hyperelastic potential of the form

$$\Psi = \frac{\mu}{2}(I_1^e - 3 - 2\ln(J^e)) + \frac{\lambda}{2}\ln^2(J^e), \tag{4.36}$$

where $I_1^e = \mathrm{tr}(\mathbf{C}^e) = \mathrm{tr}(\mathbf{B}^e)$ is the first invariant of $\mathbf{C}^e$ and $\mathbf{B}^e$, $I_3^e = \det(\mathbf{C}^e) = \det(\mathbf{B}^e) = J^{e2}$ is the third invariant of $\mathbf{C}^e$ and $\mathbf{B}^e$, and μ and λ are the shear modulus and Lame's first parameter, respectively. The second Piola-Kirchhoff stress tensor follows

$$\mathbf{S}^e = 2\frac{\partial\Psi}{\partial\mathbf{C}^e} = (\lambda\ln(J^e) - \mu)\mathbf{C}^{e-1} + \mu\mathbf{I}\,. \tag{4.37}$$

Alternatively, Kirchhoff stress is given by

$$\tau^e = 2\mathbf{B}^e\frac{\partial\Psi}{\partial\mathbf{B}^e} = (\lambda\ln(J^e) - \mu)\mathbf{i} + \mu\mathbf{B}^e\,, \tag{4.38}$$

where $\mathbf{i}$ is the spatial second-order identity tensor. The rationale for introducing both the Lagrangian and the Eulerian stress tensors is that the finite element implementation can be formulated for either setting. Obviously, both expressions of the stress are equivalent.

Many soft tissues are characterized by a high degree of collagen content [43]. Collagen is the most common structural protein in animals. It is observed in the microstructure of tissues as a fiber network [254, 255]. Mechanically, this fibrous architecture endows tissues with a characteristic exponential behavior under tensile loading [178]. Among several hyperelastic strain energy potentials that capture this

response, we employ the one proposed by Gasser-Ogden-Holzapfel (GOH) showing nearly incompressible hyperelastic and anisotropic behavior [57],

$$\begin{aligned}
&\Psi = \Psi_{\text{iso}}(\overline{\mathbf{C}}^e) + \Psi_{\text{aniso}}(\overline{\mathbf{C}}^e, \mathbf{H}_\alpha) + \Psi_{\text{vol}}(J^e) \text{ with} \\
&\Psi_{\text{iso}}(\overline{\mathbf{C}}^e) = \frac{\mu}{2}(\overline{I}_1^e - 3), \\
&\Psi_{\text{aniso}}(\overline{\mathbf{C}}^e, \mathbf{H}_\alpha) = \frac{k_1}{2k_2}(\exp{(k_2\langle\overline{E}_\alpha\rangle^2)} - 1), \text{ and} \\
&\Psi_{\text{vol}}(J^e) = \frac{\lambda}{2}\left(\frac{J^{e2}-1}{2} - \ln(J^e)\right),
\end{aligned} \tag{4.39}$$

where $\overline{I}_1^e = J^{e-\frac{2}{3}} I_1^e$ is the first invariant of $\overline{\mathbf{C}}^e$, the isochoric part of $\mathbf{C}^e$, and $\overline{E}_\alpha \equiv \overline{\mathbf{C}}^e : \mathbf{H}_\alpha - 1$ is the pseudo-invariant with respect to the symmetric generalized structure tensor $\mathbf{H}_\alpha = \kappa\mathbf{I} + (1-3\kappa)\bar{\mathbf{a}}_\alpha \otimes \bar{\mathbf{a}}_\alpha$ with fiber direction $\bar{\mathbf{a}}_\alpha = \mathbf{F}^g\mathbf{a}_{0\alpha}/|\mathbf{F}^g\mathbf{a}_{0\alpha}|$ in the intermediate configuration, $\mathbf{a}_{0\alpha}$ in the reference configuration. The notation $\langle\cdot\rangle$ in Eq. (4.39) denotes the Macaulay brackets. The parameters k_1, k_2, and κ capture the response of the fiber family: k_1 describes the tensile response, k_2 is dimensionless and expresses nonlinearity of the fiber response, and κ is another dimensionless parameter that indicates dispersion in the range 0 to 1/3, from perfectly anisotropic to perfectly isotropic. The second Piola-Kirchhoff stress tensor of GOH potential can be derived from the strain energy,

$$\begin{aligned}
\mathbf{S}^e &= 2\frac{\partial\Psi_{\text{iso}}}{\partial\mathbf{C}^e} + 2\frac{\partial\Psi_{\text{aniso}}}{\partial\mathbf{C}^e} + 2\frac{\partial\Psi_{\text{vol}}}{\partial\mathbf{C}^e} \\
&= \mu\frac{\partial\overline{I}_1^e}{\partial\mathbf{C}^e} + 2k_1\langle\overline{E}_\alpha\rangle\exp\left(k_2\langle\overline{E}_\alpha\rangle^2\right)J^{e-\frac{2}{3}}\mathbb{P} : \frac{\partial\overline{E}_\alpha}{\partial\overline{\mathbf{C}}^e} + \frac{\lambda}{2}\left(J^e - \frac{1}{J^e}\right)\frac{\partial J^e}{\partial\mathbf{C}^e},
\end{aligned} \tag{4.40}$$

where

$$\mathbb{P} = \mathbb{I} - \frac{1}{3}\mathbf{C}^{e-1}\otimes\mathbf{C}^e = \mathbb{I} - \frac{1}{3}\overline{\mathbf{C}}^{e-1}\otimes\overline{\mathbf{C}}^e, \tag{4.41}$$

is the fourth order projection tensor, with $\mathbb{I} = \frac{1}{2}(\mathbf{I}\overline{\otimes}\mathbf{I} + \mathbf{I}\underline{\otimes}\mathbf{I})$ the fourth-order identity tensor, $\{\bullet\overline{\otimes}\circ\}_{ijkl} = \{\bullet\}_{ik}\{\circ\}_{jl}$ and $\{\bullet\underline{\otimes}\circ\}_{ijkl} = \{\bullet\}_{il}\{\circ\}_{jk}$. The derivatives in (4.40) can be expanded further,

$$\frac{\partial \overline{I}_1^e}{\partial \mathbf{C}^e} = J^{e-\frac{2}{3}}\left(\mathbf{I} - \frac{1}{3}\overline{I}_1^e\overline{\mathbf{C}}^{e-1}\right), \quad \frac{\partial \overline{E}_\alpha}{\partial \overline{\mathbf{C}}^e} = \mathbf{H}_\alpha, \quad \text{and} \quad \frac{\partial J^e}{\partial \mathbf{C}^e} = \frac{J^e}{2}\mathbf{C}^{e-1}\,. \tag{4.42}$$

The corresponding Kirchhoff stress can be obtained by pushing-forward the second Piola-Kirchoff stress tensor,

$$\boldsymbol{\tau}^e = \mathbf{F}^e\mathbf{S}^e\mathbf{F}^{e\top} = \mu(\overline{\mathbf{B}}^e - \frac{1}{3}\overline{I}_1^e\mathbf{i}) + 2k_1\langle\overline{E}_\alpha\rangle\exp\left(k_2\langle\overline{E}_\alpha\rangle^2\right)J^{e-\frac{2}{3}}(\overline{\mathbf{h}}_\alpha - \frac{1}{3}(\overline{\mathbf{C}}^e : \mathbf{H}_\alpha)\mathbf{i}) + \frac{\lambda}{4}(J^{e2}-1)\mathbf{i}, \tag{4.43}$$

where $\overline{\mathbf{B}}^e = J^{e-\frac{2}{3}}\mathbf{B}^e$ is the isochoric part of $\mathbf{B}^e$ and $\overline{\mathbf{h}}_\alpha = \overline{\mathbf{F}}^e\mathbf{H}_\alpha\overline{\mathbf{F}}^{e\top} = \kappa\overline{\mathbf{B}}^e + (1-3\kappa)\mathbf{a}_\alpha\otimes\mathbf{a}_\alpha$ is the push-forward of the symmetric generalized structure tensor of $\mathbf{H}_\alpha$ with $\mathbf{a}_\alpha = \overline{\mathbf{F}}^e\overline{\mathbf{a}}_\alpha = J^{e-\frac{1}{3}}\mathbf{F}^e\overline{\mathbf{a}}_\alpha$ is the fiber vector in the current configuration.

4.2.6 Constitutive model for growth

Continuing directly from Eq. (4.35) the rate of change of mass dictates the change in $\mathbf{F}^g$. Furthermore, recalling the different types of growth, the rate of change in mass can be directly linked to the evolution of the scalar field ϑ^g. The constitutive equation for the rate of change of this scalar field, $\dot{\vartheta}^g$, is often coupled to either mechanical cues, or to biological processes independent of mechanical input [145]. Mechanically-coupled growth is separated into stress-driven [217] or strain-driven [131] approaches,

$$\dot{\vartheta}^g = k^g(\vartheta^g, \vartheta^e)\phi^g(\mathbf{M}^e) \text{ or } \dot{\vartheta}^g = k^g(\vartheta^g, \vartheta^e)\phi^g(\mathbf{F}^e), \tag{4.44}$$

where $\mathbf{M}^e = \mathbf{C}^e\mathbf{S}^e$ is the Mandel stress which is the power conjugate to $\mathbf{L}^g$ [256], and $\phi^g(\cdot)$ is the growth criterion that activates growth based on whether the stress or strain exceeds a certain threshold. The function $k^g(\vartheta^g, \vartheta^e)$ dictates the shape of the

curve. An overview of different functions for $k^g(\vartheta^g, \vartheta^e)$ and $\phi^g(\cdot)$ are available in the literature [80, 98, 257, 258]. For example, the strain-driven approach from [175] is

$$\begin{aligned} k^g(\vartheta^g) &= \frac{1}{\tau}\left(\frac{\vartheta^{\max} - \vartheta^g}{\vartheta^{\max} - 1}\right)^{\gamma} \quad \text{and} \\ \phi^g(\vartheta^e) &= \langle \vartheta^e - \vartheta^{\text{crit}} \rangle = \langle \frac{\vartheta}{\vartheta^g} - \vartheta^{\text{crit}} \rangle, \end{aligned} \tag{4.45}$$

where τ^{-1} adjusts the adaptation speed, $\vartheta^{\max}$ is the upper limit of growth, γ regulates the shape of the growth curve, and ϑ^{crit} controls the homeostatic state [145]. We have recently proposed a growth rate curve with saturation as the input increases [98]. Using a Hill function to control the growth rate with saturation at increasing ϑ^e we have

$$\dot{\vartheta}^g = \frac{k(\vartheta^e - \vartheta^{\text{crit}})^n}{K^n + (\vartheta^e - \vartheta^{\text{crit}})^n} \tag{4.46}$$

with biological parameters k, K, and n [98].

On the other hand, non-mechanically coupled growth is also relevant, for instance during morphogenesis or development. In these situations, the growth rate could be coupled to biological factors or cytokines [83]. Here we do not couple the growth field to other inputs but only deal with prescribed functions of growth as a function of time and location

$$\vartheta^g = 1 + R(\mathbf{X}, t). \tag{4.47}$$

4.2.7 Finite element implementation

The numerical implementation of the examples shown in the following sections was achieved by programming a user subroutine in the nonlinear finite element package Abaqus (Dassault Systems, Waltham, MA), similar to [175].

The global problem of finding the displacements incrementally is left to the Abaqus nonlinear solver. Our user subroutine is used at the integration point level. For each

integration point, we keep an internal variable with the value of the growth field ϑ^g at the end of the previous converged step. The integration point subroutine takes in the current total deformation $\mathbf{F}$ and updates ϑ^g. For the mechanically-coupled growth problem, $\vartheta^g_{t+\Delta t}$ is determined by an implicit Euler backward scheme

$$\mathsf{R}^g = \vartheta^g_{t+\Delta t} - \vartheta^g_t - \dot{\vartheta}^g \Delta t\,, \tag{4.48}$$

where R^g is the residual of the local growth update problem, and $\vartheta^g_{t+\Delta t}$ and ϑ^g_t are the growth values at the integration point at the current and previous time steps, respectively. Eq. (4.48) is solved via Newton-Raphson iterations [175]. Once growth has been updated, the elastic deformation is calculated from $\mathbf{F}^e = \mathbf{F}\mathbf{F}^{g-1}$, and the corresponding stress is evaluated.

The global Newton-Raphson iterations carried out by the Abaqus solver require the stress tensor and the consistent tangent. Thus, our user subroutine first calculates the fourth order Eulerian tangent $\mathbf{c}$ by linearization of the elastic Kirchhoff stress in Eqs. (4.38) or (4.43) with respect to $\mathbf{B}^e$,

$$\mathbf{c} = 4\mathbf{B}^e \frac{\partial^2 \Psi}{\partial \mathbf{B}^e \partial \mathbf{B}^e} \mathbf{B}^e = \mathbf{c}^e + \mathbf{c}^g\,, \tag{4.49}$$

where $\mathbf{c}^e$ corresponds to the partial derivative when $\mathbf{F}^g$ is held constant, and it corresponds to the usual elastic constitutive moduli. In contrast, $\mathbf{c}^g$ is the derivative at constant $\mathbf{F}$. For the non-mechanically coupled growth problem defined in Eq. (4.47), ϑ^g is a function of the reference position and time only, and $\mathbf{c}^g = 0$. For an overview of the specific form of $\mathbf{c}^g$ for different growth formulations, the reader is referred to [259].

The tangent $\mathbf{c}$ is further modified to obtain the tangent corresponding to the Jaumann stress rate used in Abaqus: $\mathbf{c}^{\text{abaqus}} = (\mathbf{c} + \frac{1}{2}(\tau\overline{\otimes}\mathbf{i} + \mathbf{i}\overline{\otimes}\tau + \tau\underline{\otimes}\mathbf{i} + \mathbf{i}\underline{\otimes}\tau))/J$. The user subroutine allows us to solve for the evolving deformation of the growing body. During postprocessing, we use the shape functions to interpolate $\mathbf{F}^g$ and calculate the geometric incompatibility tensor $\mathbf{G}$ in Eq. (4.10). Code for the different examples is also attached as part of this submission.

4.3 Results

We first quantify the incompatibility in four illustrative examples in which the growth field is entirely prescribed, i.e., it is not coupled to any mechanical input. The growth fields for these examples are summarized in Table 4.1. The examples are chosen to show the features of each type of growth and also the consequences of seeing different characteristics for the gradients of growth across the body. For each of these cases we compute the metrics of incompatibility defined in the Methods section, and show the corresponding residual stress when no other external forces are applied to the body. Next, we turn our attention to mechanically-coupled growth examples which correspond to relevant biomedical applications. The first of these examples is brain atrophy which involves volume growth. The second is skin expansion where area growth is considered. The last example is cortical folding of the brain with fiber growth based on axonal orientation.

Table 4.1.: Kinematics of growth for non-mechanically coupled examples

Growth type	Growth tensor	Growth indicator
Isotropic volume growth (unidirectional field)	$\mathbf{F}^g = \sqrt[3]{\vartheta^g}\mathbf{I}$	$\vartheta^g = 1 + \frac{1}{4}X_1 t$
Isotropic volume growth (multi-directional field)	$\mathbf{F}^g = \sqrt[3]{\vartheta^g}\mathbf{I}$	$\vartheta^g = 1 + \frac{1}{4}f(R)t,\ R = \sqrt{X_1^2 + X_2^2 + X_3^2}$
Area growth	$\mathbf{F}^g = \sqrt{\vartheta^g}\mathbf{I} + (1 - \sqrt{\vartheta^g})\mathbf{N}_0 \otimes \mathbf{N}_0$	$\vartheta^g = 1 + \frac{1}{4}f(R)t,\ R = \sqrt{X_1^2 + X_2^2}$
Fiber growth	$\mathbf{F}^g = \mathbf{I} + (\vartheta^g - 1)\mathbf{f}_0 \otimes \mathbf{f}_0$	$\vartheta^g = 1 + \frac{1}{4}X_2 t$

4.3.1 Isotropic volume growth driven by a unidirectional field

We start with the simplest example for non-mechanically coupled isotropic volume growth. The domain of $1 \times 1 \times 1$ mm is discretized with $1,000$ C3D8 elements and the growth variable ϑ^g is prescribed as a function of time and space

$$\vartheta^g := 1 + \frac{1}{4}X_1 t \tag{4.50}$$

with time $t \in [0, 1]$. This function leads to a 25% volume increase across the domain (Fig. 4.1**a**). The growth field is non-uniform and, furthermore, it changes only in one direction. The rationale for this field is to isolate a simple pattern of growth that can be caused by a morphogen gradient for example.

The finite element model has 1,331 nodes and we constrain only three translations and three rotations in order to allow free deformation except for rigid body motions. No natural boundary conditions are applied. For the material behavior we consider

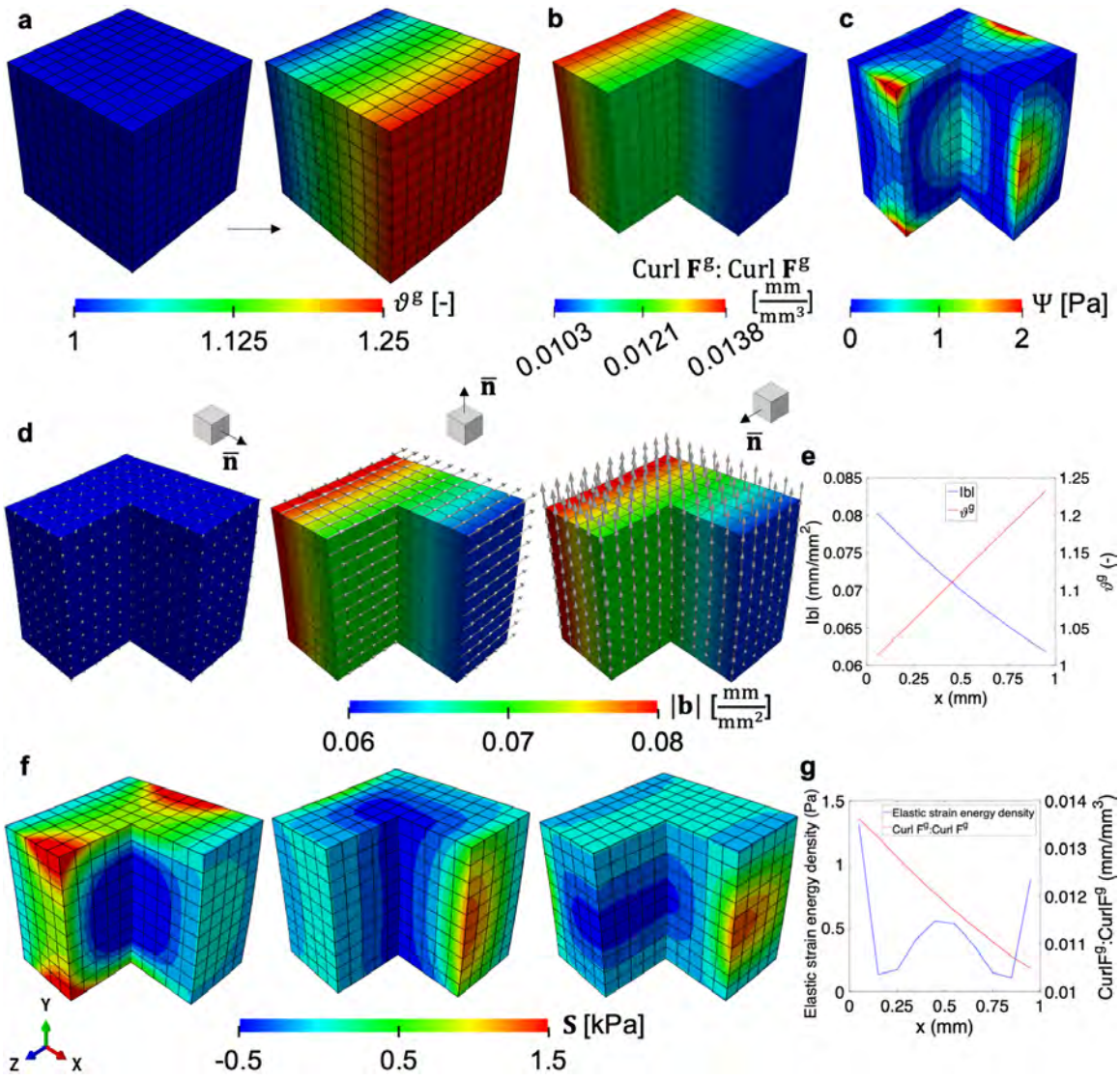

Fig. 4.1.: Continued on the following page.

Isotropic growth guided by a unidirectional field. Finite element model of a simple cube deforms in response to a linear growth field, ϑ^g, with respect to the X_1 direction (**a**). Based on this growth field, the invariant of the incompatibility tensor $\mathrm{Curl}\,\mathbf{F}^g$: $\mathrm{Curl}\,\mathbf{F}^g$ is obtained (**b**). There are only six constraints to prevent rigid body motion, but elastic free energy accumulates across the domain due to the incompatibility of the growth field (**c**). The local Burgers vector density **b** is derived with respect to the standard basis in 3D Euclidean space, $\bar{\mathbf{n}}$ (**d**). The arrows in (**d**) are scaled relative to the magnitude of $|\mathbf{b}|$. For $\bar{\mathbf{n}}$ along the X_1 direction, there is no incompatibility. For the other two directions, **b** lies on the plane defined by $\bar{\mathbf{n}}$ and orthogonal to the growth direction. The magnitude of $|\mathbf{b}|$ shows an inverse trend compared to the growth value ϑ^g (**e**). The components of second Piola-Kirchhoff stress, S_{33} and S_{22}, are matched with the local Burgers vector direction in (**d**) respectively when $\bar{\mathbf{n}}$ is not X_1 direction (second and third in **f**), while S_{11} is plotted when there is no local Burgers vector (first in **f**). The free energy density and the invariant $\mathrm{Curl}\,\mathbf{F}^g$: $\mathrm{Curl}\,\mathbf{F}^g$ are also plotted (**g**), showing that while incompatibility decreases along X_1, the strain energy is highest at the boundary, with another local maximum at the center of the domain.

the neo-Hookean hyperelastic potential introduced before, with $\mu = 0.55$ MPa [98] and the initial compressibility $\nu = 0.4$. Upon growth, the cube of material deforms solely due to growth into the configuration depicted in Fig. 4.1**a**. The contour plot in this panel is the growth variable ϑ^g, showing the desired gradient along X_1.

The amount of incompatibility can be boiled down to the single invariant $\operatorname{Curl}\mathbf{F}^g : \operatorname{Curl}\mathbf{F}^g$, which is motivated by similar scalar fields in gradient plasticity related to energy stored as a consequence of crystal defects [224, 225]. While in our case the scalar field does not correspond to an energy quantity, it is an invariant field which overall relates to the degree of incompatibility and is therefore useful to visualize. The scalar $\operatorname{Curl}\mathbf{F}^g : \operatorname{Curl}\mathbf{F}^g$ changes in the same direction of the gradient of ϑ^g (Fig. 4.1**b**), which matches the intuition that incompatibility is related to mismatch between adjacent differential volumes with different growth. Note, however, that even though the gradient of the volume change is constant, the incompatibility metric is not. This occurs because even though the volume growth increases linearly with X_1, the growth tensor is actually not a linear function of ϑ^g. To achieve volume growth of ϑ^g, a differential volume element has to grow $\sqrt[3]{\vartheta^g}$ in all directions.

The local Burgers vector density $\mathbf{b}$ can be calculated for any plane in the intermediate configuration. We choose the standard basis in 3D Euclidean space as the normals of interest, e.g., $\bar{\mathbf{n}} = \mathbf{F}^g\mathbf{e}_1/|\mathbf{F}^g\mathbf{e}_1|$ and so on for the other two directions (Fig. 4.1**d**). For the plane corresponding to the growth gradient, $\bar{\mathbf{n}} = \mathbf{F}^g\mathbf{e}_1/|\mathbf{F}^g\mathbf{e}_1|$, the Burgers vector vanishes. This occurs because on the plane orthogonal to the growth gradient, growth is uniform and therefore compatible. This follows directly from the definition of $\operatorname{Curl}\mathbf{F}^g$ in Eq. (4.15). The local Burgers vector density in the other two planes is restricted to the corresponding plane. This was noted in the derivation of $\mathbf{G}$ for the different growth types. In the case of isotropic growth fields it is always true that $\bar{\mathbf{n}}^\top\mathbf{G}\bar{\mathbf{n}} = 0$ for any normal $\bar{\mathbf{n}}$. In this example it also becomes evident that $\mathbf{b}$ is orthogonal to the growth gradient. The magnitude of the local Burgers vector density $|\mathbf{b}|$ is also not constant over the domain (Fig. 4.1**e**). Instead, maybe albeit surprisingly, the magnitude is greater in the region with least growth, and decreases

as growth increases. This can be explained by the fact that $\mathbf{G}$ is scaled by the determinant of the permanent volume change. Even though on one end of the cube the growth is small, the relative difference in the differential volume elements is greater in these regions compared to the relative mismatch in size between adjacent volume elements that have undergone more substantial growth.

To visualize the consequences of nonuniform growth on the development of residual stress, the second Piola-Kirchhoff stress tensor $\mathbf{S}$ is represented along each of the $\mathbf{b}$ directions in Fig. 4.1**d** and the result is depicted in Fig. 4.1**f**. (For the first panel of Fig. 4.1**f**, since the Burgers vector is not defined, we showed the first component of the second Piola-Kirchhoff stress S_{11}.) There are residual stresses in all three directions. The magnitude of the stress is not necessarily aligned with the magnitude of the local Burgers vector density. To get a better understanding of how the elastic deformation is distributed, Fig. 4.1**c** shows the contours of the elastic strain energy, and Fig. 4.1**g** compares the elastic strain energy against the scalar invariant of incompatibility $\operatorname{Curl}\mathbf{F}^g : \operatorname{Curl}\mathbf{F}^g$.

The mechanical equilibrium problem that gives rise to $\mathbf{F}^e$ is not trivial. Even when no external forces are considered and the only driver for $\mathbf{F}^e$ is the incompatibility of $\mathbf{F}^g$, the elastic deformation $\mathbf{F}^e$ has not just lead to compatibility $\operatorname{Curl}\mathbf{F} = 0$, but also minimize Ψ (which is a nonlinear function of $\mathbf{F}^e$) and satisfy the vanishing of the normal stress at the boundaries. As a result, even though the geometry of the incompatibility has the elegant and simple features expected based on the analytical derivation Eq. (4.16), the stress field is more intricate. Take the first component of the second Piola-Kirchhoff stress S_{11} shown in the first column of Fig. 4.1**f**. The stress on the faces with normal $\mathbf{e}_1$ or $-\mathbf{e}_1$ have zero stress, as required. Along the other two directions, the stress goes from tension at the boundary to compression at the center. Similar trends are observed for the other two components, S_{33} and S_{22} (second and third columns of Fig. 4.1**f**).

4.3.2 Isotropic volume growth driven by a multi-directional vector field

In the second example we consider a half sphere with radius $R_0 = 1$ mm discretized with $1,920$ C3D8 elements and $2,300$ nodes. Material properties, boundary conditions, and the range of ϑ^g are the same as in the previous example, but in this case we consider radial growth as stated in Table 4.1. The amount of growth is a monotonic increase function of the variable $R = \sqrt{X_1^2 + X_2^2 + X_3^3}$. This example is motivated by evidence that tumors grow more at the outer layers which have more access to nutrients compared to the core of the tumor which may even be necrotic [240]. In the simplest case, we consider once again the linear increase in growth rate $\dot{\vartheta}^g = \frac{1}{4}R$. However, we also consider other functions of $\vartheta^g(R)$ that are nonlinear, either concave or convex (Fig. 4.2**f**). In particular, Fig. 4.2**a** shows two different growth fields; in one case growth increases slowly near the core and more rapidly near the outer surface, while in the other case we have a very rapidly increasing growth near the core compared to near the outer surface.

To analyze the incompatibility we focus on the spherical basis vector field $\bar{\mathbf{n}}_r$, $\bar{\mathbf{n}}_\phi$, and $\bar{\mathbf{n}}_\theta$, called radial, meridional, and circumferential respectively. As can be expected based on the previous example and the derivation for $\operatorname{Curl}\mathbf{F}^g$ in Eq. (4.15), the local Burgers vector density vanishes for the planes defined by the growth gradient $\bar{\mathbf{n}}_r$. The growth is uniform within each concentric sphere forming the tumor and there is no incompatibility in the infinitesimal area elements making up these spheres. Incompatibility arises from the mismatch in growth between different concentric layers of the tumor. The local Burgers vector density $\mathbf{b}$ is shown for the other two directions of interest in Fig. 4.2**b** and **c**. When the plane of interest for the characterization of the Burgers vector is defined by the normal $\bar{\mathbf{n}}_\phi$, $\mathbf{b}$ is circumferential, and for $\bar{\mathbf{n}}_\phi$ $\mathbf{b}$ is meridional. This observation, again, aligns with the remarks of the previous example and with the derivation of $\mathbf{G}$ in Eq. (4.16).

The nonlinearity of the growth rate translates to the degree of incompatibility. In particular, the magnitude of the local Burgers vector density $|\mathbf{b}|$ is proportional to the

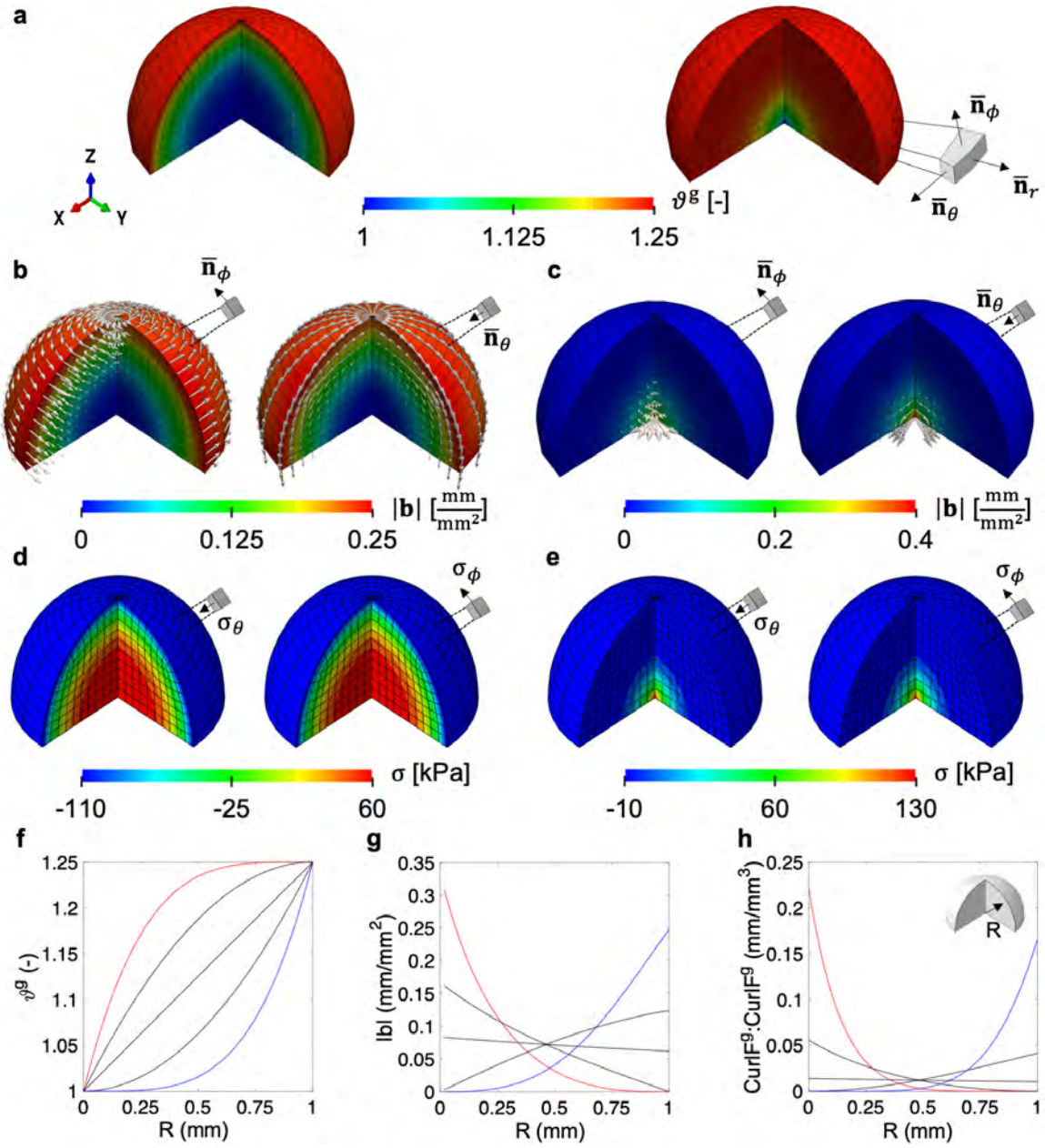

Fig. 4.2.: Isotropic volume growth guided by a multi-directional field with different growth distributions. an increasing gradient of ϑ^g from the inner core to the outer shell (**a**, left) and a case in which ϑ^g increases rapidly at the core and slowly at the outer layers (**a**, right). The local Burgers vector density is computed for each of the two cases and for planes defined by the spherical basis vector corresponding to meridional and circumferential directions $\bar{\mathbf{n}}_\phi$ and $\bar{\mathbf{n}}_\theta$. (**b**, **c**). The Burgers vector vanishes for planes defined by the radial direction $\bar{\mathbf{n}}_r$ and are thus not shown. (Continued on the following page.)

Stress components aligned with the direction of the Burgers vectors show similar trends to the degree of incompatibility for the two cases considered (**d**, **e**). The growth fields considered, in addition to the two cases illustrated in the top panels, are shown in **f**, were the blue curve is the case shown in the left column of **a**, and the red curve is the right column of **a** . The magnitude of the local Burgers vector density $|\mathbf{b}|$ is greater for higher growth gradients, but also greater for smaller growth values (**g**). The scalar metric $\operatorname{Curl}\mathbf{F}^g : \operatorname{Curl}\mathbf{F}^g$ shows the same trends as the magnitude of the local Burgers vector density (**h**).

magnitude of the growth gradient. Note that if the growth increases rapidly at the core compared to the outer region, the magnitude of the local Burgers vector density is higher at the core and decreases toward the outer layers as the growth gradient decreases (red curve in Fig. 4.2**g**). In contrast, when the growth shows an increasing gradient with respect to R, $|\mathbf{b}|$ increases with respect to R as well. Compare this to the case in which growth rate is constant across the tissue. In such case, there is still a small variation in $\mathbf{b}$ as a function of R because, as discussed before, the magnitude of growth also contributes to $\mathbf{b}$. However, the scaling of $\mathbf{b}$ by the growth amount is barely noticeable when compared to the effect of the nonlinear functions $\vartheta^g(R)$ with large gradients $|\nabla_0 \vartheta^g|$ relative to the growth ϑ^g.

Residual stresses in the absence of any traction or body force align with the incompatibility as characterized by the local Burgers vector density. For instance, for the case in which growth is slower at the core compared to the outside, the circumferential and meridional components of the Cauchy stress tensor (Fig. 4.2**d**) show radial patterns aligned with the features of the $\mathbf{b}$ field in Fig. 4.2**d**. Similarly, residual stresses follow the observations of the local Burgers vector density for the case in which growth is faster at the core compared to the periphery (Fig. 4.2**e**). In either case, there is a transition from tension to compression along the radial direction, which has also been shown in [240].

To reduce the incompatibility characterization to a single invariant scalar field, we once again opt for $\operatorname{Curl}\mathbf{F}^g : \operatorname{Curl}\mathbf{F}^g$, plotted with respect to R in Fig. 4.2**h**. The trends are similar to what happens with the local Burgers vector density: higher gradients of growth lead to higher incompatibility in general, while for the same gradient higher growth leads to less incompatibility. When compared to the previous example, it is obvious that the same amount of overall growth produced by some field ϑ^g can lead to very different residual stresses depending on the gradient $\nabla_0 \vartheta^g$.

4.3.3 Transverse isotropic area growth

Thin biological membranes and epithelial tissues also undergo growth and remodeling during development and in response to environmental cues [152]. For instance, skin grows in development, in response to our body weight, and in pregnancy [136]. The knowledge that skin responds to stretch by growing has been leveraged for the clinical application of tissue expansion [106]. Computational models of skin growth within the volumetric growth framework have been shown to accurately capture the clinical scenario using a transversely isotropic in-plane area growth [131]. Before we consider a more realistic problem, we first explore the case of a disc with prescribed area growth

$$\vartheta^g := 1 + \frac{1}{4}Rt \tag{4.51}$$

where $R = \sqrt{X_1^2 + X_2^2}$ is the radial coordinate on the plane and $t \in [0, 1]$ is time. The corresponding growth tensor $\mathbf{F}^g$ for area growth is given Eq. (4.18), and in this case the normal is simply $\mathbf{N}_0 = \mathbf{e}_3$. We partition a flat disc or radius $R_0 = 1$ mm and height $h = 0.5$ mm into $2,080$ C3D8 elements and $2,808$ nodes (Fig. 4.3). The growth contour ϑ^g is shown in (Fig. 4.3**a**). The boundary conditions, time for the simulation, and resulting range of the growth indicator ϑ^g are the same as in the previous two examples, but the constitutive model is now different. For this problem we consider the anisotropic GOH model.

Two kinds of fiber orientation are considered, radial and circumferential. With this example we want to further illustrate that the development of residual stress is linked to both the need for an incompatible $\mathbf{F}^e$ that balances out the incompatibility introduced by $\mathbf{F}^g$, as well the mechanical equilibrium problem, which depends on the specific constitutive model. The geometric incompatibility tensor $\mathbf{G}$ does not depend on the material model being used, but only on the growth field $\mathbf{F}^g$. There is an alternative derivation for the geometric incompatibility tensor $\mathbf{G}$ in terms of the elastic deformation alone $\mathbf{F}^e$ (see Eq. (4.12)), but the two are equivalent. Thus, even

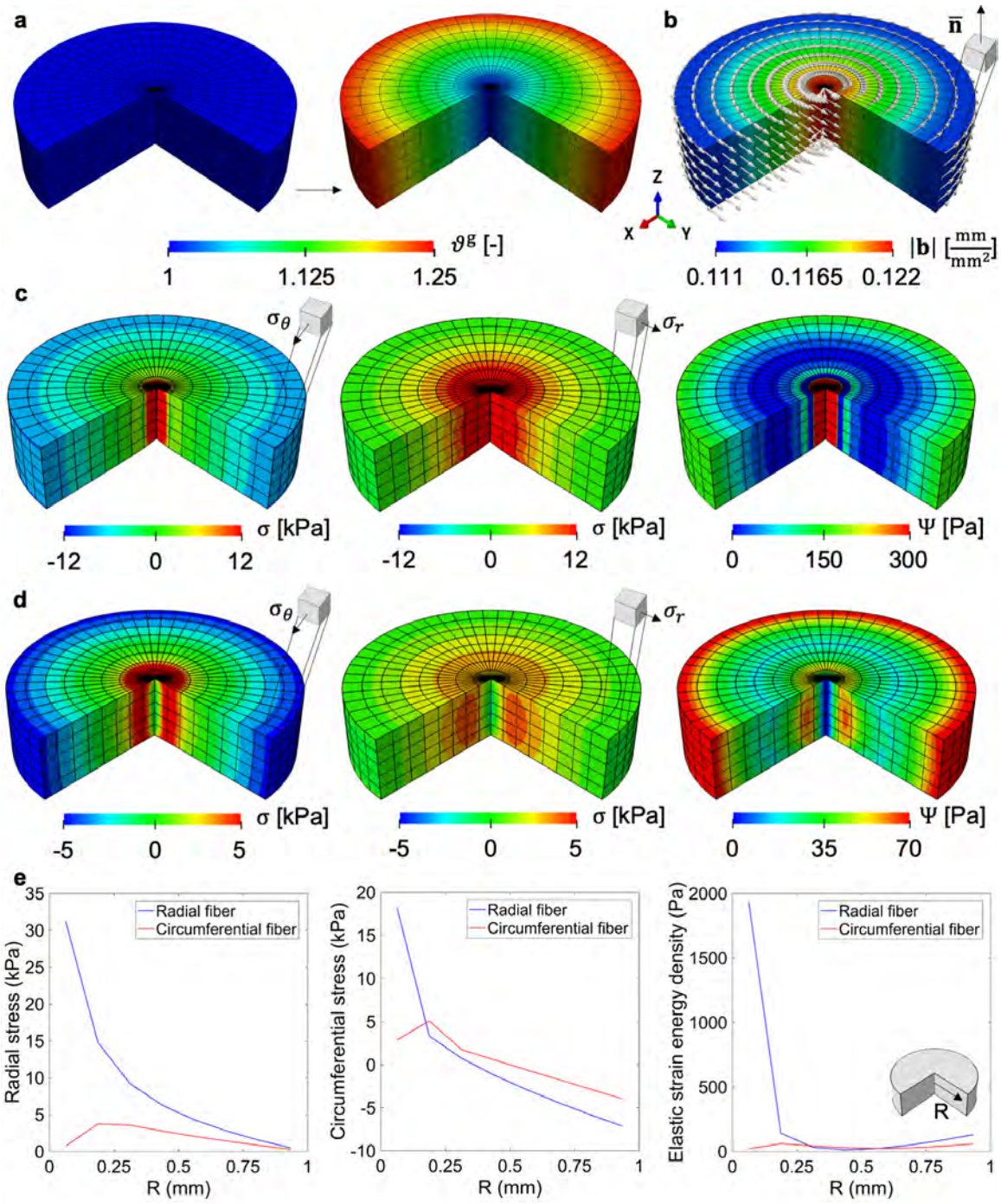

Fig. 4.3.: In-plane area growth: A flat disc grows in area driven by the linearly varying growth field ϑ^g along the radial direction (**a**). Even though the material is anisotropic, the amount of incompatibility is independent of the material behavior. The local Burgers vector density for the plane, defined by $\mathbf{e}_3$ is aligned circumferentially (**b**). Residual stress, however, do depend on whether the direction of anisotropy is radial (**c**) or circumferential (**d**). (Continued on the following page.)

The patterns in the elastic deformation are similar in both cases, with the circumferential component of the stress going from tension to compression from the center to the boundary of the disc. In contrast, the radial component of the stress has to satisfy a traction free boundary condition, and the stress decreases from the center to the periphery. Because the Gasser-Ogden-Holzapfel model leads to increasing stress when fibers are in tension, the overall stresses from radially aligned fibers are larger compared to circumferential fibers. Plots of σ_r, σ_θ, and Ψ with respect to R are shown in (**e**).

when $\mathbf{G}$ is computed from $\mathbf{F}^e$, it is still independent of the mechanical equilibrium problem and the choice of material model. For our example, we compute the local Burgers vector density and observe that it is circumferentially aligned on the plane (Fig. 4.3**b**). This circumferential alignment is indeed what we expected based on the derivation for $\mathbf{b}$ for area growth in Eq. (4.22).

Even though the growth field and incompatibility metrics remain the same, the residual stresses change if the GOH material is considered with a radial fiber family (Fig. 4.3**c**) or circumferential fiber family (Fig. 4.3**d**). We report the circumferential stress σ_θ, radial stress σ_r, and free energy density Ψ. When the fiber is radially distributed, as expected, stress along fiber direction is higher than the stress in the circumferential direction (Fig. 4.3**c**). The radial component of the stress is in tension and the stress is higher at the center compared to the periphery of the disk, where it vanishes because of the boundary condition. The circumferential direction follows a more similar pattern compared to the previous cases, with tension at the center and gradually transitioning to compression at the outer layers just as in the simple tumor example. If the fiber orientation is circumferential, the trends in the stress are similar but overall the stresses and strain energy are lower, particularly due to the lack of fibers in tension in the radial direction (Fig. 4.3**d**).

The residual stress patterns follow the geometric constraints of the entire body. Clearly, the outer boundary of the disk has to satisfy a zero normal stress component, and in consequence the stress in the radial direction decreases from the center to the periphery. While the pattern of deformation is similar in both cases, when the fibers are aligned radially they contribute to higher stress. For the circumferential component, the elastic deformation is similar to the previous example, with a transition from tension to compression [240]. For clarity, plots of σ_r, σ_θ, and Ψ with respect to the radial direction are shown in Fig. 4.3**e**.

4.3.4 Uniaxial fiber growth

Anisotropy arising from fibrous microstructures is a key feature of biological materials. This is not only important for the mechanical behavior, as seen in the previous example, but also for the way they grow and remodel. For example, tissues such as muscle grow preferentially in the fiber direction [247]. Computational models of muscle growth within the finite volume growth framework have accurately captured the observations that muscles adapt to mechanical cues by growing or shrinking in length [248]. For this example, consider a cylindrical domain with the cross sectional area $\pi/4\,\mathrm{mm}^2$ and length 1 mm and discretized with 960 C3D8 elements and $1,243$ nodes (Fig. 4.4**a**). Only the minimum set of essential boundary conditions that prevent rigid body motion are imposed. The fiber direction in the domain is constant and aligned with the basis vector $\mathbf{f}_0 = \mathbf{e}_1$. We restrict our attention to the neo-Hookean hyperelastic potential. The prescribed growth field is

$$\vartheta^g := 1 + \frac{1}{4} X_2 t \text{ with } t \in [0, 1]\,. \tag{4.52}$$

The resulting growth is up to 25% in length at the top of the fiber, with no growth at the bottom of the fiber (Fig. 4.4**a**). Note that the gradient of growth is in the direction $\mathbf{e}_2$, orthogonal with respect to the fiber direction, but growth actually occurs along the fiber direction. Our choice for this growth field directly follows the derivation of the geometric incompatibility tensor $\mathbf{G}$ for fiber growth, where we show that the magnitude of the local Burgers vector density $|\mathbf{b}|$ is greatest when the growth gradient is orthogonal to the fiber direction. The associated local Burgers vector density corresponding to the plane $\mathbf{e}_3$ is shown in Fig. 4.4**b**. The local Burgers vector density $\mathbf{b}$ shows a small variation from greater values at the bottom of the fiber to smaller values at the top. This inverse trend with respect to the growth variable is the same feature from the previous examples and it is due to the scaling of the geometric incompatibility tensor by the Jacobian ϑ^g (see Eq. (4.27)). The Burgers vector aligned with the fiber direction.

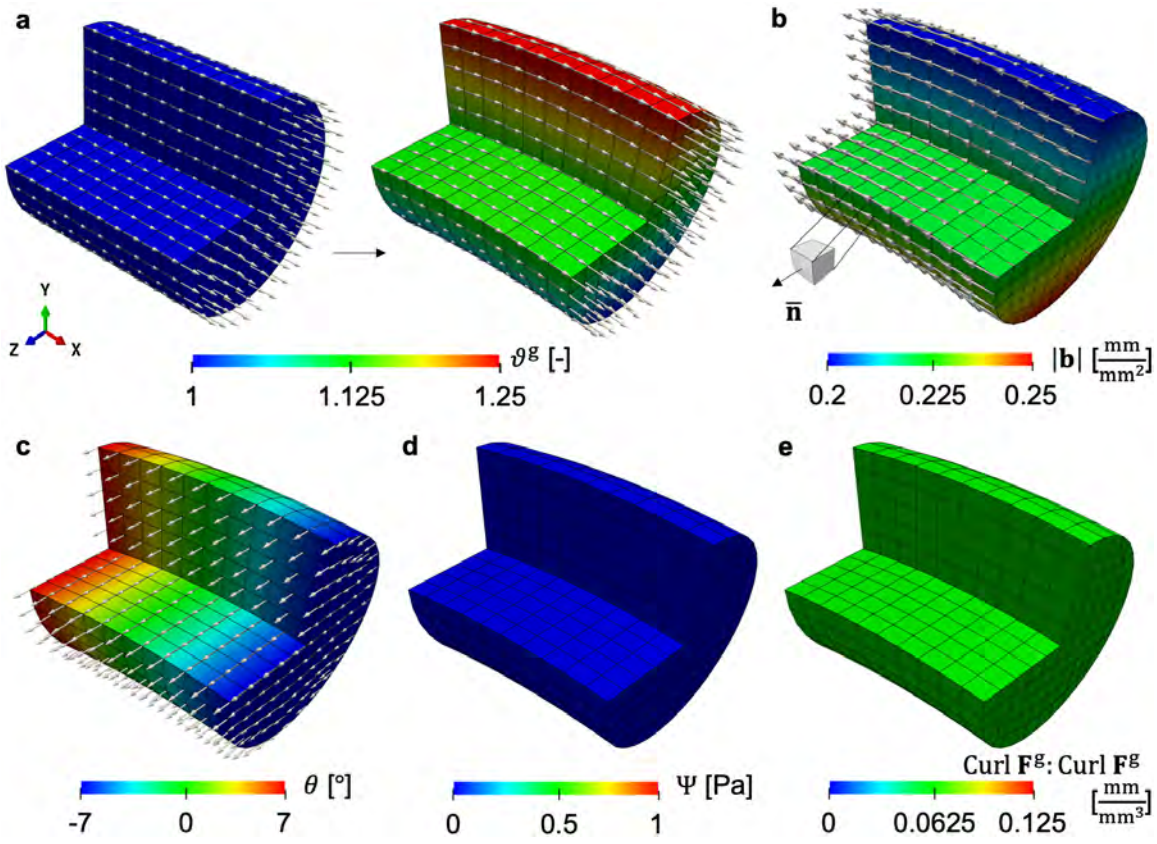

Fig. 4.4.: Fiber growth with linear field ϑ^g is modeled in a cylinder-shaped finite element model. The reference and current configurations are shown (**a**). The associated local Burgers vector density is calculated on the plane normal to $\bar{\mathbf{n}} = \mathbf{e}_3$ (**b**). The body undergoes pure bending. The stress, however, is zero everywhere as reflected in the strain energy contour (**d**). In fact, the elastic deformation is a pure rotation field around $\mathbf{e}_3$ (**c**). The scalar invariant of incompatibility $\operatorname{Curl}\mathbf{F}^g : \operatorname{Curl}\mathbf{F}^g$ is constant and nonzero over the domain (**e**).

In contrast to previous examples, in this case the residual stress is zero everywhere in the domain. Instead of showing the residual stress contour, we show the free energy density (Fig. 4.4**d**) and the scalar invariant of incompatibility $\operatorname{Curl}\mathbf{F}^g : \operatorname{Curl}\mathbf{F}^g$ (Fig. 4.4**e**). Note that there is incompatibility induced by the growth field, and that the cylinder deforms due to the prescribed growth. Yet, there is no residual stress. Recall that the elastic deformation tensor should counteract the incompatibility introduced by $\mathbf{F}^g$. However, the polar decomposition of $\mathbf{F}^e$ in Eq. (4.4) reveals that a pure rotation field would be able to get a globally compatible $\mathbf{F}$ with no stress. This is in

fact what is happening here. In matrix form, using the Cartesian basis, the growth tensor is

$$\mathbf{F}^g = \begin{bmatrix} 1 + aX_2 & 0 & 0 \\ 0 & 1 & 0 \\ 0 & 0 & 1 \end{bmatrix}, \tag{4.53}$$

for some non-zero value a. This growth field is incompatible as illustrated in Fig. 4.4**b** and **e**. We propose that the elastic deformation can be a rotation $\mathbf{F}^e = \mathbf{R}^e$. In matrix form

$$\mathbf{F}^e = \begin{bmatrix} \cos\theta & \sin\theta & 0 \\ -\sin\theta & \cos\theta & 0 \\ 0 & 0 & 1 \end{bmatrix}. \tag{4.54}$$

This rotation should be such that the total deformation $\mathbf{F} = \mathbf{F}^g\mathbf{F}^e$ is compatible. The total deformation gradient is

$$\mathbf{F} = \begin{bmatrix} (1 + aX_2)\cos\theta & \sin\theta & 0 \\ -(1 + aX_2)\sin\theta & \cos\theta & 0 \\ 0 & 0 & 1 \end{bmatrix}. \tag{4.55}$$

To show that this is the case, all we need to do is to show that there is a vector field whose gradient leads to Eq. (4.55). Consider

$$\varphi = \left(X_2 \sin(aX_1) + \frac{1}{a}\sin(aX_1), X_2\cos(aX_1) + \frac{1}{a}\cos(aX_1), X_3 \right). \tag{4.56}$$

The deformation gradient $\mathbf{F}$ in Eq. (4.55) is actually the gradient of the map φ in Eq. (4.56), with $\theta = aX_1$. Furthermore, this has to be the solution of the problem since, by reducing to a rotation, $\mathbf{F}^e$ leads to zero stress and also satisfies the mechanical equilibrium problem. Numerically, Fig. 4.4**c** shows that the elastic deformation $\mathbf{F}^e$ from our finite element solution is actually a pure rotation around $\mathbf{e}_3$ that varies along X_1 as expected.

4.3.5 Brain atrophy

Commonly, the idea of tissue growth is associated with an increase in mass; however, as noted after introducing Eq. (4.3), volume loss can also be considered, as in the case of tissue atrophy. A representative example is atrophy and shrinkage of the brain as a result of amyloid-β accumulation and tau protein malfunction [260]. Coupled to a nonlinear reaction-diffusion model that captures the propagation of the misfolded proteins in pyron-like diseases, brain volume loss has been modeled with a nonlinear finite element model [82, 243]. Here, we look into the incompatibility and residual stress that arises from the heterogeneous growth patterns associated with reaction-diffusion coupling. For the reader interested in details on the theory, finite element implementation, and simulations for the coupled reaction-diffusion model of brain atrophy, please consult [82, 243].

One of the main features of the models in [82, 243] is the relative shrinkage rate between gray and white matter tissues. Gray matter undergoes faster volume loss than white matter [244]. From the mismatch in the growth field at the boundary between gray and white matter it is expected that residual stresses will arise.

Here we start from the two configurations of the brain: the reference, healthy geometry, and the shrunken, atrophied configuration (Fig. 4.5**a**). The maximum volume loss is about 30%. The corresponding residual stresses from growth are heterogeneously distributed in the brain (Fig. 4.5**b**). To improve visualization, slices with normals given by the standard basis in 3D Euclidean space are presented (Fig. 4.5**c**-**e**).

It can be observed from the different cross sections that atrophy takes place mostly on the outer gray matter while the inner white matter has almost no volume loss (Fig. 4.5**c**). As a result, sharp growth gradients are expected near the interface of these two tissues. Indeed, after computing the geometric incompatibility tensor $\mathbf{G}$ and the corresponding local Burgers vector density $\mathbf{b}$ for each of the planes of interest, we can observe that the degree of incompatibility characterized by the magnitude $|\mathbf{b}|$ is

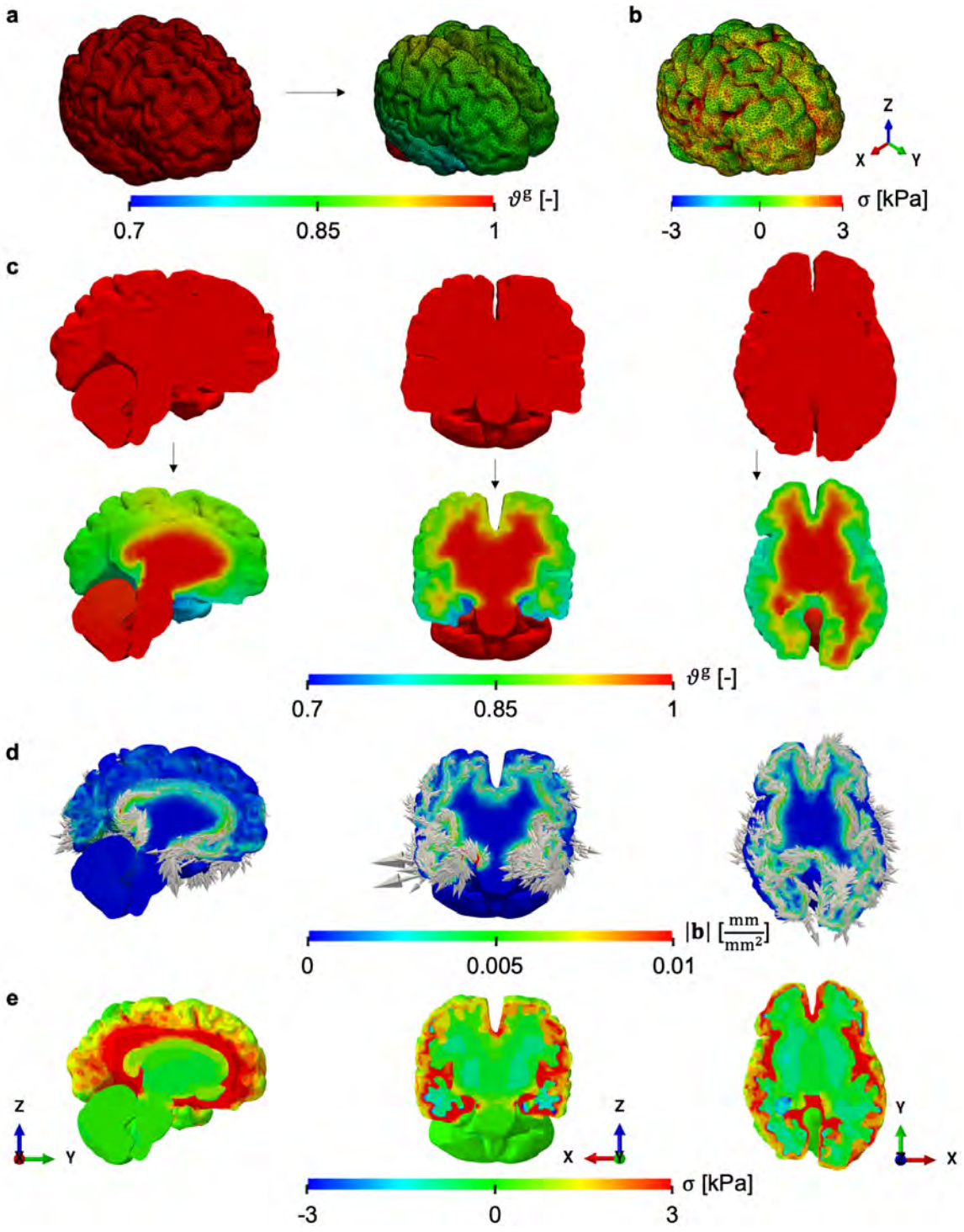

Fig. 4.5.: Isotropic volume shrinkage or negative growth caused by diffusion-reaction of misfolded proteins in the human brain. Growth field ϑ^g in the reference and current configuration (**a**) and the maximum principal stress field seen on the outer surface of the brain (**b**). (Continued on the following page.)

Representative cross-sections in the sagittal, coronal, and axial direction (left to right column in **c**-**e**) show that the inner white matter undergoes almost no shrinkage while the outer gray matter has up to 30% volume loss (**c**). The local Burgers vector density can be calculated solely based on the growth field, showing greater incompatibility at the interface between gray and white matter because of the higher growth gradients (**d**). The Burgers vectors are in the plane and aligned with the interface between the two types of brain tissue (**d**). Maximum principal stress on the sections of interest reflects the incompatibility characterization, with greater stress at the interface between gray and white matter (**e**).

concentrated near the interface (Fig. 4.5**d**). The maximum principal stress visualized on the same planes aligns with the geometric measure of the incompatibility (Fig. 4.5**e**). Similar to $|\mathbf{b}|$, stress σ localizes at the interface between gray and white matter and decreases towards the outer brain surface. Thus, in this case, the characterization of the necessary geometric incompatibility based solely on the growth field provides useful intuition regarding the resulting stress field.

4.3.6 Area growth induced by skin expansion

Skin, like all soft tissues, adapts to mechanical cues via growth and remodeling [261]. This knowledge has been leveraged in the clinical setting to gain skin for reconstructive purposed in tissue expansion [177, 246]. In tissue expansion, a balloon-like device is implanted subcutaneously and dilated over a period of months to stretch skin supra-physiologically and trigger its growth [7]. Previous work by our group has resulted in computational models of skin expansion [131] as well as a porcine experimental model to better understand skin mechanobiology [97]. Some of our experimental work revealed the existence of a complex residual strain field even after releasing the skin from external loads and constraints [116]. Here we start from the modeling of tissue expansion within the finite volume growth and quantify the geometric incompatibility tensor for commonly-used expander shapes and its connection to residual stress.

We create finite element models of 10×10 cm skin patches with thickness $h = 0.3$ cm discretized with $3,200$ C3D8 elements and $5,043$ nodes. Four different expander geometries are considered: rectangle-, circle-, square-, and crescent-shaped (Fig. 4.6**a**). The expanders are inflated to 50 cc and this volume is maintained for 7 days before deflation, analogous to an individual inflation step in the clinical setting [97]. For these simulations, the neo-Hookean model of our previous work is considered [98], although, like for most collagenous tissues, anisotropy can play a role in the mechan-

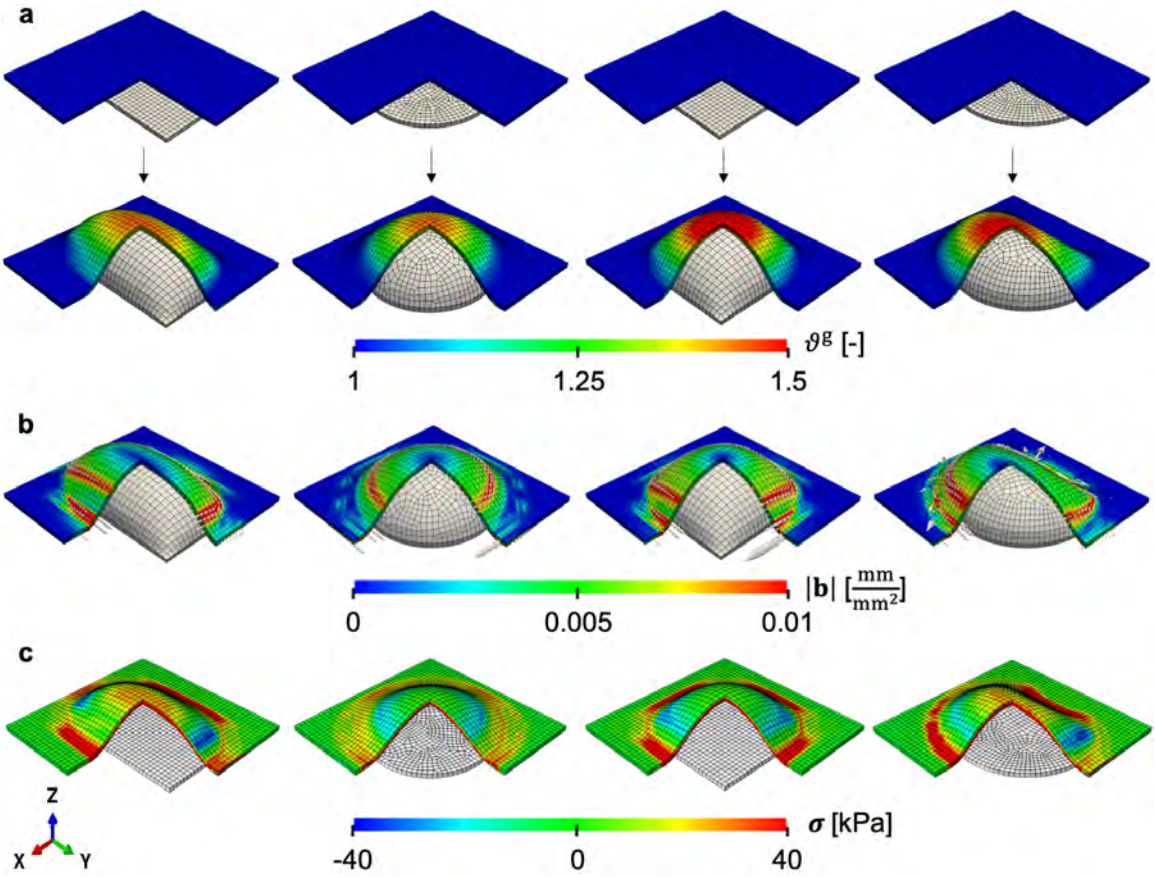

Fig. 4.6.: Area growth in tissue expansion. Growth ϑ^g following inflation with four different expander geometries (rectangle-, circle-, square-, and crescent-shaped) shows greatest area increase at the apex compared to the periphery (**a**). The local Burgers vector density and its magnitude on the skin plane determined by the surface normal shows larger magnitude in regions of higher growth gradients (**b**). The corresponding residual stress contours from maximum principal stress also shows similar features (**c**).

ical behavior and subsequent growth [97, 180]. The constitutive model for growth is the one introduced in Eq. (4.46).

Inflating the expanders to 50 cc induces area growth up to 50% with respect to the original area (Fig. 4.6**a**). The area increase depends on the shape of the expander. The square expander results in the largest area growth and the circular expander yields the smallest growth. In all cases, the growth field is characterized by greater area gains at the apex of the expander and gradually less toward the periphery of the

expanded region. The local Burgers vector density $\mathbf{b}$ is calculated based on the growth field on the plane normal to $\bar{\mathbf{n}} = \mathbf{e}_3$ (Fig. 4.6**b**). Similar to the previous example and due to the fact that the geometric incompatibility tensor $\mathbf{G}$ is directly linked to the gradient of ϑ^g, the magnitude of the local Burgers vector density $|\mathbf{b}|$ is generally greater in regions of steep growth gradient. There are other factors at play, such as the total growth as discussed in the first three examples. $|\mathbf{b}|$ is greater right at the base of the expander, where there is a rapid transition between regions that are not stretched and not growing to regions being affected by the expander. Another region of high growth gradient is due to the contact and the shape of the expander. The apex has the largest growth ϑ^g, but it is actually free of incompatibility. After deflation, we observe that the maximum principal stress shows similar features compared to the incompatibility metrics (Fig. 4.6**c**). Tension of about 40 kPa occurs at the base, with regions of 40 kPa compression at the zones of contact between expander and skin, which also have large incompatibility in terms of $|\mathbf{b}|$.

4.3.7 Axon growth in brain development

The exact mechanisms of cortical folding in the brain are not yet fully understood. However, abnormal folding is associated with impaired brain function and psychological diseases [250]. Some of the theories that have been proposed to explain brain folding include the differential growth between different brain regions due to both mechanical and biological cues. Finite element and theoretical models [250, 262] have been developed to improve our understanding of cortical folding, in particular the expected tissue mechanics associated with the emerging brain morphology. The essential model of cortical folding is that of a bi-layered system coupled to the finite growth theory.

We start from the finite element model proposed in [250] which considers the role of axon orientation on the resulting instabilities of the bi-layered system, as represented by Eq. (4.23) for fiber growth. The rectangular domain of 3×1 cm with

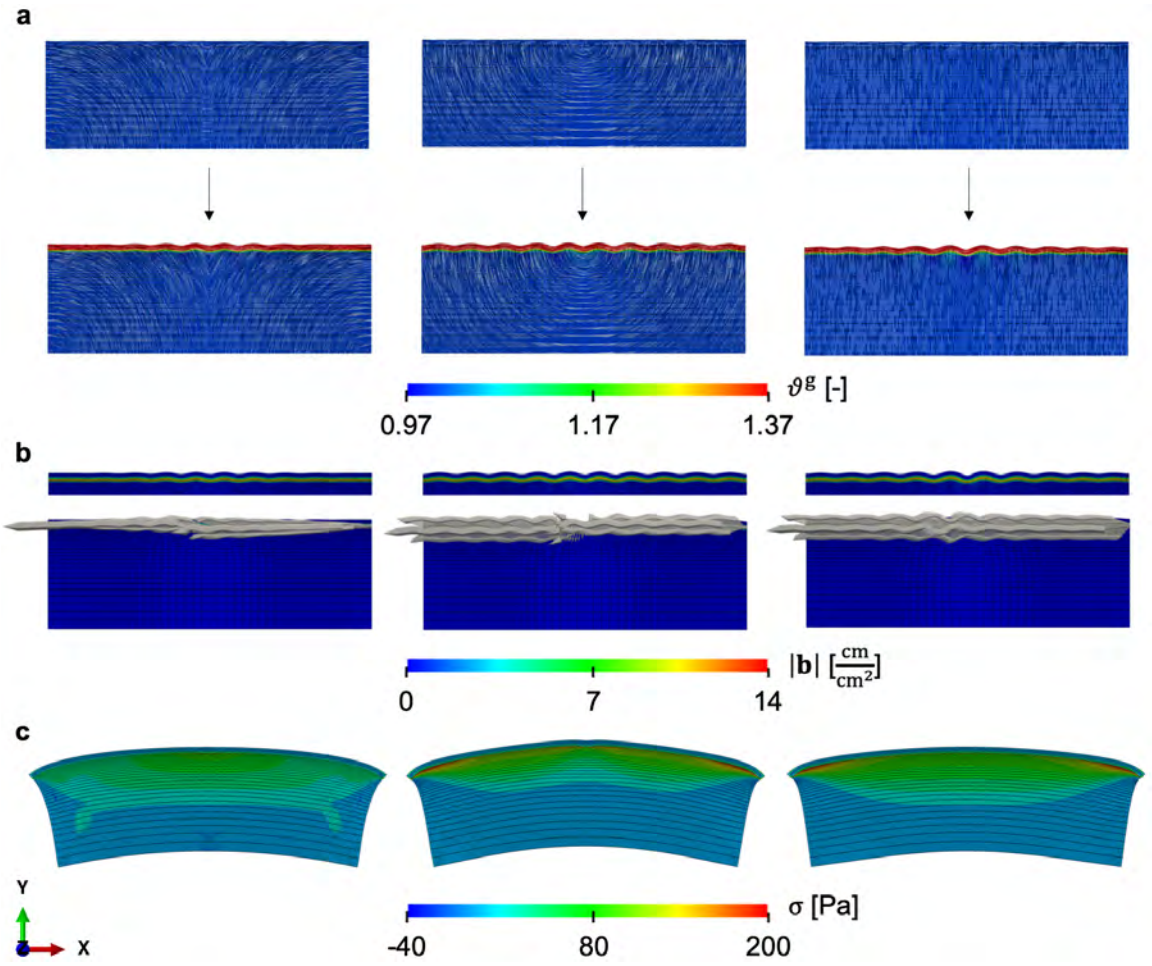

Fig. 4.7.: Bi-layered system to capture cortical folding taking into account the axonal fiber orientation. The top layer, the cortex, has a constant growth rate, while the bottom layer, the subcortex, shows stretch-driven fiber growth in the direction of the axons. Folding patterns emerge for three different axon orientations: curved outward, concentric, normal to the interface (**a**, left to right). The local Burgers vector density is calculated on the plane normal to $\bar{\mathbf{n}} = \mathbf{e}_3$ and it shows that the incompatibility due to growth occurs mostly at the interface between cortex and subcortex (**b**). Removing all constraints and external forces, the only residual stress left is due to the incompatible growth field, which shows that the maximum principal stress occurs at the interface between the two layers (**c**).

thickness 0.05 cm is discretized into 6,000 C3D8 elements and 12,462 nodes. The top, gray matter (cortex), has thickness of 0.05 cm, while the lower region in the domain is the white matter (subcortex). Three different axon orientations $\mathbf{f}_0$ in the subcortex in the reference configuration are considered: curved outward, concentric,

and straight (Fig. 4.7**a**). The cortex is allowed to grow only in the $\mathbf{e}_1$ direction. Although not relevant for the incompatibility characterization, for the buckling instability patterns we note that there is a difference in the shear modulus between the cortex and subcortex $\mu_{\text{gray}}/\mu_{\text{white}} = 3$. The growth rate between the two layers also differs, with $\dot{\vartheta}^g_{\text{cortex}}/\dot{\vartheta}^g_{\text{axon}} = 0.1$. We simulate a time of 75 days, fixing $\dot{\vartheta}^g_{\text{cortex}}$ to 0.008/hour. The growth field $\vartheta^g_{\text{cortex}}$ is not mechanically coupled, while the other hand, the axon growth in the subcortex is stretch driven [250].

The differential growth between the two layers and the constraints at the ends of the domain lead to the characteristic patterns of folding seen in the brain (Fig. 4.7**a**). Most of the growth is observed on the top layer of the system, but, resulting from the instability and subsequent fold formation, some growth is observed along the axon orientation in the subcortex. The greatest growth gradients are observed at the interface between the two layers of the domain. Given $\mathbf{F}^g$ in Eq. (4.23), we compute the geometric incompatibility tensor $\mathbf{G}$ and then the local Burgers vector density $\mathbf{b}$ on the plane normal to $\bar{\mathbf{n}} = \mathbf{e}_3$. The Burgers vector density has its greatest magnitude precisely at the interface between the cortex and subcortex, where the gradient of growth is sharpest. This is the expected behavior of the system. The ideal scenario in which no axon growth is considered but only differential isotropic growth between the two layers is considered would lead to zero incompatibility in either region. In that case, folds would still form, and the cause for residual stress would be the mismatch along the interface of the two layers [263]. In fact, an experimental confirmation is presented in [264], where two thin strips of elastomers are deformed elastically to a different extent (and therefore without any incompatibility) and then glued together. The bi-layered system shows the expected instabilities and buckling patterns, but in the end the only source of incompatibility is precisely at the interface. In our example, incorporating the axon orientation and growth leads to Burgers vectors mostly aligned with the interface (Fig. 4.7**b**). The direction of the axons does affect the pattern and magnitude of $|\mathbf{b}|$, as the gradient between cortex and subcortex is greater when the axons are normal to the cortex (second and third columns in Fig. 4.7**a**), as opposed

to the case in which axons approach the interface tangentially (first column in Fig. 4.7**a**).

The buckling patterns typical of the folded brain exist because of the constraints applied to the system, which is fixed at both ends. We are interested in the residual stress patterns when there are no external loads and the only constraints imposed are those that prevent rigid body motion. The residual stress field that arises solely by the incompatibility is shown in Fig. 4.7**c**. We restrict our attention to the maximum principal stress. There is peak tension at the subcortex right below the interface with the cortex, particularly for the cases in which the axon orientation is normal to the interface. For the case in which the axon orientation is tangential to the interface, the incompatibility is less pronounced and the residual stress is also much lower. Moving away from the interface, the stress decreases. In the cortex, stresses are actually very small. The growth in the cortex is uniform and this layer is stiffer that the subcortex. Then, releasing all constraints leads to a constant bending of the top layer. This overall bending exerts the tensile stresses at the top of the softer subcortex, with small variations corresponding to the growth field in the axon direction. Yet, as stated before, the variations in the growth field within the subcortex are small compared to near the interface with the cortex.

4.4 Discussion

The exact microscopic origin of residual stress in soft tissues is still an open question. It is generally accepted, however, that the prestress field at the macroscopic level is a consequence of constant growth and remodeling of living matter [148, 213, 230]. Growth and remodeling can be captured within a continuum mechanics framework in a manner akin to plasticity by splitting the deformation gradient into growth and elastic contributions [123,215]. This split is linked to the idea of incompatibility [219], a notion of mismatch and discontinuity between differential volume elements at the microscopic scale. In crystal plasticity, these concepts are linked to lattice defects.

Although the interpretation is not the same for soft tissues, we borrow from the concepts of crystal plasticity to describe the kinematics of incompatibility due to growth. Through this paper, we have presented the distinctive features of the geometric incompatibility tensor that exist for three general growth formulations: volume, area, and fiber growth. We also compute the geometrically necessary incompatibility for three realistic biomedical problems. Although we focus on the geometry of incompatibility, we show that some features of the residual stress field are closely related to the incompatibility field.

The primary object of the present work was to introduce the geometric incompatibility tensor $\mathbf{G}$ in the context of growth and remodeling. This tensor is based on the definition of the Burgers vector, which is a measure of the failure to close circuits in a surface after the application of the irreversible deformation $\mathbf{F}^g$. The generalization of the Burgers vector calculation for any normal $\mathbf{n}$, together with a localization argument, yields the tensor $\mathbf{G}$ and is closely related to the Curl operator. In the finite volume growth theory, the tensor $\mathbf{F}^g$ is constrained by the biology and by the anatomy, or microstructure, of the tissue. Growth is also connected to the thermodynamic balance laws which connect the tensor $\mathbf{F}^g$ to the scalar mass source. These constraints on $\mathbf{F}^g$ allow us to derive specific features of $\mathbf{G}$ for different growth modes. The most prominent feature is that the degree and direction of incompatibility depend on the magnitude and direction of the growth gradient. There are more subtle features that were discussed for the individual growth models.

To better understand these incompatible fields we started with very simple illustrative examples. A key task in our manuscript was the numerical implementation of the different growth problems and the subsequent calculation of the incompatibility metrics within the finite element framework. To that end, we were able to compare our simulations against the analytical derivations. The finite element calculations further cemented some of the observations about $\mathbf{G}$ and the local Burgers vector density $\mathbf{b}$. For example, the simple examples also showed that there is no incompatibility in the direction of the growth gradient and that for a given plane defined by normal

$\mathbf{n}$ the Burgers vector has to lie in that plane. In contrast, we did not devote much attention to the residual stress resulting from the incompatible growth field. The stress field is more complex because there are several factors that come into play and not just the geometry of the deformation. Clearly the $\mathbf{F}^e$ field is generally dependent on the overall geometry and boundary conditions [240]. That being said, our numerical implementation naturally delivers the residual stresses in our simulations and allows us a side by side comparison of incompatibility patterns and the resulting stress field. The last of the representative examples allowed us to showcase that there are incompatible growth fields that do not lead to stress, something that is better understood for crystals [234]. In our fiber growth example, we showed how a pure rotation $\mathbf{F}^e = \mathbf{R}^e$ is sufficient to obtain a total deformation that is inherently compatible and entails no residual stress.

Our idealized problems enabled us to point out the distinctive features of the geometry of incompatibility and to showcase the finite element implementation which we make available with this manuscript. Yet, we are interested in understanding how these incompatible fields look like in realistic applications. We know that residual stress is a feature of living tissue and that it is important for function [265]. Hence, having presented our tools, we applied them to three relevant biomedical questions. In the brain, for example, we observed that the gradient of growth during development and atrophy is highest at the interface between white and gray matter, and that is the region with the highest degree of incompatibility and also residual stress. The perfect experimental analogy of an ideal system is the work by Budday et al. [264], where the compatible deformation of two layers before being glued together leads to residual stress due to the mismatch of deformation at the interface. Our numerical example in the brain adds additional complexities compared to the idealized experiment. For example, the growth of axons in the white matter can increase or decrease the degree of incompatibility depending on their orientation with respect to the interface.

From the tissue expansion simulations we also gained valuable insights. It has been discussed in previous computational models, clinical experience, and animal

experiments, that there is more growth at the apex compared to the periphery [115, 177]. Here we show that, in fact, the residual stress is highest at the periphery and at the beginning of the contact region between expander and skin. These regions coincide with the sharpest gradients of growth and our incompatibility metrics.

This work is not without limitations. One of the open questions in this work is the precise connection between the geometry of incompatibility and the residual stress. While the metrics introduced do align in general with the development of residual stress, more work is needed to elucidate this relationship in more detail. The other main limitation is that we have fully focused on the split of the deformation gradient into growth and elastic contributions. This approach is useful in practice, describes growth and remodeling accurately, and is amenable to efficient finite element implementations [259]. However, comparison against other descriptions of growth and remodeling is our future endeavor, such as the evolution of natural configurations for individual constituents [230], or the notion of a higher-dimensional reference configuration [228, 229]. Finally, one open question that we will also continue to investigate in the near future is a better interpretation of the geometry of incompatibility for soft tissues. As we stated repeatedly in the manuscript, soft tissues do not have lattice defects or dislocations. While our analysis is useful at the continuum scale, it leaves unanswered the microscopic and molecular origin of incompatibility in living matter.

4.5 Conclusion

Within the finite volume growth framework, residual stress arises due to the incompatibility of the growth field. Here we explore in detail the geometric characterization of this incompatibility. We implement the calculations of growing tissues and the geometric incompatibility tensor $\mathbf{G}$ into a nonlinear finite element framework. We showcased idealized scenarios and also relevant biomedical applications. Therefore, we expect that this work will further our insight into the origin and characterization of residual stress in soft tissue, which can be instrumental in understanding disease

and designing clinical interventions in which growth and remodeling of soft tissue plays a central role.

5. MECHANICAL CHARACTERIZATION OF SKIN IN VIVO USING A SUCTION DEVICE

Abstract: One of intrinsic characteristics of skin is high variation in the mechanical properties across different demography and even between individuals. Therefore, accurate characterization of mechanical properties of skin is a crucial ingredient to anticipate stress value after deformation. However, it is still a challenge because *in vivo* status of skin itself prevents us utilizing traditional method, e.g., uniaxial tensile test. Simultaneously, anisotropic feature results from distributed fiber family is one of outstanding characteristics which is also difficult to characterize in *in vivo* state. In reconstructive surgery, it is also important to know mechanical behavior of patient's skin since better understanding on stress value after resurfacing is beneficial to improve surgical outcome, in which unexpected high stress can give rise to any delayed wound healing or wound complications. To capture mechanical properties of skin *in vivo*, suction device, Cutometer, which applies negative pressure to deform skin, has been utilized, but anisotropic feature is usually ignored in the analysis. To also measure anisotropic characteristic, we propose elliptical opening of the suction device, which usually has a circular opening. Newly proposed shape is designed by finite element (FE) model, which enacts a forward model in framework of inverse problem. In order to capture skin properties inversely, we make use of Bayesian framework which also enables us to take into account uncertainty quantification of the solution of inverse problem. By seeking more efficient way to solve the inverse problem, FE model, which is an expensive forward function, is substituted with Gaussian process regression. In addition, the approach to solve inverse problem is also designed to enhance efficiency by using active learning algorithm.

5.1 Motivation

Skin is the largest organ in human body and enacts various roles as barriers against external factors, pathways for materials, and homeostasis, and so forth [266]. One of intrinsic features of the skin is high variation of mechanical and biological response across different demography and even body locations of a person [178]. In reconstructive surgery, especially, the mechanical properties of the skin are important information in preoperative stage so as to plan optimal surgical scenario or avoid the delayed wound healing since unexpected high stress after reconstructive surgery can take place wound complications [267–269]. The mechanical properties of the skin is closely related to the level of stress according to the external force, and hence accurate measurement of mechanical characteristics of skin is of practical importance for robust surgical plan. However, characterization of mechanical behavior of skin is nontrivial because of *in vivo* state, which yields non stress-free state [9] as well as difficulty to utilize a conventional testing methodology such as the uniaxial tensile test. To overcome the difficulties, a suction test accompanied with negative pressure has been proposed such that the maximum height by the negative pressure is measured in *in vivo* state. The measurement of deformation is, however, usually not compatible with the conventional way to express mechanical characteristics of solid. For example, the height at apex characterized directly at different time interval enacts the representative quantities for aging effect [184], scar tissue [270], and epidermal hydration [271].

In this response, the inverse problem accompanied with finite element (FE) method has enacted a bridge to derive the conventional expression for mechanical properties of skin from unconventional expression for that [272]. For instance, the conventional stress-strain relations are indirectly derived from FE analysis once the corresponding mechanical property of skin is matched to the deformation. Matching the results of FE analysis and the corresponding mechanical property of the skin can be carried out by the approach of inverse problem. Beyond the suction device, previous studies

have solved the inverse problem via *in vivo* and noninvasive ways such as indentation test [26, 76], *in situ* tension test [178], and suction test [27, 75, 273], to name a few. Those studies usually make use of the manner with least square error to optimize the unknown mechanical properties of skin through experiment, FE analysis, or both of them.

Here, we make use of Cutometer (Courage + Khazaka Electronic, Germany), one of suction devices, to characterize mechanical properties of skin *in vivo*. Unlike previous studies using the suction device, we develop new design including non-circular opening, e.g., elliptical opening, in order to capture anisotropic nature of skin. Our thought experiment is realized by FE analysis, which shows the suction device with 2 and 8 mm circular opening as well as elliptical opening of 4 mm minor and 8 mm major axis.

In the light of the solution of inverse problem, evaluation of a forward function is an essential factor which dominates the optimized solution [274]. If the forward function is expensive to evaluate frequently, surrogate model can be used alternatively [275]. Inadequate selection of a surrogate model, however, can yield overfitting or underfitting issue when the solution is predicted. To avoid such danger, Gaussian process (GP) regression has been utilized to express the latent forward function [274]. For example, GP posterior can enact a forward function, and it is also beneficial for the gradient-based optimization because derivatives of GP posterior is only dependent on the kernel function. Consequently, we can know the gradient of a forward function through direct calculation of the kernel function and also the availability of differentiation based on the characteristic of kernel function [187].

Solution of inverse problem is typically achieved by minimization of the least square error of the loss function with iterative algorithm. It is widely utilized but there is a limitation that the solution is a deterministic outcome regardless of the degree of uncertainty. To circumvent such limitation, Bayesian perspective can also be immersed into the optimization such that a solution has a point-wise value as well as the corresponding uncertainty [274]. Based on the tractability to evaluate integral

of marginal likelihood, Markov Chain Monte Carlo (MCMC) sampling can be used to derive the distribution of solution.

The aim of this paper is to propose the solution for the inverse problem to achieve the mechanical properties of skin through *in vivo* and noninvasive manners, especially to capture the anisotropic feature of skin. We make use of Cutometer for the suction test with negative pressure. To build the forward function space, FE analysis of the suction test is employed, and GP regression bridges relation between the mechanical properties of skin (input) and the associated deformation (output) over the function space, i.e., GP surrogate model substitutes the forward function of FE analysis. Bayesian perspective is applied to obtain the solution of the inverse problem. To circumvent difficulty to evaluate marginal likelihood, we adopt MCMC sampling to express predictive posterior distribution.

5.2 Methods

5.2.1 Suction test

In general, Cutometer has two sizes of circular hole such as 2 and 8 mm diameters, through which negative pressure is applied on the skin and the deformation of skin is measured by laser-based manner (left in Fig. 5.1**a**). There are two different loading profiles to investigate the behaviour of skin with Cutometer, one is the linearly increasing loading and the other is the instant loading. For both cases, maximum height at the apex is recorded. In this study, we only focus on the skin response to the instant loading, meaning that hyperelastic behavior of skin is only considered. There are a couple of possible values of pressure and we take into account three profiles, 30, 40, and 50 kPa. Only with circular opening, however, it is not possible to capture anisotropic feature of skin, which is basically the effect of fiber dispersion along specific orientation on the skin plane [178]. To overcome this limitation, we develop elliptical opening entrance with 8 mm major axis and 4 mm minor axis, which is fit to 8 mm circular opening entrance (Fig. 5.1**b**). The elliptical opening entrance

is applicable to the measurement of anisotropy efficiently because the deformation of skin by Cutometer is not axisymmetric.

Given two circular opening entrances and one elliptical opening entrance, total five measurements are available, namely single measurement per circular opening entrance and three measurements per elliptical opening entrance (bottom in Fig. 5.1**b**). Note that we rotate the fiber orientation by 45° two times, instead of rotating the elliptic

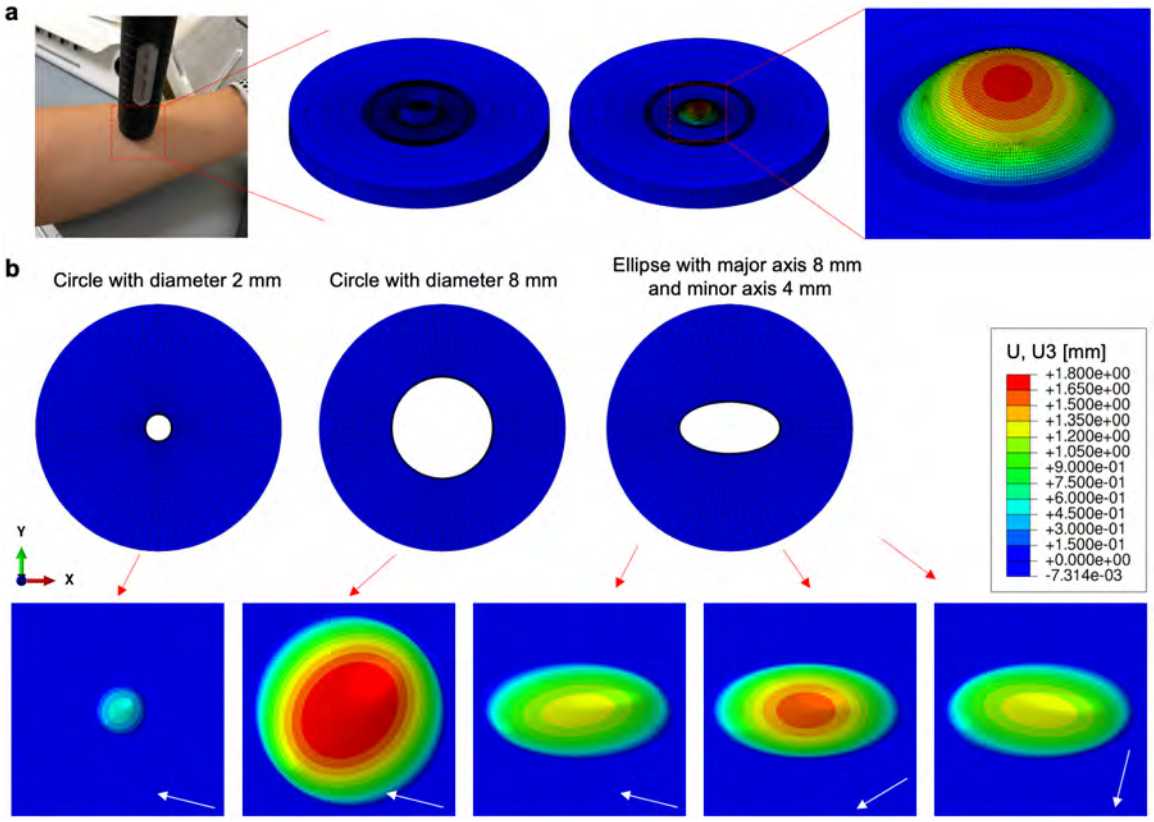

Fig. 5.1.: Finite element (FE) model for Cutometer which applies the negative pressure on the skin. Cutometer is placed on the skin to apply negative pressure and designed by FE model in order to simulate skin deformation and measure the maximum height (**a**). The same skin is tested with different opening shape (2 and 8 mm circular opening and elliptical opening with minor axis 4 mm and major axis 8 mm) (**b**). Note that fiber orientation is varied when the measurement is implemented using elliptical opening pressures (white arrows in **b**). Those five different tests are available for three different pressure values, and therefore total 15 tests are carried out per the same skin. Each test is independent and, hence, assumed as independent events although mechanical properties of the skin is the same.

opening entrance. It is manifest that five maximum heights are different although the same mechanical properties of skin is used. Those five measurements are implemented at the same value of pressure, but as we mentioned before, there are three values of pressure such as 30, 40, and 50, and hence total 15 measurements are obtained per single set of skin properties.

5.2.2 Finite element analysis

Following the previous section, it is needed to design Cutometer device as 3D FE model to be able to represent anisotropic characteristics of skin. (Fig. 5.1**a**). We implement FE analysis using the nonlinear FE package Abaqus (Dassault Systems, Waltham, MA). There are three different models. For 2 mm circular opening entrance, the domain of interest is discretized into 99, 640 C3D8H elements and 110, 671 nodes, while for 8 mm circular opening entrance, the domain of interest is discretized into 103, 952 C3D8H elements and 117, 891 nodes. For elliptical opening entrance, skin part is discretized into 116, 780 C3D8H elements and 129, 624 nodes. To be specific, we assume that skin shows incompressible behavior by using hybrid element, which contains additional degree of freedom such that the nodal displacements at each element only contribute the calculation of deviatoric strain and stress. In each model, there are two distinct regions such as deformable and rigid parts, in which skin is only deformable during simulation while Cutometer device, meaning opening entrance, enacts a rigid body. Skin part, especially, is divided into anisotropic and isotropic layers, where only top layer of 1.7 mm has anisotropic behavior, while the rest of skin part is assumed as isotropic deformation. The thickness value of layers is referred from [27].

As a constitutive model for anisotropic and isotropic layer in the skin part, we make use of Gasser-Ogden-Holzapfel (GOH) model for anisotropic behavior and neo-Hookean model for isotropic behavior [57]. Let us define basic kinematics' quantity. Deformation gradient tensor $\mathbf{F}$ is a linear transformation of points from the reference

to current configuration. We need the right and left Cauchy-Green tensors, denoted $\mathbf{C} = \mathbf{F}^\top\mathbf{F}$ and $\mathbf{B} = \mathbf{F}\mathbf{F}^\top$, respectively. Deviatoric part of $\overline{\mathbf{F}}$ is $J^{1/3}\mathbf{F}$ where $J = \det\mathbf{F}$, and $\overline{\mathbf{C}}$ and $\overline{\mathbf{B}}$ can also be defined from $\overline{\mathbf{F}}$. First of all, strain energy density function for incompressible GOH materials is expressed like

$$\begin{aligned}
&\Psi = \Psi_{\text{iso}}(\overline{\mathbf{C}}) + \Psi_{\text{aniso}}(\overline{\mathbf{C}}, \mathbf{H}_\alpha) \\
&\Psi_{\text{iso}}(\overline{\mathbf{C}}) = \frac{\mu}{2}(\overline{I}_1 - 3) \text{ and} \\
&\Psi_{\text{aniso}}(\overline{\mathbf{C}}, \mathbf{H}_\alpha) = \frac{k_1}{2k_2}(\exp{(k_2\langle\overline{E}_\alpha\rangle^2)} - 1),
\end{aligned} \tag{5.1}$$

where $\overline{I}_1 = J^{-\frac{2}{3}}I_1$ is the first invariant of $\overline{\mathbf{C}}$ and $\overline{E}_\alpha \equiv \overline{\mathbf{C}} : \mathbf{H}_\alpha - 1$ is the pseudo-invariant with respect to the symmetric generalized structure tensor $\mathbf{H}_\alpha = \kappa\mathbf{I} + (1 - 3\kappa)\overline{\mathbf{a}}_\alpha \otimes \overline{\mathbf{a}}_\alpha$ with fiber direction $\overline{\mathbf{a}}_\alpha$ in the reference configuration. To be specific, $\overline{\mathbf{a}}_\alpha$ is represented as a unit vector and its direction is defined by θ. μ is the shear modulus and expresses stiffness of ground tissues, while parameters k_1, k_2, and κ capture the response of the fiber family: k_1 describes the tensile response, k_2 is dimensionless and expresses nonlinearity of the fiber response, and κ is another dimensionless parameter that indicates dispersion in the range 0 to 1/3, from perfectly anisotropic to perfectly isotropic. The notation $\langle\cdot\rangle$ in Eq. (5.1) denotes the Macaulay brackets. Eq. (5.1) is only for the top layer of skin to account for anisotropic behavior, while the bottom layer of skin is designed by incompressible neo-Hookean material, which strain energy density function has only $\Psi_{\text{iso}}(\overline{\mathbf{C}})$ in Eq. (5.1). Two layers in the skin part share the same shear modulus μ value, but fiber orientation $\overline{\mathbf{a}}_\alpha$ is assigned only at the upper layer of skin part.

Each model shares the same essential boundary conditions for skin part such that both the bottom surface and the region just below the Cutometer part are constrained by three translational degree of freedom. To be specific, we do not make use of a contact condition between Cutometer and skin parts in order not to cause computational difficulty toward convergence, but instead the surface just below the Cutometer part is fixed. The Cutometer part, it is fully fixed. Natural boundary

condition is only the negative pressure applied and the surface area to apply the negative pressure is determined based on the shape of Cutometer opening entrance (first row in Fig. 5.1**b**).

5.2.3 Gaussian process regression

GP defines a probability measure over the function space, that is, random variables are collected from the function space such that any finite subset of the random variables has a joint Gaussian distribution [187]. We substitute GP regression for the forward function which is FE analysis in this study. Let $\mathcal{D} := (\mathbf{X}, \mathbf{Y})$ be the input and output training dataset such that input

$$\mathbf{x}_i = (\mu^{(i)}, k_1^{(i)}, k_2^{(i)}, \kappa^{(i)}, \theta^{(i)}) \in \mathbf{X} \subset \mathbb{R}^5 \text{ with } i = 1, \cdots, n \tag{5.2}$$

consists of mechanical properties $\mu^{(i)}$, $k_1^{(i)}$, $k_2^{(i)}$, and $\kappa^{(i)}$ in Eq. (5.1) and fiber direction $\theta^{(i)}$, and the corresponding output becomes

$$\mathbf{y}_i = (y_1^{(i)}, \cdots, y_{15}^{(i)}) \in \mathbf{Y} \subset \mathbb{R}^{15} \text{ with } i = 1, \cdots, n \tag{5.3}$$

which contains the maximum height values of skin with respect to different opening entrances and different pressure values applied. The number of training dataset is equal to n. To be specific, $y_1^{(i)}, y_2^{(i)}, y_3^{(i)}$ are the maximum height values with 2 mm circular opening entrance by pressure 30, 40, and 50 kPa, respectively. Similarly, $y_4^{(i)}, y_5^{(i)}, y_6^{(i)}$ are the maximum height values with 8 mm circular opening entrance per each pressure value. On the other hand, $y_7^{(i)}, y_8^{(i)}, y_9^{(i)}$ are the maximum height values with elliptical opening entrance when fiber orientation becomes $\theta + 0°$, $\theta + 45°$, and $\theta + 90°$ and pressure value is 30 kPa. Likewise, other two pressure values, 40 and 50 kPa, are also applied, and the corresponding output is obtained with similar manner. Importantly, we treat each output in $\mathbf{y}_i$ independently because each measurement does not affect other measurements. At kth output, for example, $y_k^{(i)} = f_k(\mathbf{x}_i) + \epsilon_k^{(i)}$ is

the output expression after adding Gaussian noise $\epsilon_k^{(i)} \sim \mathcal{N}(0, \sigma_{G_k}^2)$ where $\sigma_{G_k}^2$ is the unknown variance and to be determined. Here, we assign the function f_k as GP such that

$$f_k(\cdot)|\theta \sim \mathcal{GP}\left(m(\cdot;\theta), k(\cdot,\cdot;\theta)\right), \tag{5.4}$$

where θ is called hyperparameters of the noise-free covariance function, $m(\cdot;\theta)$ is the mean function, and $k(\cdot,\cdot;\theta)$ is the covariance function or kernel function. f_k as GP is trained by $\mathcal{D}_{t_k} = \{\mathbf{x}_i, f_k(\mathbf{x}_i)\}_{i=1}^n$ which is kth training dataset with the number of dataset n. Our prior belief is encoded on our choice of the mean and covariance function. If there is no prior knowledge on the mean of $f_k(\cdot)$, we can select $m(\cdot;\theta)$ to be zero mean function, which is common in most applications. For the covariance function $k(\cdot,\cdot;\theta)$, we make use of the squared exponential,

$$k(\mathbf{x}_i, \mathbf{x}_j;\theta) = s^2 \exp\left(-\frac{1}{2}(\mathbf{x}_i - \mathbf{x}_j)^\top \mathbf{\Lambda}^{-1}(\mathbf{x}_i - \mathbf{x}_j)\right). \tag{5.5}$$

The hyperparameters can now be explicitly defined as $\theta = (\sigma_{G_k}^2, s, l_1, \cdots, l_5)$. The parameter s (> 0) is the signal strength; $l_1, \cdots, l_5$ are called characteristic length scales corresponding to each input, they are all positive, and enter Eq. (5.5) via $\mathbf{\Lambda} = \mathrm{diag}(l_1^2, \cdots, l_5^2)$.

Given input training dataset $\mathbf{X}$, the prior GP on the corresponding kth response output is a normal distribution such as

$$\mathbf{f}_k|\mathbf{X}, \theta \sim \mathcal{N}(\mathbf{0}, \mathbf{K}) \quad \text{with} \quad \mathbf{f}_k = (f_k(\mathbf{x}_1), \cdots, f_k(\mathbf{x}_n)), \tag{5.6}$$

where $\mathbf{K}$ is the covariance matrix expressed by the kernel function at the input data points. To be specific, the matrix $\mathbf{K}$ has (i,j) components $k(\mathbf{x}_i, \mathbf{x}_j;\theta)$ in Eq. (5.5), and it is symmetric and positive semi-definite. The conditional distribution of $\mathbf{f}_k$ given $\mathbf{y}_k$ is represented as a multi-variate and isotropic Gaussian distribution. Recalling that any finite subset of random variables has a joint Gaussian distribution, the joint

distribution of $\mathbf{y}_k$ and a new test output $f_k(\mathbf{x}^*)$ also follows a normal distribution such that

$$f_k(\mathbf{x}^*)|\mathbf{X}, \mathbf{y}_k, \mathbf{x}^*, \theta \sim \mathcal{N}\left(\mu_k(\mathbf{x}^*;\theta), \sigma_k^2(\mathbf{x}^*;\theta)\right), \tag{5.7}$$

where the predictive mean and variance at $\mathbf{x}^*$ are respectively defined as

$$\mu_k(\mathbf{x}^*;\theta) = \mathbf{k}(\mathbf{x}^*, \mathbf{X};\theta)(\mathbf{K} + \sigma_{G,r}^2 \mathrm{I})^{-1}\mathbf{y}_k \tag{5.8}$$

and

$$\sigma_k^2(\mathbf{x}^*;\theta) = k(\mathbf{x}^*, \mathbf{x}^*;\theta) - \mathbf{k}(\mathbf{x}^*, \mathbf{X};\theta)^\top(\mathbf{K} + \sigma_{G,r}^2 \mathrm{I})^{-1}\mathbf{k}(\mathbf{X}, \mathbf{x}^*;\theta)\,. \tag{5.9}$$

We make use of GP posterior $f_k(\mathbf{x}^*)$ in Eq. (5.7) as a forward function to solve the inverse problem for mechanical properties of skin such that the predictive mean μ_k in Eq. (5.8) enacts the forward function value at the unknown input point $\mathbf{x}^*$. Furthermore, the variance σ_k^2 is used as the uncertainty quantification for μ_k.

To build training dataset, we select n as 100 and generate $\mathbf{X}$ by Latin hypercube sampling (LHS) when the range of input dataset follows Table 5.1 which is derived from $[23, 60, 180]$. Given $\mathbf{X}$, we run 15 different FE simulations independently in order to obtain training output dataset. We allow automatic relevance determination for each length-scale and make use of maximum log marginal likelihood to fit the hyperparameters θ. We make use of GPy [195] for GP regression.

Table 5.1.: Ranges for the parameters used to describe the mechanical behavior of skin including anisotropy $[23, 60, 180]$

Parameter	Range
μ [kPa]	[4.774, 6.804]
k_1 [kPa]	[3.800, 209.300]
k_2 [-]	[52.530, 161.860]
κ [-]	[0.133, 0.333]
θ [°]	[0, 180]

5.2.4 Semi-particle approximation

We adopt Bayesian framework to infer the solution of inverse problem. Recall that we want to infer new $\mathbf{x}$, which is mechanical properties of skin, corresponding to new $\mathbf{y}$, which is the maximum height of skin deformation measured by Cutometer. Because we substitute GP regression for a forward function, which causes model uncertainty induced by surrogate model, it needs to consider uncertainty induced by inference of posterior distribution through the solution of inverse problem. To address this aspect, we make use of the approximate solution of the posterior distribution $p(\mathbf{x}|\mathbf{y}, \mathcal{D})$ such that [274]

$$p(\mathbf{x}|\mathbf{y}, \mathcal{D}) \approx p(\mathbf{x}|\mathbf{y}, \theta^*, \mathcal{D}) = \int p(\mathbf{y}|\mathbf{x}, \mathbf{f})\, p(\mathbf{f}|\mathbf{x}, \theta^*, \mathcal{D}) \mathrm{d}\mathbf{f} p(\mathbf{x}), \tag{5.10}$$

where θ^* is obtained by the maximum log likelihood, the prior of $\mathbf{x}$ is the uniform distribution over the range shown in Table 5.1, i.e., $p(\mathbf{x}) \propto 1(\mathbf{x})$, and the likelihood of new output data $\mathbf{y}$ is chosen to be Gaussian such as $p(\mathbf{y}|\mathbf{x}, \mathbf{f}) = \mathcal{N}(\mathbf{y}|\mathbf{f}, \sigma^2\mathbf{I})$. The parameter σ^2 expresses output error, e.g., measurement noise, and is imposed by noninformative prior distribution as inverse Gamma distribution such that $p(\sigma) = \mathcal{IG}(\sigma|\alpha, \beta)$ with $\alpha = 10$ and $\beta = 0.5$. Although Eq. (5.10) does not explicitly represent prior $p(\sigma)$, inference on σ is also achieved through Bayesian framework. Recalling that we utilized GP posterior as a forward function, $p(\mathbf{f}|\mathbf{x}, \theta^*, \mathcal{D})$ is also Gaussian distribution defined by GP posterior.

As we mentioned before, each surrogate output is independent, and therefore $p(\mathbf{y}|\mathbf{x}, \mathbf{f})$ and $p(\mathbf{f}|\mathbf{x}, \theta^*, \mathcal{D})$ can be expressed by multiplication of each component, implying that

$$p(\mathbf{x}|\mathbf{y}, \mathcal{D}) \approx p(\mathbf{x}|\mathbf{y}, \theta^*, \mathcal{D}) = \prod_{k=1}^{15} \left(\int p(y_k|\mathbf{x}, f_k)\, p(f_k|\mathbf{x}, \theta_k^*, \mathcal{D}) \mathrm{d}f_k \right) p(\mathbf{x}). \tag{5.11}$$

The evaluation of the above integral is analytically tractable because $p(y_k|\mathbf{x}, f_k)$ and $p(f_k|\mathbf{x}, \theta_k^*, \mathcal{D})$ are both Gaussian distribution, but marginal likelihood of right side of Eq. (5.11) can be analytically intractable based on prior $p(\mathbf{x})$. In this study, we assign the noninformative prior $p(\mathbf{x})$ as inverse Gamma distribution. To circumvent this possible issue, predictive posterior distribution can be represented by MCMC sampling. We make use of NO-U-Turn sampler (NUTS), which is from Hamiltonian Monte Carlo algorithm, in PyMC3 [276].

5.2.5 Active learning

If the forward function is expensive, collecting the training dataset itself is a burden. Accordingly, the size of training dataset can be limited and, consequently, epistemic error can also be increased [277, 278]. To effectively overcome this limitation, we suggest an active learning for regression problem such that the initial training dataset is increased point by point based on results of current regression and, then, the training dataset is updated to build new surrogate and make a regression (Algorithm 1). Our active learning algorithm aims to search new training input point $\mathbf{x}^*$ which is close to not only the maximum posterior point, $|\mu_k' - \mu_k(\mathbf{x}_r)|$, but also high epistemic error point, $\sigma_k(\mathbf{x}_r)^2$ (line 6 in Algorithm 1). Once $\mathbf{x}^*$ is selected from $\boldsymbol{R}$, the corresponding FE simulation is run to acquire output data, and those input and output pair is added to previous training dataset. This procedure is repeated for all $M = 15$ output independently. Staring from $n = 100$, Algorithm 1 is implemented to add $m = 10$ more training data points.

5.3 Results

We test the solution of inverse problem in Eq. (5.11) using Table 5.2, where we generate 5 test input points by LHS and run FE analysis to obtain the corresponding output. Before starting the active learning algorithm, the number of initial training

Algorithm 1 Active learning algorithm with Gaussian process regression

Require: Desired size of active set m, the number of output dimension M, training dataset $\mathcal{D}_{t_k} = \{\mathbf{x}_i, f_k(\mathbf{x}_i)\}_{i=1}^{n}$ at kth output dimension, M independent Gaussian processes respectively trained by $\mathcal{D}_{t_1}, \ldots, \mathcal{D}_{t_M}$, mean $\mu_k(\cdot)$ and variance $\sigma_k(\cdot)^2$ from regression by kth Gaussian process, extra input dataset $R = \{\mathbf{x}_{n+1}, \mathbf{x}_{n+2}, \ldots, \mathbf{x}_{n+N}\}$

for $j := 1, \ldots, m$ **do**
  Find $\mathbf{x}'$ as the mean value from Eq. (5.11)
  for $k := 1, \ldots, M$ **do**
    Find $\mu'_k = \mu'_k(\mathbf{x}')$
  end for
  $\mathbf{x}^* \leftarrow \underset{\mathbf{x}_r \in R}{\arg\min} \sum_{k=1}^{M} \frac{|\mu'_k - \mu_k(\mathbf{x}_r)|}{\sigma_k(\mathbf{x}_r)^2}$
  for $k := 1, \ldots, M$ **do**
    $\mathcal{D}_{t_k} \leftarrow \mathcal{D}_{t_k} \cup \{\mathbf{x}^*, f_k(\mathbf{x}^*)\}, R \leftarrow R \setminus \mathbf{x}^*$
    Update kth Gaussian process with $\mathcal{D}_{t_k}$
  end for
end for

dataset n is 100. The corresponding inference per each test dataset is represented in Figs. 5.2 to 5.6.

The prediction only using initial training dataset can be effectively improved if active learning algorithm (Algorithm 1) is applied to update the training dataset,

Table 5.2.: Test dataset for the model calibration

No.	Pressure [kPa]	Mechanical properties					Max. height [mm]				
		μ [kPa]	k_1 [kPa]	k_2 [-]	κ [-]	θ [°]	Circle ϕ2 mm	Circle ϕ8 mm	Ellipse $\theta + 0°$	Ellipse $\theta + 45°$	Ellipse $\theta + 90°$
	30						0.530	2.049	1.390	1.579	1.355
1	40	5.351	175.063	69.145	0.251	137.924	0.568	2.294	1.503	1.739	1.461
	50						0.595	2.434	1.573	1.835	1.527
	30						0.509	2.298	1.528	1.476	1.517
2	40	4.910	100.771	106.547	0.316	41.569	0.538	2.581	1.643	1.580	1.629
	50						0.558	2.737	1.708	1.640	1.693
	30						0.518	1.801	1.054	1.420	1.505
3	40	5.965	143.531	91.165	0.155	107.884	0.560	1.965	1.115	1.518	1.624
	50						0.590	2.054	1.153	1.576	1.694
	30						0.545	1.875	1.570	1.307	1.099
4	40	6.273	71.746	156.563	0.205	178.501	0.585	2.054	1.709	1.374	1.149
	50						0.612	2.137	1.785	1.411	1.179
	30						0.602	1.988	1.582	1.364	1.395
5	40	6.574	14.143	139.314	0.253	26.804	0.638	2.326	1.726	1.433	1.469
	50						0.662	2.488	1.791	1.468	1.507

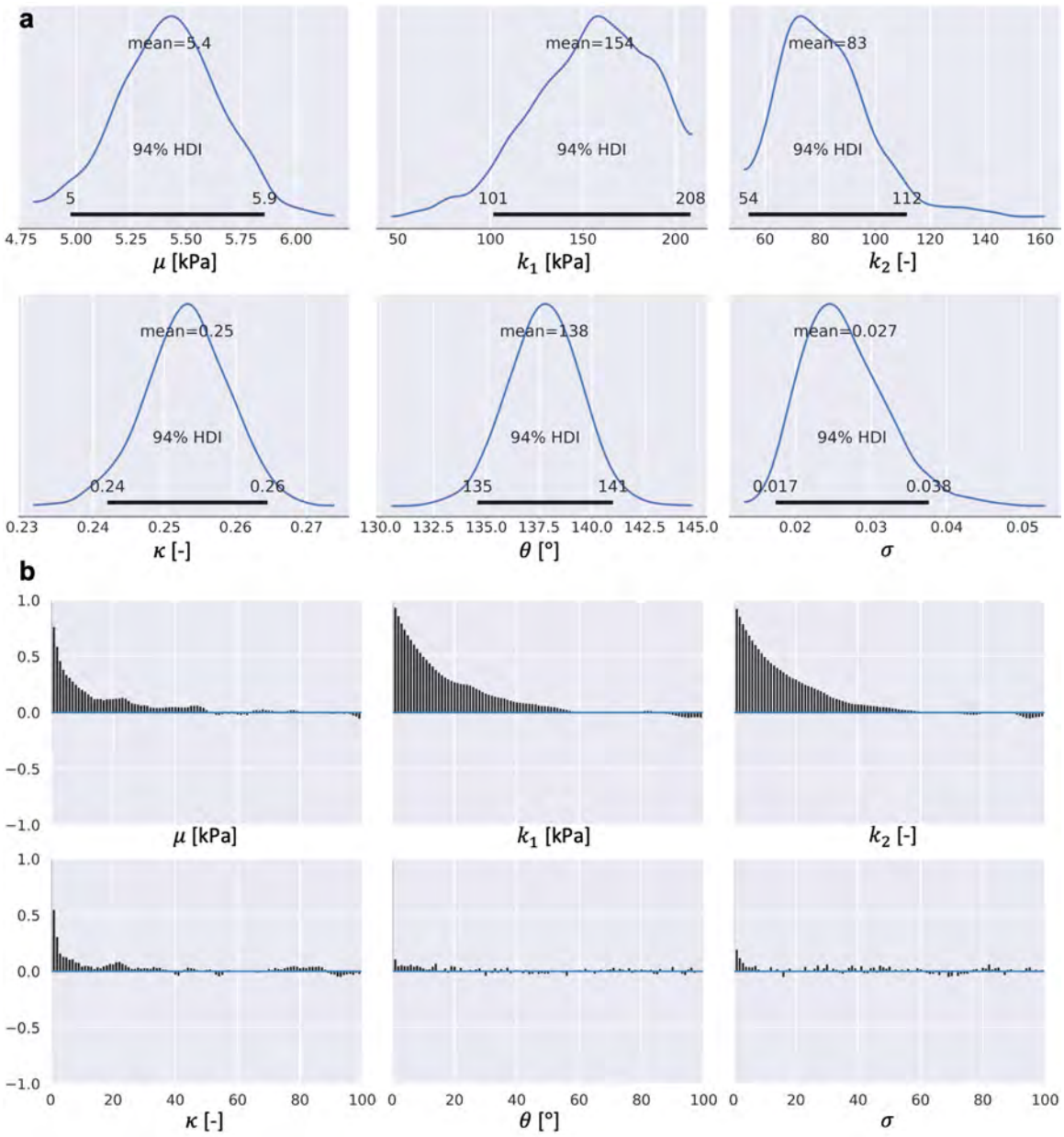

Fig. 5.2.: The solution of inverse problem for first test dataset in Table 5.2 when the initial training dataset is only given. μ, k_1, k_2, κ, and θ are the input $\mathbf{x}$ and σ is the standard deviation of distribution for output y. (**a**) Each plot denotes probability density function by sampling from predictive posterior distribution. (**b**) Autocorrelation per each input $\mathbf{x}$ and σ is shown after burn-in.

because the number of training data points is increased based on algorithm, not arbitrary way. Prediction by sampling also shows 94% highest density interval (HDI)

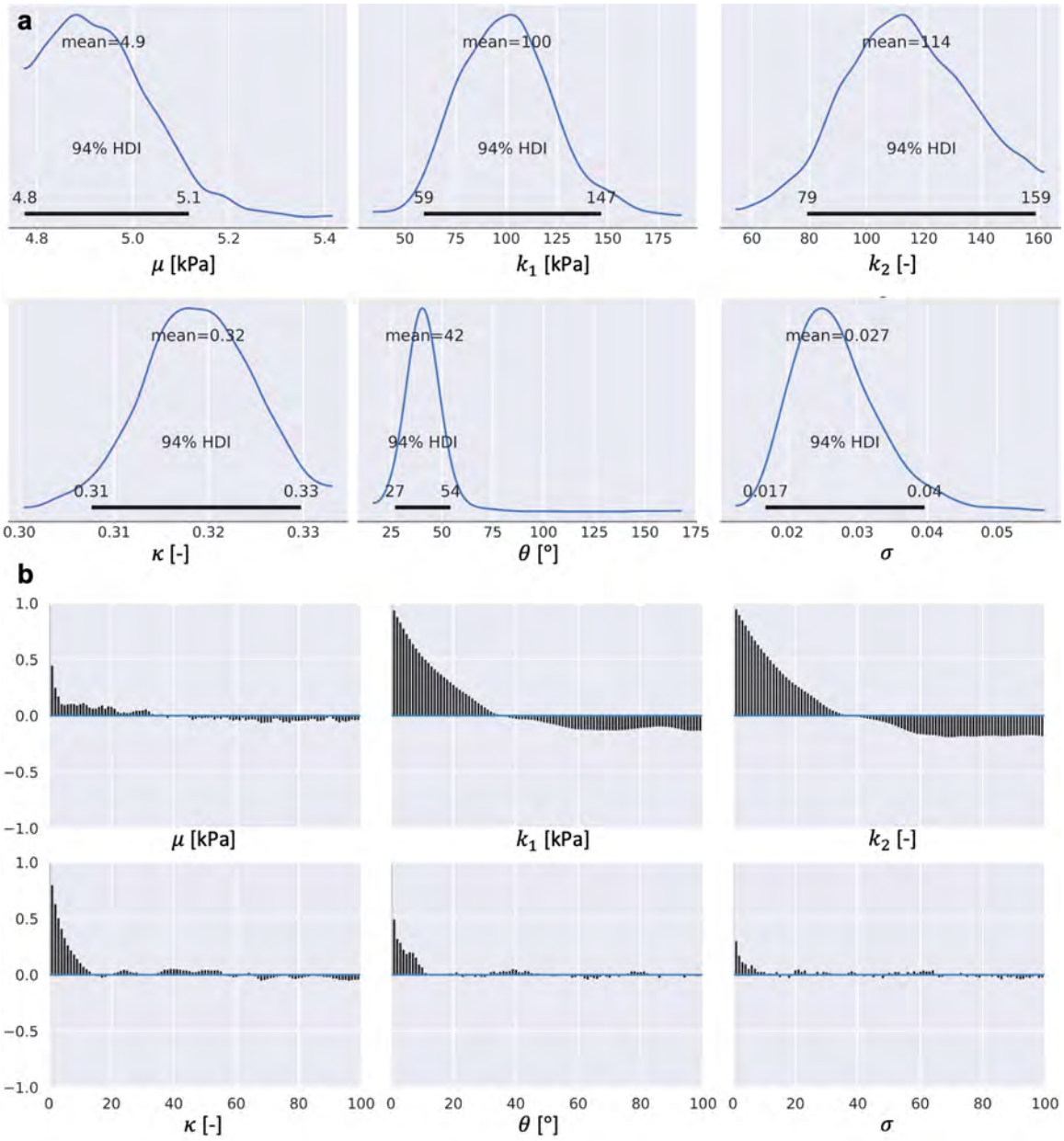

Fig. 5.3.: The solution of inverse problem for second test dataset in Table 5.2 when the initial training dataset is only given. μ, k_1, k_2, κ, and θ are the input $\mathbf{x}$ and σ is the standard deviation of distribution for output y. (**a**) Each plot denotes probability density function by sampling from predictive posterior distribution. (**b**) Autocorrelation per each input $\mathbf{x}$ and σ is shown after burn-in.

in Figs. 5.2**a** to 5.6**a**. In addition, each inference by sampling is examined by auto-

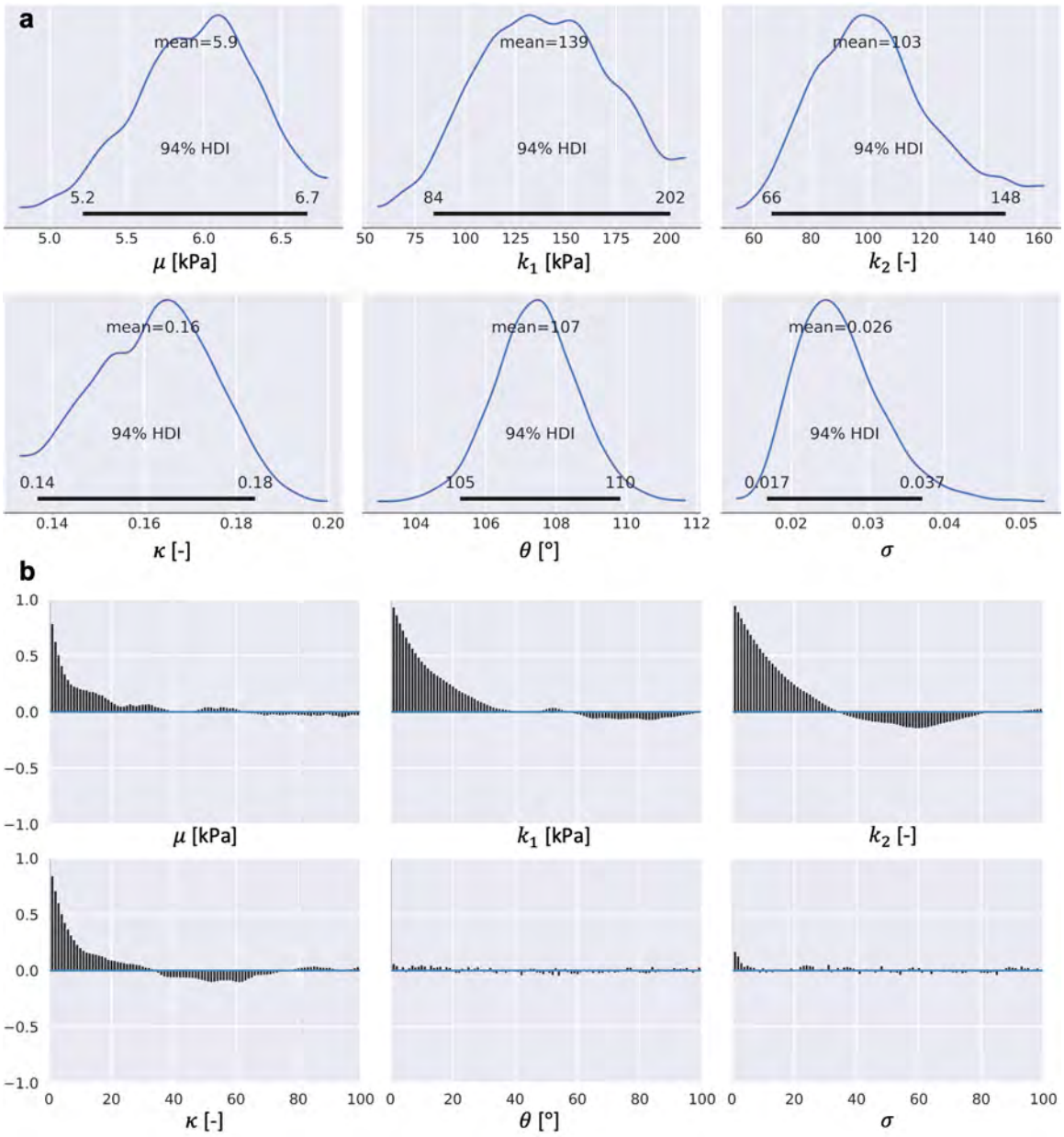

Fig. 5.4.: The solution of inverse problem for third test dataset in Table 5.2 when the initial training dataset is only given. μ, k_1, k_2, κ, and θ are the input $\mathbf{x}$ and σ is the standard deviation of distribution for output y. (**a**) Each plot denotes probability density function by sampling from predictive posterior distribution. (**b**) Autocorrelation per each input $\mathbf{x}$ and σ is shown after burn-in.

correlation (Figs. 5.2**b** to 5.6**b**). As more sampling is proceeded, the autocorrelation is decreased, meaning that convergence is achieved.

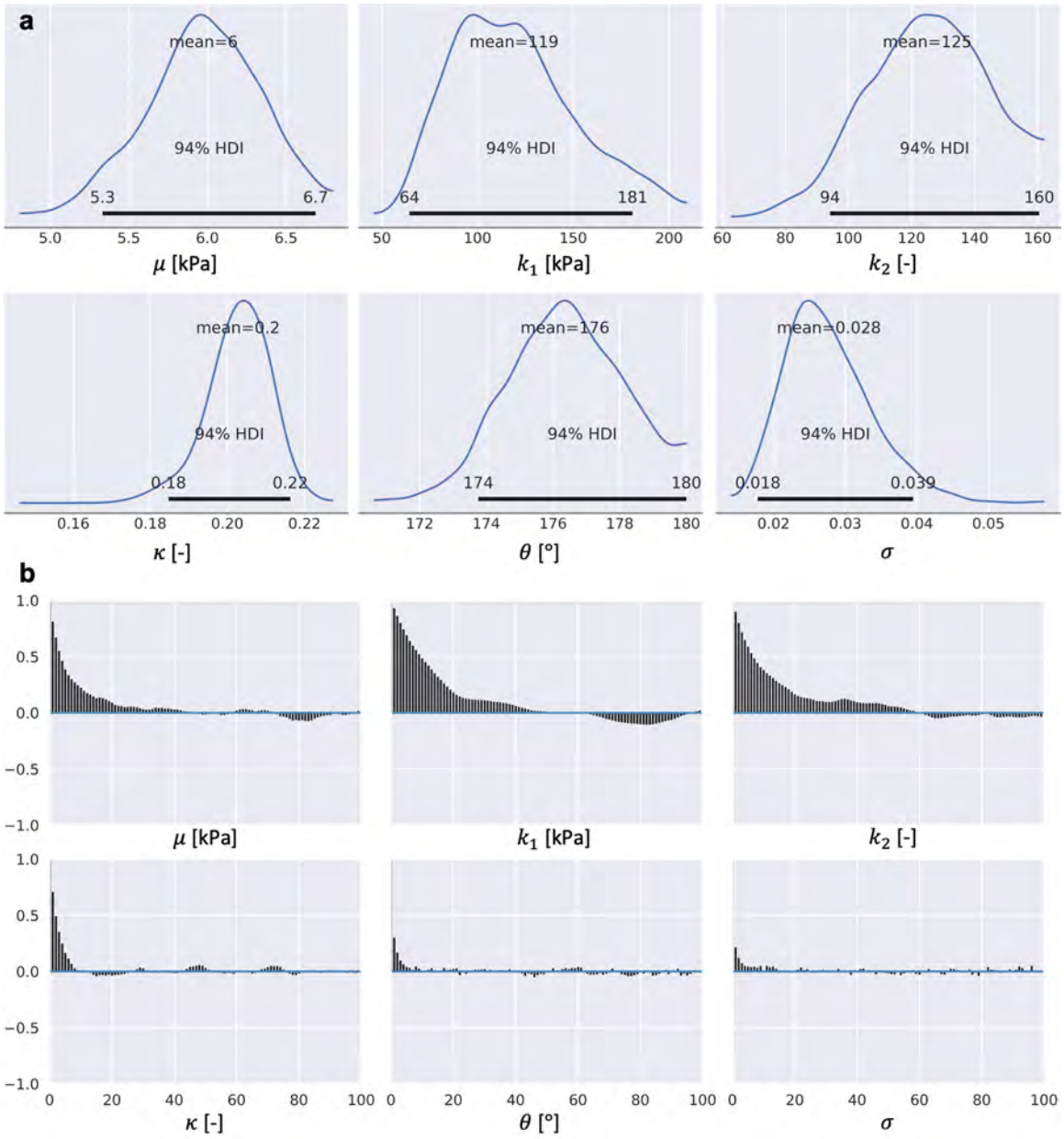

Fig. 5.5.: The solution of inverse problem for fourth test dataset in Table 5.2 when the initial training dataset is only given. μ, k_1, k_2, κ, and θ are the input $\mathbf{x}$ and σ is the standard deviation of distribution for output y. (**a**) Each plot denotes probability density function by sampling from predictive posterior distribution. (**b**) Autocorrelation per each input $\mathbf{x}$ and σ is shown after burn-in.

To compare Table 5.2 with Figs. 5.2 to 5.6, root mean square error (RMSE) is calculated for all test dataset (Table 5.3), showing that the Bayesian approach

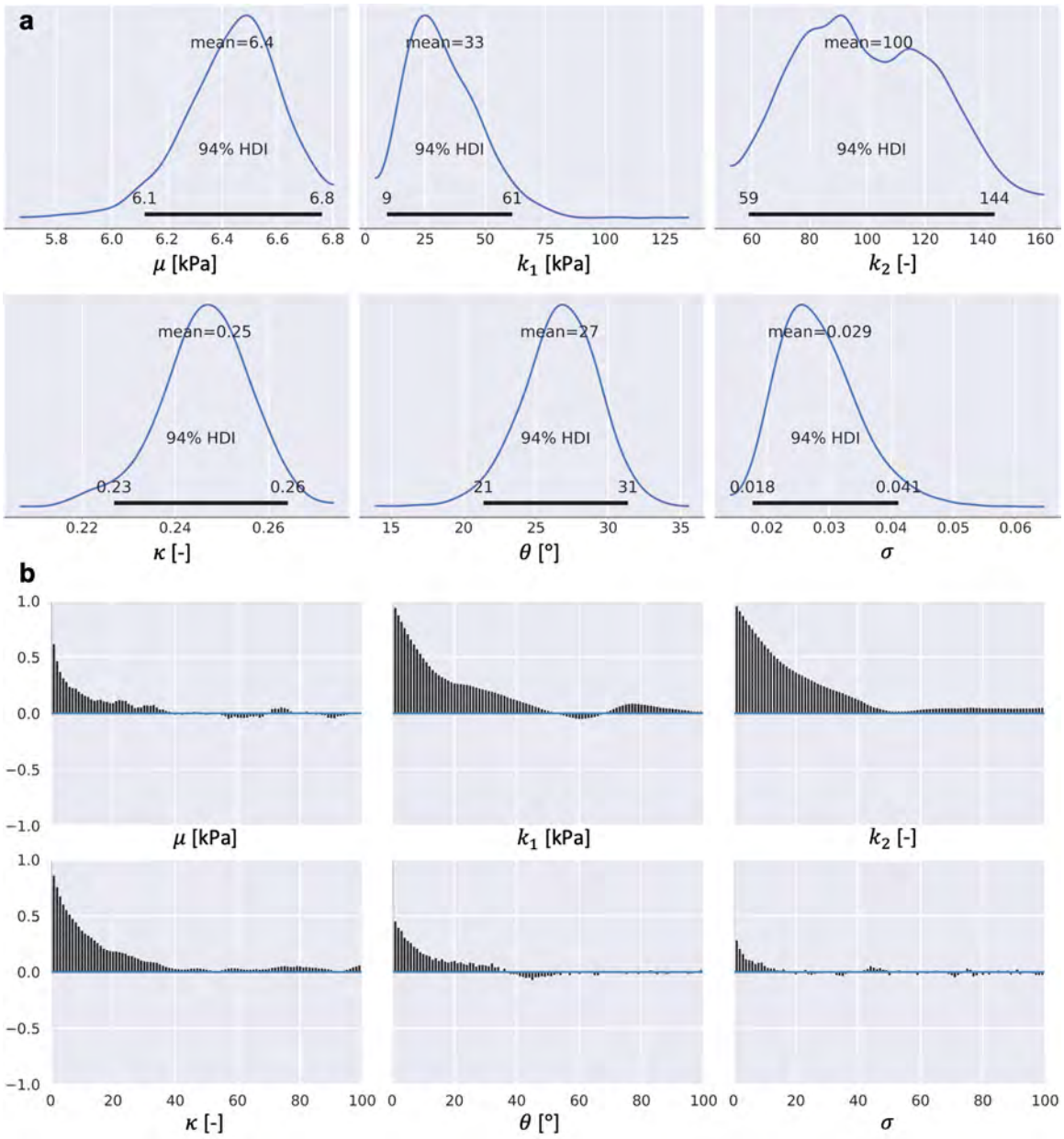

Fig. 5.6.: The solution of inverse problem for fifth test dataset in Table 5.2 when the initial training dataset is only given. μ, k_1, k_2, κ, and θ are the input $\mathbf{x}$ and σ is the standard deviation of distribution for output y. (**a**) Each plot denotes probability density function by sampling from predictive posterior distribution. (**b**) Autocorrelation per each input $\mathbf{x}$ and σ is shown after burn-in.

is feasible for our inverse problem. Predictions for second and third test dataset outperform other predictions. By observing each component of prediction, μ, κ, and

Table 5.3.: Performance on the solution of inverse problem with initial training dataset is quantified by root mean square error (RMSE). Predictive mean of posterior distribution is compared with the test input dataset shown in Table 5.2.

No.	μ [kPa]	k_1 [kPa]	k_2 [-]	κ [-]	θ [°]	RMSE
1	5.4	154	83	0.25	138	11.275
2	4.9	100	114	0.32	42	3.357
3	5.9	139	103	0.16	107	5.681
4	6	119	125	0.2	176	25.438
5	6.4	33	100	0.25	27	19.500

Table 5.4.: Performance on the solution of inverse problem after adding 10% more training dataset is quantified by root mean square error (RMSE). Predictive mean of posterior distribution is compared with the test input dataset shown in Table 5.2.

No.	μ [kPa]	k_1 [kPa]	k_2 [-]	κ [-]	θ [°]	RMSE
1	5.4	155	81	0.25	138	10.422
2	5.0	93	117	0.32	43	5.860
3	5.9	145	98	0.16	108	3.127
4	5.9	114	126	0.2	172	23.503
5	6.5	27	112	0.25	27	13.501

θ are captured with good accuracy, while k_1 and k_2 show poor performance. Based on implication of k_1 and k_2, which indicate mechanical properties of fiber family, the deformation by negative pressure on the surface is less sensitive to longitudinal mechanical characteristics. On the other hand, it can be understood that κ and θ, which imply dispersion and orientation of fiber family, are more dominant factor for the deformation. We confirmed that our Bayesian solution to the inverse problem can capture anisotropic nature of skin as well as hyperelastic feature.

Taking advantage of the active learning algorithm (Algorithm 1), 10% more training dataset are sequentially collected based on the algorithm. We also make use of the same test dataset to validate the performance of the active learning algorithm. With the same manner shown in Figs. 5.2 to 5.6, the solution of inverse problem with 10% more training dataset is represented in Figs. 5.7 to 5.11, respectively. To better compare the solution with true dataset, Table 5.4 summarizes the performance with

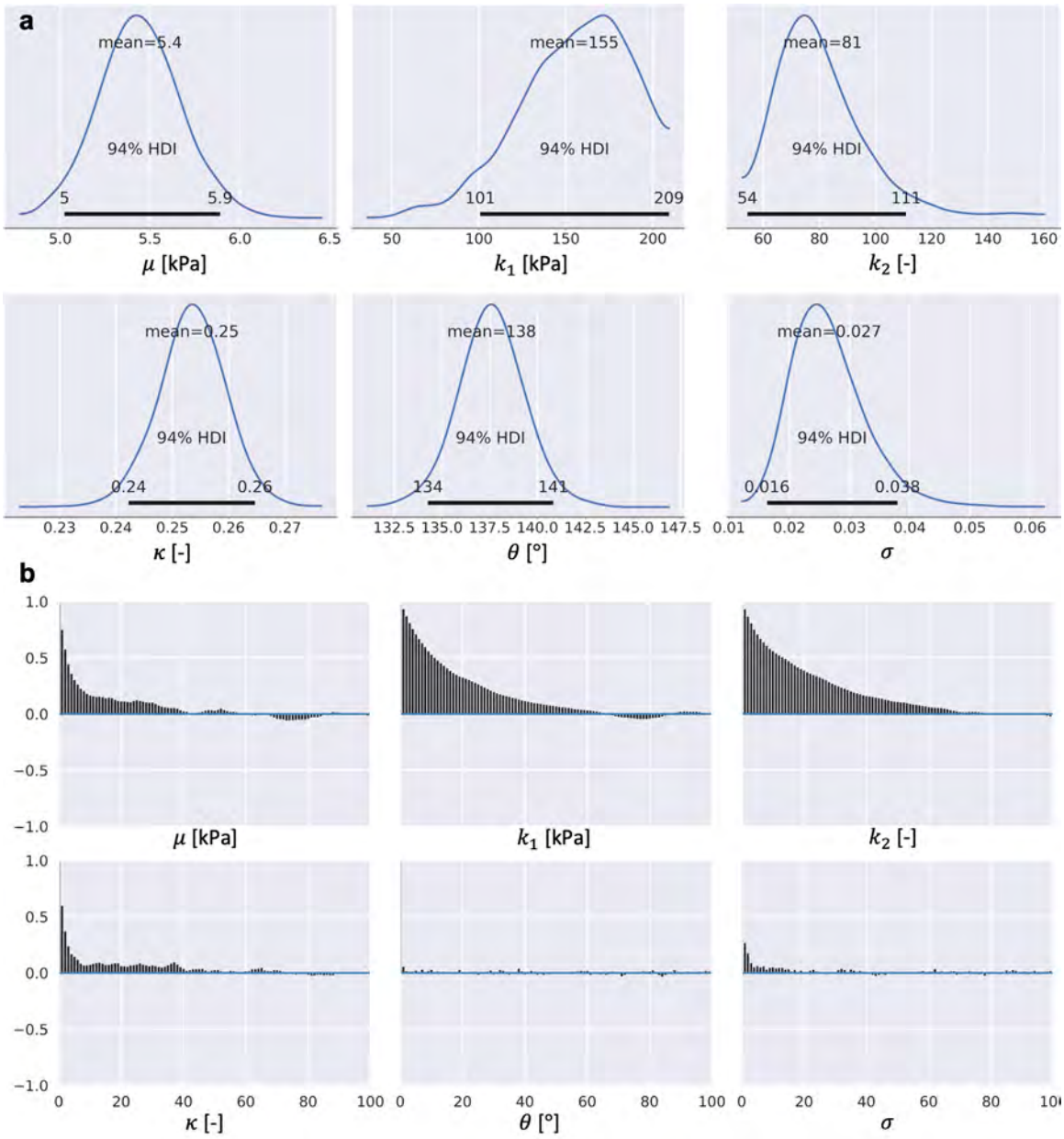

Fig. 5.7.: The solution of inverse problem for first test dataset in Table 5.2 after adding 10% more training dataset. μ, k_1, k_2, κ, and θ are the input $\mathbf{x}$ and σ is the standard deviation of distribution for output y. (**a**) Each plot denotes probability density function by sampling from predictive posterior distribution. (**b**) Autocorrelation per each input $\mathbf{x}$ and σ is shown after burn-in.

respect to RMSE, in which effect by adding 10% more training dataset can be quan-

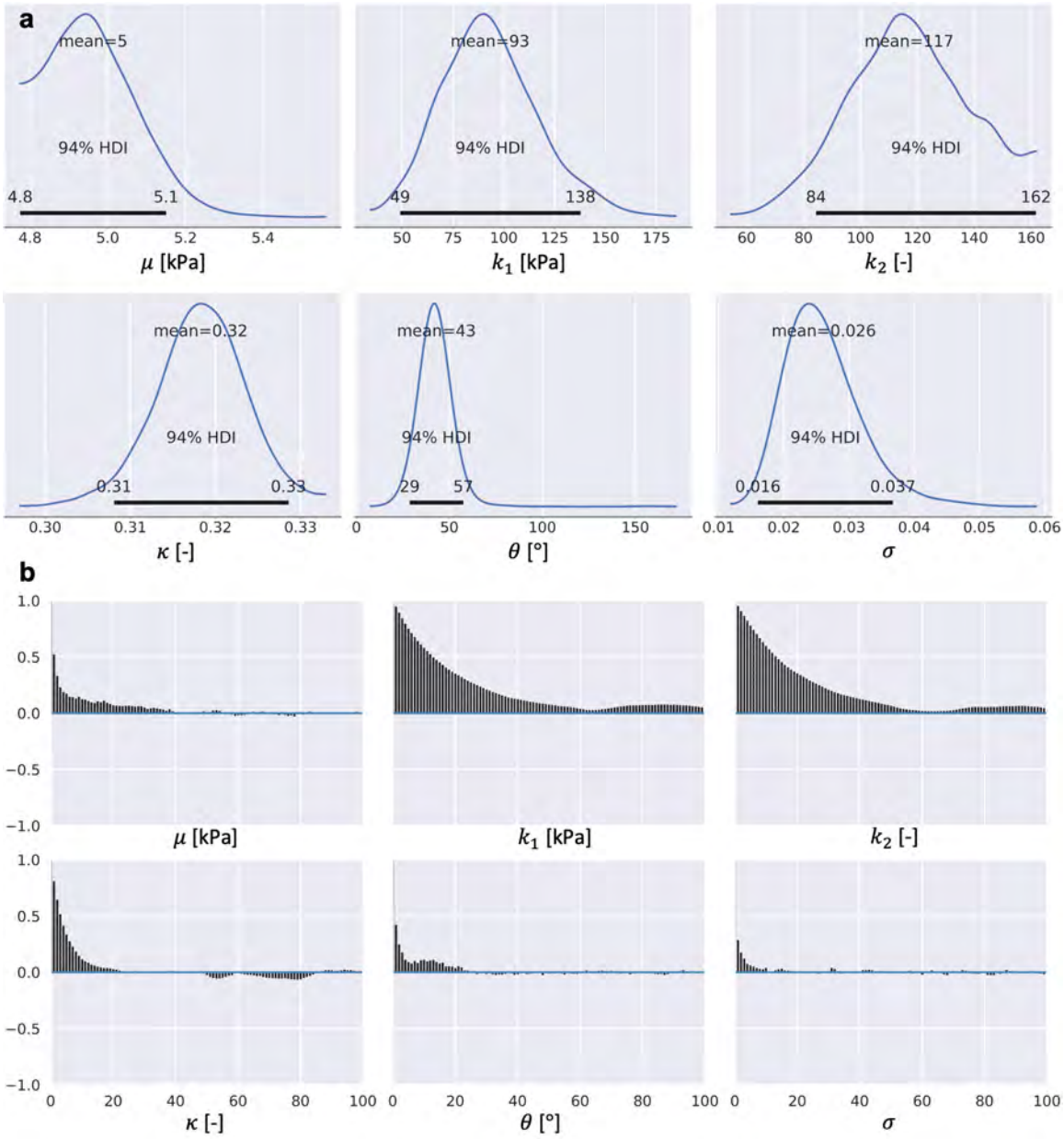

Fig. 5.8.: The solution of inverse problem for second test dataset in Table 5.2 after adding 10% more training dataset. μ, k_1, k_2, κ, and θ are the input $\mathbf{x}$ and σ is the standard deviation of distribution for output y. (**a**) Each plot denotes probability density function by sampling from predictive posterior distribution. (**b**) Autocorrelation per each input $\mathbf{x}$ and σ is shown after burn-in.

tified. Except second test dataset, adding 10% more training dataset is beneficial to improve the solution of inverse problem.

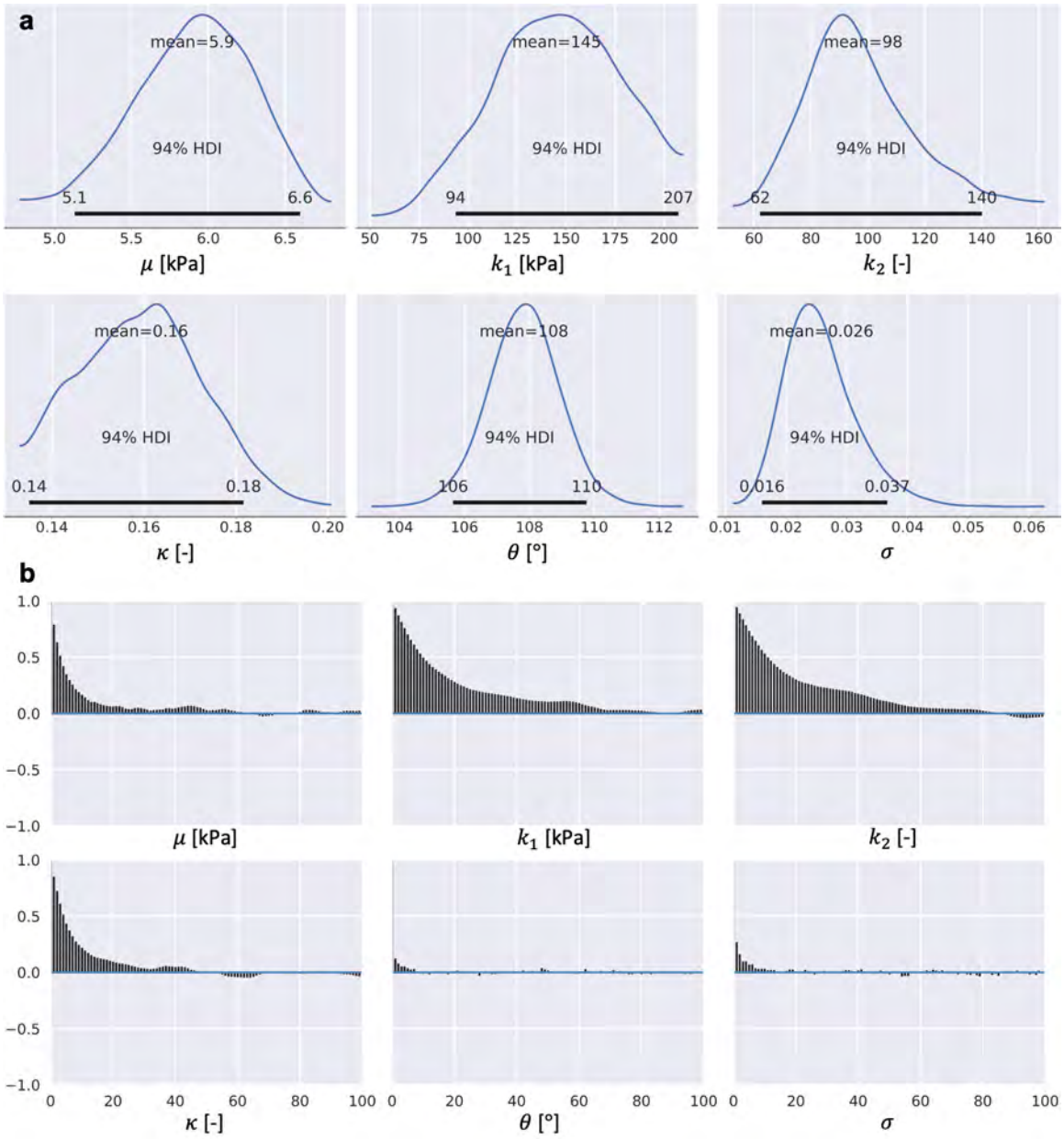

Fig. 5.9.: The solution of inverse problem for third test dataset in Table 5.2 after adding 10% more training dataset. μ, k_1, k_2, κ, and θ are the input $\mathbf{x}$ and σ is the standard deviation of distribution for output y. (**a**) Each plot denotes probability density function by sampling from predictive posterior distribution. (**b**) Autocorrelation per each input $\mathbf{x}$ and σ is shown after burn-in.

More substantial evaluation on the active learning algorithm can be carried out between different sampling approaches by active learning algorithm and random addi-

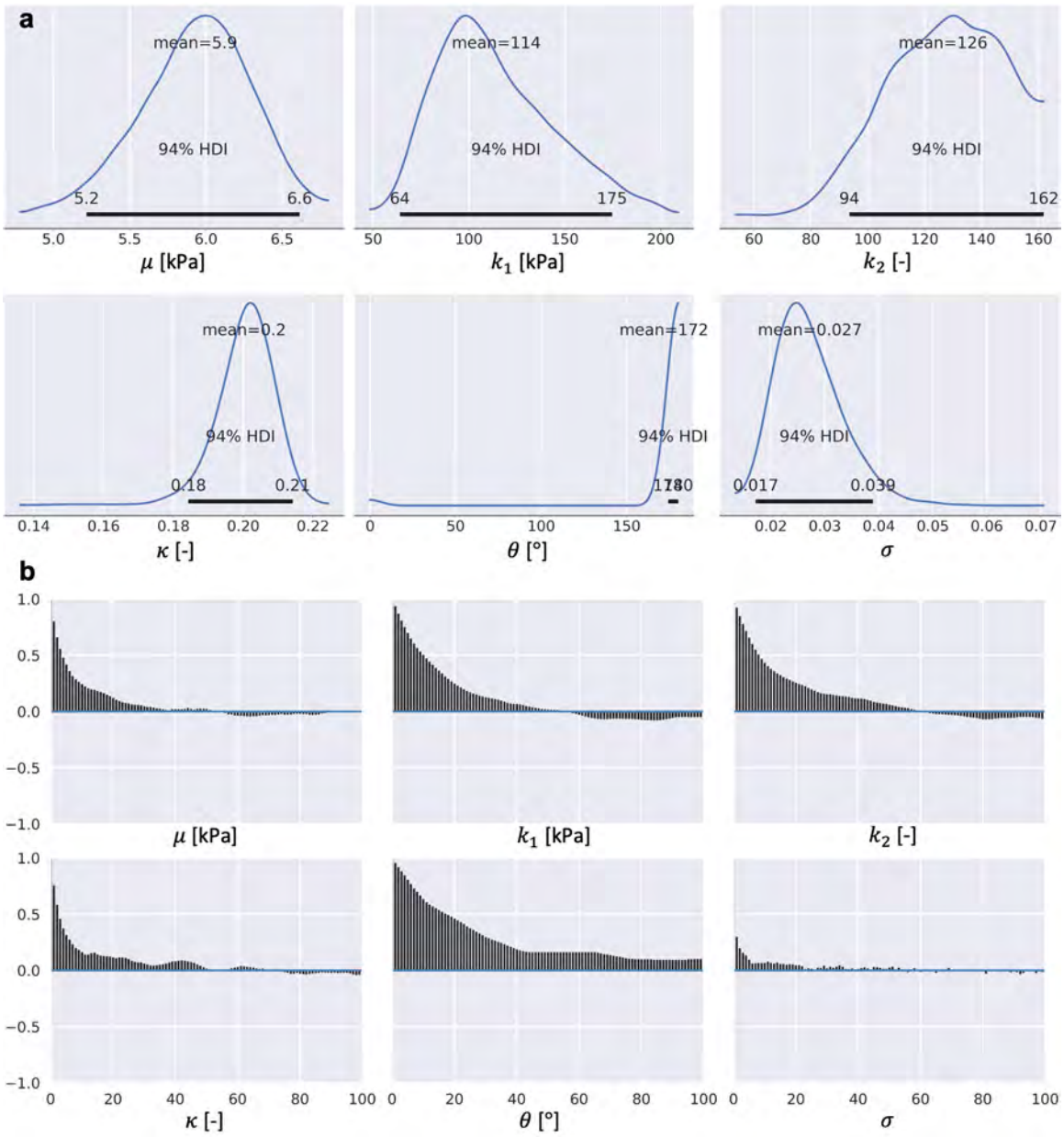

Fig. 5.10.: The solution of inverse problem for fourth test dataset in Table 5.2 after adding 10% more training dataset. μ, k_1, k_2, κ, and θ are the input $\mathbf{x}$ and σ is the standard deviation of distribution for output y. (**a**) Each plot denotes probability density function by sampling from predictive posterior distribution. (**b**) Autocorrelation per each input $\mathbf{x}$ and σ is shown after burn-in.

tion. To do so, 10 more training dataset is generated by LHS and added to the initial training dataset, and the same procedure to obtain the solution of inverse problem is

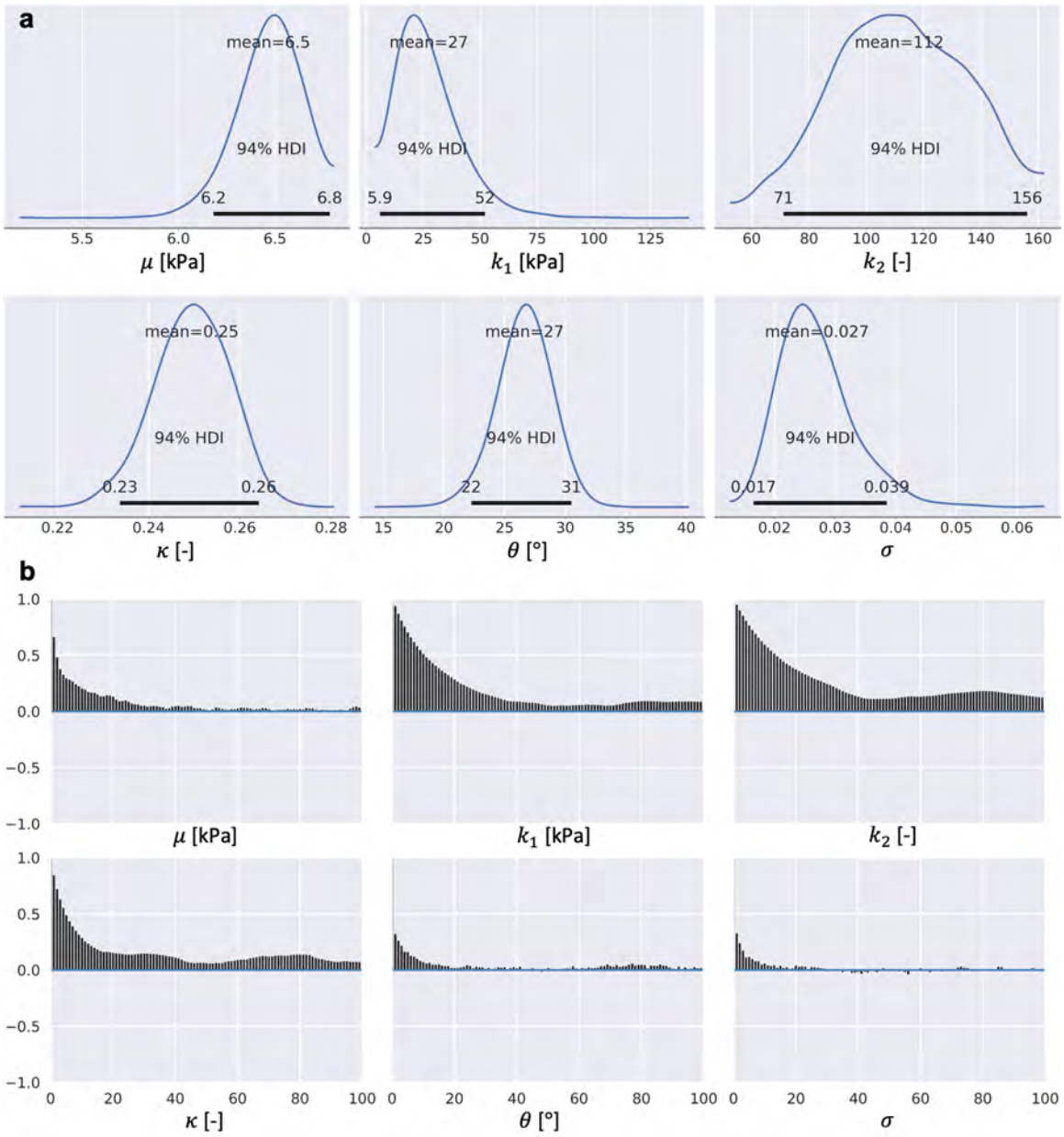

Fig. 5.11.: The solution of inverse problem for fifth test dataset in Table 5.2 after adding 10% more training dataset. μ, k_1, k_2, κ, and θ are the input $\mathbf{x}$ and σ is the standard deviation of distribution for output y. (**a**) Each plot denotes probability density function by sampling from predictive posterior distribution. (**b**) Autocorrelation per each input $\mathbf{x}$ and σ is shown after burn-in.

applied. The results are summarized by the similar manner with that by the active learning algorithm (Table 5.5), enabling us to validate the performance of the ac-

Table 5.5.: Solution of inverse problem after adding random 10% more training dataset is quantified by root mean square error (RMSE). Predictive mean of posterior distribution is compared with the test input dataset shown in Table 5.2.

No.	μ [kPa]	k_1 [kPa]	k_2 [-]	κ [-]	θ [°]	RMSE
1	5.4	150	85	0.25	138	13.263
2	4.9	104	108	0.32	41	1.604
3	5.9	141	103	0.16	107	5.427
4	5.8	131	120	0.2	177	31.146
5	6.4	32	103	0.25	27	18.098

tive learning algorithm (compare Table 5.4 with Table 5.5). The second test dataset only shows better prediction by random increase of training dataset, but other four points in test dataset obviously undergo outperforming caused by the active learning algorithm.

5.4 Conclusion

The aim of the study is to make a solution for the inverse problem seeking for mechanical properties of skin. Making use of suction device, Cutometer, different shapes of opening entrance are designed by finite element model. We validate that newly proposed design for opening entrance is appropriate to capture the anisotropic nature of skin. Finite element model for Cutometer is substituted with Gaussian process surrogate by seeking for computational efficiency. Bayesian approach has been a main spirit to suggest the solution of inverse problem and able to provide sound prediction. We also develop the active learning algorithm to overcome high computational cost to build high density of training dataset, and the performance of the active learning algorithm is validated by comparing with that of random sampling.

6. VIRTUAL SURGERY: OBTAINING ACCURATE PATIENT-SPECIFIC GEOMETRIES WITH INEXPENSIVE AND FLEXIBLE IMAGING TECHNOLOGIES

Abstract: Excessive mechanical stress leads to wound healing complications following reconstructive surgery. However, this knowledge is not easily applicable in clinical scenarios due to the difficulty in measuring stress contours during complex tissue rearrangement procedures. Computational tools have been proposed as an alternative to address this need, but obtaining patient specific geometries with an affordable and flexible setup has remained a challenge. Here we present a methodology to determine the stress contours from a reconstructive procedure on a patient-specific finite element model based on multi-view stereo (MVS). MVS is a noninvasive technology that allows reconstruction of 3D geometries using a standard digital camera, making it ideal for the operating room. Finite element analysis can then be used on the patient-specific geometry to perform a virtual surgery and predict regions at risk of complications. We applied our approach to the case of a 7-year-old patient who was treated to correct a cranial contour deformity and resect two large areas of scalp scarring. The simulation showed several zones of high stress, particularly near the suture lines at the distal ends of the flaps. The patient did show delayed healing and partial flap tip necrosis at one of such predicted regions at the 30-day follow up visit. Our results further establish the application of computational tools in individualized medical scenarios to advance preoperative planing and anticipate regions of concern immediately after surgery.

6.1 Motivation

Local flaps are routinely used for reconstruction after removal of tumors, birth defects and hypertrophic scars, to name a few examples [102, 279]. The state of stress influences the healing process and can lead to complications such as tissue necrosis, delay of healing, and wound dehiscence [2, 3]. However, directly measuring stress in the operating room is not practically feasible beyond very controlled settings and ideal clinical cases [6], and stress contours in complex surgeries are not intuitive.

Computational simulations have been proposed to optimize flap design, but have been limited to idealized and generic cases [14, 16–19]. In clinical practice, general principles have been established to guide flap design, but every patient requires an individualized treatment [7,32]. Three-dimensional (3D) imaging tools, such as stereo vision systems, have been successfully used in biomedical applications, but require specialized equipment and careful calibration [280, 281]. Recent efforts in computer vision, however, have led to multi-view stereo reconstruction (MVS), which relies on a large set of uncalibrated images of a static scene taken from different angles with a standard digital camera [282]. This technique is accurate, inexpensive, and does not require a restrictive experimental setup [283], making it ideal for routine clinical use.

To advance preoperative planning and anticipate wound healing complications, we present an innovative approach that enables individualized reconstructive surgery simulations based on MVS reconstruction in the operating room. We anticipate that our approach will enable acquisition of new kinds of data to gain a better understanding of how mechanical cues contribute to wound complications in humans, and to establish new preoperative planning tools based on finite element simulations.

6.2 Methods

6.2.1 Clinical case

The patient is a 7-year-old female who underwent resection of a giant nevus of the posterior scalp in infancy, which was complicated by infection and osteomyelitis, requiring debridement of the occipital calvarium. At the beginning of the current treatment, she had a cranial contour deformity, residual nevus, and unstable scar with ulceration and alopecia (Fig. 6.1). Her healthy scalp was expanded to grow skin that would be needed after excision of the scars. A tissue expander was placed and filled to 309 ml over 3 months. A cranioplasty implant (Biomet Corporation, Warsaw, IN) was manufactured using computer tomography (CT) scan data.

Surgery for tissue expander removal, cranioplasty, and resection of residual scar and nevus was performed. Two portions of the scalp were resected. The cranioplasty implant was put in place and covered with the skin flaps generated with tissue expansion. The scalp was closed with absorbable sutures and the patient was seen at 3 and 30 days for follow up visits. A small area of delayed healing developed at the T-junction of the occipital incision at the 30-day visit (Fig. 6.1). After standard care, this region healed without further complications.

6.2.2 Patient-specific model based on multi-view stereo reconstruction

The 3D model was created by capturing photos with a standard digital camera pre and intra-operatively, and processing the images with Recap360 (Autodesk, San Rafael, CA), a commercial MVS algorithm. The skin configurations captured were: preoperative, immediately after expander removal, immediately after excision of the skin defects, and after skin closure (Fig. 6.2).

A CT scan was acquired ahead of the surgery for designing of the cranioplasty implant. A surface mesh was reconstructed from the CT scan using 3D Slicer [284]. Since the surgery involved only the scalp region, details distant to the scalp were

Fig. 6.1.: 7-year-old female with residual scarring and a cranial contour defect (**a**): Her scalp was grown with a tissue expander (**b**). Patient at the 3-day follow up visit after cranioplasty and tissue rearrangement (**c**) and at the 30-day follow up visit (**d**).

smoothed out (Fig. 6.3). The 3D model of the skull was modified to correct the defect, analogous to placing the implant but producing a single geometry. The skull mesh consisted of 6,807 nodes and 13,608 triangles (Fig. 6.3).

Skin, as most connective tissues, is naturally prestrained [12,116]. The skin geometry during surgery, immediately after expander removal, is assumed to be tension-free and thus taken as the initial geometry for the simulation. Skin excisions were virtually performed based on the MVS geometries for the various time points of surgery. The resulting surface was converted into a tetrahedral volume mesh assuming a thickness of 3.6 mm [285]. The final discretization consisted of 35,909 nodes, and 141,497 elements (Fig. 6.3).

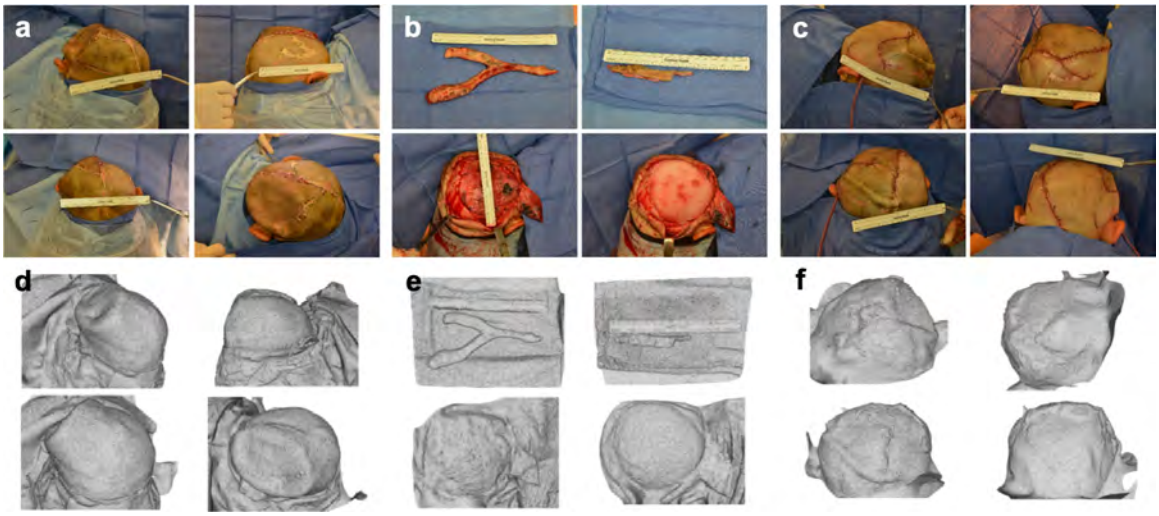

Fig. 6.2.: Patient-specific three-dimensional (3D) geometry generation: For each model, photographs are taken from multiple angles (**a**,**b**,**c**), then converted to 3D geometries using Multi-view stereo (**d**,**e**,**f**). Models are generated at different time points: immediately after expander removal (**a**,**d**), after scar excision and cranioplasty inset (**b**,**e**), after skin closure (**c**,**f**).

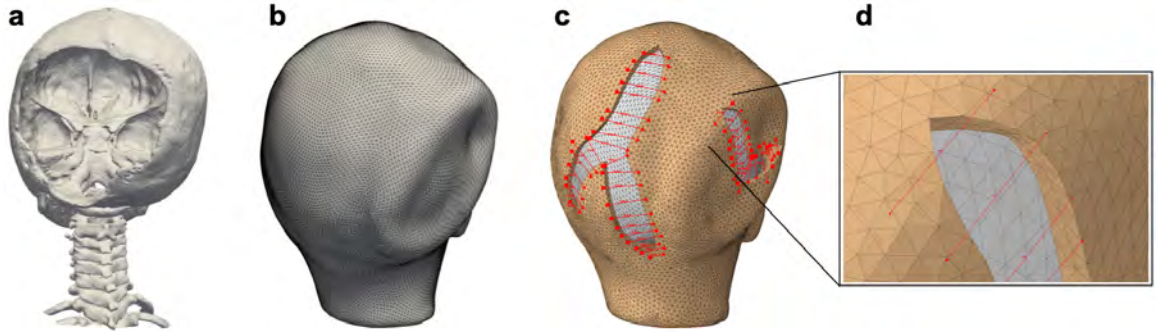

Fig. 6.3.: CT scan data was used to obtain the geometry of the skull (**a**) and to complement the skin geometry obtained with multi-view stereo (**b**). The skull defect was corrected and a single geometry accounting for both skull and implant was placed beneath the scalp, and the two large defects were removed from the skin model according to the surgical procedure (**c**). The defects were sutured closed by assigning linear connectors between pairs of nodes (**d**).

6.2.3 Constitutive model

Skin is a thin transversely anisotropic material that can be described as hyperelastic and nearly incompressible [118]. Let points $\mathbf{X} \in \Omega_0$ constitute the reference

body and points $\mathbf{x}(\mathbf{X}) \in \Omega$ the current state. The collagen fiber network in skin has a preferred orientation $\mathbf{e}_0$ in the reference configuration. The deformation gradient $\mathbf{F} = \partial\mathbf{x}/\partial\mathbf{X}$ for nearly incompressible materials is decomposed into isochoric $\widehat{\mathbf{F}}$, and volumetric $\mathbf{F}^{\text{vol}}$ parts

$$\mathbf{F} = \widehat{\mathbf{F}}\mathbf{F}^{\text{vol}}, \tag{6.1}$$

with $\widehat{\mathbf{F}} = J^{-1/3}\mathbf{F}$, $\mathbf{F}^{\text{vol}} = J^{1/3}\mathbf{I}$, $\mathbf{I}$ the second-order identity tensor, and $J = \det(\mathbf{F})$ the volume change. The right Cauchy-Green deformation tensor $\mathbf{C}$ is related to the isochoric component $\widehat{\mathbf{C}}$,

$$\widehat{\mathbf{C}} = J^{-2/3}\mathbf{C} = \widehat{\mathbf{F}}^{\top}\widehat{\mathbf{F}}\,. \tag{6.2}$$

We use the strain energy function proposed by Gasser-Ogden-Holzapfel (GOH) [57] which is a validated model for collagenous tissues including skin [118],

$$\psi = \widehat{\psi} + \psi^{\text{vol}} + \psi^{\text{aniso}}, \tag{6.3}$$

where $\widehat{\psi}$, ψ^{vol}, and ψ^{aniso} are the isochoric, volumetric, and anisotropic contributions respectively. The isochoric term is of neo-Hookean type

$$\widehat{\psi} = \frac{\mu}{2}(\overline{I}_1 - 3), \tag{6.4}$$

where μ is the shear modulus and $\overline{I}_1 = \widehat{\mathbf{C}} : \mathbf{I}$. The volumetric term is

$$\psi^{\text{vol}} = \frac{K}{2}\left(\frac{J^2 - 1}{2} - \ln(J)\right), \tag{6.5}$$

where K is the bulk modulus. The anisotropic term accounts for the fiber contribution,

$$\psi^{\text{aniso}} = \frac{k_1}{2k_2}\left(\exp(k_2\langle\overline{E}\rangle^2) - 1\right), \tag{6.6}$$

where k_1 describes the tensile response, k_2 is dimensionless and expresses nonlinearity of the fiber response, and κ is the parameter that directly relates to dispersion in the

fiber orientation distribution. For example, $\kappa = 1/3$ indicates isotropy, while $\kappa = 0$ means perfectly aligned fibers (fully anisotropic).

$\overline{E}$ encodes the degree of anisotropy

$$\overline{E} \equiv \kappa(\bar{I}_1 - 3) + (1 - 3\kappa)(\bar{I}_4 - 1), \tag{6.7}$$

where the fiber direction $\mathbf{a}_0$ defines the fourth pseudo-invariant,

$$\bar{I}_4 = \mathbf{a}_0^\top \widehat{\mathbf{C}} \mathbf{a}_0 \,. \tag{6.8}$$

Since fibers can only sustain tension, the Macauley bracket $\langle \overline{E} \rangle = (|\overline{E}| + \overline{E})/2$, was used in Eq. (6.6). The second Piola-Kirchhoff stress tensor follows directly from the strain energy,

$$\mathbf{S} = 2\frac{\partial \psi}{\partial \mathbf{C}} = \widehat{\mathbf{S}} + \mathbf{S}^{\text{vol}} + \mathbf{S}^{\text{aniso}} \,. \tag{6.9}$$

Each term in Eq. 6.9 can be expanded,

$$\begin{aligned}
\widehat{\mathbf{S}} \quad &= 2\frac{\partial \widehat{\psi}}{\partial \mathbf{C}} \quad &&= \mu \left(J^{-\frac{2}{3}} \mathbf{I} - \frac{1}{3} \bar{I}_1 \mathbf{C}^{-1} \right) \\
\mathbf{S}^{\text{vol}} \quad &= 2\frac{\partial \psi^{\text{vol}}}{\partial \mathbf{C}} \quad &&= \frac{K}{2}(J^2 - 1)\mathbf{C}^{-1} \\
\widehat{\mathbf{S}}^{\text{aniso}} \quad &= 2\frac{\partial \psi^{\text{aniso}}}{\partial \mathbf{C}} \quad &&= 2k_1 \exp(k_2 \langle \overline{E} \rangle^2) \langle \overline{E} \rangle \left(\kappa \frac{\partial \bar{I}_1}{\partial \mathbf{C}} + (1 - 3\kappa) \frac{\partial \bar{I}_4}{\partial \mathbf{C}} \right) .
\end{aligned} \tag{6.10}$$

Finally, the expression for the Cauchy stress tensor can be obtained by the push-forward of $\mathbf{S}$,

$$\boldsymbol{\sigma} = \frac{1}{J} \mathbf{F} \mathbf{S} \mathbf{F}^\top \,. \tag{6.11}$$

Parameters matching the specific patient demographic were not available and we used parameters corresponding to adult female human skin [60]: $\mu = 4.773$ kPa, $K = 2$ MPa, $k_1 = 4.770$ kPa, $k_2 = 161.862$, and $\kappa = 0.236$. To approximate the fiber orientation we employed the Cox lines [286].

6.2.4 Finite element model of reconstructive surgery

Simulations were run using Abaqus Standard (Dassault Systems, Waltham, MA). The GOH constitutive model is available in this implicit nonlinear finite element package. The model consisted of 107,727 degrees of freedom. Contact between the scalp and calvarium was considered frictionless. Stitches were modeled as linear constraints between pairs of nodes (Fig. 6.3). To match the clinical setting as closely as possible, mid-thickness nodes in the interior of the domain but close to the edge of the flaps were selected. The distance between pairs of stitched nodes was gradually decreased to close the flaps. Skin-skin contact along the suture lines was considered frictionless. The suturing pattern was assigned manually based on the postoperative photographs and models (see Figs. 6.1 and 6.2). Suturing in the simulation was done sequentially. We were not interested in the stress history during scalp closure but only in the final stress contours. MVS models throughout the closure process were not captured for the same reason. The displacement of the connectors was assigned based on the distance between the skin edges in the reference configuration.

We expect that the stress distribution will be sensitive to the fiber dispersion κ. Thus, we performed two more simulations in addition to using the baseline parameters: $\kappa = 0$ to capture perfectly aligned fibers, and $\kappa = 0.333$ for the isotropic case.

6.3 Results

Fig. 6.4 shows the current configuration for the skin for the three values of κ. The geometry predicted with the model matches the 3-day follow up photograph (see Fig. 6.1). The resulting von Mises stress contours and fiber distribution are shown on the current configuration (Fig. 6.4). The stress patterns are similar for the three simulations. Five dominant high stress areas are highlighted, and the average stress in these regions are reported in Table 6.1. Kinks or sharp corners, such as in regions A, C, and D, experience distortions and high stress values. In the clinical setting, these

corners can lead to standing cones resulting from differential tissue advancement and stretch in the middle of the closure, reflected as tissue folding at the corners. We expect that the high stress due to the discretization and the nodal constraints at these locations should not have any significant effect on the planning efficacy of the model as we know clinically that these points are not a concern for the surgeon. In contrast, distal ends of flaps, such as B and E, are the primary concern [287].

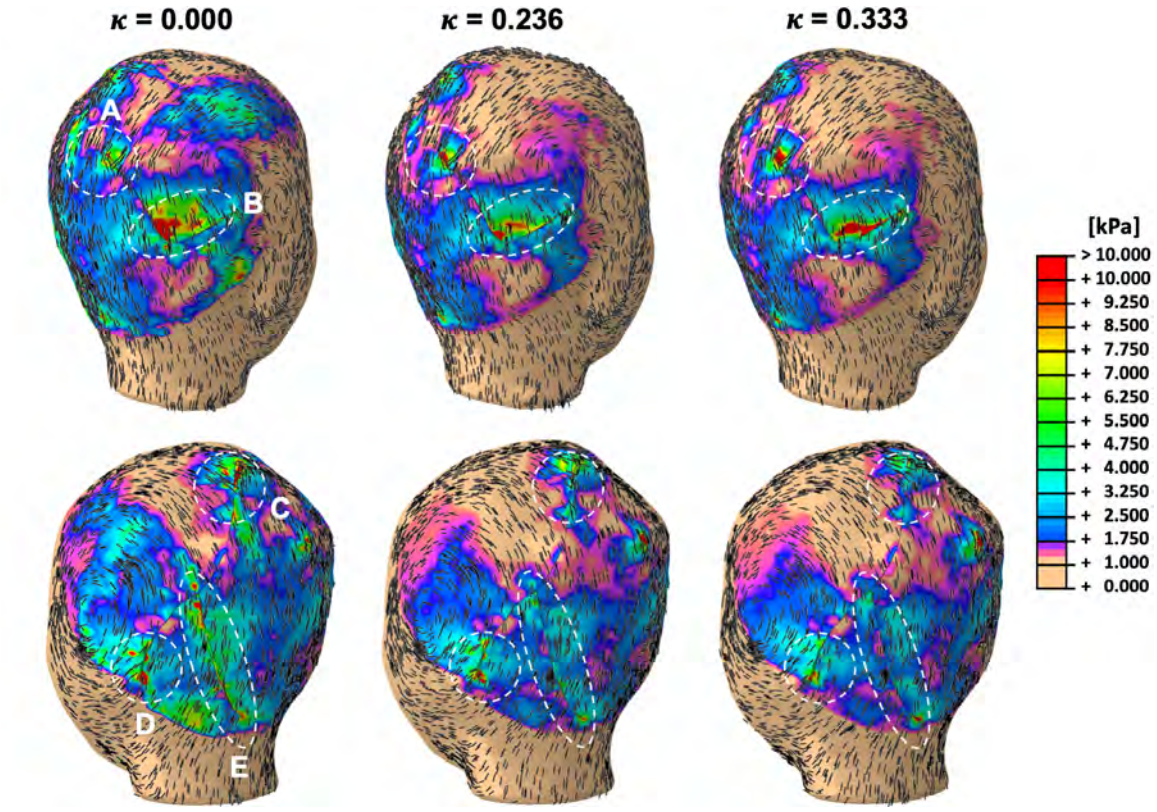

Fig. 6.4.: Current configuration and von Mises stress distribution resulting from the finite element simulation for three values of the fiber dispersion, κ. The fiber orientation on the scalp is also visualized. The anisotropic case κ of 0.000 leads to the highest stress at the distal ends of the flaps B and E (left). κ of 0.236 corresponds to the parameter value taken from the literature (middle). The perfectly isotropic condition is done by setting κ to be 0.333 (right).

Table 6.1.: Average nodal stress for regions shown in Fig. 6.4

	A (kPa)	B (kPa)	C (kPa)	D (kPa)	E (kPa)
$\kappa = 0.000$	2.924	4.729	2.979	4.335	3.927
$\kappa = 0.236$	2.837	4.117	2.203	3.939	2.563
$\kappa = 0.333$	4.724	4.207	1.853	3.247	2.331
Volume (mm^3)	2618	4072	8184	2882	7409

6.4 Discussion

Here we demonstrate the finite element simulation of a complex procedure on a patient-specific geometry. Our approach follows from our previous work on the mechanical analysis of common flap designs [14]. There is a general consensus that high stress can result in significant complications [3]. A method to measure skin tension in the operating room has been recently proposed but requires specialized equipment, provides only force between two points, and is limited to small defects [6, 8]. Computational simulations are an alternative but have been limited to generic geometries [17, 19, 287]. In order to make finite element simulations fully relevant for the clinical context, patient-specific models are needed. We address this gap with MVS due to its accuracy, flexibility and affordability [288]. An alternative that we plan to use in the future are new, portable 3D stereo systems [114].

Human skin is anisotropic and incorporating a fiber distribution in the model is critical. Clinically, skin tension lines are used to design flaps. We used Cox lines, but considered an unknown dispersion parameter κ to capture the sensitivity of the stress to the degree of anisotropy. The highest stresses are achieved if skin is fully anisotropic ($\kappa = 0$). This situation leads to the worst-case scenario and could be used as an upper bound.

The study considered here showcases the difficulty in anticipating stress contours in a complex patient geometry, especially when the fiber direction is considered. The high tissue stresses predicted along one of the limbs of the Y-shaped suture line up to the T-junction (Fig. 6.4, area E), did manifest clinically as partial flap tip necrosis

and delayed healing in the follow-up visit (Fig. 6.1). Application of our method to multiple tissue rearrangement cases is needed to validate the model completely; nonetheless, our results are encouraging since they are aligned with clinical findings and surgical judgment.

This study is not without its limitations. The magnitude of the stress profile is sensitive to the other material parameters in addition to κ. We employed parameters for human skin reported in the literature [23]. However, material properties of skin vary with age, gender, anatomical location, and from patient to patient [182]. Recently, novel devices have been proposed to test skin noninvasively in order to estimate the material parameters [8, 27, 289, 290]. These technologies will facilitate measurement of patient-specific skin parameters in the future to improve the accuracy of the results.

6.5 Conclusion

We propose a method to anticipate regions at risk of wound healing complications based on pre and intraoperative 3D patient-specific models generated with MVS. Nonlinear finite element simulations taking skin anisotropy into account can be performed on this individualized settings to predict the stress distribution on the skin resulting from reconstructive surgery. A key feature of the proposed approach is that it only requires a standard digital camera to generate patient-specific 3D models, making it immediately applicable to clinical settings. Future refinement of this method by incorporating patient-specific skin parameters will yield a robust instrument for preoperative flap design simulation to yield minimal tension at closure and minimize complications.

7. RECONSTRUCTION OF THE SCALP: THE MECHANICAL SIGNATURE OF THE ROTATION FLAP

Abstract: Excessive tension near a wound or sutured region can delay wound healing or trigger complications. Measuring tension in the operating room is challenging, instead, non-invasive methods to improve surgical planning are needed. Rotation flaps are common to correct cleft palate. Multi-view stereo (MVS) allows creation of patient-specific three-dimensional (3D) geometries based on a set of photographs taken with any common digital camera. The patient-specific 3D geometry is imported into a finite element analysis platform to perform a virtual procedure according to the surgeons plan. The simulation predicts the final geometry after surgery and the mechanical stress contours over the entire skin surface. Uncertainty in the parameters can be incorporated, for instance, degree of tissue anisotropy. Two melanoma resection cases are presented. Preoperative, patient-specific 3D geometries from MVS are used to perform virtual rotation flap surgeries in both cases. The resulting mechanical tension distribution shows a consistent spatial pattern in both predictions. The resulting tension is strongly dependent on the degree and direction of anisotropy in the tissue. The predicted geometry from the virtual surgery shows good agreement with the geometry captured at the end of the actual procedure performed in these patients. Mechanical stress profiles over patient-specific geometries can be achieved through personalized finite element simulations. Patient-specific skin properties are still a challenge to completely calibrate and validate the models, yet, spatial patterns of tension are strongly dependent on the flap geometry and can still guide decision making. Furthermore, noninvasive mechanical testing of skin is becoming increasingly feasible, providing confidence that virtual surgery tools in the clinical setting can become a reality in the near future.

7.1 Motivation

Over 34 million surgeries are performed in the US annually, each one requiring optimal wound healing [291, 292]. Tissue tension, also termed mechanical stress, is one of the factors contributing to wound complications costing more than four billion dollars annually [4]. Animal and *in vitro* studies have demonstrated that excessive stress leads to hypertrophic scarring, wound dehiscence, and tissue necrosis [35, 36]. However, we are still unable to quantitatively predict skin stress and deformation during wound closure in routine clinical practice [8]. Surgeons rely on tactile sensation and experience to estimate acceptable tension and soft tissue deformation at closure. Anticipating stress distribution of skin tissues based on preoperative information can thus help optimize individualized treatment plans.

The head and neck region is one of the most prevalent areas for reconstructive procedures. For instance, skin cancer is the most common cancer, and 80% of basal cell carcinomas are in the head and neck [293]. The first option of treatment for skin cancer is surgical excision, which leaves a skin defect that requires reconstruction with local flaps, tissue expansion, free flaps, or skin grafting [294,295]. Recently, novel devices aimed at reducing mechanical stress on wounds have shown decreased scarring in humans [4]. Success with stress shielding devices for simple wounds underscores the importance of minimizing stress for optimal healing. However, these devices have been used for simple, uniform excision patterns in which application of the device and reduction in stress is straightforward. Planning in the head and neck region is challenging for large skin lesions because of the anatomical constraints, complex three-dimensional (3D) geometry, and unique surgical plan and skin mechanics for each patient. Hence, measuring stress contours and the overall healing result is currently impossible in the head and neck. To bridge this gap, fortunately, computational tools and simulation of virtual surgeries have been proposed as a powerful means to anticipate stress profiles over realistic skin geometries [14, 15].

Multiple aspects of craniofacial surgery also require understanding of soft tissue changes under uncertain conditions, such as complex craniofacial cases in which scalp reconstruction is essential for coverage of hardware, implants, and/or bone graft. Facial contour change with orthognathic surgery could also benefit from predictive modeling of soft tissue changes following skeletal movement. A number of predictive methods using past experience and simple overlay techniques have been described to estimate these changes [296–299], yet none of them represent a robust model of soft tissue deformation under stress.

We present two cases of skin cancer reconstruction on the scalp for which rotation flaps were eventually used as advanced proof of concept in utilizing our methodology in modeling soft tissue stresses. Our methodology relies on obtaining 3D patient-specific geometries using multi-view stereo (MVS) [115, 288], a flexible and powerful algorithm from computer vision that relies on feature matching across photographs taken from different angles. A commercial finite element (FE) analysis framework is used to perform the virtual procedure [99]. To investigate the effect of anisotropy, a fiber distribution field according to Cox lines is imposed [286]. We also investigate the flap design in idealized geometries in order to isolate the effect of individual flap parameters on the resulting stress distribution.

7.2 Methods

7.2.1 Clinical cases of melanoma resection in the scalp

Two patients undergoing melanoma resection in the scalp volunteered to participate in this IRB-approved study. Patient 1 was a 73-year-old adult male, and patient 2 was a 62-year-old adult male. Both patients were scheduled for surgical removal of melanoma lesions in the scalp. On the day of surgery, photographs of the patients geometry were acquired preoperatively for 3D geometry reconstruction. A standard digital camera was used to collect approximately 30 photographs of the patients head

and neck region from different angles, making sure that the patients remained static during photograph acquisition.

Intraoperatively, the melanoma lesions were excised together with surrounding tissue. For patient 1, two regions were excised, one in the frontal scalp measuring approximately 4.8 cm in diameter, and a second region in the posterior scalp with a diameter of 2.5 cm. For patient 2, a single lesion was excised, 3.6 cm in diameter, in the posterior scalp. Rotation flaps were performed in both scenarios to close the wounds.

In both cases the amount of skin removed prevented primarily closure of the wounds. In patient 1, the frontal defect was too large to attempt any tissue rearrangement strategy, and this wound was instead treated with a skin graft. The rotation flap in the posterior defect was closed without inducing unacceptably high tension for patient 1. In patient 2, the rotation flap was not fully sutured closed to prevent excessive tension in the skin.

7.2.2 Patient-specific computational models of tissue rearrangement

Preoperative photographs were processed with MVS to produce patient-specific geometries (Fig. 7.1). MVS identifies common points in photographs taken from different angles and uses these correspondences to solve for the camera positions and orientations [300]. Then, an optimization routine expands the set of feature points to recreate a detailed 3D surface of the scene [282].

The preoperative models were used to perform virtual procedures according to the treatment plan of the patients (Fig. 7.2). Namely, in patient 1, excision of the two lesions and the surrounding tissue was executed, and the incision pattern corresponding to a rotation flap for the posterior scalp defect was also created. For patient 2, a circular region in the posterior scalp was removed and a rotation flap designed.

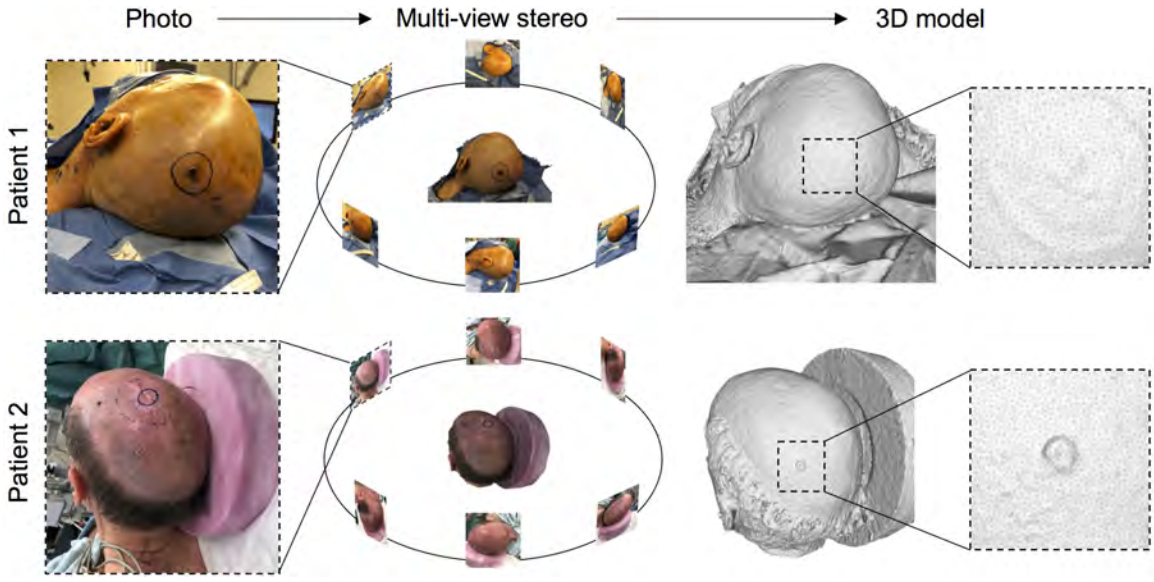

Fig. 7.1.: Preoperative, patient-specific 3D geometry reconstruction of two clinical cases of melanoma resection: 73-year-old adult male (patient 1) and 62-year-old adult male (patient 2) were photographed from different angles and multi-view stereo was used to extract the preoperative 3D scalp geometry.

Volume models were created from the surfaces by considering a thickness of 3 and 3.3 mm for patients 1 and 2 respectively. The final discretization of the model corresponding to patient 1 consisted of $35,466$ tetrahedral elements and $12,278$ nodes. The model for patient 2 was made of $75,282$ elements and $25,394$ nodes. In addition to modeling the skin, a skull geometry was generated to constraint the deformation and motion of the skin during the simulation. The 3D skull geometry was considered as a rigid body, i.e., no deformation of the bone was allowed.

7.2.3 Finite element analysis

Skin, like all soft connective tissues in the human body, shows nonlinear and anisotropic mechanical behavior dominated by the preferred orientation of collagen fibers in the dermis [45, 301, 302]. We incorporate this response into our model using the material model proposed by Gasser, Ogden and Holzapfel (GOH) [59, 118]. The

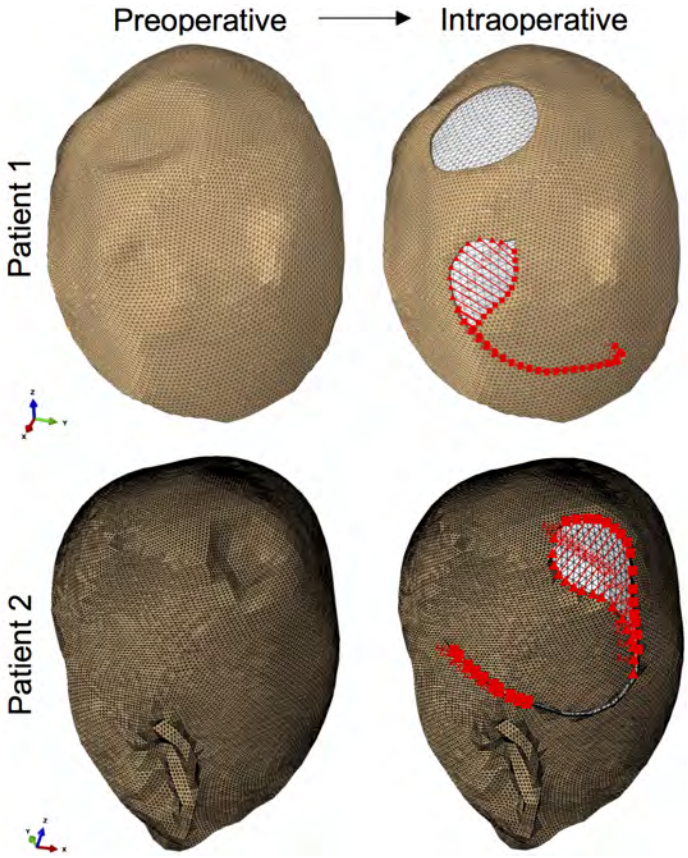

Fig. 7.2.: Preoperative patient-specific models were processed to virtually execute the treatment plan. Patient 1 underwent resection of two skin lesions, one posterior and one anterior. A posterior defect was removed in the scalp of patient 2. Sutures are imposed in a finite element framework to closely recreate the clinical setting.

FE simulations were run using the commercial software package Abaqus Standard (Dassault Systems, Waltham, MA).

Mechanical properties of skin change with age, gender, anatomical location, and even from one patient to another. Based on measurements of skin mechanics available in the literature, and considering the age and gender of both patients in this study, parameters for a 44-year-old male from the literature were assigned [23, 51, 60]. Unfortunately, the experimental datasets of skin mechanics *in vivo* are still limited and patient specific parameters were unavailable. Tissue anisotropy was also taken into consideration. Similarly to the choice of material properties, the fiber orientation was

assigned based on previous work which showed that Cox lines are a suitable indicator of anisotropy in the scalp [286].

The FE simulations solves the mechanical equilibrium problem corresponding to the manipulation of the tissue and closing of the defect. To closely match the clinical procedure, sutures are imposed by constraining the nodes on the opposite edges of the flap (red lines in Fig. 7.2). During the virtual tissue rearrangement process, the skin is allowed to slide over the skull geometry assuming frictionless contact.

7.2.4 Rotation flap design optimization

In the two patient-specific scenarios, the design of the flap was based on the preoperative plan. However, one of the advantages of computer models is the ability to simulate alternative scenarios. We created a general simulation of a rotation flap with the parameters shown in Fig. 7.3). We then investigated the sensitivity of the predicted tissue tension by varying the parameters of the flap design. Namely, we considered three parameters: the angle of rotation ϕ, the orientation of the flap with respect to the skin tension lines θ, and the normalized length of the back cut c/r.

7.3 Results

7.3.1 Patient-specific models

Fig. 7.4 shows the comparison between the postoperative result obtained with the virtual model, and the real postoperative geometry. The contour plots on the FE model represent the mechanical stress distribution on the skin. In particular, here we show the maximum principal stress distribution, which is a metric of stress typically used in engineering design.

The geometries predicted in Fig. 7.4 align with the postoperative photographs. For patient 1, the stress profile is approximately 30 kPa near the distal end. Only a few points exceeded stress values of 100 kPa. There is also a small stress concentration

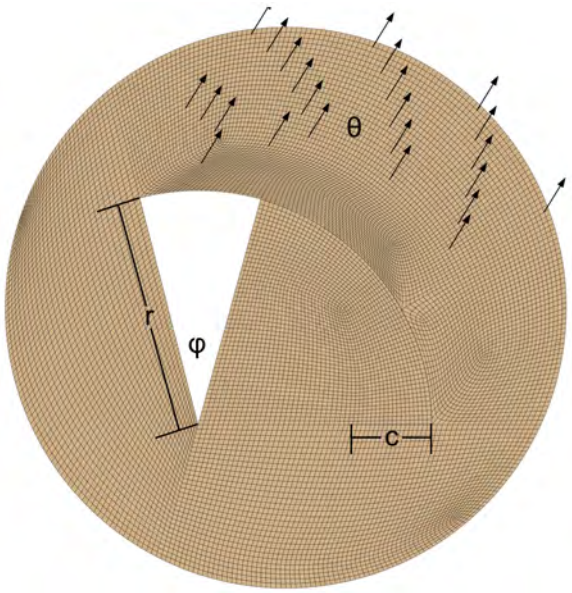

Fig. 7.3.: General rotation flap design parameterized by three variables. Rotation angle ϕ, orientation with respect to skin tension lines θ, and relative back cut length c/r

at the base of the flap. The simulation for patient 2 shows higher stresses compared to patient 1. For patient 2, the distal end of the flap in patient 2 show stresses around 90 kPa, with a few points reaching 180 kPa. The reason for this difference can be attributed to the anatomical constraints present in the second case. The rotation flap for patient 2 was designed close to the left ear. As a consequence, skin was stretched more in order to close the flap of patient 2, inducing larger stress, and preventing closure along the entire flap contour, just as it occurred during the actual procedure. For comparison, previous work on a porcine model established that stresses of approximately 200 kPa led to hypertrophic scarring [4]. No similar data exists for human wounds.

Despite differences in defect size and patient geometry, the rotation flap in the patient geometries induced high stress at the distal end. In the second patient, this tension extended to the proximal end of the flap, forming a continuous band of high stress. In patient 1, on the other hand, while there was a stress concentration at the base of the flap, there was not a band of high tension across the entire flap.

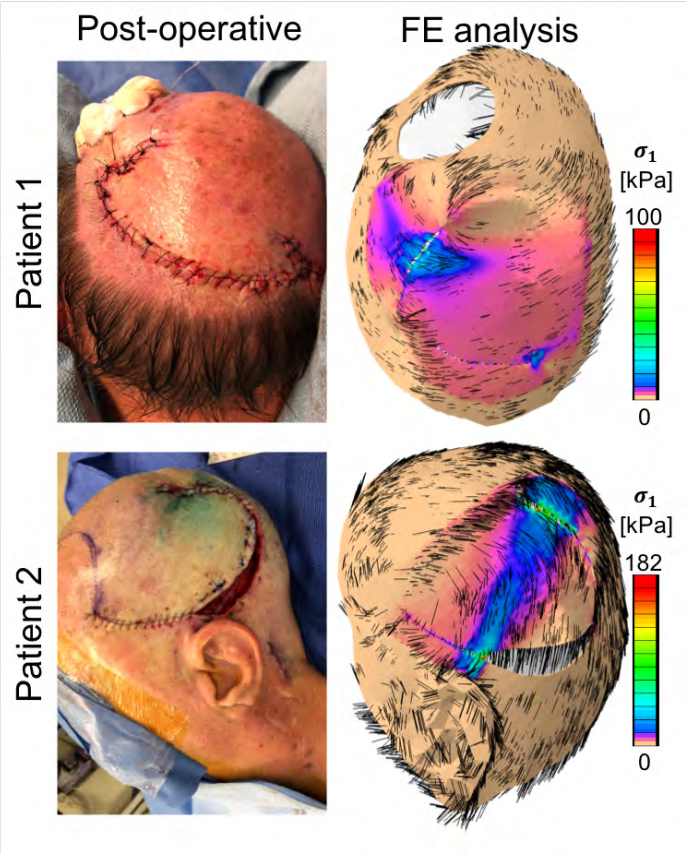

Fig. 7.4.: Postoperative geometries for the two clinical cases presented in this study. The left column shows photographs taken immediately after the tissue rearrangement procedure. The results of the finite element simulation predict final geometries consistent with the real procedure as well as associated mechanical stress contours. For patient 1, a stress concentration occurs at the distal end, with maximum principal stress averaging 30 kPa. For patient 2, a band of high stress connects the proximal and distal regions.

7.3.2 Generic rotation flap model

The general rotation flap model depicted in Fig. 7.3 is used to evaluate the influence of individual flap parameters on the mechanical stress distribution. For consistency, we refer to the edge adjacent to the back cut (c) as the proximal edge of the flap, and the edge towards the defect into which the flap is to be rotated (r) as the distal edge of the flap (see Fig. 7.3). Fig. 7.5 shows three simulations of the general rotation flap for three flap orientations $\theta = 0°, 45°, 135°$ with respect to

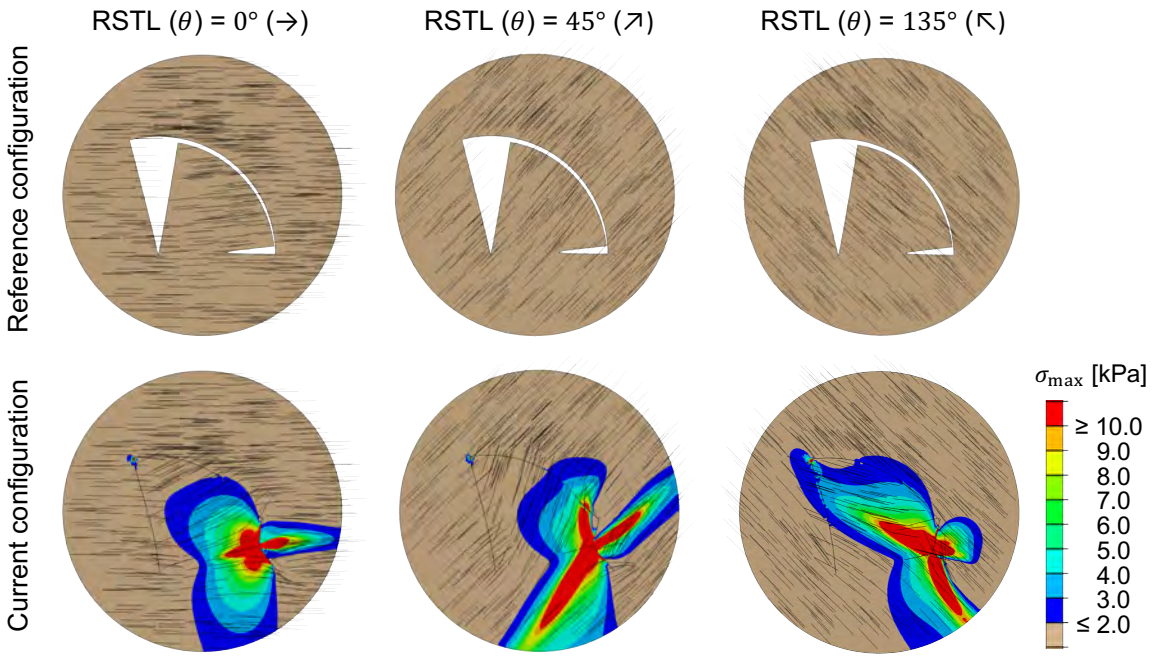

Fig. 7.5.: General rotation flap simulations show that flap orientation with respect to relaxed skin tension lines (anisotropy direction) is the most important parameter. Depending on flap orientation there is either no stress at the distal end, or, in the worst-case scenario, a stress band can extend from the proximal to the distal end.

the anisotropy direction. Fig. 7.6 shows the variation in stress when the angle of rotation is $\phi = 30°$, for three different relative back cut lengths and three different fiber orientations. Fig. 7.7 shows nine simulations with the angle of rotation $\phi = 45°$, varying the other parameters. Finally, Fig. 7.8 shows nine more simulations with the angle of rotation $\phi = 60°$. From this array of simulations, it is clear that the fiber angle is the most sensitive parameter. Accordingly, the variation in the stress profile for the different fiber angle is reported as seen in Fig. 7.5.

Based on our simulations, we identified the orientation of the flap with respect to the skin tension lines to be the most important choice during flap design. In all cases, we see a stress concentration at the base, with a band of high stress aligned with the fiber orientation. These results suggest that, in an ideal setting, the rotation flap should not lead to high stress at the distal end. Instead, higher stresses are expected at the base of the flap. However, if the skin tension lines extend across the flap,

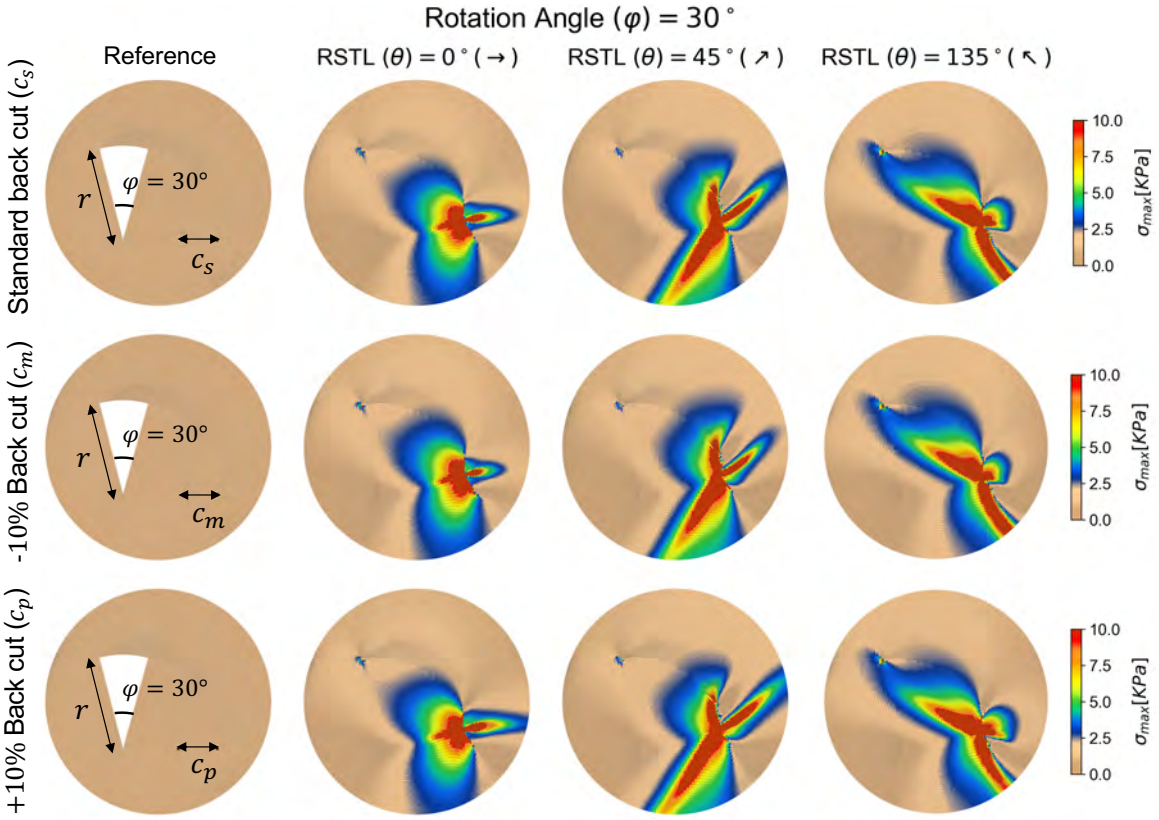

Fig. 7.6.: Variation in stress profile for the angle of rotation $\phi = 30°$ and changing the other two parameters, the relative back cut length c/r and the fiber orientation θ.

from the distal to the proximal end, a band of high stress can connect the two ends. Comparison between the ideal flap design and the patient-specific simulations also underscores the importance of anatomical constraints in the patient cases. Based on the simulations shown in Figs. 7.5 to 7.8, orientation the flap such that the fibers are horizontal with respect to the rotation, $\theta = 0°$, and designing the flap with the smallest angle of rotation, $\phi = 30°$ in this case, leads to the smallest tension.

7.4 Discussion

The objective of this study was to create patient-specific FE models to anticipate mechanical stress distributions resulting from tissue rearrangement surgeries. The

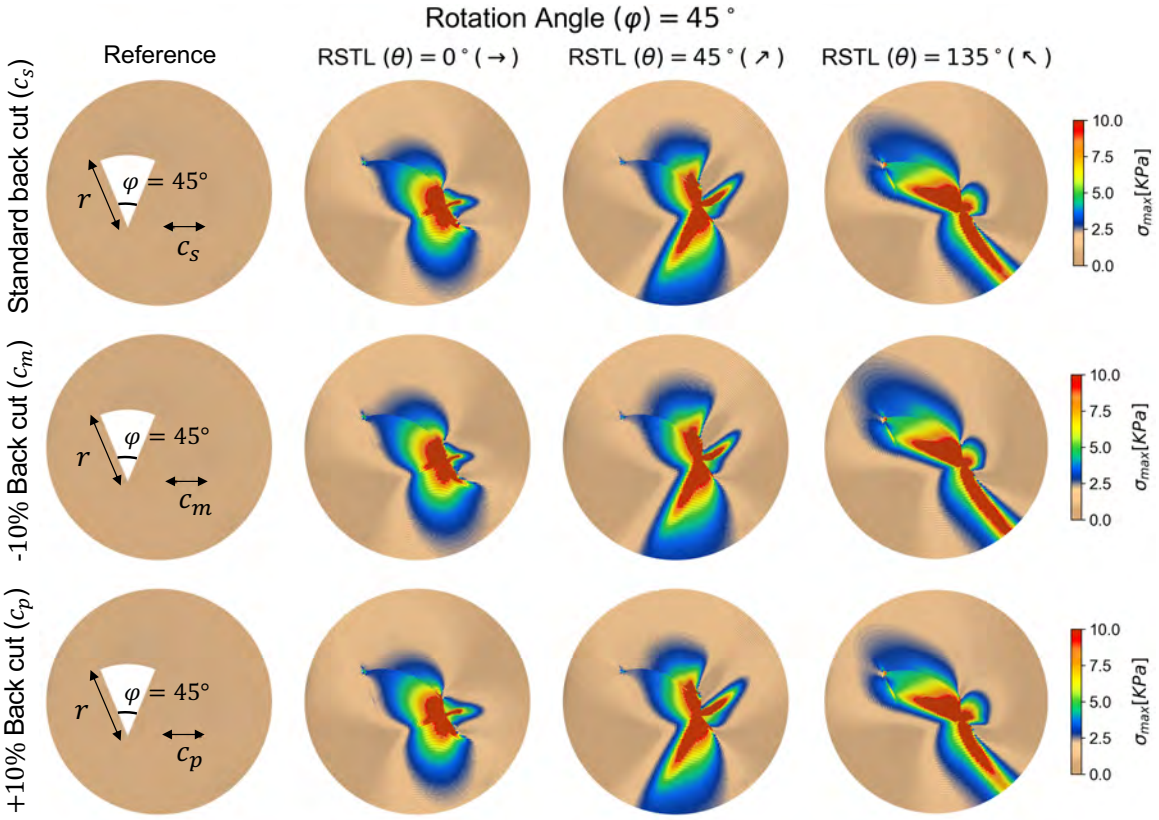

Fig. 7.7.: Variation in stress profile for the angle of rotation $\phi = 45°$ and changing the other two parameters, the relative back cut length c/r and the fiber orientation θ.

models of two skin cancer patients were created based on the preoperative geometry captured via MVS. This computer vision technology relies only on a set of photographs taken with any standard digital camera. In the cases presented here, a smartphone camera was used. We have previously shown that MVS reconstruction induces small errors, less than 10% [196], and with an average of 2% [116]. Therefore, MVS offers a flexible and easy-to-use methodology to create accurate preoperative models of reconstructive surgery [99]. Alternatives include 3D cameras, which are becoming common in clinical practice [97, 114].

The simulation of the tissue rearrangement step requires the definition of the skins material behavior. The lack of patient-specific material properties is certainly one limitation of the present study. The parameters used here were based on re-

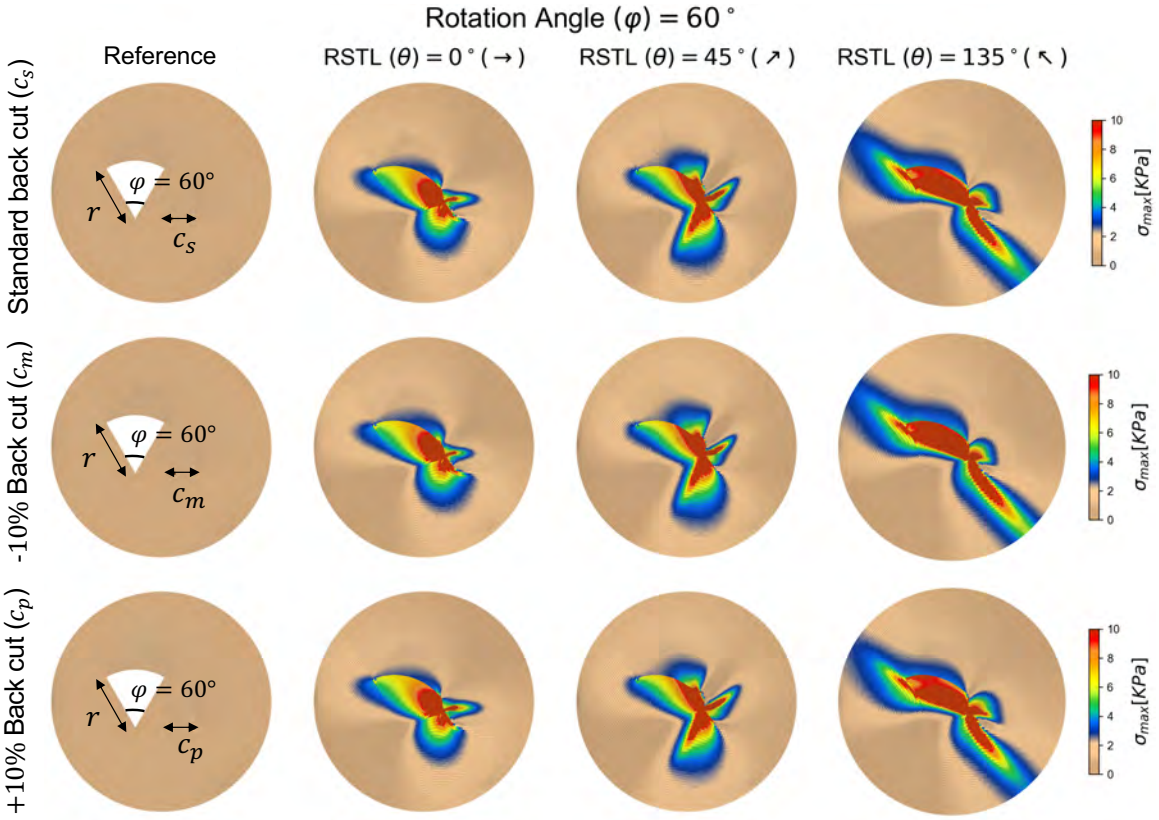

Fig. 7.8.: Variation in stress profile for the angle of rotation $\phi = 60°$ and changing the other two parameters, the relative back cut length c/r and the fiber orientation θ.

ports of skin mechanical properties available in the literature [23, 51, 60]. However, material parameters are expected to vary with age, gender, and anatomical location [184]. Therefore, measuring individual properties is essential to create truly patient-specific models. Fortunately, new technologies are being developed, which enable noninvasive measurement of skin mechanics *in vivo* [27, 303]. Even in the absence of patient-specific geometries, the predicted geometry from our simulations matched qualitatively the postoperative photographs. Our simulations showed that, due to the anatomical constraints in the second scenario, higher stresses were expected for patient 2 compared to patient 1. In fact, the rotation flap for patient 2 could not be fully sutured due to concerns that the tension on the skin was too high.

Furthermore, the values of stress we computed align with what has been reported for porcine models of excisional wounds closed under tension [3, 4].

The most interesting finding from this study is the critical effect of anisotropy and anatomical constraints in the resulting stress pattern. We created simulations of a general rotation flap design and varied three parameters. We found that, in the ideal case, the rotation flap should not lead to high stress at the distal edge when the angle of rotation is small and the flap is oriented such that skin tension lines are horizontal with respect to the direction of rotation. Conversely, we saw that if the skin tension lines are aligned obliquely, a band of high stress can extend over the flap, towards the distal edge, potentially leading to complications. The ideal rotation flap simulations showcase the use of FE to optimize flap designs, but, at the same time, comparison with patient-specific cases revealed the importance of individual anatomical constraints. This information is essential to optimize outcomes of flap design in areas where high tension is anticipated, which is often observed in scalp reconstruction. Although techniques such as galeal scoring and wide undermining can also decrease final tissue tension, orientation of the flap relative to tissue tension lines is a key parameter which is often overlooked during flap design. Table expansion can be utilized to further stretch the flap, and this technique could be incorporated through preoperative FE analysis of flap design. Pre-planning flap orientation with the aid of FE analysis can optimize the final reconstruction and extend the outcomes of traditional means for relaxing tissues during flap transfer.

These two cases of reconstruction after cancer resection demonstrate the workflow in the simplest setting, i.e., one layer of skin (ignoring galea) over a non-deformable surface (the calvarium). By incorporating the multiple planes of the face and their respective tissue qualities, we hope to apply these concepts to modeling soft tissue stress as applied to all areas of head and neck reconstruction. Reliable scalp reconstruction is essential for coverage of hardware, implants, and/or bone graft in craniofacial surgery, and by facilitating preoperative planning for scalp advancement, significant complications could be avoided. Facial contour change with orthognathic surgery is

often evaluated in retrospect, and predictive modeling of soft tissue changes following skeletal movement could greatly improve patient expectation and outcomes.

7.5 Conclusion

Mechanical stress profiles over patient-specific geometries can be achieved through personalized finite element simulations. Furthermore, simulations of defects treated with rotation flaps show that smaller rotation angles and orienting the flap such that the skin tension lines are horizontal with respect to the flap leads to the lowest tension. Such applications of finite element models could significantly improve outcomes of scalp coverage over implants and/or hardware, and prediction of soft tissue contour following orthognathic surgery. Our analysis shows that flap orientation with respect to skin tension lines and anatomical constraints are crucial to minimize excessive tension.

8. UNCERTAINTY PROPAGATION THROUGH VIRTUAL SURGERY SIMULATION

Abstract: Excessive mechanical stress following surgery can lead to delayed healing, hypertrophic scars, and even skin necrosis. Measuring stress directly in the operating room over large skin areas is not feasible and nonlinear finite element simulations have become an appealing alternative to predict stress contours on arbitrary geometries. However, this approach has been limited to generic cases, when in reality each patient geometry and procedure is unique, and material properties change from one person to another. In this manuscript, we use multi-view stereo to capture the patient-specific geometry of a 7-year-old female undergoing cranioplasty and complex tissue rearrangement. The geometry is used to setup a nonlinear finite element simulation of the reconstructive procedure. A key contribution of this work is incorporation of material behavior uncertainty. The finite element simulation is computationally expensive and it is not suitable for uncertainty propagation which would require many such simulations. Instead, we run only a few expensive simulations in order to build a surrogate model by Gaussian process regression of the principal components of the stress fields computed with these few samples. The inexpensive surrogate is then used to compute the statistics of the stress distribution in this patient-specific scenario.

8.1 Motivation

Complications such as delayed healing, wound dehiscence, and hypertrophic scarring are associated with excessive mechanical stress near a wound [2,3]. Unfortunately, measurements of stress in the operating room are not yet practically possible outside of very particular scenarios [6]. Instead, surgeons have to rely on their manual estimation to anticipate regions at risk of complications. However, tissue rearrangement

procedures often lead to nonintuitive stress distributions, for example, following tissue expansion [287, 304]. Without predictive tools, wound healing complications and suboptimal healing outcomes will continue to be a concern.

To overcome this challenge, finite element (FE) simulations of reconstructive surgery have started to gain popularity in recent years [17, 287, 305]. In our previous work, we have advanced this field of application by considering three-dimensional geometries and nonlinear material and geometric response, but an important limitation has been the use of a single set of material properties on ideal scenarios. In reality, each patient has a unique geometry and requires an individualized procedure, and skin mechanical properties vary considerably with age, gender, and from one person to another [1, 182, 306].

In this manuscript, we use multi-view stereo (MVS) to capture the patient-specific geometry of a 7-year-old female undergoing a cranioplasty procedure with complex tissue rearrangement following skin expansion. This individualized geometry is one of the ingredients for our nonlinear FE model. The other requirement is the constitutive law to describe skins mechanical behavior. Skin is a collagenous tissue, and the strain energy originally proposed by Gasser-Ogden-Holzapfel (GOH) [57] to describe arteries has been determined appropriate for skin tissues as well [60, 180]. However, patient-specific material response is often not available. To rigorously assess the effect of material behavior uncertainty on the expected stress distribution, one approach is to run a large number of simulations to compute the relevant statistics. The patient-specific FE model is too computationally expensive for this kind of brute-force analysis. Instead, we run only a few of these expensive simulations to sample a broad parameter space and interpolate the stress fields from these sampled points using a Gaussian process regression (GPR) [274, 307]. The surrogate model constructed in this manner is inexpensive and can be easily used to quantify the effect of material behavior uncertainty in our patient-specific reconstructive surgery model.

Surrogate models have been used for engineering applications such as battery life prediction, multi-physics simulations in nuclear engineering, and solar irradiation

prediction, to name just a few examples [308–310]. Surrogates based on nonlinear FE simulations have been used in multidisciplinary design optimization problems where a large number of function evaluations are needed to find a local minimum [311], or in the study of other physical processes such as impact dynamics and combustion [312]. GPR is a Bayesian method based on the assumption that the stress field response as a function of the parameter space is a sample from a random field [307]. This prior assumption is combined with inputoutput observations using Bayes rule. The resulting posterior Gaussian process (GP) captures our state of knowledge after observing the simulation data. In addition, the Bayesian nature of the GPR allows the quantification of the epistemic uncertainty induced by the limited simulation data.

In this study, the quantity of interest is the stress field over the FE mesh. However, the geometry of realistic patient-specific clinical scenarios consists of hundreds of thousands of nodes. Thus, trying to interpolate the response surface in this high-dimensional space is inefficient, it would require learning thousands of scalar functions. An additional step is needed to circumvent this issue. Physics-based phenomena usually have an underlying simpler structure or dominant modes [313]. The high-dimensional result from the FE simulation can then be projected onto this low-dimensional space. Here, we show that principal component analysis (PCA) can be used to identify the low-dimensional space needed for the GPR step [187].

8.2 Methods

8.2.1 Constitutive model

Skin, like most collagen-based soft tissues, can be described as a hyperelastic, anisotropic and nearly incompressible material [118]. Skin shows a typical nonlinear response characterized by an exponential-like stress-strain curve associated with a gradual straightening of the initially undulated collagen fiber network [178]. Several constitutive equations have been proposed over the past decades to describe biological tissues, and there is an increasing emphasis on constitutive models based

on microstructure considerations [314]. At the same time, these models need to be computationally efficient, and there is a tradeoff between explicitly considering fiber orientation distributions versus simplified, integral descriptions of the fiber families [60, 63, 178, 315]. A widely adopted strain energy function that has been deemed appropriate to describe skin is the one proposed by GOH [57]. Before introducing the expression for the strain energy, we briefly summarize the continuum mechanics framework for skin modeling. Let points $\boldsymbol{\chi} \in \Omega_0$ constitute the reference body and points $\boldsymbol{x}(\boldsymbol{\chi}) \in \Omega$ the current state. The deformation gradient $\mathbf{F} = \partial \boldsymbol{x} / \partial \boldsymbol{\chi}$ contains the local information of the motion. In the reference configuration, the preferred fiber orientation is $\mathbf{a}_0$, and this vector is mapped to $\mathbf{a} = \mathbf{F}\mathbf{a}_0$ in the current state. For nearly incompressible materials we decompose the deformation gradient into isochoric $\widehat{\mathbf{F}}$, and volumetric $\mathbf{F}^{vol}$ parts,

$$\mathbf{F} = \widehat{\mathbf{F}}\mathbf{F}^{\mathrm{vol}}, \tag{8.1}$$

with $\widehat{\mathbf{F}} = J^{-1/3}\mathbf{F}$, and $\mathbf{F}^{vol} = J^{1/3}\mathbf{I}$. The second-order identity tensor is denoted $\mathbf{I}$, and $J = \det(\mathbf{F})$ is the volume change. The right Cauchy-Green deformation tensor $\mathbf{C}$ can also be split to obtain its isochoric part

$$\widehat{\mathbf{C}} = J^{-2/3}\mathbf{C} = \widehat{\mathbf{F}}^{\top}\widehat{\mathbf{F}}\,. \tag{8.2}$$

We can now introduce the GOH strain energy

$$\psi = \widehat{\psi} + \psi^{\mathrm{vol}}. \tag{8.3}$$

Due to the assumptions of near incompressibility, the strain energy is decomposed first into two contributions, $\widehat{\psi}$, and ψ^{vol}, which correspond to the isochoric and volumetric terms respectively. The isochoric term is further decomposed into isotropic and anisotropic contributions, $\widehat{\psi} = \widehat{\psi}^{\mathrm{iso}} + \widehat{\psi}^{\mathrm{aniso}}$. The isotropic part is modeled as a neo-Hookean material

$$\widehat{\psi}^{\mathrm{iso}} = \frac{\mu}{2}(\bar{I}_1 - 3), \tag{8.4}$$

where μ the shear modulus, and $\overline{I}_1 = \widehat{\mathbf{C}} : \mathbf{I}$ is the first invariant of $\widehat{\mathbf{C}}$. The volumetric term is also standard for nearly incompressible neo-Hookean materials

$$\psi^{\text{vol}} = \frac{K}{2}\left(\frac{J^2-1}{2} - \ln(J)\right), \tag{8.5}$$

with K the bulk modulus. The isotropic and volumetric terms jointly describe the underlying isotropic material in which the collagen network is embedded. The anisotropic term of the strain energy is then associated with the behavior of the collagen network,

$$\widehat{\psi}^{\text{aniso}} = \frac{k_1}{2k_2}\left(\exp(k_2\langle\overline{E}\rangle^2) - 1\right), \tag{8.6}$$

where

$$\overline{E} \equiv \kappa(\overline{I}_1 - 3) + (1-3\kappa)(\overline{I}_4 - 1) \tag{8.7}$$

captures the deformation of the fiber family.

The fibers have a preferred orientation $\mathbf{a}_0$ in the reference configuration, but not all fibers are necessarily aligned with this direction, instead, they are distributed with a dispersion κ. When $\kappa = 0$ the fibers are perfectly aligned parallel to $\mathbf{a}_0$, and when $\kappa = 1/3$ the fibers are distributed isotropically and the fiber direction $\mathbf{a}_0$ carries essentially no information. The microstructure parameter κ acts thus as a weight of two invariants of $\widehat{\mathbf{C}}$. The first invariant was introduced before in Eq. (8.4). The fourth pseudo-invariant appearing in Eq. (8.7) is the stretch along $\mathbf{a}_0$,

$$\overline{I}_4 = \mathbf{a}_0^{\top}\widehat{\mathbf{C}}\mathbf{a}_0\,. \tag{8.8}$$

The anisotropic response is fully parameterized by k_1 and k_2. These parameters can be associated with a physical interpretation. k_1 is related to the tensile properties of the fiber family, and k_2 is a parameter of nonlinearity of the fiber family.

The second Piola-Kirchhoff stress tensor for a hyperelastic material can be immediately retrieved from the strain energy function,

$$\mathbf{S} = 2\frac{\partial \psi}{\partial \mathbf{C}} = \widehat{\mathbf{S}}^{\text{iso}} + \mathbf{S}^{\text{vol}} + \widehat{\mathbf{S}}^{\text{aniso}} . \tag{8.9}$$

For completeness we expand each term,

$$\begin{aligned}
\widehat{\mathbf{S}}^{\text{iso}} &= 2\frac{\partial \widehat{\psi}}{\partial \mathbf{C}} &&= \mu \left(J^{-\frac{2}{3}}\mathbf{I} - \frac{1}{3}\bar{I}_1 \mathbf{C}^{-1} \right) , \\
\mathbf{S}^{\text{vol}} &= 2\frac{\partial \psi^{\text{vol}}}{\partial \mathbf{C}} &&= \frac{K}{2}(J^2 - 1)\mathbf{C}^{-1} , \\
\widehat{\mathbf{S}}^{\text{aniso}} &= 2\frac{\partial \psi^{\text{aniso}}}{\partial \mathbf{C}} &&= 2k_1 \exp(k_2 \langle \overline{E} \rangle^2) \langle \overline{E} \rangle \left(\kappa \frac{\partial \bar{I}_1}{\partial \mathbf{C}} + (1 - 3\kappa)\frac{\partial \bar{I}_4}{\partial \mathbf{C}} \right) .
\end{aligned} \tag{8.10}$$

In what follows we report the von Mises stress as a convenient scalar measure of the stress distribution in our reconstructive surgery simulations. Thus, we push forward the second Piola-Kirchhoff stress tensor to get the Cauchy stress tensor,

$$\boldsymbol{\sigma} = \frac{1}{J}\mathbf{F}\mathbf{S}\mathbf{F}^{\top} . \tag{8.11}$$

Taking into account all the contributions to the strain energy, the material response is parameterized by μ, K, k_1, k_2, and κ. We choose the value of K to be the largest possible value that still guarantees convergence of the FE simulation while penalizing volume changes as much as possible. Since K is essentially a penalty term for the volume change, a large K enforces incompressible behavior more closely. The parameter κ is set to 1/3 or, equivalently, the fiber family is considered isotropically distributed. This assumption is made in part because we lack information of the preferred orientation $\mathbf{a}_0$. More importantly, based on published reports of human skin mechanical behavior and microstructure, the collagen fiber family does have a preferred orientation but with a large dispersion [60, 180], hence approximating $\kappa = 1/3$ is reasonable. Table 8.1 summarizes the range of GOH model parameters for human skin based on the literature [60, 180].

Table 8.1.: Range of Gasser-Ogden-Holzapfel model parameters based on Ref. [60,180]

Parameter	Range	Mean
μ [MPa]	[0.004774, 0.2014]	0.04498
k_1 [MPa]	[0.000380, 24.530]	4.9092
k_2 [-]	[0.133, 161.862]	76.64134

To showcase the nonlinearity of the material response and the effect of uncertain material properties we show the stress-stretch curves for three different tensile tests: uniaxial, off-biaxial, and equibiaxial. Analytical solutions are easily computed for these cases and incompressibility can be imposed exactly. We use λ_{xx}, λ_{yy}, and λ_{zz} to indicate the amount of stretch with respect to the x, y, and z directions, respectively. The corresponding normal stresses are σ_{xx}, σ_{yy}, σ_{zz}. The uniaxial test is defined by setting $\sigma_{yy} = \sigma_{zz} = 0$ and varying λ_{xx}. In the off-biaxial case we set $\sigma_{zz} = 0$ and $\lambda_{yy} = 1$. For the equibiaxial case $\sigma_{zz} = 0$ and $\lambda_{yy} = \lambda_{xx}$. Solid lines in Fig. 8.1 correspond to the material response when the parameters are chosen to be the mean reported in Table 8.1. To showcase the importance of material parameter uncertainty in these simple scenarios, the parameters are assumed uniformly distributed over the range presented in Table 8.1, and 5,000 values of the parameters are sampled. The gradient shading in the plots of Fig. 8.1 represents varying percentile from 2.5 to 97.5 of the resulting stress distribution.

8.2.2 Patient-specific model

In this study, we present the case of a 7-year-old female who underwent resection of two large portions of the scalp together with cranioplasty. The patient originally had resection of a giant congenital pigmented nevus in infancy that was complicated by infection and led to the debridement of the occipital calvarium. At the time of the treatment presented here, the patient needed correction of the contour deformity of the cranium, had residual nevus at the incision, and unstable scar with ulceration in two regions of the scalp. During the surgery, an occipital Y-shaped scar and a

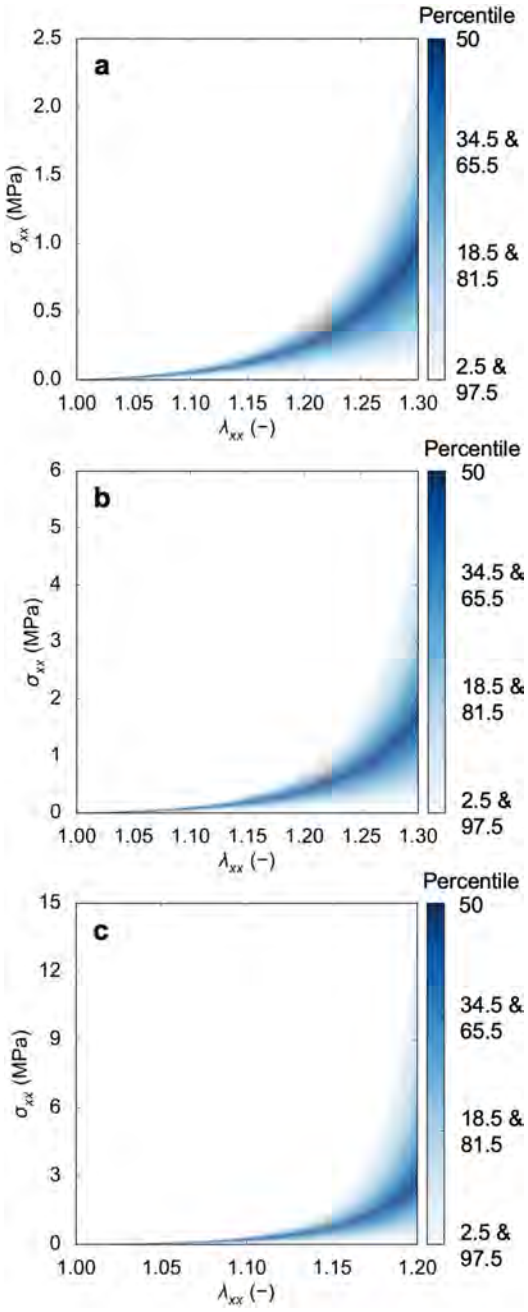

Fig. 8.1.: Analytical solution of (**a**) uniaxial tensile test, (**b**) off-biaxial tensile test, and (**c**) equi-biaxial tensile test to showcase the Gasser-Ogden-Holzapfel model. 5,000 triads (μ, k_1, k_2) are drawn from a uniform distribution over the range in Table 8.1. The gradient shading indicates varying percentile of stress value at each stretch.

right temporal C-shaped scar were resected, and the cranium defect was fixed with a polymer implant.

We use MVS to capture the three-dimensional (3D) geometry of the patient at different time points of the treatment. MVS is based on capturing two-dimensional (2D) pictures of a static object or scene from multiple angles. Feature matching across pairs of photographs then provides information to solve for the camera position and orientation, and once this is solved for many more points can be projected and matched between photos to generate a dense 3D point cloud [282]. Geometries generated with Recap360 (Autodesk, San Rafael, CA) are shown in Fig. 8.2 (first row). Photos were taken pre, intra and postoperatively in order to document the entire treatment with 3D snapshots. Importantly, skin, like most biological tissues, is prestrained *in vivo*. Skin after expander removal is in a relaxed configuration and this geometry was taken as the reference and assumed stress-free.

In addition to the visible patient-specific geometry obtained with MVS, this particular case was not limited to superficial tissue rearrangement but required correction of the cranium. We reconstructed the skull geometry from a CT scan that had been used clinically to design the polymer implant (Fig. 8.2, second row).

As shown in Fig. 8.2 (third row), we performed some post-processing steps to eliminate unnecessary parts and simplify the patient-specific geometry without losing any essential information. Geometry simplification was done with Meshlab [316] and Blender (Amsterdam, the Netherlands). The Y-shaped scar and right temporal C-shaped scar were removed in our *virtual* procedure based on the 3D models taken intraoperatively. The triangular surface was converted to a volumetric mesh by considering a thickness of 3.6 mm. This value of thickness has been reported for young females [285]. The skin consisted of 9,962 nodes and 30,328 tetrahedral elements. Finally, the simplified skull, which consisted of 6,807 nodes and 13,608 triangular elements, was positioned inside the scalp mesh as shown in Fig. 8.2 (last row).

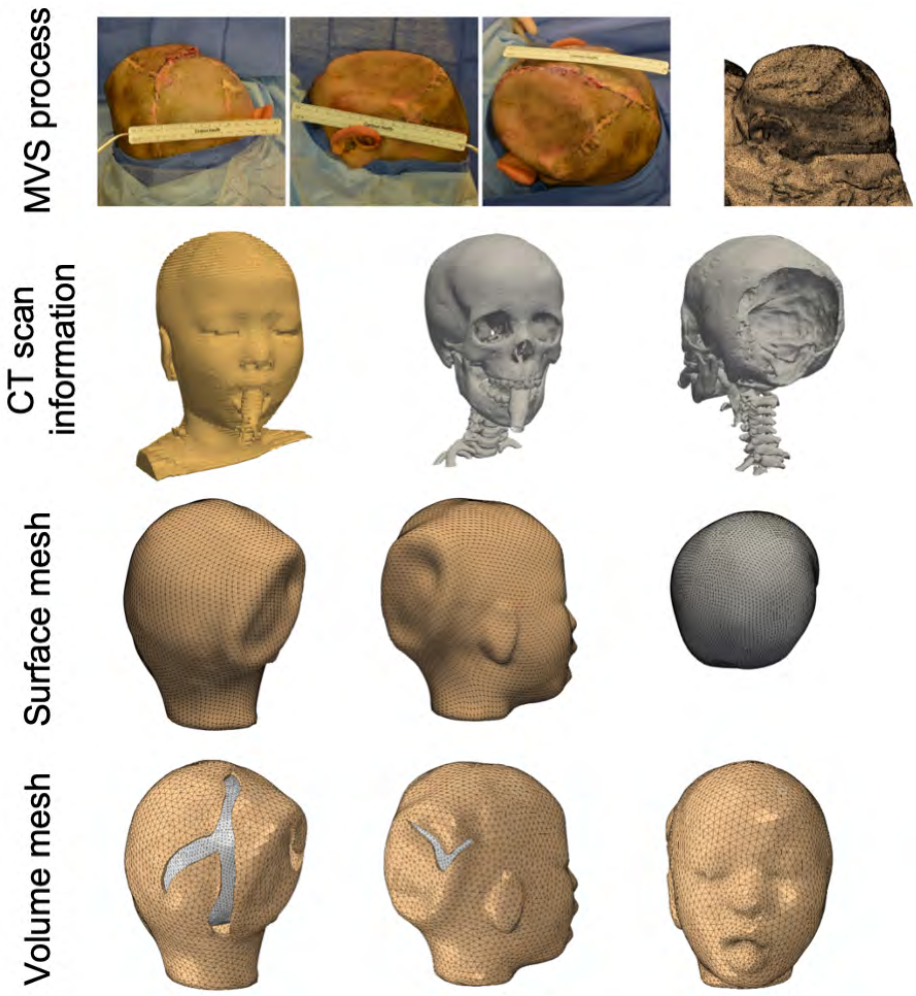

Fig. 8.2.: For multi-view stereo (MVS) reconstruction, photos captured from several angles are used to generate a 3D geometry (1st row); A CT scan was used to generate the skull geometry (2nd row); Skin after tissue expander removal was assumed stress-free and used as reference, the MVS and CT scan geometries were combined and simplified (3rd row); Scalp defects were removed based on the intraoperative MVS models and the scalp mesh was converted to a volume mesh (4th row).

8.2.3 Finite element simulations

We used Abaqus Standard (Dassault Systems, Waltham, MA), an implicit nonlinear FE commercial software package, to run the reconstructive surgery simulations. The skull mesh was defined as a rigid body and its position fixed. The skin was modeled as hyperelastic and described by the GOH strain energy function. To prevent

rigid body motions and also to capture a realistic procedure, the skin away from the operated region was fixed.

Interaction between the scalp and skull during the surgical procedure was modeled as frictionless contact. Sutures were imposed as axial kinematics constraints between pairs of nodes. Namely, the nodes at the edge of both sides of a scar were paired and the distance between them was linearly decreased to simulate the clinical procedure.

8.2.4 Gaussian process regression

Mechanical properties of skin vary not only with age, gender, and anatomical location, but also from one patient to another [182]. Therefore, accounting for uncertainty in the material properties of skin is essential when analyzing the stress distribution caused by reconstructive surgery. Propagating the uncertainty of the material behavior through a detailed, realistic, and nonlinear model of a surgical procedure, to characterize the resulting stress distribution, is the central contribution of this manuscript.

As pointed out in Section 8.2.1, the GOH model requires three independent parameters, μ, k_1, k_2, when the material under consideration is assumed isotropic. Table 8.1 contains the mean and the range for each parameter. We assume that the parameters are uniformly distributed within the range shown in Table 8.1, and we use the Latin hypercube sampling (LHS) algorithm to draw samples from this three-dimensional parameter space [317]. We generate a total of N training samples in the parameter space. We generate a total of N training samples in the parameter space. N should be chosen with consideration of whether N training samples cover the parameter space. In practice, given an initial choice of N, the performance of the surrogate is evaluated to determine whether or not it is within a desirable tolerance. If this is not the case, the training set can be increased iteratively until the desired error is achieved. Let

$\mathbf{x}^{(n)} = \left(\mu^{(n)}, k_1^{(n)}, k_2^{(n)}\right)$ be one point generated by LHS, the total training data can be arranged as

$$\mathbf{X} = \left(\mathbf{x}^{(1)}, \cdots, \mathbf{x}^{(N)}\right) \in \mathbb{R}^{3\times N} . \tag{8.12}$$

Each column of Eq. (8.12) is used to run one FE simulation on the patient-specific model, and, in consequence, generates a M-dimensional nodal stress output $\boldsymbol{\sigma}^{(n)} \in \mathbb{R}^M$ associated with $\mathbf{x}^{(n)}$. The total stress output matrix $\boldsymbol{\sigma} = \left(\boldsymbol{\sigma}^{(1)}, \cdots, \boldsymbol{\sigma}^{(N)}\right) \in \mathbb{R}^{M\times N}$ is first centered by subtracting the mean of each row of $\boldsymbol{\sigma}$ from the corresponding row. Let $\mathbf{s}^{(n)}$ be the centered stress output, thus, the full output stress data from the training set can be expressed as

$$\mathbf{S} = \left(\mathbf{s}^{(1)}, \mathbf{s}^{(2)}, \cdots, \mathbf{s}^{(N)}\right), \quad \mathbf{S} \in \mathbb{R}^{M\times N} . \tag{8.13}$$

The mesh has a large number of nodes, in consequence, $\mathbf{s}^{(n)}$ has a high dimension M, and learning the response surface that connects the input $\mathbf{X}$ to the output $\mathbf{S}$, is problematic in this space. Instead, we seek to reduce the dimensionality of the output data. The stress contours on the patient geometry are the result of a physics-based simulation, and we expect the solution of this kind of problem to have a small number of fundamental modes or features [313]. Hence we perform PCA to reduce the dimension of the output data [187]. Let $\mathbf{W}$ be the linear transformation

$$\mathbf{WS} = \mathbf{Y} , \tag{8.14}$$

where $\mathbf{W} \in \mathbb{R}^{M\times M}$ is the transformation matrix and $\mathbf{Y} \in \mathbb{R}^{M\times N}$ is the principal component (PC) score matrix. Recall the singular value decomposition (SVD) of $\mathbf{S}$,

$$\mathbf{S} = \mathbf{U}\boldsymbol{\Sigma}\mathbf{V}^\top , \tag{8.15}$$

where $\mathbf{U} \in \mathbb{R}^{M\times M}$ is an orthogonal matrix, $\boldsymbol{\Sigma} \in \mathbb{R}^{M\times N}$ is a rectangular diagonal matrix with non-negative real numbers on the diagonal, and $\mathbf{V} \in \mathbb{R}^{N\times N}$ is also an orthogonal matrix. The columns of $\mathbf{U}$ are the orthonormal eigenvectors of $\mathbf{SS}^\top$, and the columns

of $\mathbf{V}$ are orthonormal eigenvectors of $\mathbf{S}^\top\mathbf{S}$. They are also called left- and right-singular vectors of $\mathbf{S}$. The diagonal entries of $\mathbf{\Sigma}$ are called the singular values of $\mathbf{S}$, they are the square roots of the eigenvalues of $\mathbf{S}\mathbf{S}^\top$ and $\mathbf{S}^\top\mathbf{S}$, and are sorted in decreasing order. Rearranging Eq. (8.15) as

$$\begin{aligned}\mathbf{U}^{-1}\mathbf{S} &= \mathbf{U}^\top\mathbf{S} \\ &= \mathbf{\Sigma}\mathbf{V}^\top ,\end{aligned} \tag{8.16}$$

and comparing with Eq. (8.14) we arrive at

$$\mathbf{U}^\top\mathbf{S} = \mathbf{Y} . \tag{8.17}$$

The rows of $\mathbf{W} = \mathbf{U}^\top$ are called the PC, and the rows of $\mathbf{Y}$ are called the PC scores and they are the projection from the original data, $\mathbf{S}^{(n)}$, to the PC basis. Since the data has been centered prior to the SVD, scaling the square of the singular values by $1/(N-1)$ represents the variance in the data. In other words, the singular values express how the information of each column of $\mathbf{S}$ is distributed when expressed in the PC basis. Thus, choosing a certain criterion, for instance wanting to capture 99% of the total variance in the data, the first singular values are kept and the rest of the PC are ignored. This truncation of the linear space is also typical in image compression algorithms [318]. The truncated basis $\mathbf{W'}$ has dimensions $M' \times M$, and the corresponding PC scores are

$$\mathbf{Z} = \left(\mathbf{z}^{(1)}, \cdots, \mathbf{z}^{(N)}\right) \in \mathbb{R}^{M' \times N} \tag{8.18}$$

by substituting $\mathbf{W'}$ instead of $\mathbf{W}$ into Eq. (8.14). If the variance is concentrated in a few PC, then $M \gg M'$ and a significant reduction of the dimensionality of the data is achieved (Compare Eq. (8.18) with Eq. (8.13)).

Let $\mathcal{D} \equiv \{(\mathbf{x}^{(n)}, \mathbf{z}^{(n)})\}_{n=1}^{N}$ be the set made out of the training input parameters $\mathbf{x}^{(n)}$ paired with their corresponding observation of the truncated PC score $\mathbf{z}^{(n)}$, obtained from the FE simulation and PCA. In what follows, we seek to learn a scalar function

for each of the PC scores, M' functions in total. We look at the mth PC score; $\mathbf{z}_m \in \mathbb{R}^N$ is the vector with all the training observations for that score. We assume that for any one of those observations, the following relation holds

$$z_m^{(n)} = f_m\left(\mathbf{x}^{(n)}\right) + \varepsilon_m\,, \tag{8.19}$$

where $\boldsymbol{\varepsilon}_m = \left(\varepsilon_m^{(1)}, \ldots, \varepsilon_m^{(N)}\right) \in \mathbb{R}^N$ has independent and identically distributed Gaussian noise with zero mean and variance $\sigma_{ns,m}^2$. The Gaussian noise models the discrepancy between the surrogate and the FE simulation output in order to enhance numerical stability in factorization of the covariance matrix including the Gaussian noise [319]. We model our prior state of knowledge about f_m using a Gaussian process (GP),

$$f_m(\cdot) \sim \mathcal{GP}(\mu_m(\cdot), k_m(\cdot))\,, \tag{8.20}$$

where $\mu_m(\cdot)$ and $k_m(\cdot)$ indicate mean and covariance functions respectively. Briefly, The GP means a collection of random variables in which any finite gathering has a joint Gaussian distribution [307]. Because the GP is postulated to have a zero mean function [313], the prior GP is a multivariate normal distribution of the values of $f_m(\cdot)$ at $\mathbf{X}$:

$$f_m(\mathbf{X}) \sim \mathcal{N}(\mathbf{0}, \mathbf{K}_m), \tag{8.21}$$

where $\mathbf{K}_m$ is an $N \times N$ covariance matrix. In this study, a radial basis function is utilized as kernel, such that the components of the covariance matrix are

$$\begin{aligned} K_{m(i,j)} &= k_m(\mathbf{x}^{(i)}, \mathbf{x}^{(j)}; \theta_m) \\ &= s_{f,m}^2 \exp\left(-\frac{1}{2}\left(\mathbf{x}^{(i)} - \mathbf{x}^{(j)}\right)^\top \boldsymbol{\Lambda}_m^{-1}\left(\mathbf{x}^{(i)} - \mathbf{x}^{(j)}\right)\right) \end{aligned} \tag{8.22}$$

with $\boldsymbol{\Lambda}_m = \mathrm{diag}(l_{m,1}, l_{m,2}, l_{m,3})$. In particular, $s_{f,m}^2$ is the process variance and $l_{m,1}$,$l_{m,2}$, and $l_{m,3}$ are characteristic length-scales for each of the inputs. We have to estimate the

hyperparameters $\theta_m = (s^2_{f,m},\ l_{m,1},\ l_{m,2},\ l_{m,3},\ \sigma^2_{ns,m})$. These are found by maximizing the logarithm of the likelihood of $\mathbf{z}_m$,

$$\log\ p(\mathbf{z}_m|\mathbf{X},\theta_m) := -\frac{1}{2}\mathbf{z}_m^\top\mathbf{\Sigma}_m^{-1}\mathbf{z}_m - \frac{1}{2}\log|\mathbf{\Sigma}_m| - \frac{N}{2}\log 2\pi\ . \tag{8.23}$$

$\mathbf{\Sigma}_m = \mathbf{K}_m + \sigma^2_{ns,m}\mathbf{I}$ is a covariance matrix with Gaussian noise, and $|\mathbf{\Sigma}_m|$ is the determinant of $\mathbf{\Sigma}_m$. After deciding a point estimate on θ_m, the use of Bayes' theorem combines the prior GP with the likelihood to bring the posterior GP. Bayes' theorem states that prior probability is converted to posterior probability by incorporating the evidence such as training data.

Now, we are ready to perform GPR which enables a point-wise prediction. To be specific, the posterior GP for any parameter input $\mathbf{x}^{(*)}$ is defined by Gaussian distribution,

$$f_m\left(\mathbf{x}^{(*)}\right)|\mathcal{D},\mathbf{x}^{(*)},\theta_m \sim \mathcal{N}\left(\mu_m(\mathbf{x}^{(*)};\theta_m),\sigma_m^2(\mathbf{x}^{(*)};\theta_m)\right)\ , \tag{8.24}$$

where the predictive mean and variance are

$$\mu_m(\mathbf{x}^{(*)};\theta_m) = \mathbf{k}_m^\top{\mathbf{\Sigma}_\mathbf{m}}^{-1}\mathbf{z}_m \tag{8.25}$$

and

$$\sigma_m^2(\mathbf{x}^{(*)};\theta_m) = k(\mathbf{x}^{(*)},\mathbf{x}^{(*)};\theta_m) - \mathbf{k}_m^\top{\mathbf{\Sigma}_\mathbf{m}}^{-1}\mathbf{k}_m\ , \tag{8.26}$$

respectively, and the vector $\mathbf{k}_m$ is defined as

$$\mathbf{k}_m = \left(k(\mathbf{x}^{(*)},\mathbf{x}^{(1)};\theta_m),\cdots,k(\mathbf{x}^{(*)},\mathbf{x}^{(N)};\theta_m)\right)\ . \tag{8.27}$$

In conclusion, for any parameter input $\mathbf{x}^{(*)}$, Eq. (8.24) predicts the expected mth PC score $\mu_m(\mathbf{x}^{(*)};\theta_m)$, as well as the error bars for the predictive mean which are given by the predictive variance $\sigma_m^2(\mathbf{x}^{(*)};\theta_m)$.

Step 1 in the schematic of Fig. 8.3 summarizes how to build the surrogate model. The validation of the surrogate, denoted as Step 2 in Fig. 8.3 is discussed next. Briefly, once the surrogate has been constructed, we generate a new set

$$\mathbf{X}_v = \left(\mathbf{x}_v^{(1)}, \cdots, \mathbf{x}_v^{(Q)}\right) \in \mathbb{R}^{3\times Q} \tag{8.28}$$

of Q validation inputs. Typically, N and Q are chosen to be 70% and 30% of the data, respectively. In this study, however, we finally select Q as about 20% of N based on convergence analysis (Fig. 8.4). We compute the nodal stresses in two ways, with the FE simulation and with the surrogate. Let $\mathbf{Z}_v = \left(\mathbf{z}_v^{(1)}, \cdots, \mathbf{z}_v^{(Q)}\right) \in \mathbb{R}^{M'\times Q}$ be the predictive mean of the PC scores obtained with the surrogate. We perform the inverse PCA transformation to get the predicted and centered nodal stress $\mathbf{S}_v$

$$\mathbf{S}_v = \mathbf{W'}^{\top}\mathbf{Z}_v. \tag{8.29}$$

Note that the truncated PC basis $\mathbf{W'}$ was defined previously, in Eq. (8.14), with the training data. After adding the mean of each row of $\mathbf{S}_v$ to the corresponding row, $\boldsymbol{\sigma}_v$ is finally predicted. We compare $\boldsymbol{\sigma}_v$ from the surrogate with the actual nodal stress, $\boldsymbol{\sigma}_a$, obtained from the FE simulation. In particular we quantify the l_2-norm of the error to assess whether or not the surrogate is accurate enough for our application.

8.3 Results

Before dealing with the uncertainty quantification analysis, we present the von Mises stress contours resulting from running the finite element simulation with the mean values of the GOH parameters (Table 8.1). The stress contours for this simulation are illustrated in Fig. 8.5. During the *virtual surgery*, the two scars are sequentially closed by gradually imposing the suture constraints. The occipital Y-shaped scar is sutured first as depicted in the first three panels of Fig. 8.5. The right temporal C-shaped scar is closed next. The newly grown skin from the tissue expan-

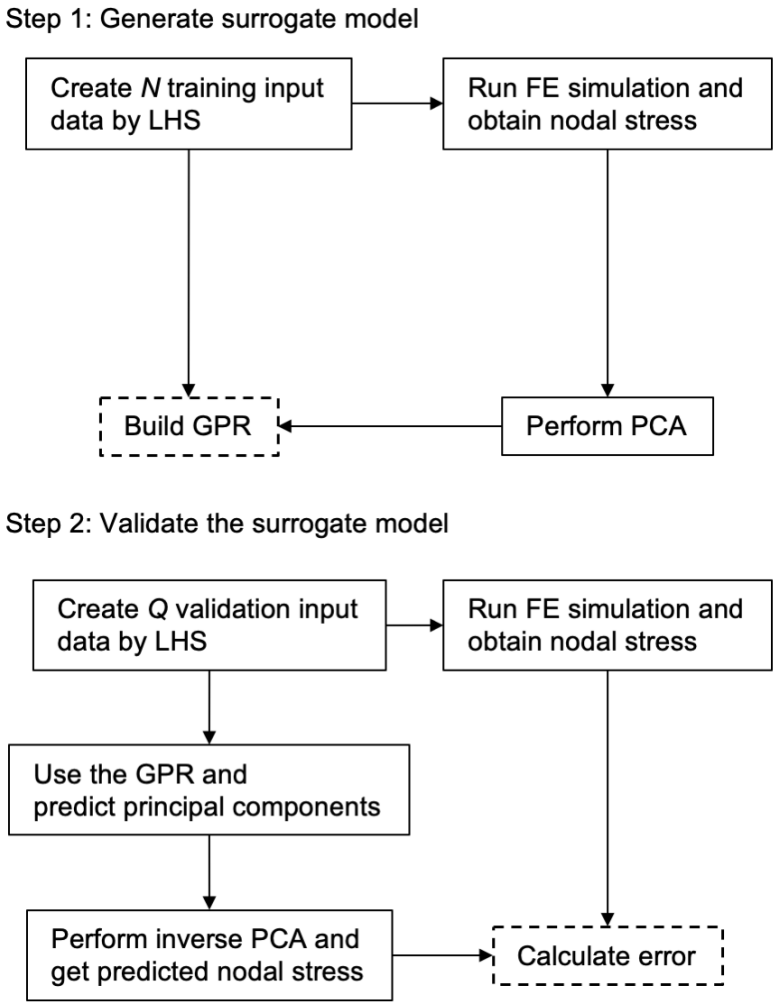

Fig. 8.3.: Surrogate model as a function of material properties by principal component analysis (PCA) of the high-dimensional stress field (Step 1); and validation process (Step 2)

sion process is especially useful in the temporal region, where a large portion of the scalp stays within a low stress range. The distal end of the flap in the temporal region does show a higher stress due to the discrepancy between the opposite edges of the scar, which are fully brought together by the suturing constraints. The T-junction of the occipital scar also shows elevated stress values. Notably, the patient showed delayed healing in this region.

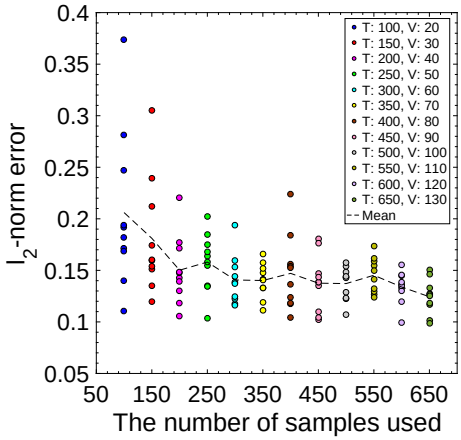

Fig. 8.4.: l_2-norm of the error between the finite element model and the surrogate prediction with respect to the number of training samples used. The number of training sample N is increased in intervals of 50, from 100 to 650.

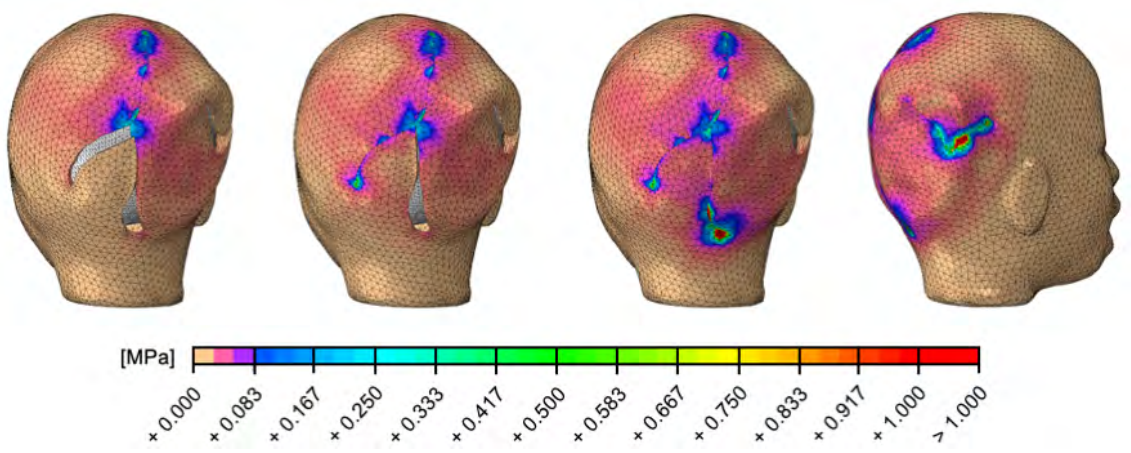

Fig. 8.5.: von Mises stress computed with the finite element simulation of reconstructive surgery on the patient-specific geometry with the mean Gasser-Ogden-Holzapfel model parameters in Table 8.1

In what follows, we will ignore any possible modeling error and thus assume that the nodal stress value from the FE simulation is the true stress. The simulation in Fig. 8.5, run with the mean of the GOH parameters, is a single observation. To propagate the uncertainty in the material parameters to the stress values, we first create a training parameter set using LHS, assuming that the parameters are uniformly distributed within the range stated in Table 8.1. We generate $N = 650$

training inputs $\mathbf{X} = \left(\mathbf{x}^{(1)}, \ldots, \mathbf{x}^{(650)}\right) \in \mathbb{R}^{3\times 650}$ that uniformly occupy the parameter space. In this case, the training sample size was decided based on a convergence analysis (Fig. 8.4). Briefly, we started with a sample size $N = 100$, generated several sets of training data, and computed the l_2-norm of the error of the surrogate over the validation. The sample size was increased up to $N = 650$ with the interval of 50. The training set of $N = 650$ gave adequate results based on this convergence analysis. Details on the quantification of the error and performance of the surrogate for $N = 650$ are provided later in this section.

For each training parameter input, $\mathbf{x}^{(n)}$, we run one finite element simulation and obtain the non-zero nodal stress values as output. For the mesh used in this model, $M = 3,886$ was the dimension of the output vector, i.e. the number of nodes with non-zero stress. These data are centered and arranged as $\mathbf{S} = \left(\mathbf{s}^{(1)}, \cdots, \mathbf{s}^{(650)}\right) \in \mathbb{R}^{3,886\times 650}$. To reduce the dimensionality of the data we do the PCA of $\mathbf{S}$. The plot in Fig. 8.6 shows the cumulative percentage of the total variance as a function of the number of PCs. The first three PCs can account for over 99.7% of the total variation of the $\mathbf{X}$, and they are visualized on scalp. Keeping only the first three PCs, the truncated PC scores are $\mathbf{Z} = \left(\mathbf{z}^{(1)}, \ldots, \mathbf{z}^{(650)}\right) \in \mathbb{R}^{3\times 650}$. As a result, the dimension of the output is reduced from $M = 3,886$ to $M' = 3$. We store the PCs since they are used later on.

After normalizing the input $\mathbf{X}$, the training data $\mathcal{D} \equiv \{(\overline{\mathbf{x}}^{(n)}, \mathbf{z}^{(n)})\}_{n=1}^{650}$ are used to build the surrogate through a GPR as explained in detail in the section 8.2.4. Before validating the surrogate model, we conduct a few mathematical experiments to investigate the sensitivity of the predictive mean with respect to each of the components of the test input $\mathbf{x}^{(*)}$. For instance, to test the influence of the first input parameter x_1, which corresponds to μ in the GOH model, we deactivate the other two parameters and evaluate $\mathbf{z}^{(*)}$ through the GPR. As shown in the first row of Fig. 8.7, we vary $x_1^{(*)}$ over the range $[0.004774, 0.2014]$ and plot the scores z_1, z_2, and z_3 in each column. Likewise, the second and third rows in Fig. 8.7 show the curves of the predicted PC scores as a function of x_2 and x_3, when the two other parameters are deactivated (set to their mean). In addition to the predicted mean of the PC scores, the 95%

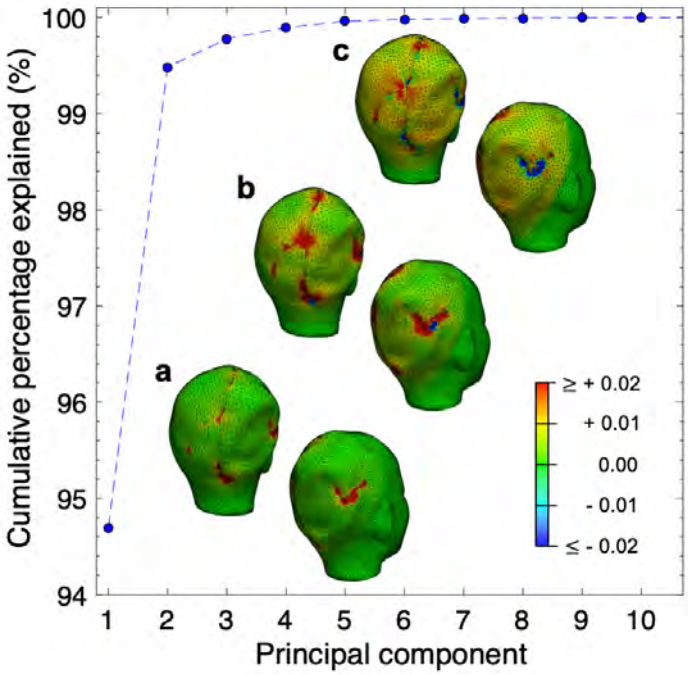

Fig. 8.6.: Information from principal component analysis. Cumulative percentage of variance explained is shown as a function of the number of principal components. The first three principal components (**a**, **b** and **c**) are plotted on the scalp.

confidence interval is also shown as a shaded area around the solid lines. To compare the prediction against the FE model, we ran additional simulations with the same $\mathbf{x}^{(*)}$ used in each of the panels in Fig. 8.7. It can be seen that the FE results fall within the confidence interval predicted by the surrogate.

For all three PC scores, the parameter x_1, associated with the isotropic response in the GOH model, is less influential than both x_2 and x_3 which capture the fiber contribution to the strain energy. The dispersion of z_1, z_2, and z_3 is consistent regardless of the change of x_1, supporting the limited influence of this input. In contrast, the dispersion of z_1, z_2, and z_3 increases with variation of x_2 and x_3. It is also worth noting that the effect of x_1 on the PC scores is fairly linear, which is expected since this parameter has a linear contribution to the strain energy. On the other hand, x_3 produces a nonlinear response. Indeed, this parameter is inside the exponential function of the GOH model.

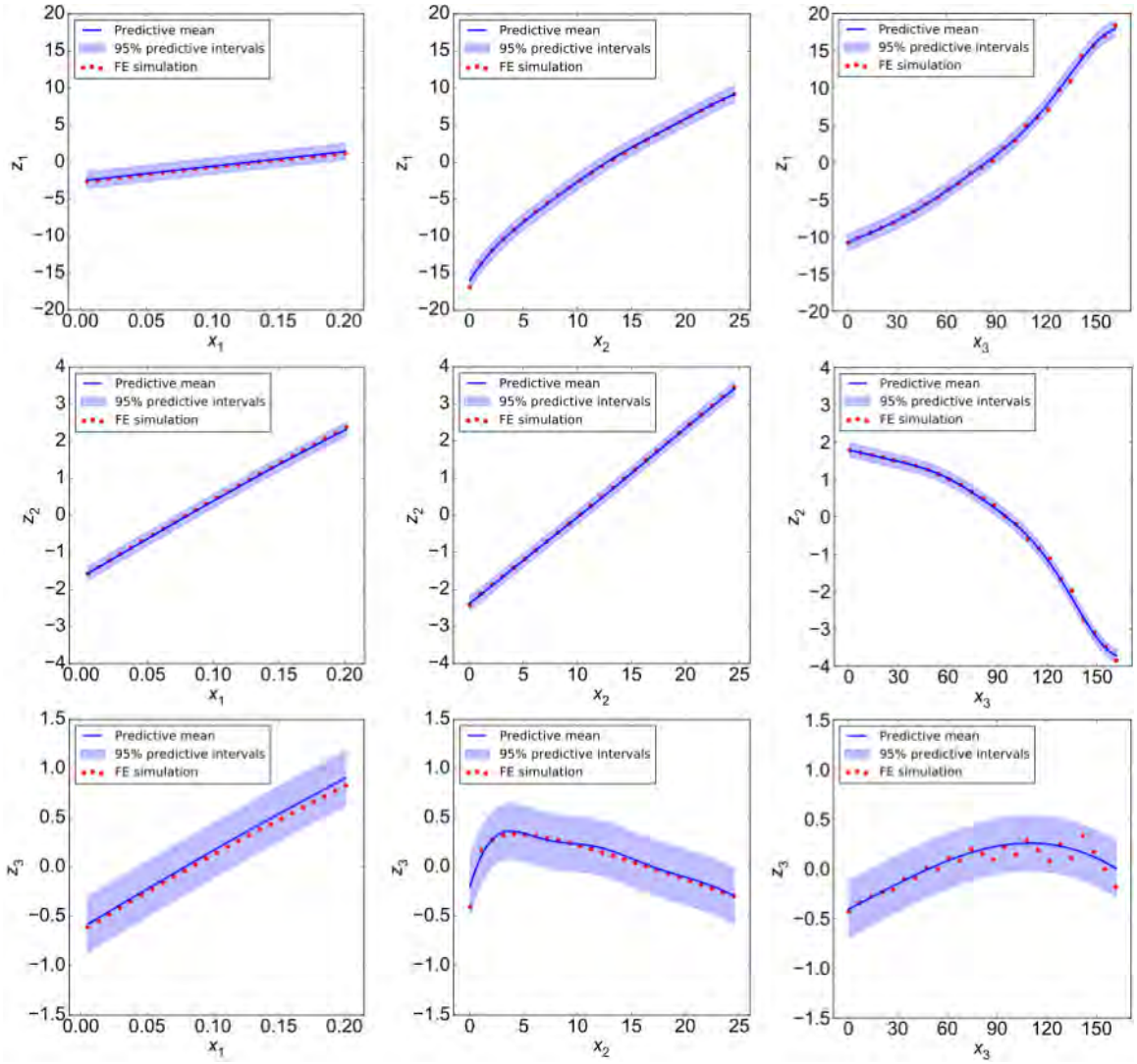

Fig. 8.7.: Response of the predicted principal component (PC) scores with respect to the Gasser-Ogden-Holzapfel model parameters. The first row corresponds to the first predicted PC score z_1; the second and third rows correspond to z_2, z_3 respectively. In each column, the predicted PC scores are plotted as a function of one of the inputs, when the other two are fixed to their mean. The first column shows variation of the predictive PC scores with respect to only x_1, whereas the other two columns are predictions with respect to x_2 and x_3, respectively. Finite element (FE) simulations corresponding to each input vector are also visualized.

In addition to investigating the influence of a single parameter at a time, we also use the surrogate to plot the contours of the PC scores over slices of the parameter space obtained from fixing one parameter at a time. The first row of Fig 8.8, for

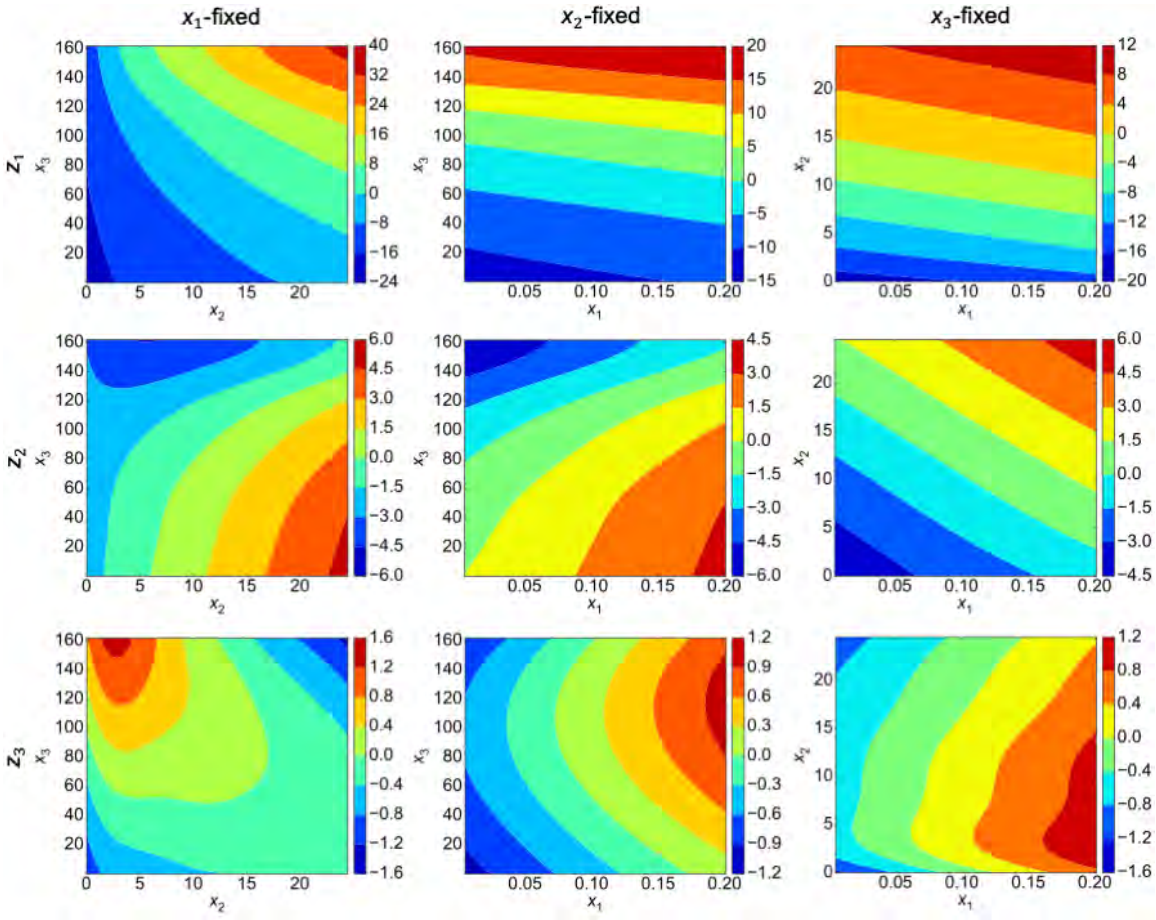

Fig. 8.8.: Contours of the predicted principal component (PC) scores, z_1, z_2, and z_3 over slices of the parameter space. The first row shows the first PC score, z_1, while z_2 and z_3 are depicted in rows two and three respectively. The first column is the slice of the parameter space obtained from fixing x_1 to its mean. The second and third columns are obtained from setting x_2 and x_3 to their respective mean.

example, shows the contours of the three PC scores as a function of x_2 and x_3 when x_1 is set to its mean. The second row of Fig 8.8 depicts contours when x_2 is fixed, and in the last row it is x_3 that is fixed. Looking at the column corresponding to the first predicted PC score, z_1, it is clear that x_2 and x_3 have a similar influence, and that both dominate against x_1. However, x_1 is important to understand the response of the second and third PC scores.

To validate the surrogate, we generate 150 new validation inputs with LHS, $\mathbf{X}_v = \left(\mathbf{x}_v^{(1)}, \ldots, \mathbf{x}_v^{(150)}\right) \in \mathbb{R}^{3\times 150}$, and pass them through the surrogate to obtain the

predicted PC scores, $\mathbf{Z}_v \in \mathbb{R}^{3\times150}$. Independently, we use the same set of inputs to run FE simulations and obtain $\boldsymbol{\sigma}_a \in \mathbb{R}^{3{,}886\times150}$. Then, $\mathbf{Z}_a \in \mathbb{R}^{3\times150}$, is obtained from projecting $\boldsymbol{\sigma}_a$ onto the truncated PC basis. The predicted and actual PC scores are plotted against each other in terms of their standardized residuals (Fig. 8.9, top row). These residuals indicate the difference between the two quantities normalized by the corresponding standard deviation reported by the GPR. Assuming that the residuals follow a standard normal distribution, 99.7% of them should fall in $[-3, 3]$, which is indeed observed. To better understand the distribution of the residuals we show the quantile-quantile plots (QQ-plots) in the bottom row of Fig. 8.9. In particular, the QQ-plots help us compare our residuals against normal quantiles. For the first and second PC scores, the quantiles of the standardized residuals do not follow a Gaussian distribution but are actually concentrated around zero. This implies that the predicted first and second PC scores are very similar to the actual PC scores from the FE model (Fig. 8.9**d** and **e**). On the other hand, the QQ-plot of the third PC score indicates that this residual follows more closely a Gaussian distribution but has a larger error than the other two PC scores (Fig. 8.9**f**). These observations imply that the surrogate prediction of the third PC score can be a source of error. However, we do not expect this to be significant since the third PC explains only about 0.3% of the total variation as shown in Fig. 8.6.

Another assessment of the surrogate is done based on the l_2-norm of the error of the nodal stress vector. $\mathbf{Z}_v$ is passed through the inverse PCA transformation, $\mathbf{W'}^{\top}$, to obtain the predicted and centered nodal stresses $\mathbf{S}_v$. After adding the means of each row of $\mathbf{S}_v$ to the corresponding row, we obtain $\boldsymbol{\sigma}_v$ and we can directly compared the surrogate to the nodal stress observed with the FE simulations (this is Step 2 in Fig. 8.3). The histogram of the l_2-norm of the error is shown in Fig. 8.10. The mean of the l_2-norm error is approximately 10%. The distribution is not normal, about 90% of the predicted stress vectors in the validation set have less than 20% error, and there are only a few outliers. To visualize the difference between the surrogate and the FE simulation for different values of the error, five different points are selected.

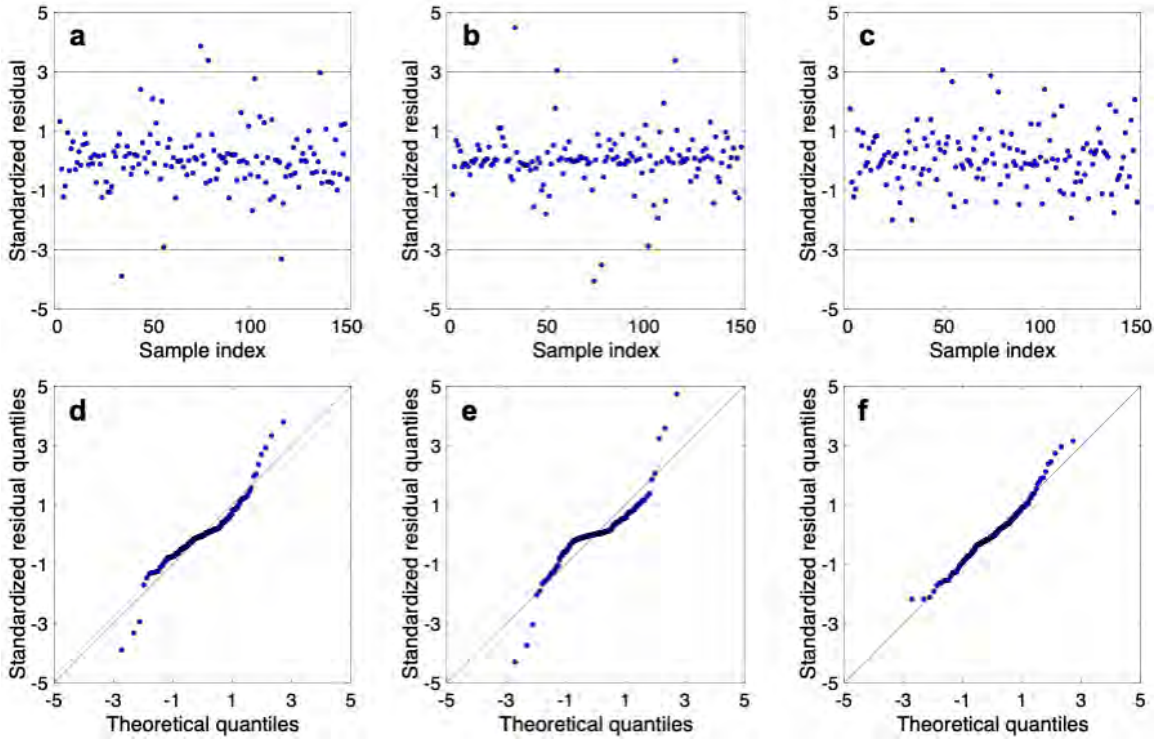

Fig. 8.9.: Comparison of the first three principal component scores between surrogate (z_{v1}, z_{v2}, and z_{v3}) and finite element simulations (z_{a1}, z_{a2}, and z_{a3}). Top row shows standardized residuals: z_{v1} (**a**); z_{v2} (**b**); z_{v3} (**c**). Bottom row shows quantile-quantile plots of the standardized residuals: z_{v1} (**d**); z_{v2} (**e**); z_{v3} (**f**)

All five cases show good qualitative agreement, even for Fig. 8.10**e** which has an error of 0.35.

The parameter intervals reported in Table 8.1 reflect a wide range of material properties corresponding to different age, gender, anatomical locations, and different individuals. Such broad input space is suitable to construct a surrogate when no other information is considered. In reality, additional knowledge may become available. For instance, noninvasive mechanical testing of the individual's skin is now possible [27], or the surgeon's assessment and belief based on her/his experience, could help to narrow down the uncertainty in the input. For example, we assume that the mean parameter values of Table 8.1 are observed exactly. That is, we assume that x_1, x_2, and x_3 are known with 100% confidence (Fig. 8.11**b**). The output of the surrogate we have considered up to this point, $\mathbf{Z}_v$, is only the predictive mean for a given input,

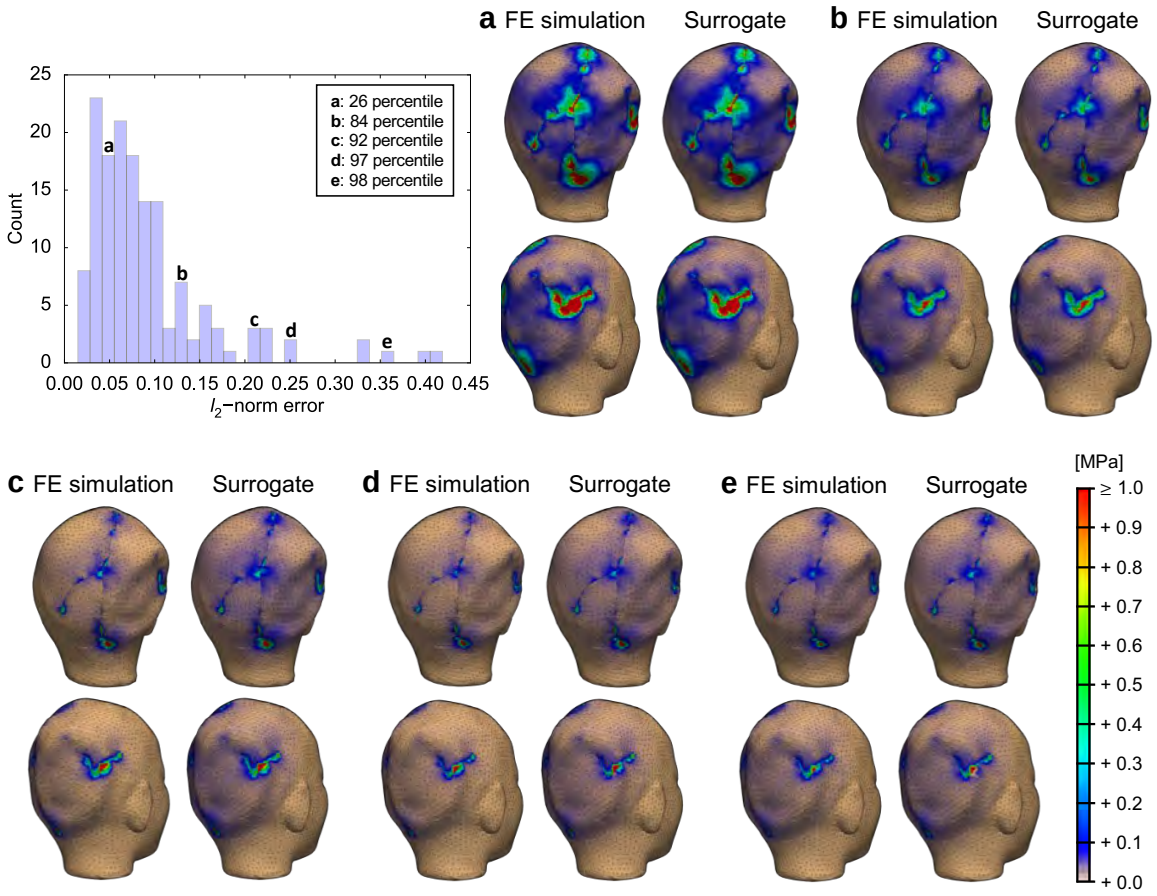

Fig. 8.10.: Histogram of the l_2-norm error, $||\boldsymbol{\sigma}_a - \boldsymbol{\sigma}_v||_2/||\boldsymbol{\sigma}_a||_2$, between the nodal stress vector computed with the surrogate and that observed with the finite element (FE) simulation. The mean error is approximately 0.1, and 90% of the validation set is below 0.2. A few validation tests are shown in **a** to **e** to show the qualitative difference in the stress contours over the scalp for different values of the error: 0.047, 0.136, 0.205, 0.249, and 0.356.

but the GPR actually defines a normal distribution. The standard deviation of this distribution is the expected error from the surrogate. The surrogate thus defines normal distributions for z_1, z_2, and z_3 (Fig. 8.11**c**). The mean and upper and lower bounds of the 95% predictive interval are represented in Fig. 8.11**a**. In other words, the stress contours in Fig. 8.11**a** are the mean and error bars represented over the scalp when we ignore the uncertainty in the material properties.

On the other hand, considering uncertain inputs, additional variation of the stress is expected. For instance, we assume that x_1, x_2, and x_3 are normally distributed,

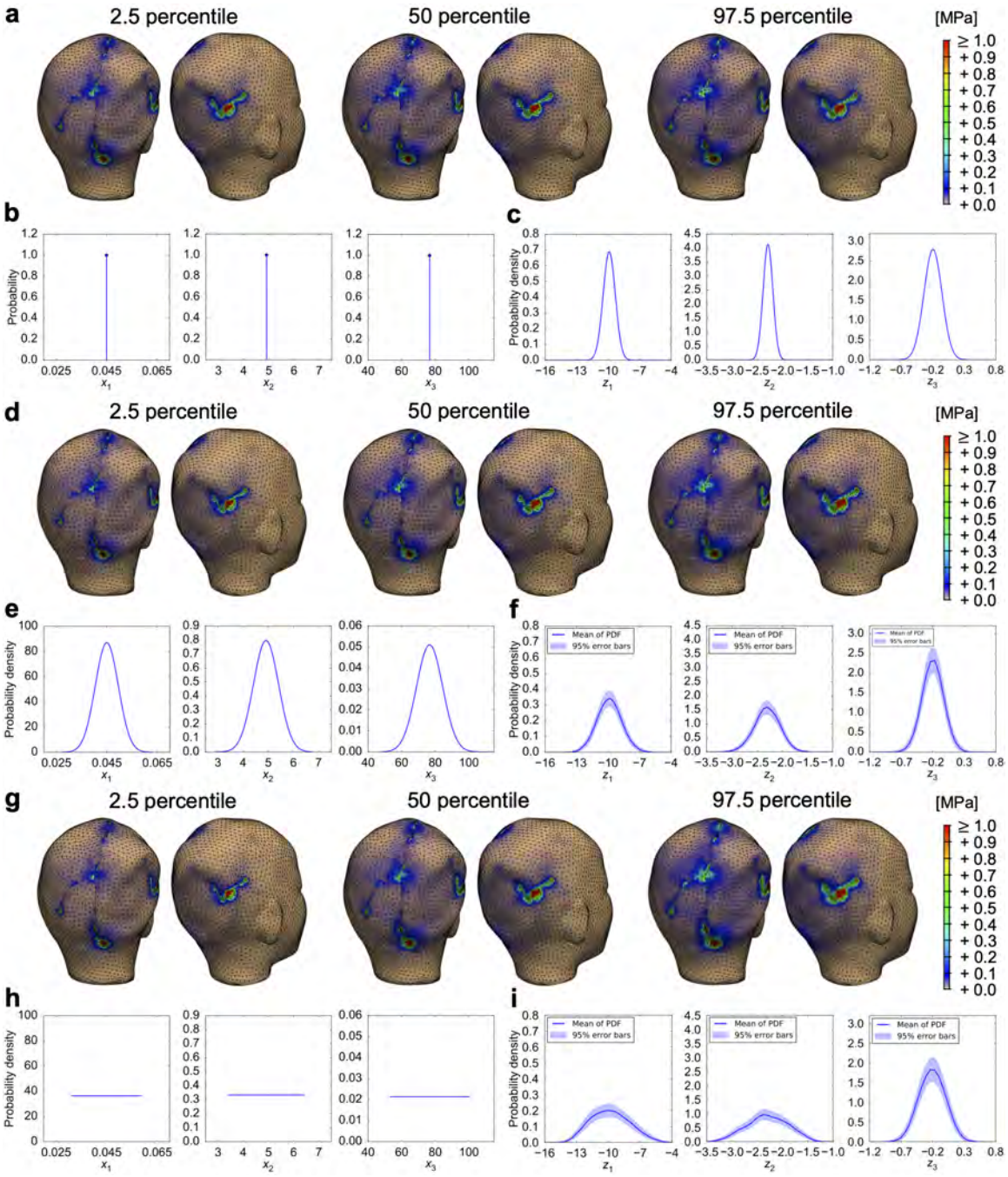

Fig. 8.11.: Prediction of stress distributions with the GPR for three different input distributions of the material properties x_1, x_2, and x_3. When x_1, x_2, and x_3 are known with 100% confidence (**b**), the predicted PC scores follow a normal distribution (**c**). The mean and upper and lower bounds of the 95% confidence interval of the von Mises stress are visualized in (**a**). (Continued on the following page.)

When the parameters are normally distributed (**e**), 10^3 PDFs of predicted PC scores are generated by sampling the GPR for a vector of the normally distributed inputs, leading to the mean and 95% error bars of the PDFs for z_1, z_2, and z_3 (**f**), and to the corresponding 95% confidence interval of the von Mises stress (**d**). A uniform distribution of the material parameters (**h**) is passed through the surrogate to get the corresponding mean and 95% error bars of PDFs of the PC scores (**i**) and confidence interval of the von Mises stress (**g**).

with standard deviation of 20% of their respective mean (Fig. 8.11**e**). Since surrogate evaluations are inexpensive, we sample a thousand points from the normal distributions of x_1, x_2, and x_3, and form a vector with these $\mathbf{x}^{(*)}$. We then sample the GPR a thousand times on this input vector to generate probability density functions (PDFs) for each z_1, z_2, and z_3. These 10^3 PDFs for each PC score are used to calculate the mean and 95% epistemic error bars of the PDF as shown in Fig. 8.11**f**. These error bars are induced by the limited number of simulations used to construct the surrogate [320]. The mean of the PDFs for z_1, z_2, and z_3 are then used to compute 2.5, 50, and 97.5 percentiles of the von Mises stress distributions (Fig. 8.11**d**). The last case we consider is a uniform distribution of the material properties in the range defined by ±20% of their mean values (Fig. 8.11**h**). Once again, 10^3 PDFs for each PC score are generated, and the mean and 95% epistemic error bar of the PDFs are plotted (Fig. 8.11**i**). The corresponding 2.5, 50, and 97.5 percentiles of the von Mises stress are also depicted in Fig. 8.11**g**.

It can be seen from these numerical experiments that the confidence interval of the PDFs for z_1, z_2, and z_3 (the shaded area in Fig. 8.11**f** and **i**) stays relatively constant and narrow as the materials become more uncertain, but the PDFs become wider as a result of the increasing uncertainty in the inputs.

We present one last investigation. Up to this point, the stress contours over the entire scalp have been considered. However, reducing the high-dimensional stress output via PCA necessarily introduces some error. The surrogate built with the entire stress field can be used to broadly explore the effect of uncertain material parameters and identify particular regions or scalar quantities of interest. For instance, based on our previous analysis, here we see that there are two locations with potentially high stress: the T-junction of the occipital Y-shaped scar, and the distal end of the right temporal scar. From this observation we define the mean stress in these two regions as new scalar quantities of interest. Clearly, since these are two scalars rather than high-dimensional stress vectors, two surrogates can be directly constructed via GPR without having to perform PCA. A similar experiment to that in Fig. 8.11 is

done. Namely, we consider that the input is known with 100% confidence (as in Fig. 8.11**b**), or with two different distributions (see Fig. 8.11**e** and **h**). Fig. 8.12 shows the corresponding distribution of the mean stress in the two regions of interest as the uncertainty in the input increases. Comparing with Fig. 8.11, we notice that the confidence intervals for the mean stress of the T-junction and the temporal scar are much tighter compared to the confidence intervals of the PDFs for the PC scores. This is expected since in Fig. 8.12 we have removed the error from the PCA step.

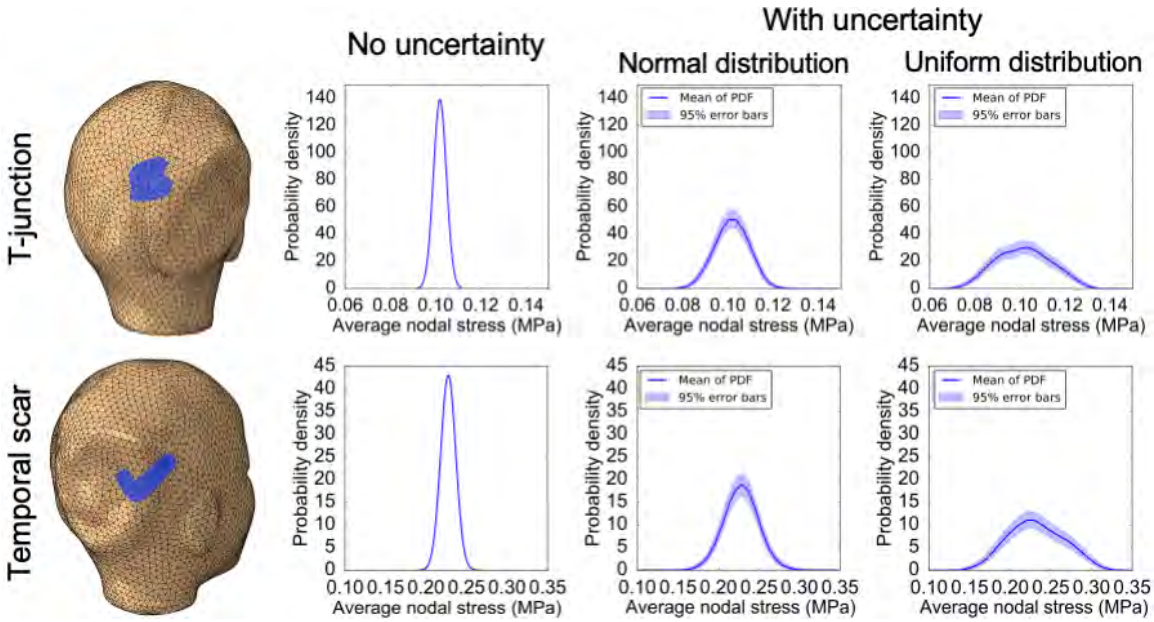

Fig. 8.12.: Uncertainty propagation of material input parameters for two scalar quantities of interest. The quantities of interest are the mean stress for two locations on the scalp: T-junction and distal end of temporal scar (left). Surrogates constructed via Gaussian process regression are used for uncertainty propagation. The distribution for the input parameters are the same as reported in Fig. 8.11**b**, **e**, and **h**.

8.4 Discussion

The stress distribution over skin flaps following a reconstructive procedure is a determining factor on the subsequent healing response. Excessive stress has been associated with poor outcomes such as hypertrophic scarring or delayed healing [2,3].

Therefore, predicting the stress contours, particularly in the vicinity of sutured regions, can help the surgeon to make a more informed decision to prevent some of these complications. Finite element simulations allow computation of the stress contours given the patient geometry, the desired procedure, and the material properties of the skin. Obtaining the geometry and defining the procedure can easily be done noninvasively [321–323]. On the other hand, the patient-specific material properties are usually hard to obtain, and even though skin has a similar behavior across human patients, the exact parameters change with age, gender, anatomical location, and from one person to another [45]. This manuscript develops tools to determine the influence of uncertain material properties on the stress contours in a realistic FE model of reconstructive surgery.

To obtain the patient-specific geometry we use MVS. This algorithm from computer graphics reconstructs a 3D geometry from a sequence of uncalibrated 2D photos [282]. The advantages of this technique are its flexibility and affordability. MVS is affordable because it only needs a standard digital camera. It is flexible because it does not require a complicated setup, the photos are taken from any location and orientation, the only constraint is to capture a sufficient number of photographs (around 30) from different angles. In this paper we took photographs pre, intra, and postoperatively, and thus we had 3D models for different time points of the surgery. This allowed us to recreate the actual procedure that was performed on the patient. However, for the clinical application, capturing just the preoperative geometry is enough in order to set up the FE model.

Even with a patient-specific geometry and a desired procedure, predicting the stress contours from a surgery is challenging because of the uncertainty in the material properties for an individual. Skin can be described as a nonlinear, transversely isotropic, hyperelastic membrane. We use the GOH strain energy because it describes collagenous tissues in general, and it has been used to accurately describe skin. Experiments on human skin fitted to the GOH model have provided some valuable data regarding a plausible range for the material parameters [60, 180]. However, our

knowledge is still very limited in this regard, and more experiments on human skin are needed to better characterize the statistics of the GOH parameters.

Given some prior of the material properties, the question that underpins this manuscript is how to propagate this uncertainty through a realistic FE simulation of a reconstructive procedure. The main challenge comes from the fact that detailed simulations are computationally demanding, and thousands of observations are needed to compute the relevant statistics. We solve this problem using PCA followed by GPR. Instead of running many simulations, we sample the parameter space and run only a few of these costly training cases. PCA is needed because the output we collect from the finite element model is a vector of nodal stresses. When dealing with realistic scenarios, the geometry is usually represented with a fine, detailed mesh made up of thousands of nodes [248,324]. In the clinical case shown here, for instance, the number of nodes showing non-zero stresses is $3,886$. Moreover, we expect to observe distinct features or modes in the stress response. PCA allows to reduce the dimensionality of the stress data. In our example, we are able to go from $3,886$ to only 3 principal components of the stress and still capture over 99% of the data variance. The last step in our methodology is to do a GPR [307]. Among several non-parametric regression methods, GPR is desirable because of its Bayesian nature, which allows us to distinguish between material uncertainty and the epistemic uncertainty induced by the limited amount of data used to construct the surrogate [325].

The surrogate computed with this approach is computationally inexpensive while still achieving a desired accuracy. With our clinical case we show that building a surrogate with 650 training samples leads to errors that are around 10% on average, and below 20% with 0.9 probability, based on a validation set of 150 cases. Having a surrogate that can be evaluated almost instantaneously, interesting questions about the response function of the stress in terms of the material properties can be explored. For instance, we plot the predictive means of the PC scores as a function of each of the inputs. We also show contours of the PC scores over slices of the input space of material properties. Based on these results we were able to learn that the first

parameter, associated with the isotropic term of the GOH model, has the less influence on the PC scores and, consequently, on the stress output. This is due to the fact that the first parameter contributes to the linear term in the GOH strain energy function and that the nonlinear fiber contribution is dominant at larger tensile strains. In this particular case, the closure of the two flaps leads to strains on the order of 20% for x, y, and z directions and hence the fiber contribution is expected to be more important. This type of information, for example, suggests that it is more valuable to do experiments in order to get a better prior distribution for the parameters of the GOH model associated with the fiber contribution.

The true potential of the surrogate is exploited by propagating the uncertainty in the material parameters to the stress distribution over the patient-specific geometry. We test three cases. When the parameters are observed with 100% confidence, the 95% confidence interval for the stress contours is determined by the error of the GPR alone. Normal and uniform distributions of the parameters were also passed through the surrogate to obtain the corresponding mean and error bars of the stress over the scalp. Interestingly, these experiments suggest that reducing the uncertainty of the parameters beyond a certain amount may not be too valuable. For example, in our case, all three distributions of the parameters considered led to predictive intervals for the stress that differed by only about 10%. This type of insight is possible because of the ability to easily propagate a prior of the parameters with the help of a surrogate based on GPR.

With our approach we were able to quantify the effect of uncertain material properties for a realistic clinical scenario. Nonetheless, our work is not free of limitations. In particular, the only source of uncertainty considered here is that of the material behavior, but incorporating uncertainty in the modeling, and especially in the geometry is a future research direction that can help delineate more general guidelines for reconstructive procedures. Additionally, here we ignored material anisotropy, but fiber orientation is another important factor that must be incorporated in the future. In fact, we recently published a paper establishing the methodology to build

the finite element model from the patient geometry acquired in the operating room, and we used the Cox lines to approximate the fiber distribution [286]. However, we ignored variations in the material parameters and limited our analysis to a single set of values taken from the literature. Nonetheless, our model showed that stresses are concentrated along the fiber vector field [99]. We have reported a similar stress distribution in our previous work dealing with ideal flap simulations [287]. Therefore, we expect that incorporating uncertainty in the anisotropy of skin will lead to principal components reflecting the gradual increase and alignment of the stress contour with respect to the fiber orientation field. Despite these limitations, this study is critical to increase our understanding of the role of uncertain material properties, a hallmark of biological materials, in the mechanical behavior of soft tissues for relevant clinical settings.

8.5 Conclusion

In this manuscript, we study the effect of uncertain material properties in realistic finite element simulations of clinically relevant procedures. In order to propagate the material uncertainty through a computationally expensive, detailed finite element model, we build a surrogate by coarsely sampling the parameter space, performing principal component analysis on this set of training stress fields to reduce the dimensionality of the data, and doing Gaussian process regression. The surrogate is inexpensive and accurate, enabling us to easily quantify important statistics of the stress contours on the patient-specific geometry given a prior distribution for the material properties.

9. PREDICTING THE EFFECT OF AGING AND DEFECT SIZE ON THE STRESS PROFILES OF SKIN FROM ADVANCEMENT, ROTATION, AND TRANSPOSITION FLAP SURGERIES

Abstract: Predicting mechanical stress contours on skin resulting from local tissue rearrangement surgeries is needed to design optimal treatment plans and avoid wound healing complications. Finite element simulations of skin tissues have been shown to be a reliable tool in preoperative planning, yet, a major obstacle in the creation of predictive software comes from the inherent uncertainty in material properties of biological materials, and the high computational cost of creating and calibrating virtual surgery models. In this study we build computationally inexpensive surrogates to easily predict stress profiles for arbitrary material parameters and a range of defect sizes in three reconstructive scenarios: advancement, transposition, and rotation flaps. The surrogates are built by first creating a training dataset of finite element (FE) simulations that cover the input space of experimentally-determined skin properties from the literature. A reduced order representation of the training data set is achieved via principal component analysis, and computationally efficient surrogates are then created through Gaussian process (GP) regression. We show that the GP surrogates predict stress contours with relative errors that are on average 2% in the l_2-norm compared to the high fidelity FE models. We apply the GP surrogates to predict differences in the probability densities of stress contours between two different age groups undergoing the same procedure. By replacing nonlinear FE models with accurate yet inexpensive models that can be evaluated for any combination of human skin material parameters and a range of defect sizes, we aim to enable calibration and prediction of stress contours in individualized clinical cases in the near future.

9.1 Motivation

Surgical reconstruction of large skin lesions demands a delicate technique to achieve the desired aesthetic outcome and preserve the functionality of the involved tissues [30]. Deformation and mechanical loading of skin resulting from reconstructive surgery is a constant concern for the clinician because excessive stress leads to poor cosmetic and suboptimal functional outcomes [4]. However, anticipating and measuring stress contours on large skin areas remains an unresolved problem [8]. Surgeons currently rely on their training and experience to manually estimate the skin tension in the operating room, but this approach is not quantitative and it is done at a stage at which changes to the surgical plan are no longer possible. Concurrently, the number of reconstructive procedures, especially in the head and neck region, is sharply increasing. For instance, the primary form of treatment for skin cancer, melanoma as well as non-melanoma, is surgical excision followed by reconstruction with local cutaneous flaps [295, 326, 327]. In 2012, 3.3 million people in the US were treated for non-melanoma skin cancer [293], and about 5% of new cancer diagnoses are melanomas [328].

Local flaps are a common reconstructive strategy for the correction of cutaneous lesions due to the advantage of using adjacent tissues with the same color, hair bearing properties, and blood supply as contiguous skin. Local flaps can be classified by vascular supply and geometric design [329]. The geometric design of a flap entails deciding the contour for the incision and the suturing pattern, i.e., which pairs of points along the edges of the flap are brought together by the sutures. In the absence of engineering design tools, the space of flap designs has been explored through trial and error. This empirical optimization process has led to many dissimilar strategies, and even to this date new flap designs continue to be proposed [8]. Three strategies -advancement, transposition, and rotation flaps- are currently the most common [329, 330] (see Fig. 9.1).

To decide on a surgical plan, known critical factors implicated in wound healing are considered. Reducing skin tension is one of the crucial preoperative assessments [1]. This is due to the fact that excessive tension at the suture lines is hypothesized to yield flap complications [5]. Mechanical cues are acknowledged as a key trigger for increased inflammation and fibrosis based on *in vitro* and animal models of wound healing [35, 36]. Yet we are still unable to incorporate this knowledge reliably in the clinical setting because measuring and predicting stress during preoperative planning and treatment execution remains unsolved.

Fortunately, computational modeling of soft tissues has emerged as a powerful tool to determine stress contours over sizable skin regions in realistic situations [14, 15]. Extensive mechanical characterization of skin samples with uniaxial, biaxial, bulge, suction tests, and with custom robotic manipulators has resulted in a comprehensive understanding of skin's mechanical behavior [23,27–29,45]. In combination with novel three-dimensional imaging techniques and progress in numerical analysis tools for thin membranes [116, 122, 127], computer simulations of patient-specific and general flap strategies have been explored [99]. These models have resulted in the quantification and prediction of stress contours aligned with clinical findings, and have offered new recommendations for treatment planning [14, 17, 99].

Even though the use of computational modeling tools such as finite element (FE) simulations has permeated into the field of surgery biomechanics and wound healing device design, there are still important obstacles to overcome. The input to an FE simulation consists of geometry, material parameters, and boundary conditions. Skin, like all biological materials, shows a wide range of values in measured mechanical properties [184]. Additionally, each patient's treatment is unique. Accounting for this uncertainty in the input of the FE model is a core barrier to the widespread use of computational tools in preoperative planning [100]. With current technologies, anticipating the stress contours of the skin for a given patient would entail evaluating a high fidelity FE model multiple times, each simulation being computationally expensive and requiring specialized software.

Surrogate and reduced-order modeling techniques have been recently proposed to overcome some of the hindrances of FE simulations in design optimization applications or scenarios requiring real-time simulations [331,332]. The main idea is to use a high fidelity, computationally expensive model offline in order to train an inexpensive surrogate. Here we build computationally efficient Gaussian process (GP) surrogates to easily predict stress profiles for arbitrary material parameters and a range of defect sizes in the three most prevalent reconstructive scenarios: advancement, transposition, and rotation flaps [329, 333]. The GP surrogates are thoroughly validated over the parameter space of experimentally-determined skin properties reported in the literature [23, 51, 334].

Importantly, the creation of the GP surrogates is grounded on Bayes' theorem, such that the posterior GP is proportional to the maximum likelihood of the training data and a prior GP [187]. In return, the GP surrogate contains not only information about the predicted value of a function, but also of the associated confidence interval of the prediction. This information of the uncertainty in the predicted stress is essential during preoperative planning, model calibration and model refinement [335].

9.2 Methods

9.2.1 Constitutive model of skin

Connective soft tissues such as the skin show a characteristic nonlinear, J-shaped strain-stress response dictated by their microstructure behavior. The middle layer of the skin, the dermis, is the load bearing layer, it consists of a wavy collagen fiber network embedded in a ground substance matrix [266]. Constitutive modeling of connective tissues inspired by the microstructure response has led to hyperelastic descriptions in which the strain energy is additively decomposed into contributions from the matrix and from the collagen fiber network [314, 336, 337]. The matrix is isotropic and nearly incompressible, while the fiber network is anisotropic and incompressible. Here, we employ the Gasser-Ogden-Holzapfel (GOH) strain energy

density function [57], originally developed to capture the behavior of arteries but that has then been adapted to model skin [14, 60]. Both matrix and collagen fiber phases share the same deformation gradient $\mathbf{F}$. Because the matrix is assumed to be nearly incompressible, $\mathbf{F}$ is decomposed according to

$$\mathbf{F} = \overline{\mathbf{F}}\mathbf{F}^{\text{vol}}, \tag{9.1}$$

where $\overline{\mathbf{F}}$ and $\mathbf{F}^{\text{vol}}$ are the isochoric and volumetric parts respectively. The volume change is quantified from the determinant of the deformation gradient $J = \det(\mathbf{F})$, which is needed to define the split in Eq. (9.1), namely: $\overline{\mathbf{F}} = J^{-1/3}\mathbf{F}$ and $\mathbf{F}^{\text{vol}} = J^{1/3}\mathbf{I}$. $\mathbf{I}$ is the second-order identity tensor. The decomposition into isochoric and volumetric terms enables the split of the strain energy density function into isochoric and volumetric terms as well

$$\psi = \overline{\psi} + \psi^{\text{vol}}. \tag{9.2}$$

Since the GOH strain energy function considers the anisotropic contribution of the collagen fiber network, $\overline{\psi}$ is further decomposed into isotropic and anisotropic terms $\overline{\psi} = \overline{\psi}^{\text{iso}} + \overline{\psi}^{\text{aniso}}$. In particular, $\overline{\psi}^{\text{iso}}$ is defined as a neo-Hookean material, while $\overline{\psi}^{\text{aniso}}$ is modeled by an exponential energy potential that reflects the fiber aligning and straightening with increasing deformation. The GOH strain energy can thus be fully expanded into all contributions

$$\psi = \frac{\mu}{2}(\bar{I}_1 - 3) + \frac{k_1}{2k_2}\left(\exp(k_2\langle\bar{I}_{\text{f}} - 1\rangle^2) - 1\right) + \frac{K}{2}\left(\frac{J^2-1}{2} - \ln(J)\right) \tag{9.3}$$

where $\overline{\psi}^{\text{iso}}$, $\overline{\psi}^{\text{aniso}}$, and ψ^{vol} expressed consecutively. The first, isotropic contribution, is dictated by $\bar{I}_1 = \overline{\mathbf{C}} : \mathbf{I}$, which is the first invariant of $\overline{\mathbf{C}} = J^{-2/3}\mathbf{C}$, with $\mathbf{C}$

the isochoric part of the right Cauchy-Green deformation tensor $\mathbf{C} = \mathbf{F}^\top\mathbf{F}$. In the anisotropic term, the pseudo-invariant $\overline{I}_\mathrm{f}$ is the deformation of the fiber network

$$\overline{I}_f = \overline{\mathbf{C}} : \mathbf{A} \quad \text{where} \quad \mathbf{A} = \kappa\mathbf{I} + (1 - 3\kappa)\mathbf{a}_f \otimes \mathbf{a}_f \,. \tag{9.4}$$

The second-order tensor $\mathbf{A}$ is a generalized structural tensor that combines the second-order identity tensor $\mathbf{I}$, and a standard structural tensor $\mathbf{a}_f \otimes \mathbf{a}_f$ defined by the preferred fiber orientation $\mathbf{a}_f$. The weighting between the isotropic and fully anisotropic terms is controlled by the parameter κ. If $\kappa = 0$ there is only energy from deformation in the direction $\mathbf{a}_f$ and the fiber contribution is perfectly anisotropic. When $\kappa = 1/3$ the fibers are randomly distributed in all direction and the fiber contribution becomes isotropic. It should also be noted that fibers are assumed to buckle in compression, which calls for the use of the Macauley bracket, i.e., $\langle\overline{I}_f - 1\rangle$ which is zero when $\overline{I}_f < 1$ and $\overline{I}_f - 1$ otherwise.

Therefore, the strain energy function in Eq. (9.3) is succinctly parameterized by: μ, the shear modulus of isotropic matrix; k_1 and k_2, collagen fiber parameters that capture the tensile properties and nonlinearity of the fiber family; and K, the bulk modulus which enforces the near-incompressibility of the matrix.

To close this section, we recall the definition of the Cauchy stress tensor

$$\boldsymbol{\sigma} = \frac{1}{J}\mathbf{F}\mathbf{S}\mathbf{F}^\top \,. \tag{9.5}$$

9.2.2 Finite element models of local flap surgery

We deal with the three most important local flap designs: advancement, transposition, and rotation flaps. A schematic of the geometry defining each of these procedures is shown in Fig. 9.1. Each incision design is embedded in a planar tissue patch, and the skin defect that needs to be removed is simplified as a circle parameterized by the diameter ϕ. We assume that our virtual surgery simulations are done in the scalp for which an average thickness of 3.5 mm is considered [338].

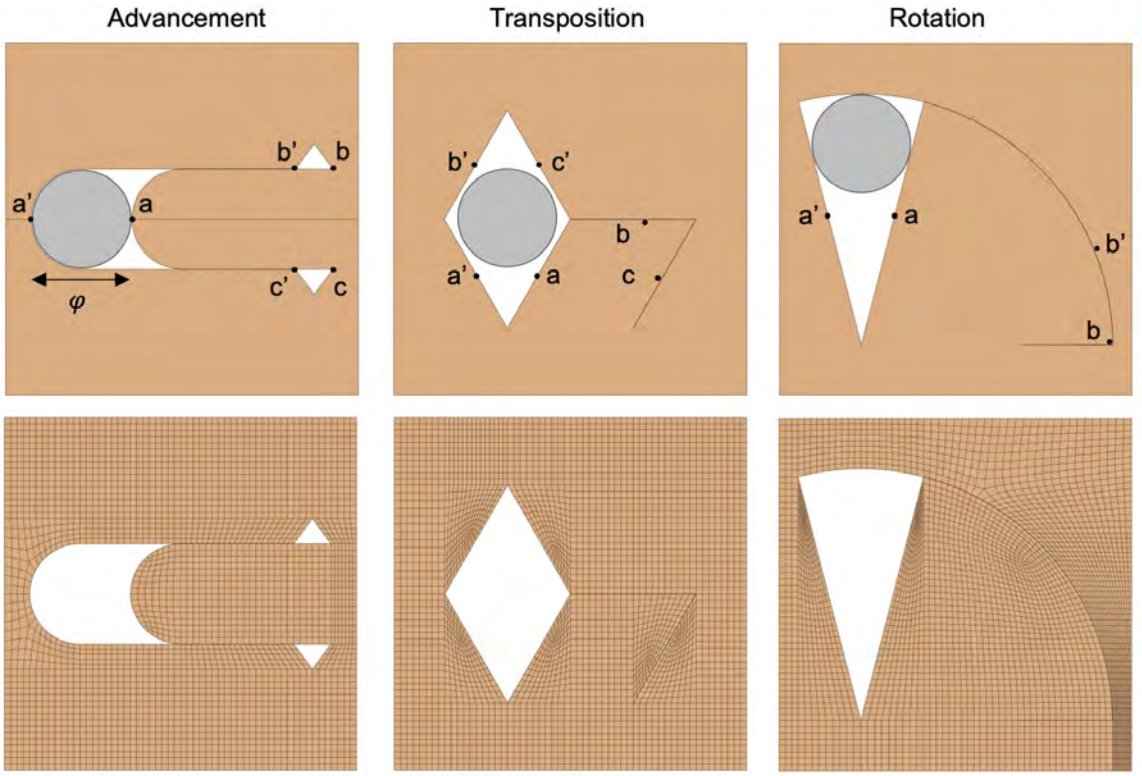

Fig. 9.1.: Local flap designs: Advancement, transposition, and rotation flaps are created to close a circular defect (upper row). The size of the defect is parameterized by its diameter, ϕ. Letter pairs (**a**, **a′**), etc., indicate points to be brought together by the sutures. Meshes for the finite element simulations are made of trilinear brick elements assuming a thickness of 3.5 mm (bottom row).

To study the influence of the defect size on the resulting stress distributions, we change the Dirichlet boundary conditions on the tissue surrounding the defect rather than creating new meshes repetitively. In other words, the fixed boundary is gradually moved inward to capture an increase in the defect size. Initially, a defect of 22.22 mm is considered for a tissue patch of 270×270 mm. We then expand the constrained region, leading to a smaller domain of 150×150 mm or, equivalently, to an increase in the defect size to a diameter of 40 mm with respect to the original tissue patch. Five increments of the fixed boundary are considered, corresponding to defects $\phi = 22.22, 25, 30, 35.29$, and 40 mm.

To evaluate the equilibrium configuration of the virtual surgery procedures, we use Abaqus Standard (Dassault Systems, Waltham, MA), an implicit nonlinear FE commercial software package. As described in the previous section, skin is described with the GOH model. Even though the form of the strain energy function is fixed, the material parameters are considered uncertain, with the exception of the fiber dispersion and the bulk modulus. We assume that $\kappa = 1/3$ and therefore the tissue behaves as isotropic. While skin does show anisotropy, the fiber dispersion has been reported to be relatively large [180], and therefore a random fiber dispersion is a reasonable approximation to capture the essential features of the stress profiles for the different surgeries. In addition, the bulk modulus K is not allowed to change freely but it is instead determined to be the highest value that guarantees convergence for all input parameters while allowing only small volume changes. Hence, μ, k_1, and k_2, are the only uncertain material parameters considered in this study.

To execute the suturing in the virtual surgery simulation, we impose linear constraints between pairs of nodes. The distance between two nodes is gradually reduced to close the flap, analogous to the clinical setting.

Eight-node linear brick elements (C3D8) with full integration are employed in the analysis. We discretize the advancement flap with $4,851$ nodes and $2,984$ elements. The transposition model consists of $10,305$ nodes and $6,490$ elements. The rotation flap is modeled with $11,871$ nodes and $7,442$ elements.

9.2.3 Material behavior uncertainty of skin tissues and creation of the training dataset

Characterization of skin mechanical properties over the past five decades has provided plausible parameters for different material models, including the GOH model [60, 180]. The range of the GOH model parameters considered here is as summarized in Table 9.1. To account for possible sources of error in the acquisition of these pa-

rameters, the parameter range is further extended to include ±20% with respect to the range in Table 9.1.

Table 9.1.: Experimentally-obtained skin material parameters for the Gasser-Ogden-Holzapfel model reported in the literature [60, 180]

Parameter	Range	Mean
μ [kPa]	[4.774, 201.4]	44.980
k_1 [kPa]	[0.380, 24530]	4909.2
k_2 [-]	[0.133, 161.862]	76.641

We remark that, based on the literature, the parameter range considered for μ spans two orders of magnitude, the range of k_1 spans six orders of magnitude, and the range for k_2 covers three orders of magnitude. The validity of such parameter space is questionable. A possible explanation for the range of k_1 and k_2 reported is that these two parameters have a limited contribution to the strain energy at small deformations. The GOH strain energy function contains an exponential term that reflects a sharp stiffening of the material as collagen fibers get aligned and stretched. This exponential behavior is governed by k_1 and k_2. Thus, some of the experimental protocols used to fit the GOH model may have failed to uniquely capture this exponential response. Additionally, we note that any arbitrary combination of μ, k_1, and k_2 may not represent a real mechanical response because of the interplay between the different parameter contributions to the skin's mechanical behavior. For example, a large value of k_1 and k_2 may compensate for a small value in μ.

However, even considering these remarks, it is advantageous to use the largest possible range of parameters reported in the literature to build the surrogate. After the surrogate is trained on the wide parameter space, it can be used to propagate narrower, realistic joint probability distributions of the parameters.

In all simulations, the bulk modulus is set to $K = 4$ MPa. This implies an equivalent Poisson's ratio [339] ranging from approximately 0.4701 to 0.4995 for the training dataset. Values near 0.4995 will satisfy near incompressibility, whereas values closer to 0.4701 will allow a slight amount of compressibility. Because K is an input

to the FE model that influences the stress output and the trends isolated through principal component analysis (PCA), we fix K even though the equivalent Poisson's ratio is not constant. A more careful determination of the skin's compressibility, as recently discussed in [340], is needed to properly incorporate variations in the bulk modulus in our analysis.

Latin hypercube sampling (LHS) is used to generate uniformly distributed GOH model parameters over the extended parameter range. Here, 900 sets of μ, k_1, and k_2 are created and used to run simulations for five different defect sizes ϕ. We run a total of $4,500$ simulations for each flap design (Table 9.2). A validation set is also created (Table 9.2). The corresponding output for each simulation is the von Mises stress field. This stress feature is used for convenience since it reduces the stress tensor field to a scalar field. However, we recognize that it may not be the most physiologically relevant. Further investigation, beyond the scope of the present manuscript, is needed to determine which features of the stress tensor are more strongly correlated to wound complications. Nevertheless, the methodology to build the surrogate described here can be easily extended to any other invariant of the stress tensor, or even to each component of the stress tensor individually.

Table 9.2.: Dimensions of the training and validation input datasets. Random μ, k_1, and k_2 are generated by Latin hypercube sampling (LHS), and for each input, five defect sizes ϕ are run.

	Training	Validation
μ, k_1, and k_2 (by LHS)	900	300
ϕ	5	5
μ, k_1, k_2, and ϕ	4,500	1,500

9.2.4 Reduced representation of the training data via principal component analysis

The quantity of interest, the von Mises stress field over the skin patch, is projected to the nodes of the FE mesh. Therefore, the output of each simulation has

a dimension equivalent to the number of nodes. For realistic nonlinear FE models used in biomedical applications, the number of nodes is on the order of thousands to tens of thousands. In the simulations shown here, the meshes are composed of $4,851$, $10,305$ and $11,871$ nodes for the different flaps. Learning the response function over this high dimensional space would entail an impractical computational cost. For a scalar valued function, if there are M training data points, building the surrogate entails $O(M^3)$ operations (see the next section on the surrogate creation). If training the surrogate with a data set that has N independent output dimensions, the total number of operations grows to $O(NM^3)$. To avoid the infeasible situation, we first do PCA on the output data set. We identify only a few, $n \ll N$ principal components (PCs) that contain most of the variance of the data, and then project the output onto this reduced space. The reduced order representation of the output brings down the computational cost of training the surrogate to $O(nM^3)$ operations [312].

Let $\mathbf{S} = (\mathbf{s}^{(1)}, \cdots, \mathbf{s}^{(M)}) \subset \mathbb{R}^N$ be the N-dimensional output data set for the M training inputs. Each row of $\mathbf{S}$ is centered by subtracting its own mean. The centered output data, $\overline{\mathbf{S}}$, undergoes a singular value decomposition

$$\overline{\mathbf{S}} = \mathbf{U}\mathbf{\Sigma}\mathbf{V}^\top , \tag{9.6}$$

where $\mathbf{U}$ is an $N \times N$ orthogonal matrix, $\mathbf{\Sigma}$ is an $N \times M$ rectangular diagonal matrix with non-negative real numbers on the diagonal, and $\mathbf{V}$ is also an $M \times M$ orthogonal matrix. The columns of $\mathbf{U}$ are the orthonormal eigenvectors of $\overline{\mathbf{S}}\overline{\mathbf{S}}^\top$, and the columns of $\mathbf{V}$ are orthonormal eigenvectors of $\overline{\mathbf{S}}^\top\overline{\mathbf{S}}$. They are called left- and right-singular vectors of $\overline{\mathbf{S}}$ respectively. The diagonal entries of $\mathbf{\Sigma}$ are called the singular values of $\overline{\mathbf{S}}$, they are the square roots of the eigenvalues of $\overline{\mathbf{S}}\overline{\mathbf{S}}^\top$ and $\overline{\mathbf{S}}^\top\overline{\mathbf{S}}$, and are sorted in descending order. Rearranging Eq. (9.6) as $\mathbf{U}^{-1}\overline{\mathbf{S}} = \mathbf{\Sigma}\mathbf{V}^\top$ exposes the PCs of $\overline{\mathbf{S}}$ to be the rows of $\mathbf{U}^{-1}$. The rows of $\mathbf{\Sigma}\mathbf{V}^\top$ are then called the PC scores. The singular values indicate the variance of $\overline{\mathbf{S}}$. Thus, the first several singular values can be used to capture most of the data variance, up to a desired threshold. For example, if the first n singular values account for 99% of total variance, those n PCs can be used as

a basis for the output and the remaining $N - n$ scores can be ignored. In the case of physical phenomena such as skin deformations and stress fields in reconstructive surgery, only a few modes of components carry the majority of the information and $n \ll N$. The truncated data set can be arranged as $\mathbf{Y} = \mathbf{U}'^{\top}\overline{\mathbf{S}} \subset \mathbb{R}^n$ where $\mathbf{U}'$ only includes the first n PCs as columns.

9.2.5 Surrogate models of reconstructive surgery using Gaussian process regression

Let $\mathcal{D} := (\mathbf{x}^{(m)}, \mathbf{y}^{(m)})_{m=1}^{M}$ be the input and output data set. We seek to learn an inexpensive approximation of the function $\mathbf{y}^{(m)} = \mathbf{f}(\mathbf{x}^{(m)})$ to replace the FE model. In this study, $\mathbf{x}^{(m)} = (\mu^{(m)}, k_1^{(m)}, k_2^{(m)}, \phi^{(m)}) \in \mathbf{X}$ consists of three different material parameters and the diameter of defect. The input data set is $\mathbf{X} = (\mathbf{x}^{(1)}, \cdots, \mathbf{x}^{(M)}) \subset \mathbb{R}^4$. The corresponding output, $\mathbf{y}^{(m)} \in \mathbf{Y}$, contains the truncated PC scores as explained in the last section. The output data set is $\mathbf{Y} = (\mathbf{y}^{(1)}, \cdots, \mathbf{y}^{(M)}) \subset \mathbb{R}^n$. Note that $\mathbf{y}^{(m)}$ has a dimension n, we use the notation $y_r^{(m)} = f_r(\mathbf{x}^{(m)})$, $r = 1, \cdots, n$, to refer to individual PC scores for a single simulation. Also, let $\mathbf{y}_r \in \mathbb{R}^M$ denote the vector with the rth PC score for all M training inputs.

Each function $f_r(\cdot)$ is fitted with a GP. A GP defines a probability measure over the function space, that is, random variables are collected from the function space such that any finite subset of the random variables has a joint Gaussian distribution [187]. Thus, each $f_r(\cdot)$ is independently modeled with a mean function, $m(\cdot;\theta)$, and covariance function, $k(\cdot,\cdot;\theta)$,

$$f_r(\cdot)|\theta \sim \mathcal{GP}\left(m(\cdot;\theta), k(\cdot,\cdot;\theta)\right),\ r = 1, \cdots, n \tag{9.7}$$

where θ are called hyperparameters of the noise-free covariance function. Our prior belief is encoded on our choice of the mean and covariance function. If there is no prior knowledge on the mean of $f_r(\cdot)$ (this is actually true in most applications), we can choose $m(\cdot;\theta)$ to be zero. In other words, the use of a zero mean function for

the prior implies that the mean of the posterior is determined only by the covariance function and the training data. Of course, if one has any prior knowledge on the mean function, this should be used and the posterior will be adjusted accordingly. For the covariance function $k(\cdot,\cdot;\theta)$, also called kernel function, we use the squared exponential,

$$k(\mathbf{x}^{(i)},\mathbf{x}^{(j)};\theta) = s^2 \exp\left(-\frac{1}{2}(\mathbf{x}^{(i)}-\mathbf{x}^{(j)})^\top \mathbf{\Lambda}^{-1}(\mathbf{x}^{(i)}-\mathbf{x}^{(j)})\right). \tag{9.8}$$

The hyperparameters can now be explicitly defined as $\theta = (s, l_1, l_2, l_3, l_4)$. The parameter s (> 0) is the signal strength; l_1, l_2, l_3, and l_4 are called characteristic length scales corresponding to each input, they are all positive, and enter Eq. (9.8) via $\mathbf{\Lambda} = \mathrm{diag}(l_1^2, l_2^2, l_3^2, l_4^2)$.

Given input data set $\mathbf{X}$, the prior GP on the corresponding response output is a normal distribution

$$\mathbf{f_r}|\mathbf{X},\theta \sim \mathcal{N}(\mathbf{0},\mathbf{K}) \quad \text{with} \quad \mathbf{f_r} = (f_r(\mathbf{x}^{(1)}),\cdots,f_r(\mathbf{x}^{(M)})). \tag{9.9}$$

where $\mathbf{K}$ is the covariance matrix built from the input points. The matrix $\mathbf{K}$ has (i,j) components $k(\mathbf{x}^{(i)},\mathbf{x}^{(j)};\theta)$, and it is symmetric and positive semi-definite.

With the assumption that the simulation model potentially includes error (e.g., PCA-introduced error, discretization error, insufficient Newton-Raphson iterations, etc.), we introduce Gaussian noise to each observation m

$$t_r^{(m)} = f_r(\mathbf{x}^{(m)}) + \varepsilon_r^{(m)}. \tag{9.10}$$

The entries of the vector $\mathbf{t_r} = (t_r^{(1)},\cdots,t_r^{(M)}) \in \mathbb{R}^M$, are called the noisy target values, and $\boldsymbol{\varepsilon_r} = (\varepsilon_r^{(1)},\cdots,\varepsilon_r^{(M)}) \in \mathbb{R}^M$ is a Gaussian noise vector. Each component of the Gaussian noise vector has zero mean and variance $\sigma_{G,r}^2$, i.e., $\varepsilon_r^{(m)} \sim \mathcal{N}(0,\sigma_{G,r}^2)$. Because the Gaussian noise is independently and identically distributed, the conditional distribution of $\mathbf{t_r}$ given $\mathbf{f_r}$ is represented as a multi-variate and isotropic Gaussian distribution. Hence, the covariance matrix of the noisy targets $\mathbf{t_r}$ becomes $\mathbf{K} + \sigma_{G,r}^2\mathrm{I}$.

The use of Gaussian noise does not only help to account for possible contamination of the training data set, but it is also needed from a numerical point of view for stability during factorization of the covariance matrix (see Eq. (9.13) below) [341].

Recalling that for a GP any finite subset of random variables has a joint Gaussian distribution, the joint prior of $\mathbf{t_r}$ with a new test output $f_r(\mathbf{x}^{(*)})$ is also a normal distribution

$$\begin{bmatrix} \mathbf{t}_r \\ f_r(\mathbf{x}^{(*)}) \end{bmatrix} \sim \mathcal{N}\left(\begin{bmatrix} \mathbf{0} \\ 0 \end{bmatrix}, \begin{bmatrix} \mathbf{K} + \sigma_{G,r}^2 \mathrm{I} & \mathbf{k}(\mathbf{X}, \mathbf{x}^{(*)}; \theta) \\ \mathbf{k}(\mathbf{x}^{(*)}, \mathbf{X}; \theta) & k(\mathbf{x}^{(*)}, \mathbf{x}^{(*)}; \theta) \end{bmatrix} \right) \tag{9.11}$$

with $\mathbf{k}(\mathbf{x}^{(*)}, \mathbf{X}; \theta) = \left(k(\mathbf{x}^{(*)}, \mathbf{x}^{(1)}; \theta), \cdots, k(\mathbf{x}^{(*)}, \mathbf{x}^{(M)}; \theta) \right) \in \mathbb{R}^M$. The joint prior Gaussian distribution of $\mathbf{t_r}$ and $f_r(\mathbf{x}^{(*)})$ is essentially a multiplication of the prior Gaussian distribution of $\mathbf{t_r}$ and the conditional Gaussian distribution of $f_r(\mathbf{x}^{(*)})$ given $\mathbf{t_r}$, which yields the posterior distribution of $f_r(\mathbf{x}^{(*)})$ according to Bayes' rule. Summarizing, the posterior distribution of $f_r(\mathbf{x}^{(*)})$ is

$$f_r(\mathbf{x}^{(*)}) | \mathbf{X}, \mathbf{t_r}, \mathbf{x}^{(*)}, \theta \sim \mathcal{N}\left(\mu_r(\mathbf{x}^{(*)}; \theta, \sigma_{G,r}^2), \sigma_r^2(\mathbf{x}^{(*)}; \theta, \sigma_{G,r}^2) \right) . \tag{9.12}$$

The predictive mean and variance at $\mathbf{x}^{(*)}$ are defined as

$$\mu_{f_r}(\mathbf{x}^{(*)}; \theta, \sigma_{G,r}^2) = \mathbf{k}(\mathbf{x}^{(*)}, \mathbf{X}; \theta)(\mathbf{K} + \sigma_{G,r}^2 \mathrm{I})^{-1} \mathbf{t}_r \, , \tag{9.13}$$

and

$$\sigma_{f_r}^2(\mathbf{x}^{(*)}; \theta, \sigma_{G,r}^2) = k(\mathbf{x}^{(*)}, \mathbf{x}^{(*)}; \theta) - \mathbf{k}(\mathbf{x}^{(*)}, \mathbf{X}; \theta)(\mathbf{K} + \sigma_{G,r}^2 \mathrm{I})^{-1} \mathbf{k}(\mathbf{X}, \mathbf{x}^{(*)}; \theta) \, . \tag{9.14}$$

The predictive mean and variance can be used as a point-wise surrogate with an error bar at $\mathbf{x}^{(*)}$. In addition to providing a predictive variance for $f_r(\mathbf{x}^{(*)})$ (without Gaussian noise), the predictive variance including the Gaussian noise variance is easily

seen to be $\sigma^2_{f_r}(\mathbf{x}^{(*)};\theta,\sigma^2_{G,r})+\sigma^2_{G,r}$ which should be interpreted as the predictive variance for $t_r^{(*)}$.

Up to this point we have explained the construction of the prior GP and how to obtain the corresponding posterior for a new input, but we have yet to obtain the values of the hyperparameters. The step of finding the hyperparameters is called GP regression, or GPR. We implement the GPR using GPy [195]. The parameters θ of the GP should be such that the likelihood of the output training data set is maximized. For numerical stability, log likelihood is preferred. Since our output is made of n independent PC scores, the marginal likelihood of each n output is independently quantified as

$$\mathcal{L}(\theta,\sigma^2_{G,r};\mathbf{X},\mathbf{t}_r) := \log p(\mathbf{t}_r|\mathbf{X},\theta,\sigma^2_{G,r}),\ r=1,\cdots,n. \tag{9.15}$$

Eq. (9.15) can be further expanded,

$$\log p(\mathbf{t}_r|\mathbf{X},\theta,\sigma^2_{G,r}) = -\frac{1}{2}\mathbf{t}_r^\top(\mathbf{K}+\sigma^2_{G,r}\mathrm{I})^{-1}\mathbf{t}_r - \frac{1}{2}\log|\mathbf{K}+\sigma^2_{G,r}\mathrm{I}| - \frac{M}{2}\log 2\pi\,. \tag{9.16}$$

Then, the hyperparameters θ and Gaussian noise variance $\sigma^2_{G,r}$ are inferred by solving the following optimization problem of

$$\theta^*,\sigma^{*^2}_{G,r} = \arg\max_{\theta,\sigma^2_{G,r}} \mathcal{L}(\theta,\sigma^2_{G,r};\mathbf{X},\mathbf{t}_r)\,. \tag{9.17}$$

BFGS optimization is employed to search for the desired θ and $\sigma^2_{G,r}$. The GPR is independently executed n times, for each of the PC scores determined in the PCA step.

We remark that even after finding the hyperparameters θ and $\sigma^2_{G,r}$, the training output consists of n PC scores for each simulation, and not directly the stress field. Consequently, the $\mu_{f_r}(\mathbf{x}^{(*)};\theta,\sigma^2_{G,r})$ at a new input $\mathbf{x}^{(*)}$ is also the rth predictive PC

score. To go back to the space of nodal stress values an inverse transform is first required. Let $\mathbf{y}_{GP}^{(*)}$ be the predictive PC scores at $\mathbf{x}^{(*)}$ such that

$$\mathbf{y}_{GP}^{(*)} = \left(\mu_{f_1}(\mathbf{x}^{(*)}; \theta, \sigma_{G,r}^2), \cdots, \mu_{f_n}(\mathbf{x}^{(*)}; \theta, \sigma_{G,r}^2)\right) \in \mathbb{R}^n \,. \tag{9.18}$$

Accordingly, the inverse PCA is defined as $\overline{\mathbf{S}}^{(*)} = \mathbf{U}'\mathbf{y}_{GP}^{(*)}$. The $\overline{\mathbf{S}}^{(*)} = (\overline{s}_1^{(*)}, \cdots, \overline{s}_N^{(*)}) \in \mathbb{R}^N$ is the predictive N-dimensional centered nodal stress built from the predictive mean of the GP surrogate. . Importantly, as just pointed out, this inverse transform leads to a recovery of the full dimension of the prediction, from n to N. Note that $\overline{\mathbf{S}}^{(*)}$ contains the stress values centered by their mean. Adding the mean values to each dimension can finally lead to the desired output from the surrogate: $\mathbf{S}^{(*)}$, the predictive nodal stress values at $\mathbf{x}^{(*)}$.

To quantitatively assess the performance of the surrogate, the l_2-norm of the relative error of the predictive stress field is computed on a validation data set (see Table 9.2). Namely, the validation data set, which consists of P points like $\mathbf{x}^{(p)}$ where $p = 1, \cdots, P$, is used to generate stress fields through the FE simulation $\mathbf{S}_{FE}^{(p)}$. Independently, the same points are evaluated with the GP surrogate to get the predictive stress $\mathbf{S}_{GP}^{(p)}$. The relative error is calculated on these fields: $||\mathbf{S}_{FE}^{(p)} - \mathbf{S}_{GP}^{(p)}||_2 / ||\mathbf{S}_{FE}^{(p)}||_2$.

An additional evaluation of the surrogate is done by computing the standardized residuals of the predictive PC scores. The stress fields from the FE simulation are projected onto the reduced basis to obtain the corresponding PC scores $\mathbf{y}_{FE}^{(p)}$. In contrast, $\mathbf{y}_{GP}^{(p)}$ are the predictive PC scores resulting from the GP, namely, the counterpart of $\mathbf{y}_{FE}^{(p)}$. Standardized residuals are defined as the difference between two PC scores normalized by the standard deviation of the PC scores.

9.3 Results

9.3.1 Training of Gaussian process surrogates for advancement, rotation, and transposition flaps

We ran a total of $M = 4,500$ FE simulations in order to generate enough data to train the surrogate (see Table 9.2). Fig. 9.2 showcases snapshots of a single simulation for each of the different flaps when the GOH parameters are set to the mean of the range shown in Table 9.1. Even though the three flaps aim at correcting the same size of lesion and correspond to the same material parameter input, the resulting stress profiles are different from one another. The advancement flap leads to a uniform stress along the flap and higher stresses at the distal end. In the transposition flap the stresses are overall higher, with a band of high stress aligned with the intermediate suture line. The rotation flap produces the lowest stresses near the region where the lesion was initially located, but it also produces the greatest stress, concentrated at the opposite end of the flap.

While the number of simulations for the training data set are the same across flap strategies, and all the simulations correspond to the same domain size, the dimension of the quantity of interest is the number of nodes. Therefore, the training output for the advancement flap has dimension $N_{\text{adv}} = 4,521$, the transposition flap has $N_{\text{trs}} = 9,633$, and $N_{\text{rot}} = 11,163$ for the rotation case. In either case, the dimension is too high to attempt a direct interpolation of the response surface, and a reduced representation is sought. We do PCA independently for each flap.

Remarkably, the first a few PCs can account for over 99% of the total variance for each of the three scenarios (Fig. 9.3). In this study, we set 99.9% of the total variance as the threshold. It must be noted that the reduction in the dimension of the training data introduces an error in addition to the interpolation error. Hence, a higher threshold for the variance quantified in the PCA step decreases this intrinsic error. At the same time, as few PCs as possible are desired to maximize the compression of the data. With a 99.9% threshold, the advancement, transposition, and rotation flaps

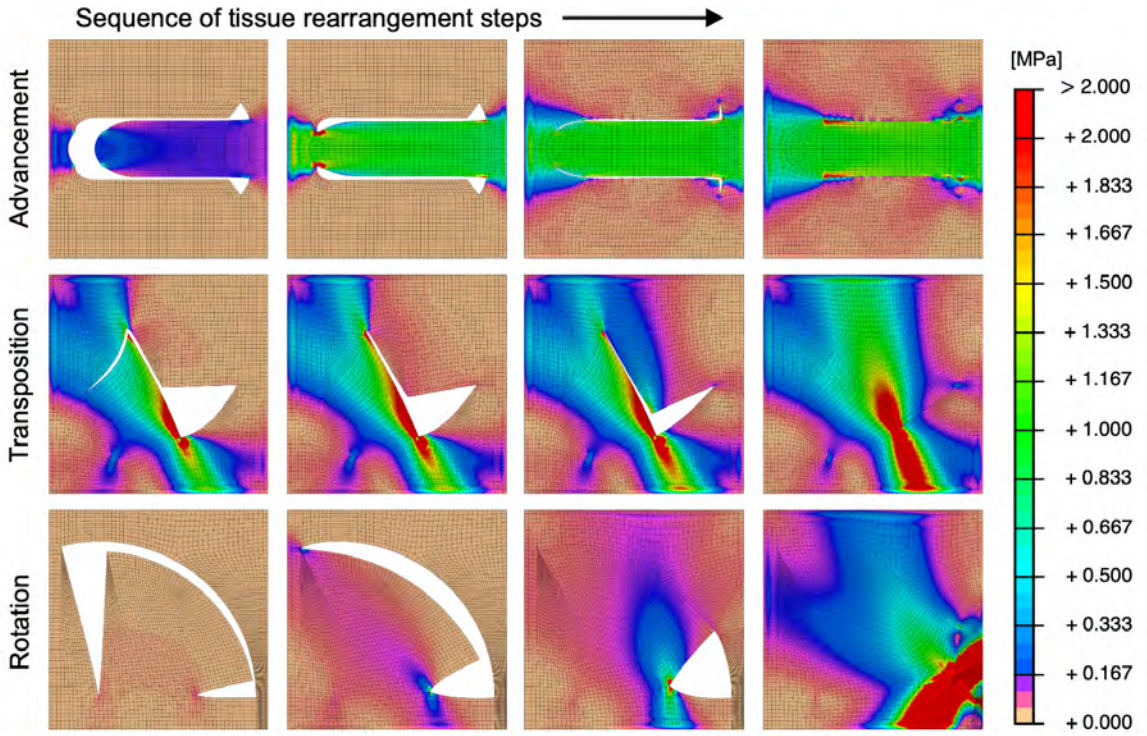

Fig. 9.2.: Results of the finite element simulation for the advancement, transposition, and rotation flaps. Sequential steps in the simulation are shown from left to right. The simulations correspond to the mean values of the parameters in Table 9.1. The contours show the von Mises stress field over the skin patches.

need only 6, 5, and 9 PCs respectively. In addition to compressing the data, the PCs are eigenvectors of the stress for the different material parameters and defect sizes, and they help to understand the dominant modes of deformation. Fig. 9.3 shows the first three PC for each of the flaps. The first PC is undoubtedly associated with the resulting stress contour, but the next two PCs show nonintuitive secondary features.

Recall the notation $\mathcal{D}_t := (\mathbf{x}^{(m)}, y^{(m)})_{m=1}^{4,500}$ for the training data set. Each flap shares the input $\mathbf{x}^{(m)}$ but has different $\mathbf{y}^{(m)}$ based on their own FE simulations and corresponding PCA. Accordingly, the vectors $\mathbf{y}^{(m)}$ have different dimension for different flaps. Three surrogates are created. In each case, the GPR is performed independently for each PC score. For the advancement flap, the resulting surrogate consists of 6 independent GPs. In the transposition flap, training the surrogate entails doing

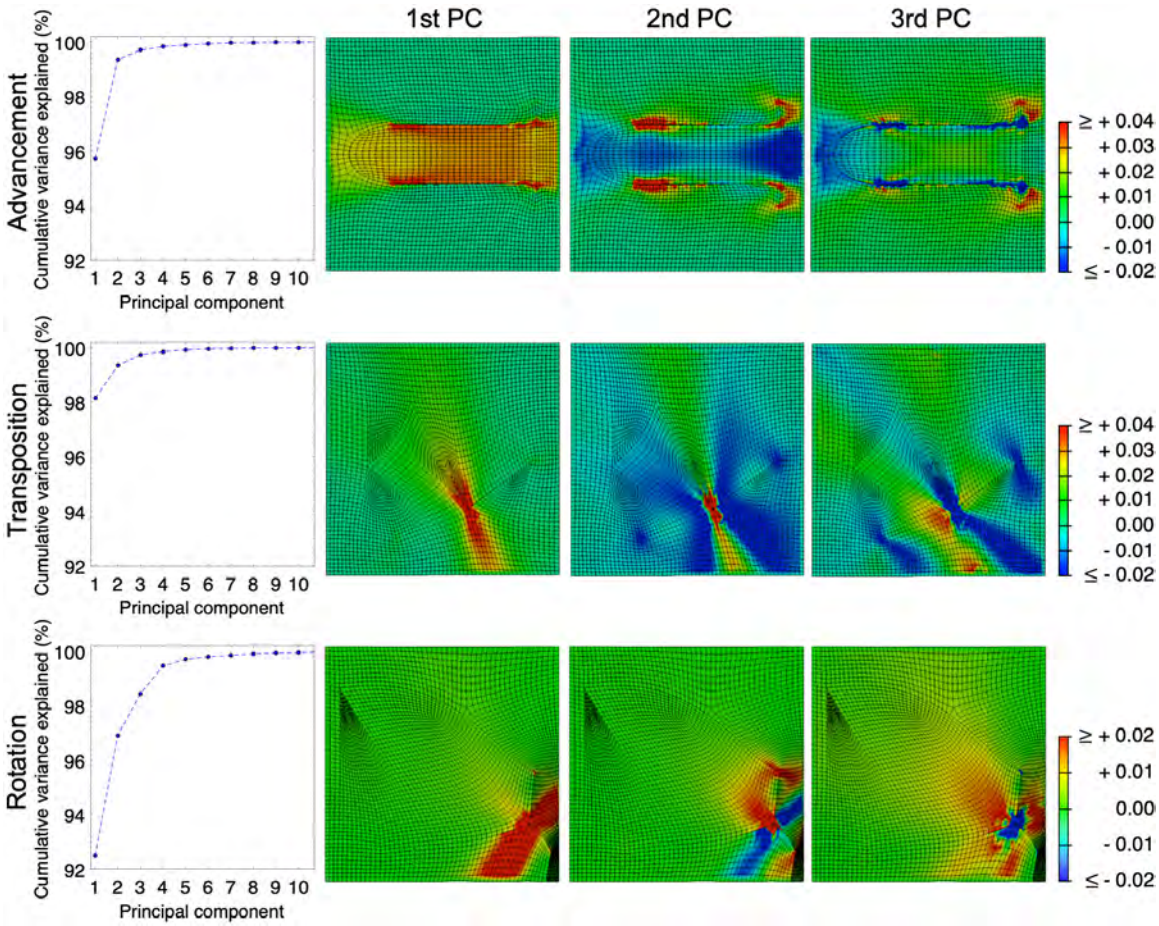

Fig. 9.3.: Principal component analysis of the training data. Cumulative variance is plotted with respect to principal component (PC). Advancement, transposition, and rotation flaps need 6, 5, and 9 PCs to account for 99.9% of total variance. The first three PCs are plotted on the finite element mesh.

the regression to fit 5 GPs. The rotation flap surrogate is made out of 9 independent GPs.

9.3.2 Validation of the virtual surgery surrogates

We denote as $\mathcal{D}_v := (\mathbf{x}^{(m)}, y^{(m)})_{m=1}^{1,500}$ the validation data set to verify the performance of the three surrogates constructed via GPR. Note that the $y^{(m)}$ of $\mathcal{D}_v$ are obtained by projecting the nodal stress output of the FE simulations $\mathcal{D}_v$ on the PCs determined previously, with the training data $\mathcal{D}_t$.

Two analyses are done to validate the surrogates. One assessment is done over the reduced dimensional space and a second error metric is obtained in the full dimensional space. The standardized residual is computed on the reduced dimensional space and it is used to quantify the epistemic error caused by the limited number of training data fed to the GPR (Fig. 9.4**a**). Most of the validation data points fall within the $[-3, 3]$ range, which is a meaningful bound since any point-wise prediction by the GP surrogate is assumed to follow a normal distribution defined in Eq. (9.12). Thus, the histograms of Fig. 9.4**a** reveal that most of the validation data points indeed fall within the 99.7% confidence range predicted by the GP surrogate. On the other hand, a small number of data points are outside the $[-3.5, 3.5]$ range, indicating that these predictions are deviated away from the confidence range. This is caused by the epistemic error of the posterior GP, and reflects regions of the parameter space that may have remained unexplored.

Another validation procedure is implemented over the nodal stress space. The predictive PC scores are passed through the inverse PCA. By constructing the full-dimensional quantity of interest, the nodal stress vectors, out of the predictive PC scores, a direct comparison to the nodal stress values from the FE simulations is possible. Histograms of the l_2-norm of the stress error are shown in Fig. 9.4**b**. We remark that the l_2-norm of the stress error includes two types of error, the one caused by PCA and the epistemic error from the GPR. Since the number of PCs to compress the data were chosen to capture 99.9% of the variance, 0.1% of the variance is intrinsically missed.

The advancement surrogate has an average l_2-norm relative error of 0.019, and 99.1% of the validation points have less than 0.1 error. The average l_2-norm relative error for the transposition flap is 0.021, with 99.5% of points with errors less than 0.1 error. In the case of the rotation flap, the distribution of the error is slightly wider, still 98.1% of the validation set falls within 0.1 error, and the average relative error in this case is 0.026. In all cases, the performance is quite satisfactory.

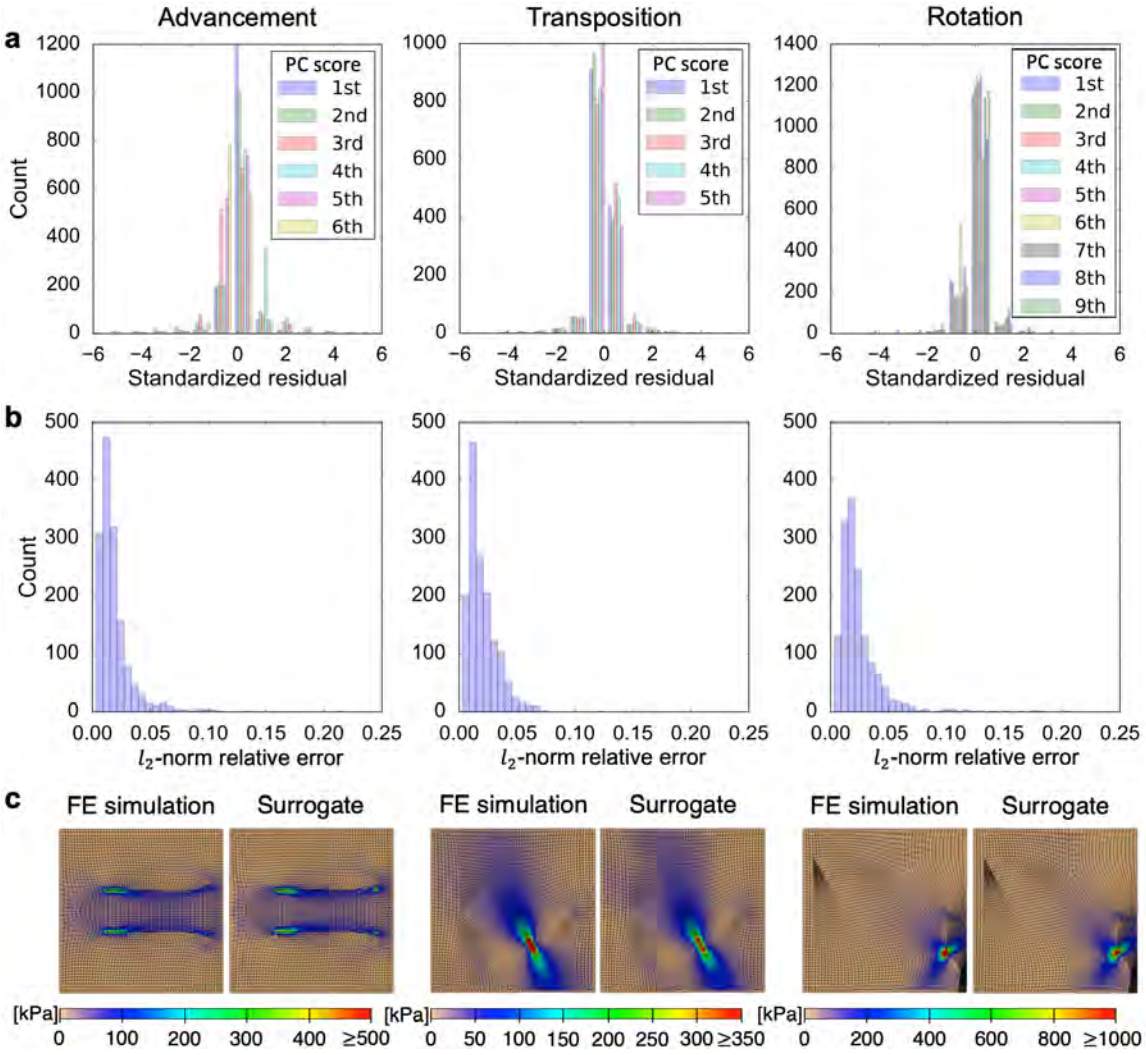

Fig. 9.4.: Validation of surrogate models: The validation data set consisting of $1,500$ inputs per flap is analyzed over the reduced dimensional space (**a**) and the full dimensional space (**b**). The histograms of the standardized residuals for the predicted principal components (PC) fall within the $[-3, 3]$ range, which corresponds to the 99.7% confidence range predicted by the Gaussian process surrogate (**a**). For each flap, the predictive means of the PC scores are inversely transformed to recover the full nodal stress dimensions, enabling the direct comparison to the finite element (FE) simulations in terms of the l_2-norm of the relative error (**b**). Errors in the stress space are less than 5% for almost all validation points, with maximum error values for advancement, transposition, and rotation flaps of 0.22, 0.12, and 0.21, respectively. The points with maximum error show nonetheless a good agreement between surrogate and FE von Mises stress fields (**c**).

To better grasp the magnitude of error, the validation point with the maximum error is plotted in Fig. 9.4**c**. Advancement, transposition, and rotation flaps have maximum errors of 22, 12, and 21%, respectively. The result of the FE simulation is plotted side-by-side with the predicted contour by the surrogate. The contours are remarkably similar, even for these cases of maximum error. Indeed, the error is large because of differences in a few nodes with high stress concentrations, which are missed by the surrogate. Therefore, these overall stress profiles further confirm the excellent qualitative prediction of the stress distribution by the surrogate, even for outlier points.

9.3.3 Application of Gaussian process surrogates to anticipate the effect of aging on the mechanics of tissue rearrangement

Once the surrogate model is validated, it can be used to rapidly and reliably predict the stress field for an arbitrary triad of material parameters (μ,k_1,k_2) and a range of defect sizes ϕ (see Table 9.1). Besides bypassing the need for an FE simulation at a particular input, the inexpensive GP surrogate enables additional investigations, such as uncertainty propagation and model calibration. In this study, the GP surrogates are used to assess the impact of correcting the same skin lesion on two different age groups: young $[60, 334]$ and elderly individuals $[60, 180]$. For the younger group, based on previous reports , it is assumed that the material parameters are normally distributed with mean $\overline{\mu}_y$ = 5.867 kPa, $\overline{k}_{1y}$ = 73.188 kPa, and $\overline{k}_{2y}$ = 73.217, and with standard deviation such that the 95% confidence interval covers ±20% of the means. For the elderly group, based on previous reports [60], the parameters are determined to have means $\overline{\mu}_e$ = 70.820 kPa, $\overline{k}_{1e}$ = 8178.59 kPa, and $\overline{k}_{2e}$ = 80.279, and, just as in the younger group, standard deviations are assumed such that the 95% confidence interval captures ±20% with respect to the mean.

Given the negligible computational cost of the GP surrogates, $1,000$ material parameters are randomly selected from the probability distribution of either the younger

or the elderly group, and the corresponding posterior GP is used to calculate 95% predictive intervals of the predictive PC scores. The surrogate is evaluated continuously for different defect sizes from 20 to 40 mm (Fig. 9.5). Only the first and second PC scores are displayed, the rest of the predicted PC scores are available in the supplementary material. Two different shaded areas are depicted for each group. First, we evaluate just the mean values, ($\overline{\mu}_y$, $\overline{k}_{1y}$, $\overline{k}_{2y}$) or ($\overline{\mu}_e$, $\overline{k}_{1e}$, $\overline{k}_{2e}$). The shaded area in this case captures the epistemic uncertainty of the surrogates when there is no uncertainty in the input, i.e., if the mean material parameters of the young and elderly individuals are the real properties for these groups, then the uncertainty in the prediction is solely based on the limited training data of the surrogates. The other shaded area for each group shows the 95% predictive intervals including epistemic as well as material parameter uncertainty.

Notably, the epistemic uncertainty is similar in the younger and elderly groups for all flap designs. Only the first two PC scores are plotted in Fig. 9.5 but the reader is referred to the supplement for the plots of the other PCs. The epistemic uncertainty does increase for subsequent PCs, but just the first two PCs capture more than 99% of the variance, hence we focus only on these two scores here. Even though the PCs are not directly a stress value, they do carry information about the stress field. Since the inverse transform from the PC scores to the nodal stress vectors is linear, the values and uncertainty in the PC scores translate linearly to the values and uncertainty in the stress fields. The fact that the epistemic uncertainty remains small in all cases, even when the variation in the PC scores is large, provides confidence that the surrogate was trained properly.

The range of variation in the PC scores for the two age groups as the defect size increases is worth emphasizing. For all flaps and both PC scores shown, the predictions for the elderly individuals always span wider ranges compared to the younger group. For the advancement flap, the predictions for the younger group vary over a very narrow range as the defect goes from 20 to 40 mm. This implies that in general the soft skin of the younger group is not sensitive to the size of the defect

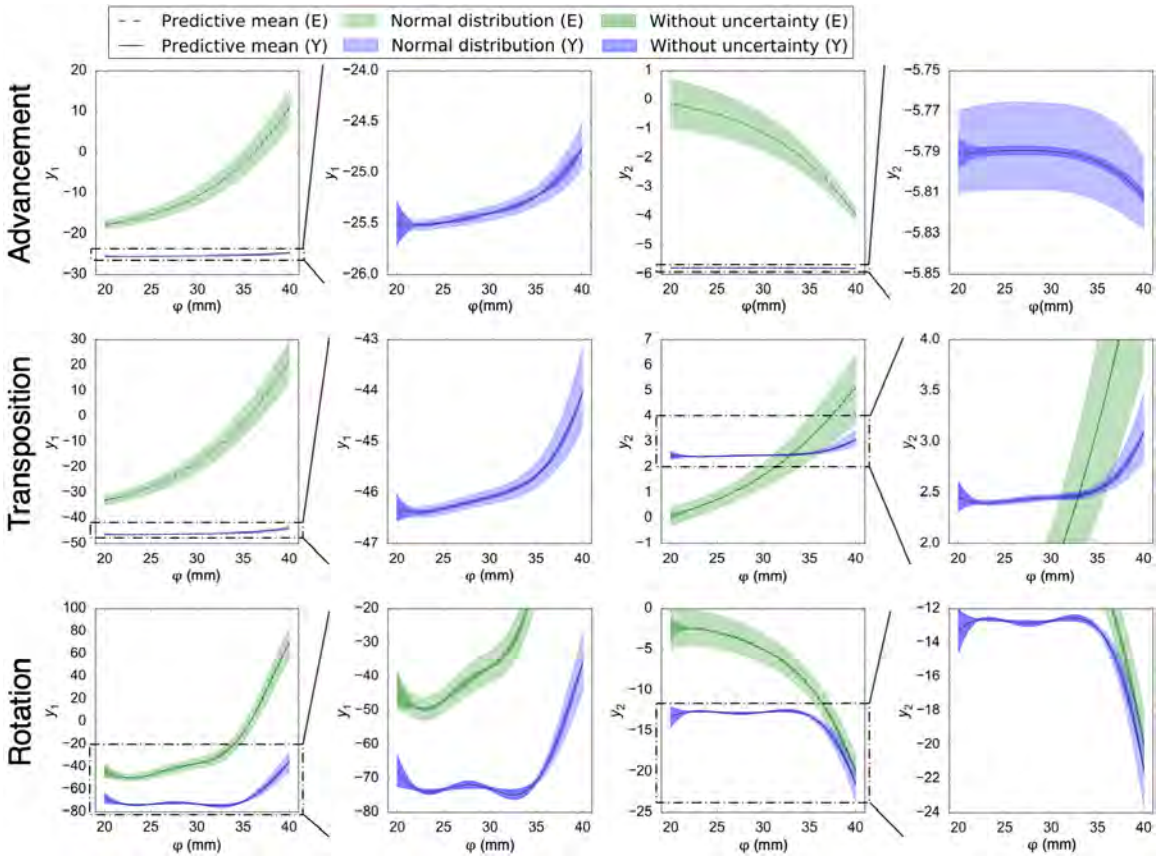

Fig. 9.5.: Predictions of the first and second principal component scores for younger (Y) and elderly (E) groups as a function of defect size ϕ: For each group, predictions are done assuming that there is no uncertainty in the parameters or that the parameters have a normal distribution. Each prediction is accompanied with 95% predictive intervals shows as shaded areas.

being corrected for the advancement flap. This is not true for the other two flaps. For the transposition flap, the response of the younger group for small defect sizes, up to approximately 31 mm, appears linear, with a sharper increase in the prediction as the skin lesion increases from 31 to 40 mm. In the elder group the two PC scores increase in a modestly nonlinear fashion as the size of the defect increases. The most interesting trend occurs for the rotation flap. In the younger group, the predicted scores are linear and insensitive for defects between 20 and 30 mm. However, there is an abrupt increase in the prediction for defects between 30 and 40 mm. In the elderly

group there is a similar response, the predicted scores are not sensitive to ϕ at small defect sizes, but the scores increase for defects larger than 30 mm.

The confidence intervals predicted as a result of the uncertainty in the material parameters are much wider than the epistemic uncertainty intervals. Additionally, the confidence intervals that include material behavior uncertainty change as the defect size increases, in contrast to the epistemic uncertainty intervals which are constant across all plots of Fig. 9.5. In the younger group, the uncertainty tends to increase with larger defect sizes, although not in all cases. For elderly individuals, the effect of material behavior uncertainty on the prediction of the PC sores is counterintuitive. One would expect that increasing stiffness and defect size would always lead to an increase in the uncertainty in the prediction of the PCs, but this is not always the case. For the advancement flap, the younger group shows a constant confidence interval, and the elder group has an increasing uncertainty for the first PC score and decreasing uncertainty in the second PC score as ϕ increases. In the transposition case, the younger group shows a clear increase in uncertainty as the defect size become larger. The elderly group also shows larger confidence intervals with change in defect size, although the trend is less noticeable. For the rotation flaps, the younger group presents a widening of the confidence interval with larger ϕ. In contrast, the elderly group shows a constant confidence interval for all ϕ for the first PC score, and a decrease in uncertainty for the second score.

The observed trends in the reduced dimensional space defined by a few PC scores provide insight into the sensitivity of the response function to the different parameter variations, yet, the PC scores are not directly stress values. Thus, to recover the original dimension of the output and to analyze the results in terms of stress fields directly, we perform the inverse PCA. Fig. 9.6 depicts the 50th percentile of the von Mises stress contours for younger and elderly groups at the smallest skin lesion evaluated with the GP surrogate, ϕ = 20 mm, as well as the largest lesion of 40 mm. The stress distributions qualitatively match those illustrated in Fig. 9.4. The advancement flap induces greater deformation and stress along the distal end, the

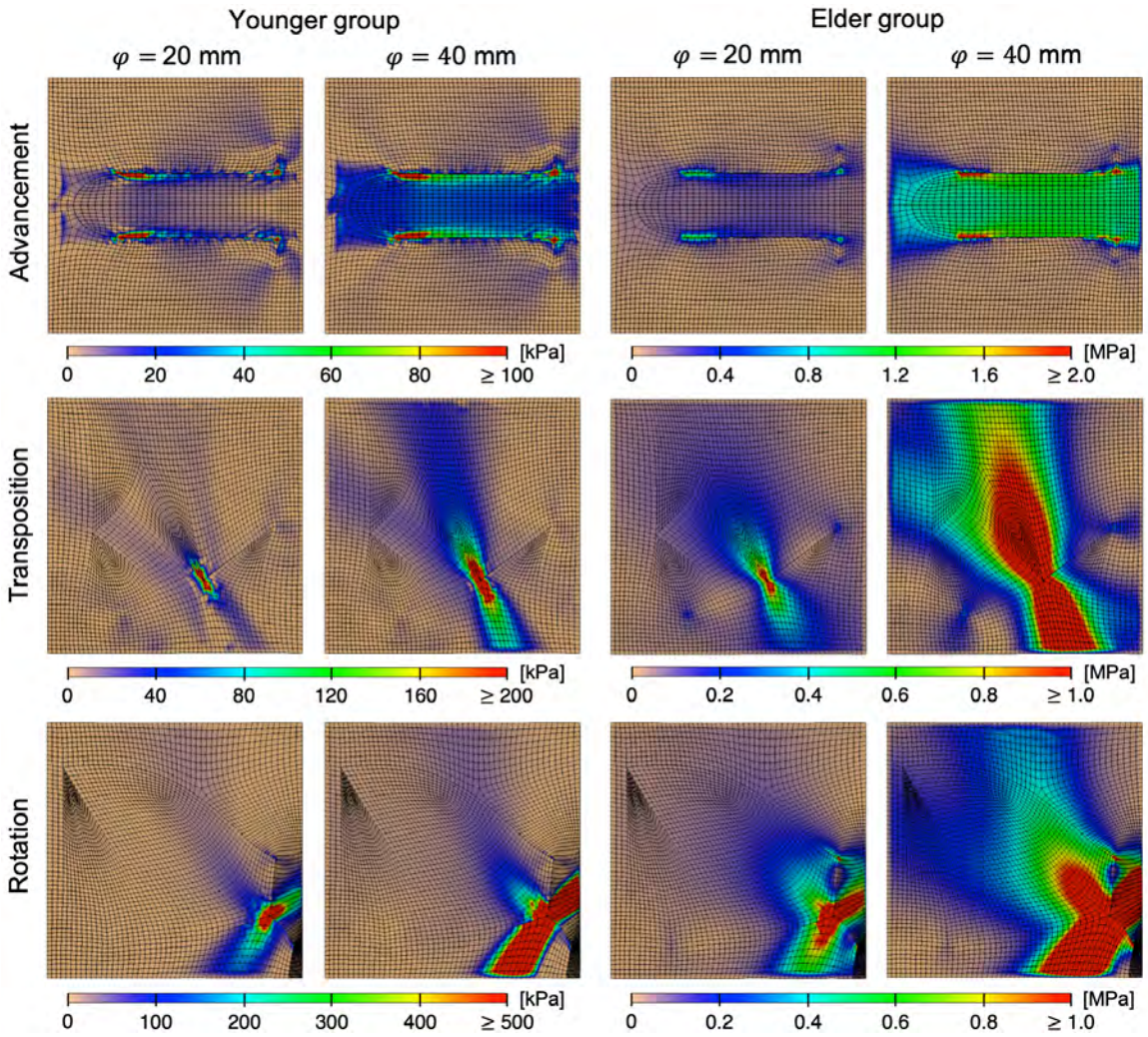

Fig. 9.6.: The surrogate model for the von Mises stress predicts younger and elderly groups. The von Mises stress contour to close biggest, ϕ = 40 mm, and smallest, ϕ = 20 mm, defect is represented for advancement, transposition, and rotation flaps.

transposition flap induces a band of high stress oblique to the flap displacement, and the rotation flap concentrates stress at the end opposite to the location of the lesion being resurfaced.

As expected, there is a clear increase in stress with larger defects. This change is particularly obvious for the younger group. For this group, in fact, the small lesion size, ϕ = 20 mm, leads to negligible stress values in the three reconstructive strategies.

For the elderly individuals, the largest defect size induces larger stresses in all cases, but the change is more noticeable in the advancement scenario.

Even though only the predictive mean is shown in Fig. 9.6, the surrogate outputs the probability distribution of the stress corresponding to the distribution of the parameters. Having a probability for the stress we can, in turn, define metrics more directly related to clinical judgement. For instance, we hypothesize, based on experiments done in pigs [4], that von Mises stresses beyond 200 kPa have a higher rate of complication. Therefore, Fig. 9.7 shows the probability of exceeding this threshold.

While clearly the elderly individuals have a higher coverage of these at-risk regions, the younger population does show some of these regions as well. For the elderly group,

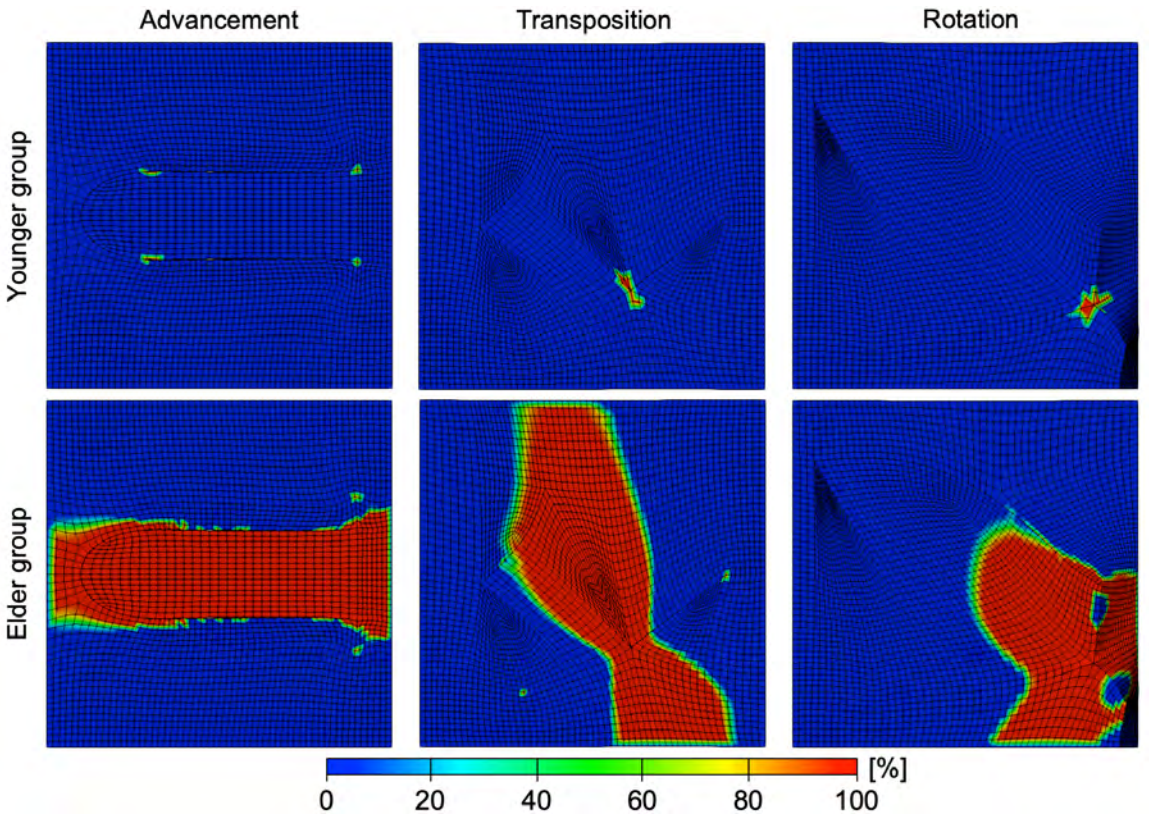

Fig. 9.7.: Probability to exceed a von Mises stress value of 200 kPa for the 30 mm defect when the material parameters of the younger and elderly groups follow a normal distribution centered around values of the parameters informed by the literature. The probability contours for this event (exceeding a threshold value) are sharper compared to the underlying stress fields.

there is a high probability of exceeding 200 kPa in all three scenarios. This trend is clearest in the advancement flap, where the entire flap is at risk, and this region extends to the surrounding skin at the distal end and at the base of the flap, whereas the skin to the sides of the flap are not affected. For the transposition flap, the region with high probability of exceeding 200 kPa is oblique to the design of the flap. In case of rotation flap, the corner opposite to the defect is the most at-risk based on the proposed metric.

Finally, we recognize that the entire stress field may not lead to the best predictor of complications in the clinical setting. We hypothesize that the stress along the suture line will provide valuable information to anticipate wound complications [3]. Thus, we also create GP surrogates for the normal component of the stress along the suture line. Fig. 9.8 shows in red the curves of the suture line at the end of the procedure for each of the flaps. The curve associated with the final suturing pattern is parameterized with respect to normalized arc length.

Fig. 9.9 shows the prediction of the normal stress along the suture curve for the younger and elderly groups for all the range of ϕ in the advancement case. The predictive mean for the two age groups corresponds to evaluating the surrogate at the mean value of the parameters, $(\overline{\mu}_y, \overline{k}_{1y}, \overline{k}_{2y})$ or $(\overline{\mu}_e, \overline{k}_{1e}, \overline{k}_{2e})$. The upper and lower

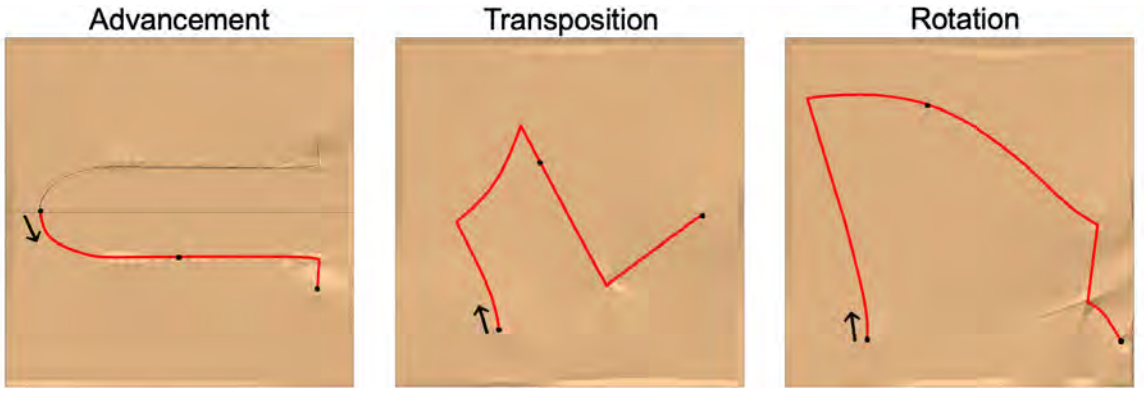

Fig. 9.8.: Suture curve at the end of the procedure for the advancement, transposition, and rotation flaps: Three points on the suture curve indicate locations 0, 0.5, and 1 in terms of normalized arc length.

bounds indicate the 95% predictive intervals resulting from the fact that the younger and elderly groups are assumed to follow normal distributions as described before. The points along the suture curve with high stress remain the same for different defect sizes. Consequently, the plots of Fig. 9.9 show vertical bands of high stress. For the younger group, the distal end, located at the beginning of the suture curve, shows the highest stress. However, there are four more bands of stress, two near the distal end, and two more narrow regions of high stress close to the base of the flap, near the Burow's triangle [342]. The normal stress along the suture curve is higher and smoother for the elderly group compared to the younger group. At smaller defect sizes, the distal end of the flap is not the most critical location in the elderly group. However, as the defect size increases, the stresses along the suture in the distal end become more important. The elderly group also shows two other bands of high stress, one near the distal end, and one near the end of the suture curve, at the base of the flap.

The contours in Fig. 9.10 show the normal stresses to the suture curve calculated with the surrogate for the transposition flap. The defect size is continuously changed in the range $\phi \in [20, 40]$ mm. The sharp corner near the end of the suture curve, at the base of the flap, experiences the highest stress in both age groups. At low defect sizes this region is narrow, and it expands as the defect size increases. In the younger group, the effect of the defect size is less noticeable compared to the elderly group. Additionally, the elderly group shows a secondary high stress feature in the range $[20, 40]$ of normalized arc-length as the defect size increases. This region corresponds to the second segment in the suture curve (see Fig. 9.8).

Fig. 9.11 showcases the distribution of the stresses along the suture curve for the rotation flap. Consistently with the observations from the stress contours in Fig. 9.6, the stress along the suture curve is highest at the distal end, whereas the region from which the defect was excised is closed with very low normal stresses. As opposed to the transposition flap, in the case of the rotation flap the band of high stress stays

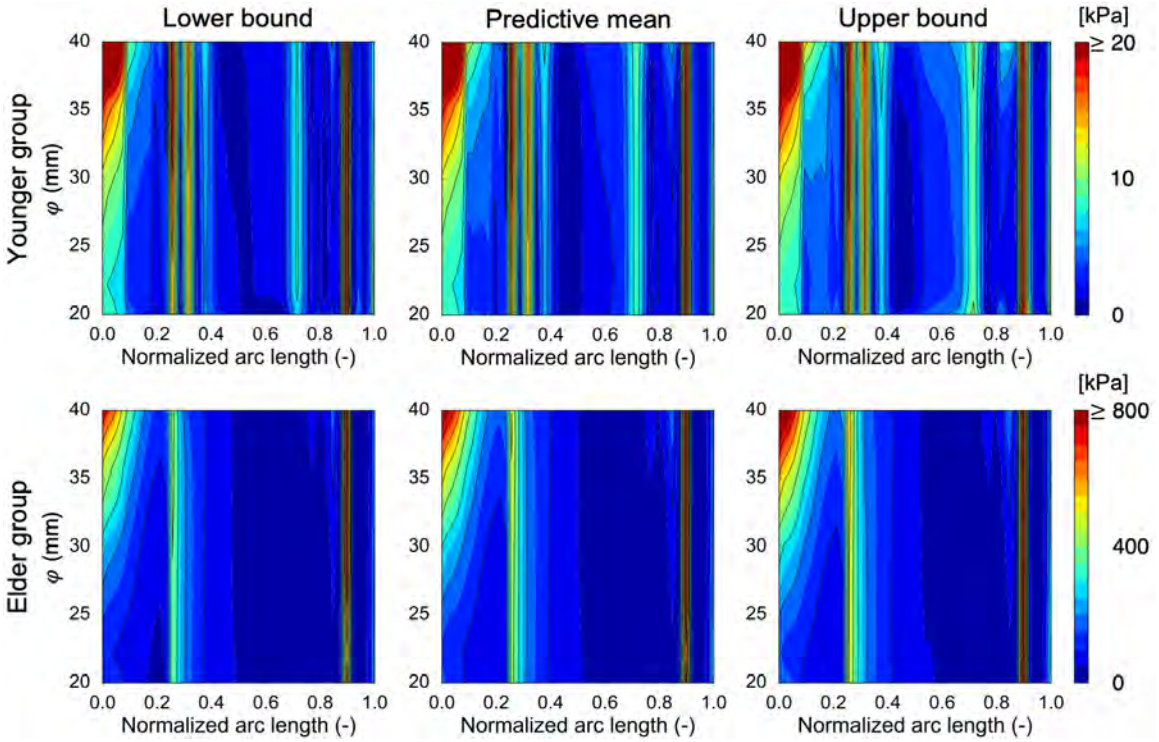

Fig. 9.9.: Normal stress along the suture curve for the advancement flap: the predictive mean is derived from the exact input value of younger and elder groups, while the upper and lower bounds of the 95% predictive intervals are obtained considering a normal distribution for younger and elderly groups. Prediction of the normal stress is plotted with respect to normalized arc length for every defect size, $\phi \in [20, 40]$ mm. The distal end of the flap, corresponding to normalized arc length in the range $[20, 40]$, shows the highest stress, which becomes a more prominent feature as the defect size increases.

relatively narrow as the defect size increases. Other features along the suture curve do become more evident, but the Y-shaped corner at the base of the flap is dominant.

9.4 Discussion

The goal of this study was to build inexpensive surrogate models to easily evaluate stress contours for arbitrary material parameters and a range of defect sizes in the three most common flap strategies used today: advancement, transposition, and rotation flaps. Here we showed that replacing high fidelity models with efficient surrogates

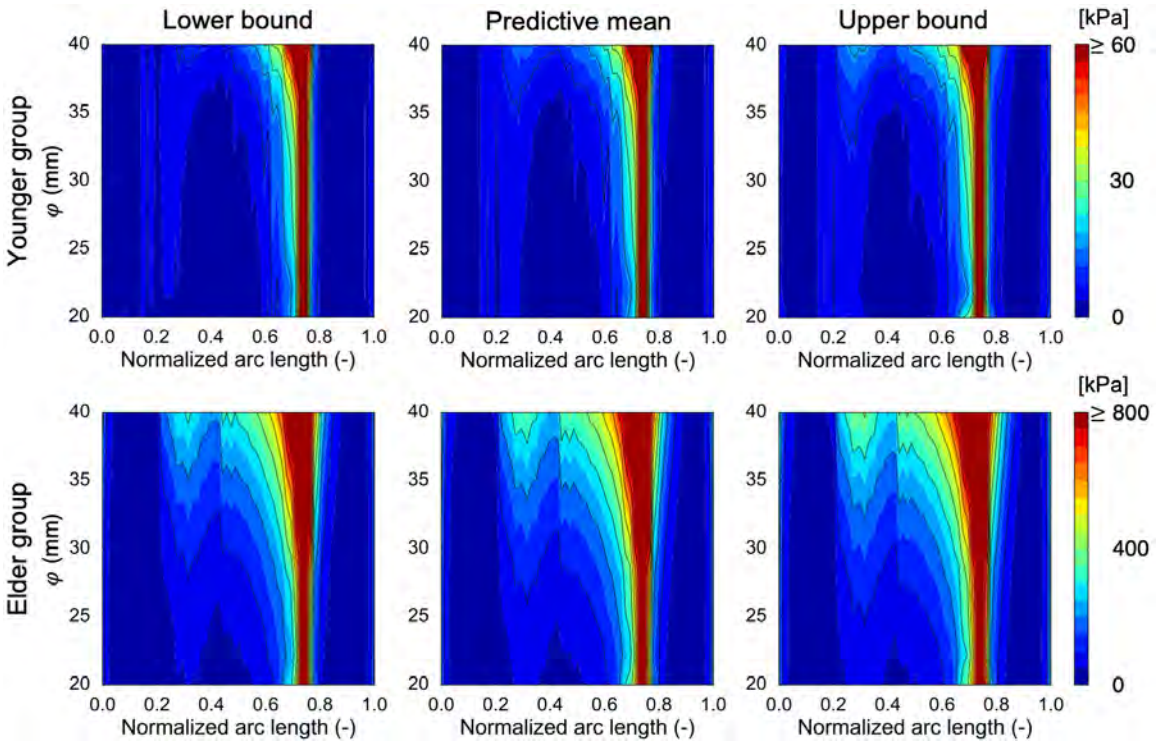

Fig. 9.10.: Normal stress along the suture curve for the transposition flap. The predictive mean is derived from the exact input value of younger and elderly groups, while the upper and lower bounds of the 95% predictive intervals follow from considering uncertain parameters for the younger and elderly groups. The y-axis in the plots depict the variation in the normal stress features as the defect size changes in the range $[20, 40]$ mm. A band of high stress appears in all plots, and corresponds to the corner point in the suture curve, near the base of the flap. The elderly group shows a widening of this high stress region with increasing defect size, as well as a secondary stress feature for the arc length region $[0.2, 0.4]$, corresponding to the second segment in the suture curve.

is possible by first taking stress contours generated with detailed simulations across the input space, and reducing the dimension of the data with PCA. This step allows compression of the training data which is essential to the computational efficiency we sought. The second step entailed the use of GPR to learn a probabilistic description of the response surface. The key advantage of GPR is the ability to quantify the epistemic uncertainty of the surrogate, which is needed to assess our confidence in any given prediction, and has implications in uncertainty propagation, surrogate model training, inverse problem solution, and model calibration.

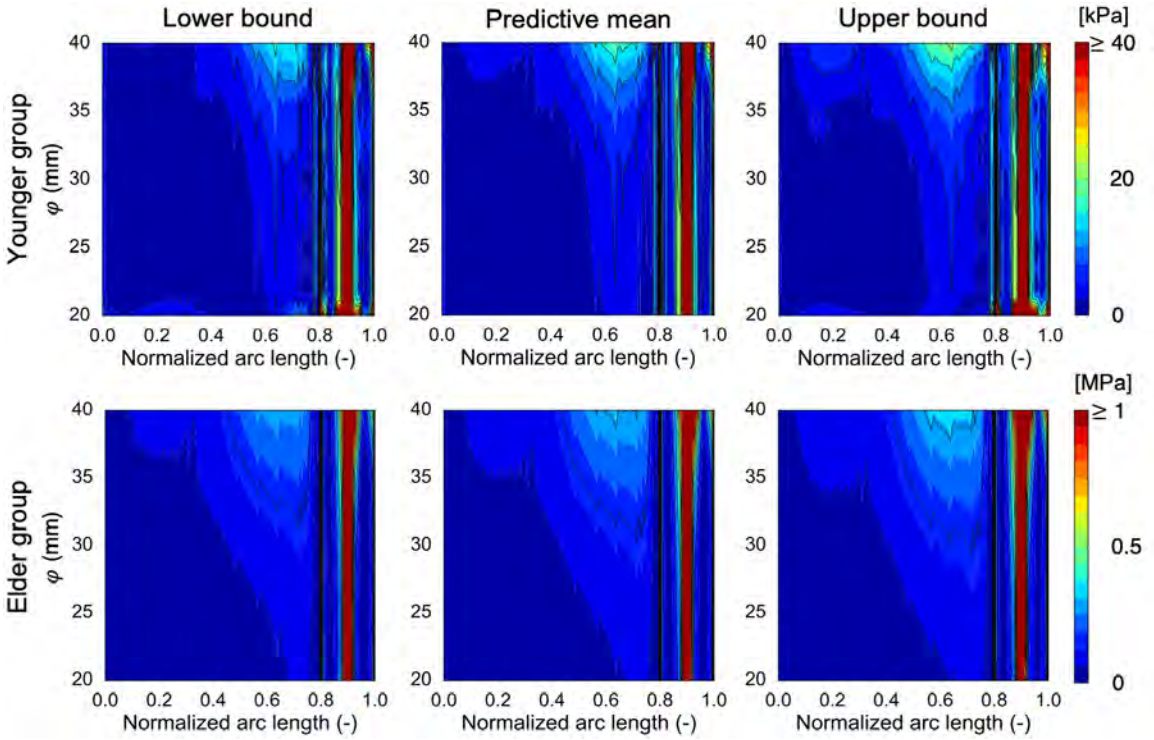

Fig. 9.11.: Normal stress along the suture curve for the rotation flap considering defects in the range $\phi \in [20, 40]$ mm. The predictive mean corresponds to evaluating the surrogate at the mean value of the parameters for the younger and elderly groups. Sampling normal distributions around these means leads to a confidence interval for the normal stress along the suture curve. The lower and upper bounds of the 95% confidence interval are shown. The stress normal to the suture curve is highest at the distal end. The band of high stress is narrow and remains constant as the defect size changes. A secondary stress feature for the arc length interval $[0.5, 0.8]$ appears as ϕ increases.

Current state of computational modeling of soft tissues has been beneficial for the adoption of surgical simulators in resident training, where a realistic deformation is needed but a predictive stress profile is not [90]. Unfortunately, this usually implies the use of a simplified model of skin's mechanical behavior. To change the landscape of application of tissue mechanics simulations, and make predictive computations of stress profiles an integral part of preoperative planning, there is a need to increase computational efficiency while keeping fidelity. A niche already exists for finite element simulations in surgical planning because stress contours are known to be a

determinant factor in wound complications but they cannot be easily anticipated or measured in the operating room [3, 8]. Yet, while finite element models are suited to address this gap, the current pipeline needs expert input and is time consuming [99, 248]. The work presented in this paper is able to replace a high fidelity model with an inexpensive one that nonetheless preserves a high accuracy. This result obviously comes at a cost, but the strategy is to spend a greater computational effort offline in order to avoid the need of the detailed finite element simulation in the clinical setting. This idea has been powerful in multi-objective design optimization [311], and to learn the constitutive behavior of materials [343]. This idea has also appeared in surgical simulators, with an emphasis on achieving real-time performance with increasingly more fidelity in the response [331].

Our work hinges on data compression with PCA, and shows that over a wide range of material properties spanning several orders of magnitude, the response of the finite element simulation can be captured with just a few degrees of freedom. PCA distills a large set of stress contours into a handful of eigenvectors or main stress modes. Even if the mesh is fine, consisting of approximately 10,000 nodes, less than 10 PCs are needed to capture 99% of the variance in the data. This is possible because the features of the stress contours are primarily driven by the geometry of the flap design, and the variation in the material behavior has a greater influence on the magnitude of these features but less so on the features themselves. This raises the question of how patient-specific geometries can influence the variation in stress contours, which is part of our ongoing work.

Interestingly, we confirm that the stress distributions are strongly dependent on the flap design. The three flaps studied produce vastly different responses. The sensitivity to the incision contour and the suturing strategy evidences a large design space that remains unexplored. The reconstructive surgery community has converged to a handful of designs guided by mechanical intuition and trial and error, without engineering optimization tools to explore the entire design space. Our results confirm some of the intuition reported by clinicians. In the case of the advancement flap,

for example, stress is high at the distal end, which has motivated guidelines for the maximum dimension of this kind of flap in order to avoid distal tip necrosis [287]. The transposition flap has been advocated as a design to direct the stress contours with respect to the skin tension lines. While we do not consider anisotropy in this study, we do see a stress band oblique to the overall displacement of the skin in the transposition case, aligned with the intention of the surgeons. The rotation flap creates a zone of high stress in the proximal end compared to the distal end. This distribution of stress in the rotation flap has not been described before. As mentioned previously, the stress contours do change with variation in the defect size and material parameters, but the features or stress modes are dictated by the flap design. These results suggest future research to elucidate the variation of the stress contours for arbitrary incision lines and suturing patterns.

Ample mechanical testing of skin has led to increasingly more accurate constitutive models, and more comprehensive documentation of skin's mechanical behavior [29, 45, 184]. At the same time there is no consensus yet as to which is the best choice of constitutive model for a particular application [118]. Additionally, the uncertainty in material behavior is an inherent feature of biological materials. These challenges have been unmet in practice, and finite element simulations with a single set of material properties are extremely common. To make computational tools a part of preoperative planning, it is imperative to build predictive tools that propagate the uncertainty in material properties and output confidence intervals for a given prediction [100]. In the present work we inform the distribution of material properties with the values available in the literature. The GOH model, common for collagenous tissues, has been used to fit the response of skin. The data is still limited, particularly since material parameters are known to vary with age, gender, and anatomical location [184]. The parameter space for the GOH model reported in the literature is extremely large, raising the question of whether or not this parameter space is reliable, and suggesting future experimental work to better characterize the mechanics of human skin. In view of our limited knowledge of the GOH parameter distributions to realistically describe

human skin, we trained the surrogates over a wide parameter space and sampled this space uniformly using LHS. This strategy leads to the creation of general surrogates that then allow us to propagate any other, more realistic and narrower probability distribution of the parameters.

Suction devices have become extremely popular in recent years because they enable *in vivo* testing of human skin, promising the acquisition of more comprehensive data on the variation of human skin mechanical behavior [27,181,303]. The data from these devices is, on the other hand, even less comprehensive compared to *ex vivo* experiments such as biaxial testing [23,344]. We foresee that *ex vivo* data will continue to refine our knowledge of material parameter distribution as a function of age, sex and anatomical location, and that the low-fidelity suction tests done *in vivo* will allow quick calibration of the prior distribution of parameters for a specific patient.

The notion of anisotropy is one that we do not address in this paper but that has been emphasized by clinicians, who use skin tension lines to guide the flap design [289,290,345,346]. Adding anisotropy as an additional source of uncertainty is a clear future direction of our research.

Based on the current information available in the literature, we used the surrogate models to explored the sensitivity of the flaps to the variation in material properties associated with aging. The degree of uncertainty over the response surface increased as the size of the defect to be corrected was increased. This is due to the nonlinear nature of the constitutive model, which becomes more pronounced at larger deformations. Surprisingly, transposition and rotation flaps for the younger group but also, to a lesser extent, in the elderly group, were not sensitive to the input data for small defect sizes. Therefore, exact measurements of skin properties are probably not critical to close relatively small defects, up to 30 mm in diameter. However, for larger defects the increase in stress becomes very sensitive to the material parameter distribution.

Focusing on the response with aging, we find that the distribution representing elderly individuals responded more sensitively to the uncertainty in the input data

compared to the younger group. This is also a consequence of the nonlinear behavior of the constitutive model which is more pronounced in stiffer tissue compared to softer tissue at a given deformation. The immediate implication of these findings is that the accurate measurement of skin properties becomes more important with aging.

We showed that the surrogates can be used to estimate zones of concern by calculating the probability of the stress passing a certain threshold. Here we assumed the threshold to be 200 kPa based on previous reports on an animal model [4]. Unfortunately, the best metric for anticipating wound complications in humans in response to excessive tension is not known yet. There is no doubt that excessive stress leads to complications [5, 292, 347], but this effect is achieved in combination with other factors such as inflammation and changes in blood supply. We hypothesized that normal stresses along the suture curve could be a good indicator of complications. This metric does capture some regions that have been reported to show complications in humans, such as the distal end of advancement flaps [287, 304]. However, it also showed locations of high normal stress at sharp corners of the suturing contour, which are not necessarily associated with complications [342]. Combining the current surrogate models with *in vivo* mechanical testing of skin with a suction device, we expect to enable model calibration for patient specific cases in order to investigate which quantities of interest derived from the stress fields are the best predictors for wound complications.

9.5 Conclusion

In conclusion, principal component analysis and Gaussian process regression have enabled us to replace high fidelity nonlinear finite element models of common flap strategies, with computationally efficient surrogates. We have demonstrated that the Gaussian process surrogates can be used to investigate the effect of material behavior uncertainty associated with aging, as well as the variation in the size of the skin lesion that needs to be corrected. The present methodology can also be extended to capture

a wider range of flap designs, skin patch geometries, and anisotropy. Paired with *in vivo* testing of skin, which is becoming increasingly feasible, we expect that our work will enable us to determine quantitatively how exactly excessive stresses correlate to wound complications, and to use this information for preoperative recommendations in the near future.

10. IMPROVING RECONSTRUCTIVE SURGERY DESIGN USING GAUSSIAN PROCESS SURROGATES TO CAPTURE MATERIAL BEHAVIOR UNCERTAINTY

Abstract: To produce functional, aesthetically natural results, reconstructive surgeries must be planned to minimize stress because excessive loads near wounds have been shown to produce pathological scarring and other complications. Presently, stress cannot easily be measured in the operating room. Consequently, surgeons rely on intuition and experience. Predictive computational tools are ideal candidates for surgery planning. Finite element (FE) simulations have shown promise in predicting stress fields on large skin patches and complex cases, helping to identify potential regions of complication. Unfortunately, these simulations are computationally expensive and deterministic. However, running a few, well selected FE simulations allows us to create Gaussian process (GP) surrogate models of local cutaneous flaps that are computationally efficient and able to predict stress and strain for arbitrary material parameters. Here, we create GP surrogates for the advancement, rotation, and transposition flaps. We then use the predictive capability of these surrogates to perform a global sensitivity analysis, ultimately showing that fiber direction has the most significant impact on strain field variations. We then perform an optimization to determine the optimal fiber direction for each flap for three different objectives driven by clinical guidelines. While material properties are not controlled by the surgeon and are actually a source of uncertainty, the surgeon can in fact control the orientation of the flap with respect to the skin's relaxed tension lines, which are associated with the underlying fiber orientation. Therefore, fiber direction is the only material parameter that can be optimized clinically. The optimization task relies on the efficiency of the GP surrogates to calculate the expected cost of different strategies when the uncertainty of other material parameters is included. We propose optimal flap

orientations for the three cost functions and that can help in reducing stress resulting from the surgery and ultimately reduce complications associated with excessive mechanical loading near wounds.

10.1 Motivation

Reconstructive surgery requires balancing long term tissue functionality while producing aesthetically natural results [7, 291, 330]. Complications such as wound dehiscence, pathological scarring, and skin necrosis are partially caused by excess stress, clinically referred to as tension, especially along suture lines [3, 35, 267–269]. However, measuring stress in the operating room is not practically possible to date with the exception of research studies [8, 348]. Thus, surgeons rely on intuition built from experience and training to estimate skin tension and plan the surgery [326, 330, 349, 350]. This approach is not quantitative, making it difficult to train residents on objective metrics. In addition, the skin tension is estimated at a point in the process where changes to the surgical plan are no longer feasible - for example, once surgical excision of a skin lesion has already occurred. In view of these limitations, high fidelity computational models of tissue mechanics can be used to recreate virtual surgery scenarios and estimate the stress distribution from a given surgical plan [14, 100]. However, a longstanding limitation of computational models is the difficulty to incorporate inherent variability and uncertainty of skin mechanical behavior between individuals [101, 184]. Another challenge is that high fidelity models are too computationally expensive for routine clinical use [17, 19]. Here, we seek to overcome these problems in the context of local cutaneous flaps by creating Gaussian Process (GP) surrogate models from detailed finite element (FE) models. The surrogate models are computationally inexpensive, yet they are accurate over a wide range of material parameters, including anisotropy. We show that these GP surrogates, being computationally affordable, can be leveraged to easily solve flap optimization tasks requiring a large number of function evaluations.

Local flaps are commonly used to repair cutaneous lesions such as skin cancer or burn lesions [295, 326, 351]. Local flaps have several aesthetic advantages over other reconstructive techniques, including having the same color, hair bearing properties, and blood supply as the skin surrounding the lesion. Local flap designs can be classified based on their geometry, i.e., the pattern of the incision and the pairs of points along the edges of the flap that are brought together by sutures [329, 352]. While new flap designs are still being proposed [8, 353], the most common are currently the advancement, rotation, and transposition flaps [329, 330] (see Fig. 10.1). Here, we start from these three flap designs and create detailed FE models to predict the resulting strain contours over the flap and surrounding skin. Strain is selected as the quantity of interest in this study because, unlike stress, strains can be measured non-invasively even in the operating room with the use of 3D photography or multi-view stereo (MVS) [99, 115]. Moreover, strain measurements have been linked to compression of the flap in the thickness direction and collapse of the microvasculature leading to ischemia and subsequent complications [354].

Previous examples of FE simulations of reconstructive surgery have improved our understanding of basic features of stress and strain profiles for common flaps. Additionally, they have already gained recognition as a promising tool for prediction of potential healing complications in personalized cases [14, 18, 99]. However, as mentioned above, FE models are computationally expensive and deterministic in nature, while flap parameters and skin material properties in clinical settings entail unavoidable uncertainties that cannot be captured with a single FE evaluation [23, 51, 185]. Instead, many FE simulations would be required to propagate uncertainties through the model, which is not feasible in routine clinical settings. Optimization of flap design using FE simulations is also challenging on a budget [17]. Thus, FE simulations are not ready for clinical use. Unfortunately, this means that current recommendations are described in qualitative terms such as *feel* or *manual estimation* of tension [349].

Machine learning tools can be leveraged to reduce the computational burden of detailed computational simulations by learning inexpensive metamodels of the original

high fidelity models [156, 355]. For example, stress and strain features as a function of different inputs can be learned using machine learning tools such as GPs [101, 160]. This and other machine learning approaches have been used in other fields of computational physics applied to medical problems, for example to replace computational fluid dynamics models with deep neural networks [168], or to capture cardiac electrophysiology [157, 159]. A recent perspective on the integration of machine learning methods and physics-based models covers more examples, and also highlights the current challenges and opportunities in this field [356].

Here, we first obtain a reduced order representation of the strain fields through principal component analysis (PCA). Then, the data consisting of the reduced output with its corresponding input (material parameters including anisotropy), is used to train a computationally efficient GP surrogate. The GP surrogates are trained on a few well-selected FE simulations, but predict stress and strain accurately for arbitrary material properties within a broad range.

The work shown in this paper extends the previous work in this area through considering anisotropy, which is a key feature of soft tissues, including skin [57, 180]. More importantly, in the clinical scenario, most of the material parameters describing skin's mechanical behavior are highly uncertain except for the anisotropy direction. Starting from the seminal work of Langer in the nineteenth century, the anatomy of skin anisotropy has been well documented [42, 357, 358]. The relaxed skin tension lines, which are associated with the underlying fiber direction, are the most common anisotropy feature used surgical planning [345]. Our sensitivity analysis reveals that the anisotropy direction is the most important material parameter affecting the final strain distribution. Since the surgeon can actually control the orientation of the flap with respect to the relaxed skin tension lines, which we consider indicative of fiber direction, we optimize the flap orientation posing objective functions that reflect clinical guidelines [32, 349, 359].

10.2 Methods

10.2.1 Automating generation of finite element models

We create a base model of the incision geometry for each of the three flaps using Abaqus Standard (Simulia, Boston, USA). Unlike previous work [101], we restrict our attention to a circular, two dimensional domain. The plane stress formulation is accurate for modeling skin because it is a thin membrane [344, 360], although more detailed models accounting for the multiple skin layers are also possible [361, 362]. In the cutaneous flaps shown here, the loading is expected to be within the skin plane and primarily under tension. Therefore, the dermis is expected to be the major contributor to the mechanical response of the tissue [37,178], and the contributions of the other two skin layers, epidermis and hypodermis, are ignored. In previous work, setting up the incision geometry, boundary conditions and material parameters was done manually. This is a time consuming, inefficient process. Our long term goal is to bypass manual model creation. As a first step in this direction, we automate input file generation with a Python script which takes inputs of a few key points and the original Abaqus input file. The script automatically identifies the flap edges, generates the suturing scheme, and imposes boundary conditions taking into account the flap edges. Automating further the geometry of the incision pattern is a logical next step, but not explored in this paper. We focus on the material behavior uncertainty and consider a single suturing scheme and a single set of fixed boundary conditions. A wider set of simulations varying the flap design more broadly is ongoing work. For the simulations in this paper only the outer edge is fixed. The suturing scheme is illustrated in Fig. 10.1. Sutures are imposed as linear constraints between pairs of nodes, which are gradually imposed to bring the corresponding edges together, analogous to the actual procedure [14]. The script for input file generation is available with this submission. To aid in convergence, we allowed some of the simulations to add dissipation for stabilization of the solver. While this introduces an error in the prediction, we enforced this error to be very small since only a small number of

simulations required this artificial dissipation and we kept the artificial energy as low as possible.

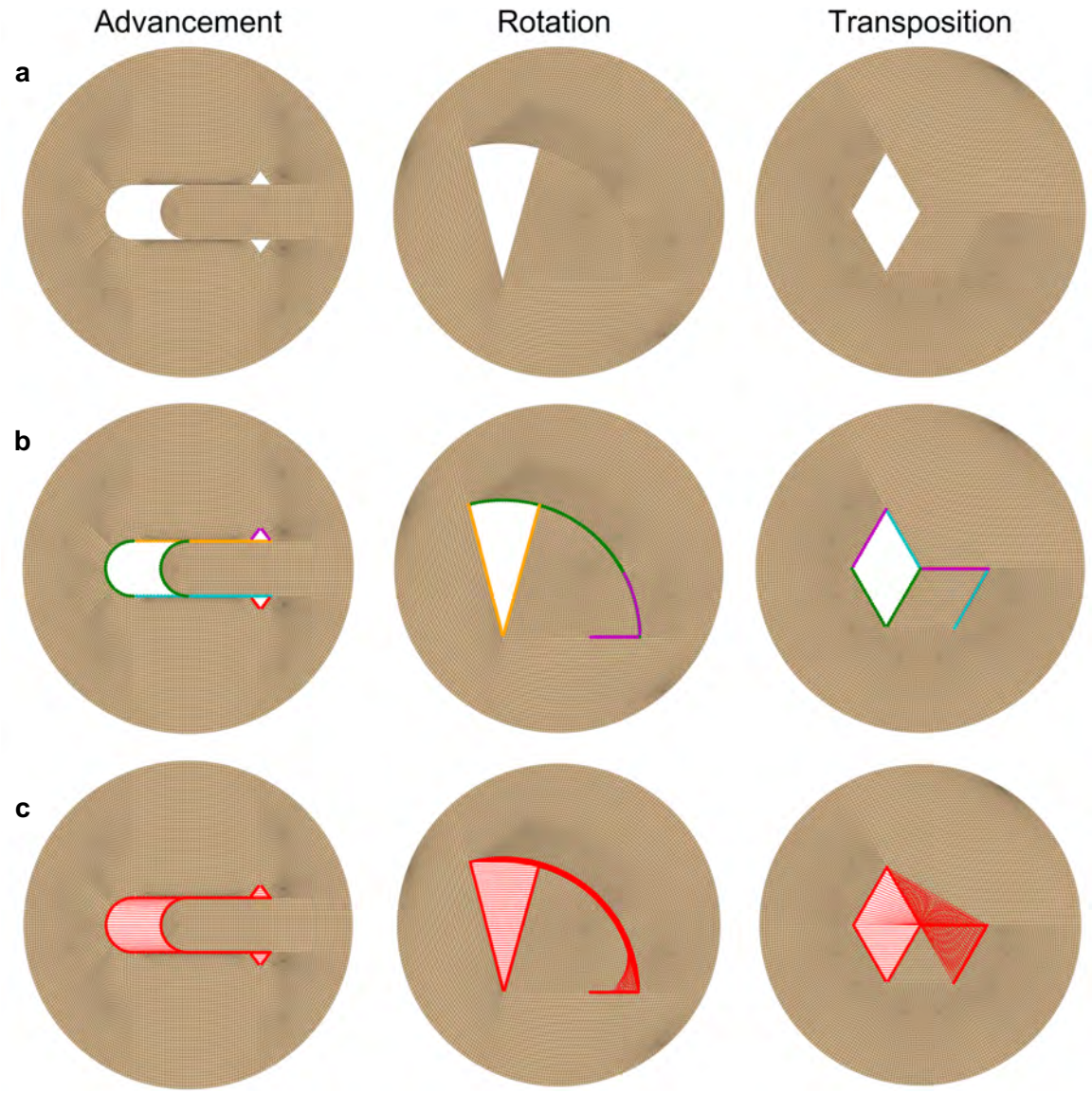

Fig. 10.1.: The three most common flap designs are advancement, rotation and transposition flaps. Finite element models of the flaps are generated semi-automatically. Base flap design generated manually in Abaqus (**a**). Automatic identification of the edges (**b**). Matching colored edges in each design are brought together by sutures to close the skin. Adjacent skin regions to the edges are also identified and used to impose essential boundary conditions. In this case, only the outer perimeter is fixed. Suturing pattern imposed as linear constraints between pairs of nodes are applied gradually to bring the flap together (**c**). In this case, the sutures are mapped across the paired edges such that they have a uniform spacing.

10.2.2 Constitutive model of skin

The mechanical response of the dermis dictates the overall behavior of skin under tension [118, 363]. The dermis is a collagenous tissue and can be considered nearly incompressible and hyperelastic [178]. Though it was originally developed to capture the mechanical behavior of arteries, the strain energy function proposed by Gasser-Ogden-Holzapfel (GOH) [57] has been adapted to model skin and is used here [23, 180]. The main features of this strain energy are its exponential behavior, and its microstructurally-inspired decomposition which naturally incorporates the influence of anisotropy due to collagen fiber networks. We briefly define the important kinematic quantities before introducing the strain energy. The deformation gradient $\mathbf{F}$ is the main kinematic object, capturing the local changes in geometry induced by the deformation map. Due to its nearly incompressible behavior, it is advantageous to split the deformation gradient into its isochoric and volumetric contributions

$$\bar{\mathbf{F}} = J^{-1/3}\mathbf{F}, \ \mathbf{F}^{\text{vol}} = J^{1/3}\mathbf{I}, \tag{10.1}$$

where $J = \det(\mathbf{F})$ is the volume change, and $\mathbf{I}$ is the second-order identity matrix. Consequently, the isochoric part of the right Cauchy-Green deformation tensor is defined as

$$\bar{\mathbf{C}} = \bar{\mathbf{F}}^{\top}\bar{\mathbf{F}}, \tag{10.2}$$

with the first invariants $\bar{I}_1 = \bar{\mathbf{C}} : \mathbf{I}$.

Additionally, we introduce the vector $\mathbf{a}_0$ in the reference configuration which specifies the direction of anisotropy. This vector field gets mapped to the vector $\mathbf{a} = \mathbf{F}\mathbf{a}_0$ upon deformation. Since we deal with a two-dimensional domain, the fiber direction can be parameterized by the single angle θ. The direction of anisotropy defines the fourth pseudo-invariant of $\bar{\mathbf{C}}$

$$\bar{I}_4 = \mathbf{a}_0^{\top}\bar{\mathbf{C}}\mathbf{a}_0 \, . \tag{10.3}$$

The collagen fibers are not necessarily perfectly aligned. In fact there is some dispersion around the preferred orientation $\mathbf{a}_0$. This dispersion can be understood as the result of fitting a uni-modal distribution to the fiber orientation distribution over a unit sphere [57]. We use the parameter κ to denote the dispersion, and we remark that this parameter is associated with the width of the orientation distribution. A value of $\kappa = 0$ would mean all fibers being perfectly aligned, while $\kappa = 1/3$ indicates uniform fiber distribution. Thus, rather than the value of the fourth pseudo-invariant alone, the fiber contribution consists of a linear combination of an isotropic term and an anisotropic term

$$\bar{E} = \kappa(\bar{I}_1 - 3) + (1 - 3\kappa)(\bar{I}_4 - 1)\,. \tag{10.4}$$

The strain energy can now be defined as a sum of a volumetric part and two isochoric parts, one that describes the isotropic ground matrix, plus the anisotropic term

$$\Psi = \Psi^{\text{vol}} + \bar{\Psi}^{\text{iso}} + \bar{\Psi}^{\text{aniso}}, \tag{10.5}$$

with the volumetric term being

$$\Psi^{\text{vol}} = \frac{K}{2}\left(\frac{J^2 - 1}{2} - \ln J\right), \tag{10.6}$$

controlled by the single parameter K which is the bulk modulus. In this work, incompressibility is imposed fully and the parameter K does not have any influence. The first contribution to the isochoric term is purely isotropic

$$\bar{\Psi}^{\text{iso}} = \frac{\mu}{2}(\bar{I}_1 - 3), \tag{10.7}$$

and parameterized by the shear modulus μ. The last term is due to the fiber family and takes the form

$$\bar{\Psi}^{\text{aniso}} = \frac{k_1}{2k_2}\left(\exp(k_2\langle\bar{E}\rangle^2) - 1\right) \tag{10.8}$$

where $\langle\cdot\rangle$ denotes the Macaulay brackets, and the parameters k_1 and k_2 have been introduced.

Thus, the material model is fully described by the inputs $[\mu, k_1, k_2, \kappa, \theta]$. Based on our previous work and a review of the literature, plausible parameter ranges are illustrated in Table 10.1 [23, 101].

Table 10.1.: Ranges for the parameters used to describe the mechanical behavior of skin including anisotropy

Parameter	Range
μ [kPa]	[4.774, 6.804]
k_1 [kPa]	[3.800, 209.300]
k_2 [-]	[52.530, 161.860]
κ [-]	[0.133, 0.333]
θ [°]	[0, 180]

10.2.3 Creating Gaussian process surrogates

To create the surrogate model, the GOH parameter space summarized in Table 10.1 is sampled N times using Latin hypercube sampling (LHS). LHS ensures that each parameter is sampled uniformly. Individual inputs are denoted as $\mathbf{x}^{(n)} = (\mu^{(n)}, k_1^{(n)}, k_2^{(n)}, \kappa^{(n)}, \theta^{(n)})$ with a total training set

$$\mathbf{X} = (\mathbf{x}^{(1)}, \cdots, \mathbf{x}^{(N)}) \in \mathbb{R}^{5\times N}\,. \tag{10.9}$$

Each $\mathbf{x}^{(n)}$ defines an FE simulation that creates a nodal strain output $\mathbf{E}^{(n)} \in \mathbb{R}^M$ where M represents the total number of free nodes in the mesh. This gives an overall strain matrix of

$$\mathbf{E} = (\mathbf{E}^{(1)}, \cdots, \mathbf{E}^{(n)}) \in \mathbb{R}^{M \times N} . \tag{10.10}$$

For each row in the overall strain matrix $\mathbf{E}$, the outputs are centered by subtracting the row's mean and dividing by its standard deviation. This gives a centered and scaled output of

$$\bar{\mathbf{E}} = (\bar{\mathbf{E}}^{(1)}, \cdots, \bar{\mathbf{E}}^{(N)}) \in \mathbb{R}^{M \times N} . \tag{10.11}$$

Since the meshes have a large number of nodes, the strain outputs $\mathbf{E}^{(n)}$ have a very high dimension M. Here, we reduce the dimensionality of this output data using principal component analysis (PCA) [187]. To perform a PCA, we define $\mathbf{W} \in \mathbb{R}^{M \times M}$ as the linear transformation

$$\mathbf{W}\bar{\mathbf{E}} = \mathbf{Y} \tag{10.12}$$

where $\mathbf{Y} \in \mathbb{R}^{M \times N}$ is the principal component (PC) score matrix. In order to find this matrix $\mathbf{W}$, the singular value decomposition (SVD) of $\bar{\mathbf{E}}$ is introduced first,

$$\bar{\mathbf{E}} = \mathbf{U}\mathbf{\Sigma}\mathbf{V}^\top , \tag{10.13}$$

which consists of orthogonal matrices $\mathbf{U} \in \mathbb{R}^{M \times M}$ and $\mathbf{V} \in \mathbb{R}^{N \times N}$, and a rectangular diagonal matrix with non-negative real numbers $\mathbf{\Sigma} \in \mathbb{R}^{M \times N}$. Multiplying Eq. (10.13) from the left by $\mathbf{U}^{-1}$, and noting that because $\mathbf{U}$ is an orthogonal matrix $\mathbf{U}^{-1} = \mathbf{U}^\top$, we obtain

$$\mathbf{U}^\top \bar{\mathbf{E}} = \mathbf{\Sigma}\mathbf{V}^\top . \tag{10.14}$$

Using Eq. (10.14), we define the PC projection in terms of the SVD such that $\mathbf{W} = \mathbf{U}^\top$ and $\mathbf{Y} = \mathbf{\Sigma}\mathbf{V}^\top$. The rows of $\mathbf{W} = \mathbf{U}^\top$ are the PCs, the rows of $\mathbf{Y}$ are the PC scores, or the projection of the original data ($\bar{\mathbf{E}}$) to the PC basis. Since we

centered the data prior to performing the SVD, the variance of the data is the square of the singular values scaled by $1/(N-1)$. Essentially, the singular values show how the information in each column of $\bar{\mathbf{E}}$ is distributed when we project it to the PC basis. Thus, we can truncate our PC values by defining a criterion, such as capturing 99% of the total variance in the data. This truncation leads to a reduced basis basis $\mathbf{W'} \in \mathbb{R}^{M' \times N}$ with PC scores $\mathbf{Z} = \mathbf{Y'} \in \mathbb{R}^{M' \times N}$. Ideally, the majority of the variance can be captured within a small number of PCs, meaning $M \gg M'$, significantly reducing the dimensionality of our initial nodal strain data. Indeed, as will be shown later, about thirty PCs capture most of the variance in our strain profiles. The GP regression is performed on the truncated PC score data

$$\mathbf{Z} = (\mathbf{z}^{(1)}, \cdots, \mathbf{z}^{(N)}) \in \mathbb{R}^{M' \times N} . \tag{10.15}$$

The training dataset consists of the corresponding inputs paired with the truncated PC scores

$$\mathcal{D} \equiv \{(\mathbf{x}^{(n)}, \mathbf{z}^{(n)})\}_{n=1}^{N} . \tag{10.16}$$

Given the training data, we are interested in performing GP regression to learn a scalar function for each PC score. For any set of observations of the mth PC score ($\mathbf{z}_m \in \mathbb{R}^N$), we are interested in the function $f_m(\cdot)$, but we consider that rather than observing the correct value of the function, we observe a noisy output

$$z_m^{(n)} = f_m(\mathbf{x}^{(n)}) + \varepsilon_m^{(n)} \tag{10.17}$$

with ε_m having independently and identically distributed Gaussian noise with zero mean and variance $\sigma_{ns,m}^2$. To learn the function $f_m(\cdot)$ from the data, we first model the prior state of knowledge about f_m using a GP

$$f_m(\cdot) \sim \mathcal{GP}(\mu_m(\cdot), k_m(\cdot)) \tag{10.18}$$

with mean and covariance functions $\mu_m(\cdot)$ and $k_m(\cdot)$, respectively. We choose a zero mean function such that the GP prior is a multivariate normal distribution over the inputs $\mathbf{X}$,

$$f_m(\mathbf{X}) \sim \mathcal{N}(\mathbf{0}, \mathbf{K}_m) \tag{10.19}$$

The covariance matrix $\mathbf{K}_m \in \mathbb{R}^{N\times N}$ contains our assumption about the regularity of the function we wish to capture. Here we use a radial basis function as a kernel, and the components of the covariance matrix follow

$$\begin{aligned} K_{m(i,j)} &= k_m(\mathbf{x}^{(i)}, \mathbf{x}^{(j)}; \zeta_m) \\ &= s_{f,m}^2 \exp\left(-\frac{1}{2}(\mathbf{x}^{(i)} - \mathbf{x}^{(j)})^\top \mathbf{\Lambda}_m^{-1}(\mathbf{x}^{(i)} - \mathbf{x}^{(j)})\right) \end{aligned} \tag{10.20}$$

with $\mathbf{\Lambda}_m = \mathrm{diag}(\lambda_{m,1}, \lambda_{m,2}, \lambda_{m,3}, \lambda_{m,4}, \lambda_{m,5})$, and each $\lambda_{m,i}$ capturing the squared characteristic length-scale of each input. The process variance is denoted $s_{f,m}^2$ in Eq. (10.8). These hyperparameters, denoted ζ_m in Eq. (10.20), are estimated by maximizing the likelihood of the observed outputs $\mathbf{z}_m$,

$$\log p(\mathbf{z}_m|\mathbf{X}, \zeta_m) \coloneqq -\frac{1}{2}\mathbf{z}_m^\top \mathbf{\Sigma}_m^{-1}\mathbf{z}_m - \frac{1}{2}\log|\mathbf{\Sigma}_m| - \frac{N}{2}\log 2\pi\,. \tag{10.21}$$

Note that due to the assumption of the noisy observations we have a covariance $\mathbf{\Sigma}_m = \mathbf{K}_m + \sigma_{ns,m}^2\mathbf{I}$, which is the sum of the GP covariance matrix plus the Gaussian noise. Having determined the hyperparameters ζ_m from maximizing Eq. (10.21), the posterior of $f_m(\cdot)$ is derived using Bayes' rule. Moreover, the posterior for any new parameter input $\mathbf{x}^{(*)}$ is also Gaussian,

$$f_m(\mathbf{x}^{(*)})|\mathcal{D}, \mathbf{x}^{(*)}, \zeta_m \sim \mathcal{N}\left(\mu_m(\mathbf{x}^{(*)}; \zeta_m), \sigma_m^2(\mathbf{x}^{(*)}; \zeta_m)\right) \tag{10.22}$$

with predictive mean and variance,

$$\mu_m(\mathbf{x}^{(*)}; \zeta_m) = \mathbf{k}_m^\top \mathbf{\Sigma}_m^{-1}\mathbf{z}_m\,, \tag{10.23}$$

and

$$\sigma_m^2(\mathbf{x}^{(*)};\zeta_m) = \mathbf{k}(\mathbf{x}^{(*)},\mathbf{x}^{(*)};\zeta_m) + \sigma_{ns,m}^2 - \mathbf{k}_m^\top \boldsymbol{\Sigma}_m^{-1}\mathbf{k}_m\,, \tag{10.24}$$

respectively. In Eqs. (10.23) and (10.24), the vector $\mathbf{k}_m$ is

$$\mathbf{k}_m = \left(k(\mathbf{x}^{(*)},\mathbf{x}^{(1)};\zeta_m),\cdots,k(\mathbf{x}^{(*)},\mathbf{x}^{(N)};\zeta_m)\right)\,. \tag{10.25}$$

In summary, Eq. (10.22) predicts the expected PC scores as the predictive mean (Eq. (10.23)), with error bars given by the predictive variance (Eq. (10.24)).

To validate the GP model, we sample independently another set of Q inputs using LHS like

$$\mathbf{X}_v = (\mathbf{x}_v^{(1)},\cdots,\mathbf{x}_v^{(Q)}) \in \mathbb{R}^{5\times Q}\,. \tag{10.26}$$

FE analyses are run for each of these Q input parameter sets for each flap to obtain truth data (the nodal strain outputs) to be compared against the GP predictions. Note that the GP predictions lie on the PC space. To obtain nodal strain outputs from the surrogates, we first use the posterior GP to obtain the predictive means of the PC scores,

$$\mathbf{Z}_v = (\mathbf{z}_v^{(1)},\cdots,\mathbf{z}_v^{(Q)}) \in \mathbb{R}^{M'\times Q}\,, \tag{10.27}$$

and then perform an inverse PCA transformation to obtain a centered prediction of the nodal strain as

$$\bar{\mathbf{E}}_v = \mathbf{W}'^\top \mathbf{Z}_v\,. \tag{10.28}$$

Lastly, reversing the centering operation that was done before PCA in the training data, we obtain nodal strain predictions that can be compared directly to the FE truth.

10.2.4 Sensitivity analysis

To understand the influence of each parameter, we perform a Sobol sensitivity analysis [197]. The method followed in this manuscript follows closely our previous work and is also aligned with the documentation of Python's SALib library [198]. The goal of this analysis is to determine which of the five inputs has the largest influence on the strain distribution. Intuitively, if there is a large variation in the results of the surrogate model when one parameter is held constant while the others vary, that parameter likely does not have a large influence on the strain distribution. By contrast, if there is only a small variation in results when that parameter is held constant, it is likely influential. The sensitivity analysis thus requires a large number of function evaluations as different parameters are varied. The Satelli sampling scheme is used to obtain a total of $S \times (2K + 2)$ samples, where S is a large number, for example on the order of a thousand, and K is the dimension of the input space. Clearly, this kind of analysis would be difficult to do with the original FE model. Instead, having trained the GPs, we can use the surrogates to perform the many function evaluations required for the sensitivity analysis. The Sobol sensitivity analysis on the outputs, obtained via GP evaluations, decomposes the variance in the model output into variance that can be attributed to each input and to the interaction between inputs.

10.2.5 Optimization of surgical plan

Another type of task that is enabled with the GP surrogates is flap optimization. As will be shown in the Results section 10.3, the fiber direction (θ) is the most important parameter for the resulting strain distribution following reconstructive surgery. While the surgeon does not control the fiber direction of the patient's skin, they do control how the flap is oriented with respect to the anisotropic features of skin, referred clinically as the relaxed skin tension lines [345]. Therefore, knowledge of the optimal fiber direction with respect to the orientation of the flap should be used for

planning a surgery, even when other parameters are unknown or uncertain. We work to determine an optimal fiber direction through minimizing cost functions.

Here we propose three cost functions informed by clinical guidelines [32, 349, 359]: (1) C_1: mean nodal strain, (2) C_2: sum of tensile strains at key points near the wound edges, (3) C_3: sum of tensile strain at key points only at the distal ends of the flaps. With $\mathbf{x} = (\mu, k_1, k_2, \kappa, \theta)$, mathematically, we have

$$\begin{aligned} C_1(\mathbf{x}) &= \mathrm{E}_{\mathrm{avg}}\,, \\ C_2(\mathbf{x}) &= \sum_{\text{Edge pts } i} \langle \mathrm{E}_i \rangle\,, \text{ and} \\ C_3(\mathbf{x}) &= \sum_{\text{Distal pts } i} \langle \mathrm{E}_i \rangle\,. \end{aligned} \tag{10.29}$$

These cost functions depend on all the material parameters. However, as mentioned, only the anisotropy direction θ is a design parameter for surgery. Thus, we introduce the random vector $\phi = (\mu, k_1, k_2, \kappa)$ capturing all the material parameters other than θ. Assuming risk neutrality, we should select θ by minimizing the expectation of the cost over the distribution of the parameters ϕ [364] such that

$$\theta^*_{rn} = \arg\min_{\theta} \mathbb{E}_{p(\phi)}[C_i]\,. \tag{10.30}$$

To calculate the expectation, we take advantage of the GP and simply draw many samples from $p(\phi)$ for a given value of θ. In practice, 1,000 samples per θ are sufficient to obtain a sufficiently converged estimate of the expectation. The minimization with respect to θ is done by calculating the expectation of the cost for a sufficiently refined grid of θ values. In our case, we find that the function is smooth enough such that 181 values of θ (all values from 0° to 180° by 1°, inclusive) are enough to interpolate the expected cost. After performing these calculations, we get the expectation for each value of θ and find the minimum.

Under the assumption of extreme risk aversion, another strategy for determining an optimal fiber direction is to minimize the worst-case scenario. In this case, the problem is

$$\theta^*_{ra} = \arg\min_{\theta} \arg\max_{\phi \in \text{supp}(p(\phi))} C_i \tag{10.31}$$

where $\text{supp}(p(\phi))$ is the support of the material parameter distribution. For the most general case, the support corresponds to the parameter range defined in Table 10.1. The maximization problem with respect to ϕ is solved with a modified particle swarm optimizer [365]. The algorithm begins by generating J random individual inputs of the form $\phi_j = (\mu_j, k_{1j}, k_{2j}, \kappa_j)$. These are the particles in the swarm. For each particle j, we then generate a random velocity ($\mathbf{v}_j(t = 0)$) and calculate its current objective value ($C_j(t = 0)$), with t a pseudo-time used in the algorithm. These objective values are set as the initial personal best locations ($\hat{\phi}_j(t = 0)$) for each particle. The best objective value of all the personal bests is the global best location ($\mathbf{g}(t = 0)$). After initialization, the iterations are attempts to adjust the location of the particles towards an optimal value. In each generation, or iteration, the velocity of each particle is updated based on

$$\mathbf{v}_j(t + 1) = \omega \mathbf{v}_j(t) + c_1 r_1(\hat{\phi}_j(t) - \phi_j(t)) + c_2 r_2(\mathbf{g}(t) - \phi_j(t)) \,. \tag{10.32}$$

Here, $\omega \mathbf{v}_j(t)$ is the inertial component and updates the velocity using the influence of the particle's current direction of movement. ω is the inertial coefficient, generally taking a value between 0.8 and 1.2. The cognitive component, $c_1 r_1(\hat{\phi}_j(t) - \phi_j(t))$, updates the velocity based on the influence of the particle's previous best position. c_1 is referred to as the cognitive coefficient and generally takes a value of approximately 2, while r_1 is a random value between zero and one. The last portion of the velocity update is the social component, $c_2 r_2(\mathbf{g}(t) - \phi_j(t))$. Again, c_2 is the social coefficient and generally takes a value of about 2 while r_2 is a random value between zero and one. This last component updates the velocity with respect to the current global

best position. Overall, each particle's velocity is updated under the influence of its current direction of motion, previous best position, and the global best position. The particle's position is then updated as

$$\phi_j(t+1) = \phi_j(t) + \mathbf{v}_j(t+1)\,. \tag{10.33}$$

If this new position is within the valid range for ϕ and has an improved objective value compared to the current personal best, it becomes the particle's personal best. The global best for the next generation is updated from the new positions at the end of the iteration. The algorithm continues until the maximum number of generations is reached or the global best solution fails to improve for 5 consecutive generations. The overall result of the optimization is then the global best position and its corresponding objective function value. This optimization is repeated 5 times to account for the stochasticity in the algorithm and ensure that we do not move forward with a sub-par optimization result.

Similar to the minimization problem in Eq. (10.30), for Eq. (10.31) we interpolate the worst cost as a function of θ by solving the maximization over ϕ for 181 values of θ. From this, we are then able to determine the value for theta that minimizes this worst case scenario.

Finally, a brief discussion on $p(\phi)$ is needed. For the most general case, we perform the optimization of the flap using the prior of the material parameters $p_0(\phi)$, which is a uniform distribution over the entire range in Table 10.1. This might be too broad of a range. Hence, we also consider a distribution for the material parameters based on one of the patient's values reported in [23].

10.3 Results

10.3.1 Exploring the effect of anisotropy in advancement, rotation and transposition flaps

To begin, we explored the impact of anisotropy on strain profiles produced from FE simulations. We ran 12 simulations taking the mean values for μ, k_1, k_2, and κ from the range in Table 10.1 and varying θ at $[0°, 45°, 90°, 135°]$. The results are shown in Fig. 10.2, where it can be observed that the overall trend of the strain profiles follows the fiber direction. While these results are only true for one set of parameters $[\mu, k_1, k_2, \kappa]$, they support the intuition that direction of anisotropy plays an important role in flap design. For instance, for the advancement flap, fibers aligned with the direction of advancement lead to high strains across the flap and surrounding skin, from the proximal to the distal ends. As the fiber is rotated to 45° with respect to the flap, the higher strains are oblique with respect to the advancement direction. Interestingly, fibers oriented perpendicular to the direction of advancement lead to compressive strains at the middle of the flap and overall small strains throughout the skin patch. The last simulation shown for advancement, $\theta = 135°$, is similar to $\theta = 45°$ since the flap is symmetric with respect to the horizontal axis.

In the rotation flap, fibers at $\theta = 0°$ result in relatively small strains near the base of the flap, with a couple of small regions under compression and a narrow bad of tissue in tension. In this case, the distal end has even lower strains. Rotating the fibers to $\theta = 45°$ results in strains being greater along that direction, and overall increasing in magnitude. This trend continues as the fibers are rotated to $\theta = 90°$. For $\theta = 135°$, a band of high tensile strains extends from the base of the flap to the distal end. As opposed to the advancement flap, the rotation design does not have any symmetry. Additionally, the strain profiles from the rotation flap are more intricate with respect to advancement, particularly near the base of the flap, due to the point at which three different edges come together in a Y-junction.

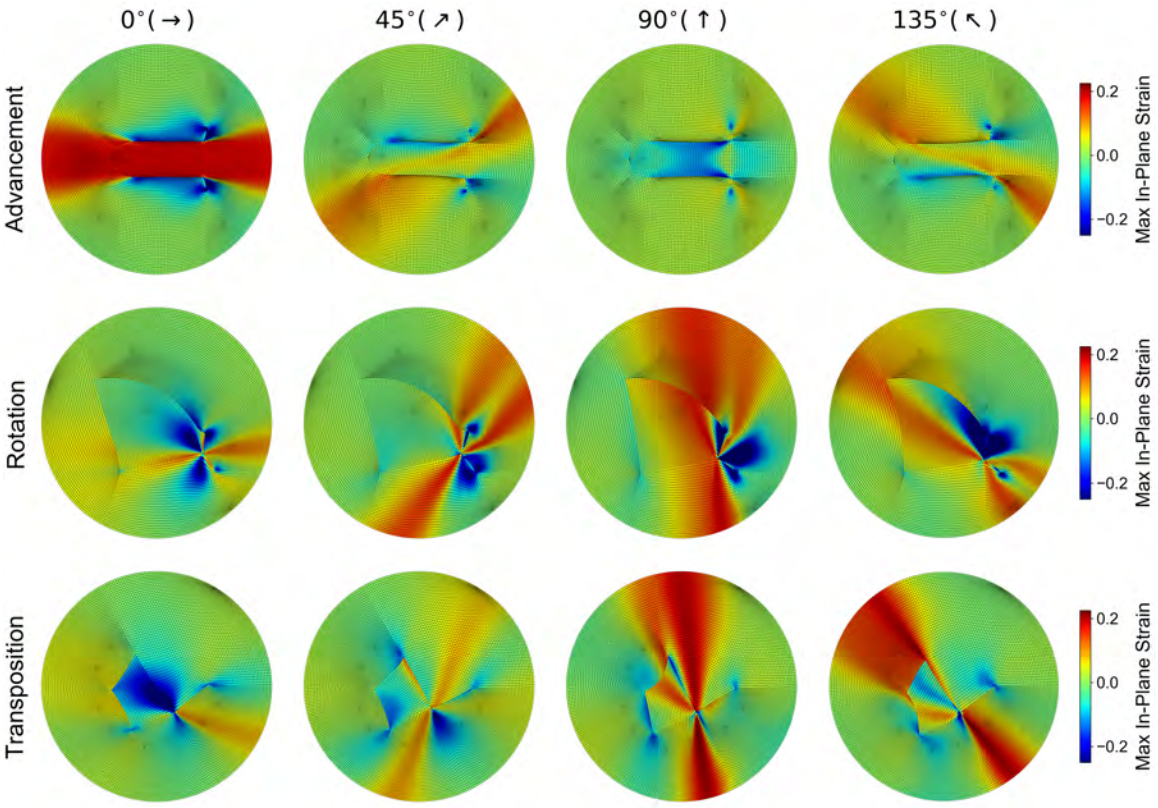

Fig. 10.2.: The distribution of maximum in-plane strain for the advancement, transposition, and rotation flaps at $\theta = [0°, 45°, 90°, 135°]$ with all other parameters at mean values of their range. Strain patterns show features spanning the entire skin region and aligning with the fiber orientation.

In the transposition case there are also no planes of symmetry, and changing the fiber gradually from $\theta = 0°$ to $\theta = 135°$ yields vastly different strain contours. The trends in the transposition flap are overall similar to the other designs, with higher strains aligned with the fiber direction. Interestingly, the transposition design entails greater reorientation of tissue, which can be seen as a more discontinuous pattern of strain across the suture lines in the current configuration. For example, when $\theta = 135°$, the bottom-right region of tissue is rotated approximately 60° before being sutured to the top-left edge. Due to the mismatch in fiber direction in the current configuration between the surrounding tissue and the distal portion of the flap that

has been rotated, the surrounding skin at the top-left region is under high tensile strain while the flap immediately adjacent is actually not subjected to higher strains.

The magnitude of the strains are different across flaps for a given orientation. For instance, when $\theta = 90°$, the advancement flap shows the smallest strains while the transposition flap has the highest strains. On the other hand, for $\theta = 0°$, the advancement flap results in the highest strains compared to the other flaps. We remark again that the results in Fig. 10.2 were obtained by fixing all other parameters to their mean. In order to conduct a rigorous sensitivity analysis over the entire parameter range, the surrogate models are needed to efficiently sample the input space.

10.3.2 Creating and validating Gaussian process surrogates

The surrogates were trained using $N = 2{,}000$ FE simulations and validated on an additional 400 parameter sets. The training and validation sets were obtained from separate LHS instances. The majority of the simulations ran without artificial energy dissipation. However, for the advancement case, a total of 159 simulations were run with some dissipation, 55 of those incurred in up to 0.0001% artificial energy with respect to total energy, 63 dissipated up to 0.001%, 30 simulations required 0.01%, 10 more needed 0.1% and only one was done with up to 1% dissipated energy with respect to total energy. For the rotation flap, 205 simulations allowed for 0.001% energy dissipation, 118 allowed 0.01%, 8 had 0.1%, and 6 were run with up to 1% of artificial energy compared to total energy. For the transposition flap, out of the total, in 230 cases the simulation was allowed to dissipate up to 0.001%, in 41 cases the maximum was capped at 0.01%, and in 10 occasions there was an allowed maximum energy dissipation of 0.1%.

After obtaining FE results for the strain distributions for each parameter set, we reduced the dimensionality of these data with PCA. Initially, the overall strain matrices had dimensions $2,000 \times 12,004$, $2,000 \times 12,218$, and $2,000 \times 12,389$ for the

advancement, rotation, and transposition flaps, respectively. Using the PCA while retaining 99% of the variation in the data, these were respectively reduced to $2,000 \times 26$, $2,000 \times 24$, and $2,000 \times 23$ datasets. The first 4 PCs for each flap alongside the cumulative variance explained with each additional PC are reported in Fig. 10.3. Unfortunately, PCs do not necessarily entail any physical meaning or intuition, as opposed to the strain fields in Fig. 10.2. It is worthwhile to point out that in previous work, ignoring anisotropy, less than 10 PCs were enough to account for 99.9% of the variance in stress profiles of the same three flap designs [101]. Thus, even though anisotropy direction and fiber dispersion are only two additional parameters with respect to previous work, they contribute to more complex strain and stress distribution over the entire skin patches, clearly seen in Fig. 10.2. Nonetheless, PCA is still able to reduce the dimensionality effectively.

We used the reduced data after truncating the PC basis at 99% of the variance, and we trained independent GPs for each PC score for each flap. Next, we evaluated the quality of the surrogate models. The validation simulations provide strain profiles and not PC scores. While indeed we are ultimately interested in the prediction of strains, first we investigated the performance of the individual GPs on the PC space. The strain profiles from the validation set were hence projected to the PC basis. Once the validation data was projected onto the reduced basis, we computed the standardized residuals for the predicted PC scores. The standardized residuals measure the difference between the prediction of the GP and the true value from the validation set, divided by the predicted variance of the GP. Results are plotted in Fig. 10.4**a**. These histograms aggregate all the PC scores, i.e., we do not separate into individual PC scores for each flap. For all flaps and all PC scores, the standardized residuals fall mostly within the $[-3, 3]$ confidence interval and are centered around zero. In other words, we know that the majority of the validation points fall within the 99.7% confidence range predicted by the GP surrogates. However, some points do lie outside this range, especially for the rotation flap. This indicates that there

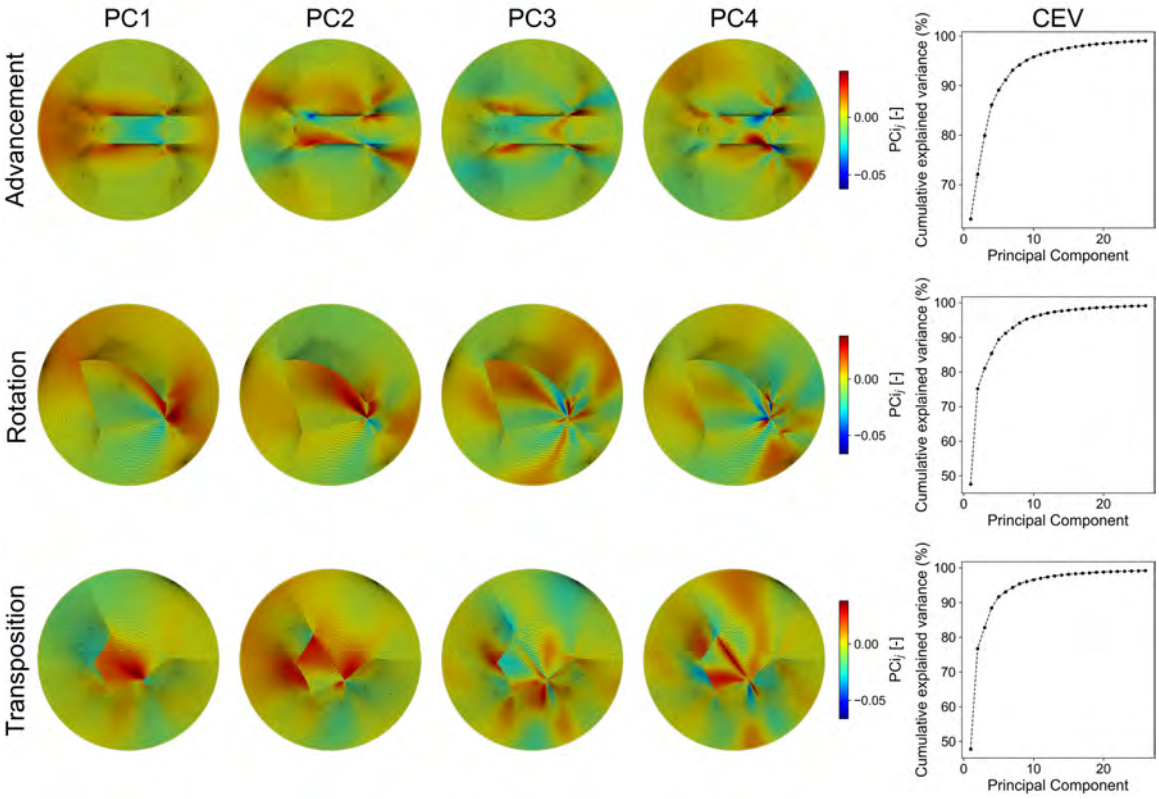

Fig. 10.3.: First 4 principal components (PCs) plotted on the finite element meshes for each of the three flaps. Cumulative explained variance (CEV) in accounting for 99% of the variation in the total data is shown in the last column for each of the flaps. The first 4 PCs explain 86.1%, 85.3%, and 88.5% of the advancement, rotation and transposition flaps respectively. PCs form an alternative basis for the strain profiles which enable compressing of the data into very few features compared to the number of nodes. Ultimately, to account for 99% of the variance, 26 PCs were kept as a truncated basis for the advancement case, 24 for the rotation, and 23 for the transposition flap.

may be areas of the parameter space that require further exploration, particularly for some of the PC scores of the rotation flap.

The PC score prediction is not necessarily an indication of the performance of the surrogate on the strain space, which is the quantity of interest. To compare directly the prediction of the surrogates to the data from the validation set, we projected the PC score prediction to the strain space using the inverse PCA transformation. Next, we examined the l_2-norm relative error of the strain prediction with respect to the

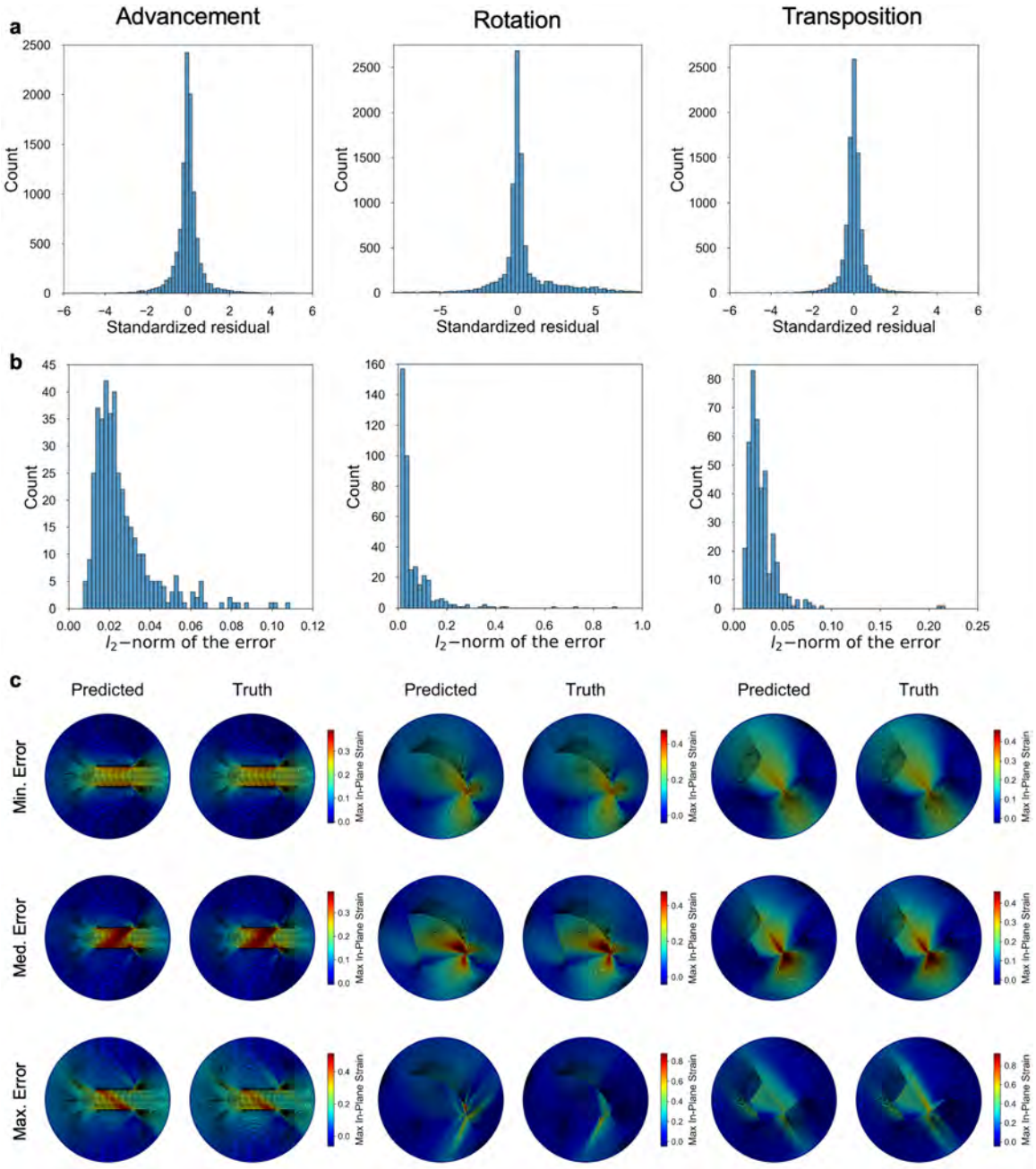

Fig. 10.4.: Standardized residuals computed from comparing surrogate predictions and validation data after it has been projected onto the principal component (PC) basis (**a**). l_2-norm of the relative error between the surrogate and the validation data (**b**). To obtain strains, the predictions of the PC scores from the individual Gaussian process surrogates are transformed via inverse PC analysis to the strain space. Surrogate predictions versus finite element simulation as truth for the minimum, median, and maximum l_2-norm relative errors (**c**).

validation set. Fig. 10.4**b** depicts histograms of the l_2-norm relative error and Fig. 10.4**c** showcases comparisons between truth and prediction for the best, median, and worst l_2-norm relative error cases for each flap. While the transposition and rotation flaps do include a few outliers in terms of the l_2-norm, the vast majority of relative error values fall below 0.1 for advancement and transposition flaps and 0.2 for the rotation flap. For the advancement flap, the maximum error is 0.109 with a mean error of 0.026 and 99.5% (398 of 400 validation simulations) of the errors falling below 0.1. The transposition flap has a maximum error or 0.216 and mean error of 0.028 with 99.25% (397 of 400 validation simulations) of the errors falling below 0.1. The rotation flap, however, has a wider distribution of error with a maximum value of 0.895, but with a mean of 0.065. In the rotation case, 82.0% of the errors fall below 0.1 (328 of 400 validation simulations). We remark that even with the wider error distribution, even the worst prediction shows qualitative agreement with the truth as seen in Fig. 10.4**c**, middle columns.

10.3.3 Sobol sensitivity analysis

Following the Methods section 10.2, we chose $S = 1{,}000$ for the sensitivity analysis, and sampled a total of $1,000 \times (2 \times 5 + 2) = 12,000$ parameter sets using the Satelli sampling scheme. For each of these inputs, we used the surrogate models to predict nodal strains. Rather than looking at the entire strain field and defining a global scalar quantity of interest, we decided to focus on the strain value at specific locations. We chose points deemed more important indicators for the clinical setting [32, 349]. These points are chosen near the suturing region, which is the zone where wound healing must take place, and that may be affected by the stress or strain more directly [3,330]. The points of interest are indicated in Fig. 10.5**a**. The results from the Sobol sensitivity analysis using as quantity of interest the strain at the specific points are depicted in Fig. 10.5**b**. These plots clearly illustrate that the fiber direction (θ) has the most significant impact on variation in the nodal strains. As opposed to the

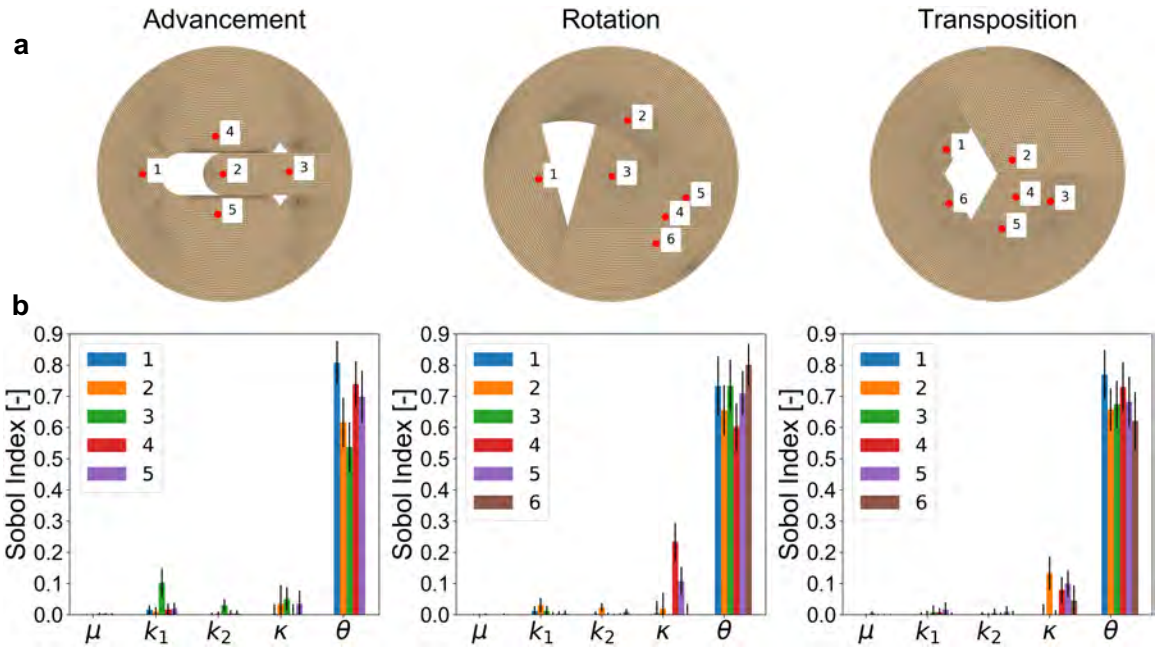

Fig. 10.5.: Locations of key points used in the sensitivity analysis and in the optimization steps (**a**). Sobol index for the nodal strain at each of the key points after completing the analysis using 12,000 predictions from the surrogate model (**b**).

results in Fig. 10.2, which show strain variations for four different angles but fixing all other parameters, here we are able to sample the entire input space efficiently using the surrogate model.

10.3.4 Optimizing flap orientation

In the clinical setting, the surgeon may not have access to reliable data on the material properties, particularly the inputs μ, k_1, k_2, κ to the model, which can only be obtained through mechanical testing [23, 178]. However, surgeons do typically have knowledge of the anisotropy direction from anatomy and visual and manual inspection [42,345]. Therefore, we decided to solve the optimization problem using the surrogate in order to find the best flap orientation with respect to the direction of anisotropy. As stated previously, excessive tension and deformation near a wound or sutured region is a cause for wound healing complications and pathological scarring [3,267]. As such,

the cost functions defined here generally focus on quantifying strain near the sutured regions. As defined previously, these functions are: i) mean nodal strain, ii) sum of tensile strains at key points near the would edges, and iii) sum of tensile strains at key point(s) only at the distal ends of the flaps. For the second cost function, all points selected for the sensitivity analysis are used. For the third cost function, point 2 is selected for the advancement flap, points 3 and 4 are selected for the rotation flap, and point 4 is selected for the transposition flap. Assuming that θ is the only input that can be controlled and that no other information is available regarding $\phi = [\mu, k_1, k_2, \kappa]$, we first considered that the prior assumption for the mechanical response $p_0(\phi)$ which is just a uniform distribution in the range of Table 10.1. Additionally, we consider two smaller, normal distributions of parameters: one surrounding the 59-year-old female parameters defined in [23] and one surrounding the mean of the parameter ranges in Table 10.1. The normal distributions here are defined to encompass ±10% of the given parameter values within 3 standard deviations on each side of the mean.

Using the methods described above, we complete both optimization problems - minimizing the expectation of the cost and minimizing the worst case scenario. The particle swarm optimization for ϕ was completed with 50 particles, a maximum of 25 generations, and optimizer hyperparameters $\omega = 1.2$, $c_1 = 2.0$, and $c_2 = 2.0$. The initial particle distribution was created by selecting 50 random values in the ranges listed in Table 10.1 and setting their initial velocities to random values between 0 and 80% of the range of values for each parameter. The results for the optimization considering the distribution ϕ_0 are illustrated in Figs 10.6-10.8 for the advancement, rotation, and transposition flaps, respectively. These plots first show the cost distributions for $\theta = [0°, 45°, 90°, 135°]$. The second column shows the cost versus θ for all 181 values of θ. The vertical lines correspond in color to the θ values selected to illustrate the cost distribution. The gray shaded region illustrates the distribution of the cost for each θ. Darker shading indicates higher frequency as values of the cost are sampled by sampling the distribution $p_0(\phi)$. The black data points in the middle columns of Figs 10.6-10.8 are the expectation of the cost for every θ. The red data

points in Figs 10.6-10.8 show the worst case scenario from the particle swarm optimization for each θ. It is evident that, even though there is some variation, in general both the expectation of the cost and the worst case scenario follow the same trend with respect to θ. Consequently, the solutions to both the optimization problems are approximately equivalent. The yellow points in the middle plots signal the value of θ for which the expected cost achieves the minimum. The last column shows the strain profile as predicted by the surrogate for the optimal points with respect to each of the cost functions.

For the advancement flap, the optimal orientation of the flap with respect to the anisotropy direction can be one of two options depending on which cost function is used. Minimizing the mean nodal strain or the sum of the strains on the key points around the suture line leads to the same optimal $\theta = 90°$. This result makes sense and follows clinical guidelines [330, 350], which recommend advancing perpendicular to the fiber orientation. When only the strain at a single point on the distal end is considered, the cost function is relatively flat and low around $\theta = 90°$, but there is also a local minimum around $\theta = 0°$. We plot this value in Fig. 10.6 to illustrate the difference, although in reality, $\theta = 90°$ also achieves a low value of the expectation of the cost function. On the other hand, the distribution of the cost for a given θ suggests that the worst case scenario for may be worse for $\theta = 90°$. The strain profile for this last cost function (minimizing only the strain at one point in the distal end of the flap) shows higher strains overall, compared to optimization based on the other two cost functions. For comparison, side by side strain profiles for $\theta = 90°$ and $\theta = 180°$ can be found in the supplement. We also remark that the cost function is symmetric around $\theta = 90°$ or $\theta = 0°$ which is expected since the flap design is symmetric.

Next, looking at the rotation flap (Fig. 10.7), we see three different optimal values for θ: 6°, 25°, and 45° for mean nodal strain, sum of all key strains, and sum of key distal strains, respectively. We no longer have the symmetry seen with the advancement flap, as the rotation flap is not symmetric across either major axis. We

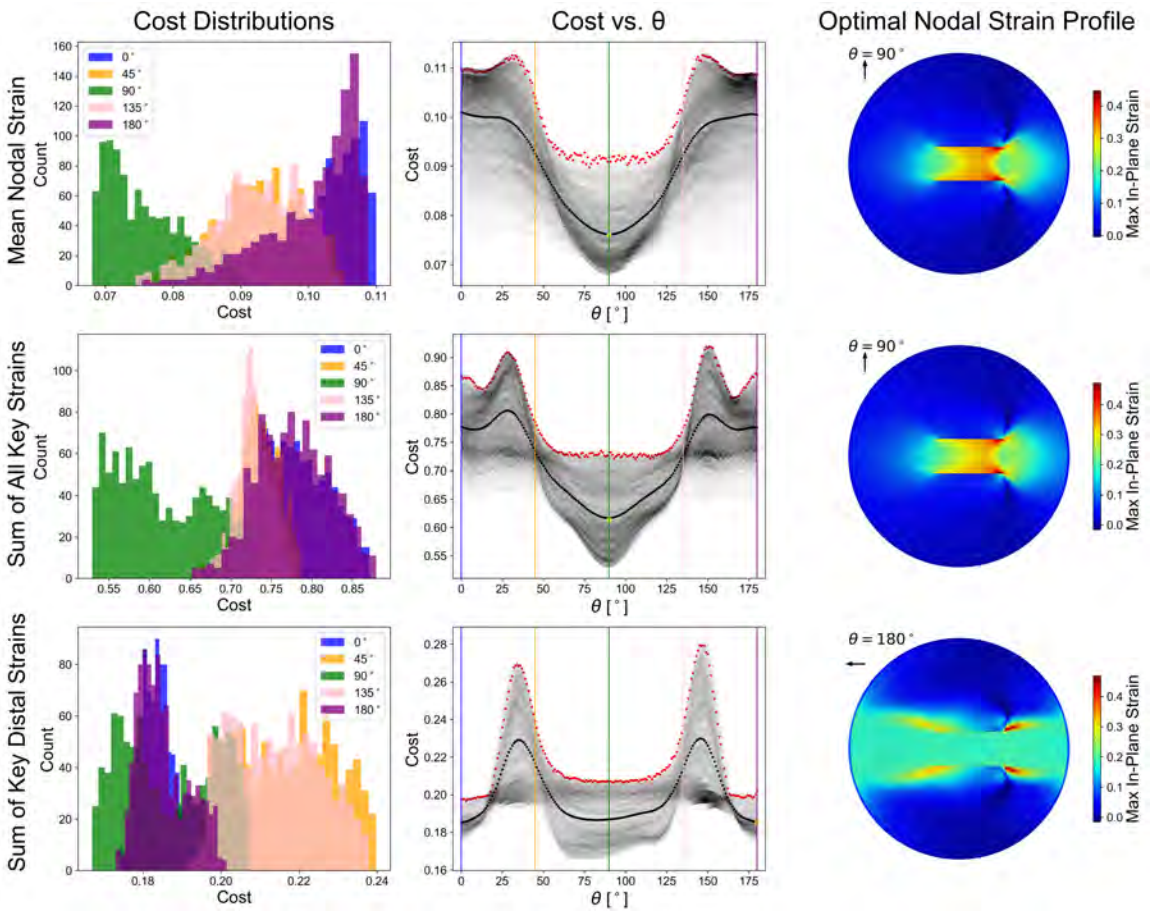

Fig. 10.6.: Results of optimization for the advancement flap. The first column shows cost distributions for five values of θ. The second column shows the cost versus θ plots. The vertical lines of different color correspond to the selected values of θ in the first column. In the middle column, the shaded area corresponds to the distribution of the cost as samples from $p_0(\phi)$ are taken. The expected value of the cost is shown as the black solid line, and the minimum of this expectation is the yellow point in the plot. The red data points show the worst case scenario computed from the particle swarm optimization for each θ. The strain profile corresponding to the minimum expected cost is shown in the third column. The rows denote the three different cost functions introduced in the main text

do, however, note that the optimal results for both objective functions are roughly equivalent as seen in the last column of Fig. 10.7. For all three functions, there is a wide distribution of the cost because we used the prior $p_0(\phi)$. Even though we will introduce narrower distributions, using the prior is still advantageous because it can provide general guidelines even when no specific patient information is available. One

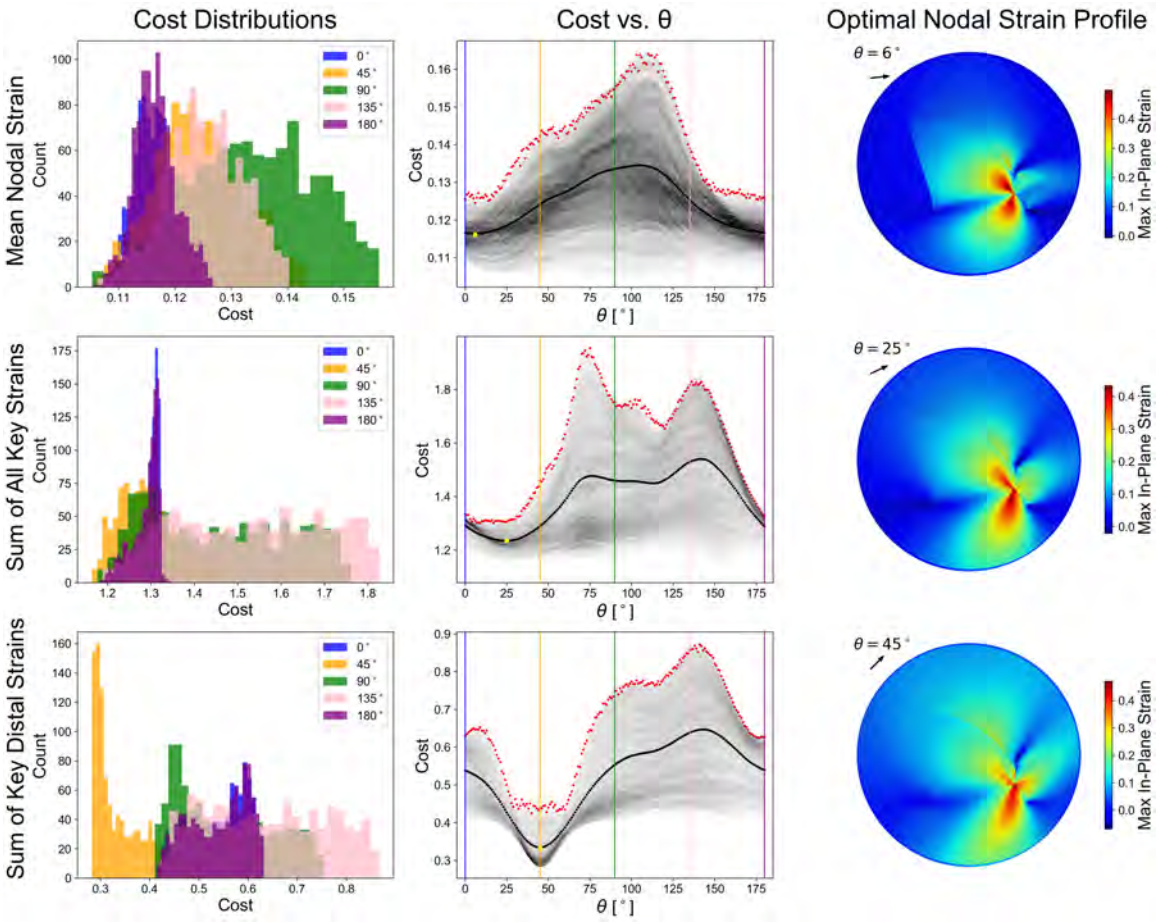

Fig. 10.7.: Results of optimization for the rotation flap. The first column shows cost distributions for five values of θ. The second column shows the cost versus θ. The vertical lines correspond to the selected values of θ in the first column. The shaded area shows the distribution of the cost obtained from sampling values from $p_0(\phi)$, the prior over the material parameters. The solid black line is the expected cost with minimum indicated by the yellow point. The red data points show the worst case scenario obtained from the particle swarm optimizer for each value of θ. The strain profile corresponding to the minimum expected cost is shown in the third column. Each row corresponds to a different cost function.

of the key insights from using this wide distribution is the dependence of the worst case scenario as a function of θ. Looking at the red points in the middle column of Fig. 10.7, it is clear that worst case scenario can vary widely as θ changes. Similar to the advancement case, the worst case scenario follows closely the trends from the

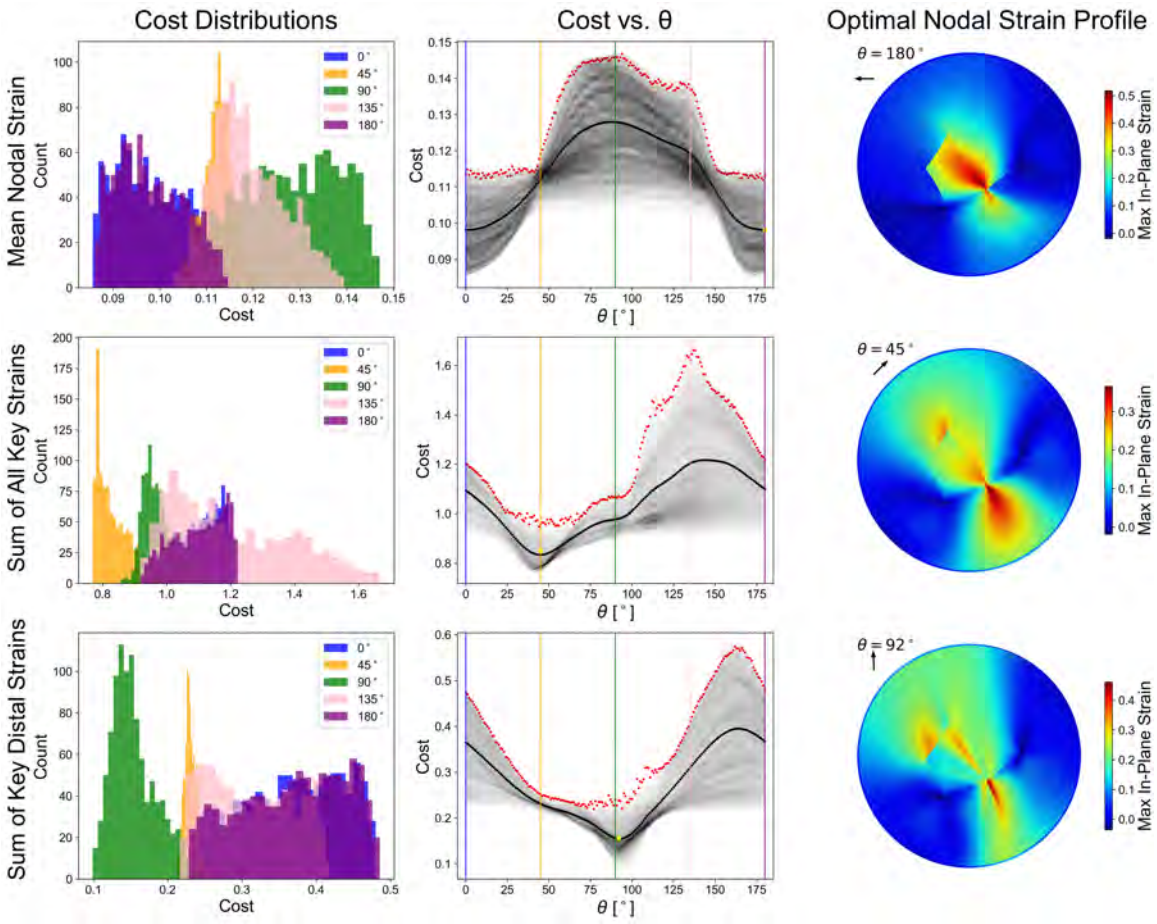

Fig. 10.8.: Results of optimization for the transposition flap. The first column shows cost distributions for five values of θ. The second column shows the cost versus θ. The vertical lines of different color correspond to the selected values of θ in the first column. The solid black line in the middle column is the curve of the expected cost as a function of θ, while the gray shaded regions show the distribution of the cost which follows from sampling material parameters from $p_0(\phi)$. The yellow points on the expected cost curve denotes the minimum of the curve. The worst case scenario for each θ obtained with the particle swarm optimizer is depicted with red points on the middle column. The strain profile corresponding to the minimum expected cost is shown in the third column.

expected cost, but offers perhaps a better argument to restrict θ to a smaller range of approximately $[10, 40]$ even when no other information is available.

For the transposition flap (Fig. 10.8), we again do not have symmetry with respect to θ. The different cost functions with respect to θ show unique features and lead to

very different optimal strain profiles. The optimal values for θ are 180°, 45°, and 92° for the mean nodal strain, sum of all key strains, and sum of key distal strains cost functions, respectively. Note that the cost functions are periodic and thus, for the mean nodal strain, the strain for $\theta = 0°$ is roughly equivalent to that for $\theta = 180°$. The worst case scenario in this flap also follows the trends from the expectation of the cost. The fact that the cost functions produce different results underscores the need to narrow down the design criteria for this flap. As mentioned in the Methods section 10.2, clinical guidelines support the idea of minimizing the overall deformation, but also suggest that points near the wound might be more at risk of complication such as wound dehiscence or scarring, while distal points in the flap may be more at risk of ischemia and necrosis [3, 330, 354]. The results shown here suggest that each of these objectives can lead to a different choice of θ and therefore a careful examination of the relative importance of each of these objectives is needed.

After evaluating the optimal design for the most general case in which no information is available for the material parameters ϕ, we narrow our scope to two cases in which instead of using the prior $p_0(\phi)$, we assume that we have knowledge of individual parameter distributions for two cases. As described above, we solved the optimization problem described in Eq. (10.30) using $p_m(\phi)$, a normal distribution around the mean of the parameter ranges described in Table 10.1, and also $p_i(\phi)$ a narrow normal distribution around the parameters of a 59-year-old female reported in [23]. In Fig. 10.9, we plot the expected value of the cost versus θ for these two distributions, $p_m(\phi)$ and $p_i(\phi)$, as well as the expected cost from the general study, $p_0(\phi)$. For the cases in which we sample from $p_m(\phi)$ and $p_i(\phi)$ we also show shaded regions around the expected cost to contrast the variation in the cost in these cases with respect to what is observed for $p_0(\phi)$ in Figs 10.6-10.8. Immediately we note that the general trend of the curves for each of the individual cases is very similar to the general case in which the wide prior $p_0(\phi)$ was used. The values for θ that minimizes cost for each of these parameters fall within a small range. We also note that the

area of uncertainty around the expected cost is much smaller than before, which is expected since now the parameters ϕ are sampled from narrower distributions.

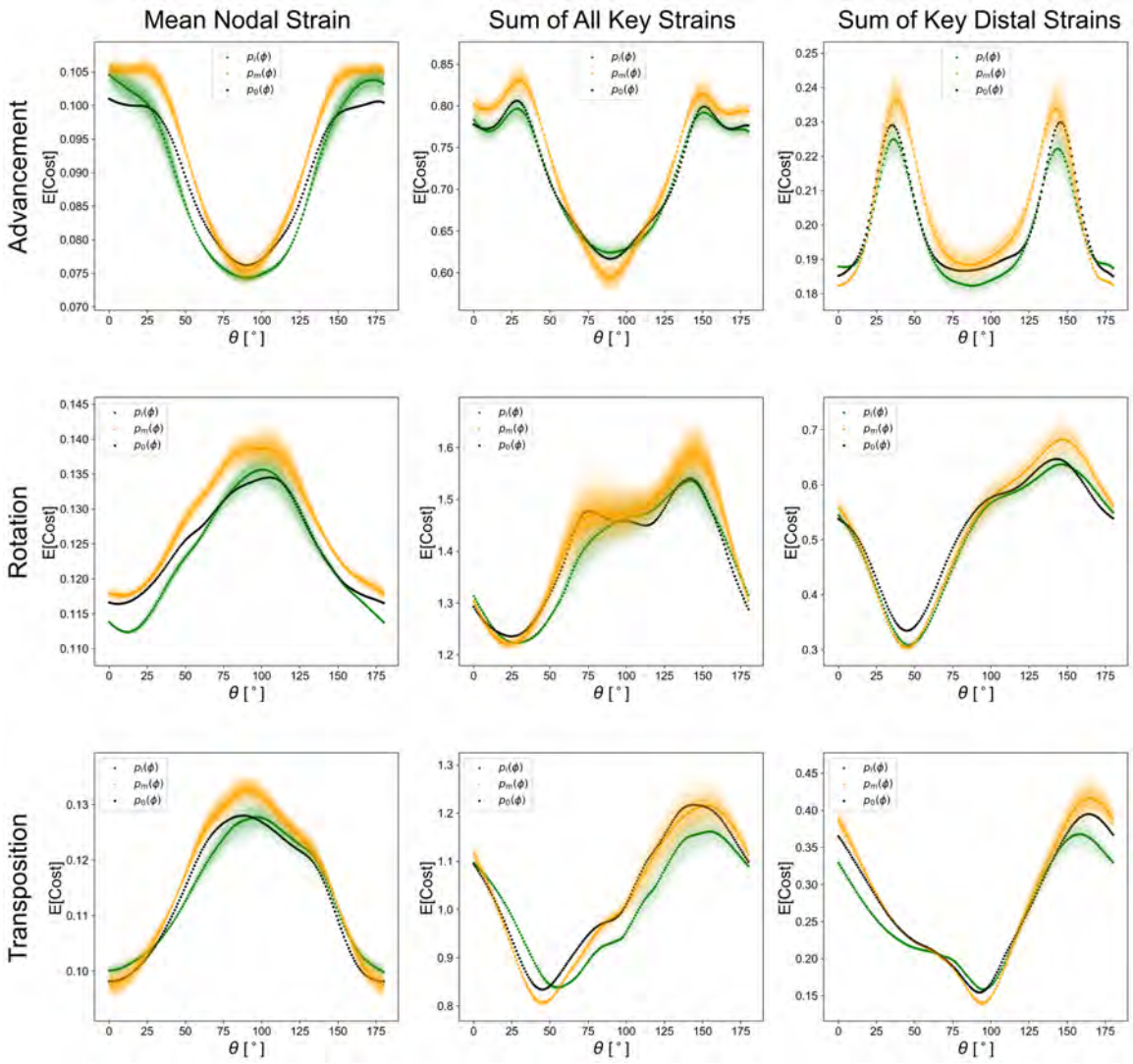

Fig. 10.9.: Expected value of cost for 3 distributions of the material parameters $p(\phi)$: entire range, uniform distribution ($p_0(\phi)$); mean of range, normal distribution ($p_m(\phi)$); and 59-year-old female, normal distribution ($p_i(\phi)$). The shaded regions around $p_m(\phi)$ and $p_i(\phi)$ indicate the cost distribution, while the solid line denotes the expectation of the cost. For the prior distribution $p_0(\phi)$ only the expected cost is shown.

10.4 Discussion

The goal of the present manuscript was twofold. First, we sought to understand the impact of anisotropy on local reconstructive surgery flaps. Second, we aimed to develop computationally inexpensive surrogate models to quickly predict strain profiles for an arbitrary set of material parameters including anisotropy, enabling tasks such as optimization, uncertainty propagation, or model calibration needed in the clinical application. We focused on the three most common local reconstructive surgery flap designs - the advancement, rotation, and transposition flaps [329, 330].

The method relies first on thoroughly but efficiently exploring the input space of material parameters with a relatively small number of well-selected and semi-automated FE simulations, about $2,000$ per flap. The input space considered is five-dimensional, including anisotropy, and is based on a well-established hyperelastic model of collagenous tissues [57, 118]. The range of the parameters was based on the literature and spans up to three orders of magnitude for some parameters [23, 51, 361]. The output data from the detailed FE model is the high-dimensional strain field, on the order of tens of thousands of nodal values, which is not suitable for building the surrogates. We showed that PCA can reduce the dimensionality to a basis of approximately 30 features that capture more than 99% of the variance in the data. The GP surrogates trained on the reduced data can accurately predict the high-dimensional strain fields for any other input within the feasible range, as evidenced by the l_2-norm of the error on the validation set. Unlike the original FE model, the surrogate is computationally inexpensive and enables fast prediction for arbitrary material properties, including anisotropy. We used the surrogates to perform a Sobol sensitivity analysis and determined that the fiber direction (θ) is the most significant parameter to variations in the strain profiles. In view of the sensitivity analysis, we posed several optimization problems to identify the best orientation of the flaps with respect to anisotropy direction.

10.4.1 Performance of Gaussian process surrogates

Overall the GP surrogates performed well on the validation set, enabling fast prediction of the full strain fields for arbitrary choice of material properties. The advancement and transposition results were very accurate, with average errors of less than 2%, while the rotation results had larger errors and standardized residuals. There are numerous possible causes for this issue. One, the nodal strains for the rotation flap may vary more than those of the transposition and advancement flap. Thus, $N = 2,000$ training data sets may not have been sufficient to fully explore the outputs space for the rotation flap. Using more simulations for training may help overcome this issue. In addition, reducing the dimensionality of the output data with PCA does entail a loss of 1.0% of the information, which could have been problematic for the rotation flap. Third, the suturing scheme for this flap leads to very intricate strain field, possibly singular, near the Y-junction at the base, which should be investigated further. A mesh sensitivity analysis was conducted for all flaps, but only for one set of parameters; yet, it is possible that the mesh is not refined enough for other regions of the parameter space. Despite larger errors in the rotation flap with respect to the other two strategies, the average l_2-norm of the relative error was still below 6.5% and this value was considered accurate enough for our purposes.

In previous work, we also looked at the same flap designs - advancement, rotation, transposition- but we considered isotropic material properties [101]. In that work we showed that a smaller training of approximately $N = 1,000$ simulations was enough to capture the response function. The material model used in [101] was the same as the one used here, yet, ignoring anisotropy, the input space consisted of only three parameters. The PCA step for the isotropic material revealed that 99.9% of the variance could be captured with less than 10 features. Here, adding two parameters for anisotropy increased the dimension of the final PC basis, with roughly 30 features needed to describe 99% of the variance. Compared to previous work, we increased the training data to $N = 2,000$, which was enough to produce very good results for the

advancement and transposition surrogates, but only acceptable errors for the rotation case. While more FE simulations are likely to improve our predictions, we considered $N = 2,000$ to be a reasonable computational expense for the resulting accuracy, given that each simulation takes approximately three to five minutes on two Sky Lake CPUs at 2.60 GHz. One of the main advantages of using GP surrogates is that they not only provide a prediction of the response function, but also of the uncertainty in that prediction. This information can be used, for example, to guide active learning strategies and run more simulations if needed, but only at points in the input space in which it would reduce the variance of the GP [157].

10.4.2 Optimal flap orientation

One key result of this study is that the fiber direction (θ) proved to be the most influential parameter on the variations in the strain profiles. This is significant because this parameter can be controlled clinically, unlike the other parameters. While a surgeon cannot control the direction of the skin's collagen fiber network, they can control the orientation of the flap with respect to the direction of anisotropy of skin. Clinically, the anisotropy direction for skin is described based on anatomy and commonly referred to as the direction of relaxed skin tension [345]. Thus, by orienting the flap in an optimal direction with respect to this direction of anisotropy, which we consider aligned with the underlying collagen network, the surgeon has some control over the resulting strain, ideally reducing complications in the healing process. While an initial optimization study was completed here, it would be useful to expand this study to gain a better understanding of the optimal value of θ for more realistic scenarios and refined cost functions. We posed three cost functions in light of clinical guidelines which suggest that surgery should minimize overall deformation, but especially deformation near the suture line and at distal ends of the flap [3,32,330,349,354]. For the advancement flap, which has the most intuitive strain distribution, the result of our optimization aligns with the clinical recommendation of advancing perpendicular

to the anisotropy direction. For the other two flaps, however, the strain distribution is more complex and the influence of the material properties is more noticeable. Our results suggest that for the rotation flap, angles in the approximate range $[10°, 40°]$ are optimal. For the transposition case, we could not identify a consistent result based on the three different objective functions. In the transposition case, minimizing the average strain yields a different result compared to minimizing the sum of the strains near the suture region, and is also different from minimizing only the strains at the distal end of the flap. Therefore, more information is needed to refine the cost function that truly leads to the best clinical outcome.

The initial optimization was done under the assumption that no information is available about the material properties of an individual. We then also explored the case in which some information is available. While having additional information reduced the uncertainty in the cost function, the results aligned with the more general case. Thus, we expect that our analysis with the most general distribution of material parameters should be useful to guide the flap design in the clinical setting, even when no information about skin material properties are available.

10.4.3 Limitations and ongoing work

There are multiple limitations to this work that should be recognized. First, even though the surrogates are accurate over a broad input space covering the material response of skin, more input parameters need to be considered. For instance, we considered a single suturing scheme and a single set of boundary conditions. Future work includes incorporating changes in geometric parameters of the flaps, such as angle of transposition or angle of rotation for these two flap designs, or base to width ratio for the advancement flap. Suturing schemes can also be optimized and should thus be considered as inputs in metamodel creation, as well as the change in boundary conditions.

Another limitation of the current work is the need for validation in the clinical setting. Numerical models of soft tissues are well-established [14, 19]. In particular regarding skin, the GOH hyperelastic material model has been deemed appropriate to capture the response of skin under tensile loading [118, 360]. However, assumption of hyperelasticity is debatable for larger time scale for which the tissue may show viscoelastic behavior [366]. The interaction between the skin and the underlying tissues is also ignored in this model, but could be important in a more realistic setting. The influence of pre-stress is also ignored in this study, but it could be an important factor [127]. Finally, *in vivo* measurem in the clinical setting [181,303,367]. Thus, while we are confident that the results shown here provide valuable insight into flap biomechanics and should be used to improve flap design, the models still need to be further validated with clinical data, which is the central task of our ongoing work.

10.5 Conclusion

In summary, we showed that a few detailed finite element simulations, paired with reduced order modeling strategies, can be used to create inexpensive yet accurate Gaussian process surrogate models of the three most common flap designs. The surrogate models enable immediate prediction of strain profiles for arbitrary material properties including anisotropy, enabling tasks such as uncertainty propagation, model calibration, sensitivity analysis, and optimization. The direction of anisotropy with respect to the flap design is the single most important parameter that the surgeon can control to optimize a desired strain objective, even when the other material parameters are completely unknown.

11. CONCLUSIONS AND OUTLOOK

This dissertation focused on improving reconstructive surgery through computational biomechanics. Even though mechanical cues are recognized as a critical factor driving wound healing complications, planning to reduce mechanical stress on tissues is still done based on each surgeon's training and experience rather than with quantitative and precise tools. Computational mechanics seems like an obvious tool to address this need, yet, simulations of tissue mechanics are not currently being used in the clinical setting. We asked why. The gaps we found are the driving motivation for the studies presented here. The core of the dissertation deals with the inherent uncertainty in biological systems. In the context of reconstructive surgery, this uncertainty is due to three sources: variability in individual patient geometry and clinical need, variability in mechanical behavior of skin, variability of biological response. To deal with the uncertainty analysis, the dissertation focused on the use of Bayesian approaches aided by machine learning.

Computational simulations of skin reconstruction require knowledge of the patient geometry, the surgery plan, and the material properties including the state of *in vivo* pre-stress. Different tools have been introduced to address each of these requirements. For example, different means of obtaining three-dimensional patient specific geometries are available, such as computer tomography scans and magnetic resonance imaging. For the case of skin, stereo-vision systems have been more common recently. Yet, these methods still rely on specialized equipment. We presented here the use of multi-view stereo (MVS) to create individual geometries. MVS requieres multiple images taken with any digital camera, and uses feature matching across pairs of photographs to back-calculate the camera position. This method is thus flexible and affordable, and we expect that it will broaden the use of computational models on patient-specific geometries. Further work on this pipeline is needed to automate the

geometric model creation to make it more robust and easy-to-use by surgeons. For example, work on creating atlas models and machine learning algorithms to improve mesh generation are one possible direction for future research in this area.

Material behavior of skin has been characterized *ex vivo* under a variety of uniaxial and biaxial loading conditions. These tests have revealed the characteristic features of skin's mechanical behavior. Like many collagen-based tissues, skin shows an exponential stiffening at larger stretches. Various strain energy functions have been proposed to describe this behavior. Thus, many efforts on this regard are restricted to considering skin as a hyperelastic material. The *ex vivo* tests have shown, besides the exponential behavior, that soft tissues are inherently variable. Skin mechanical properties change with age, anatomical location, gender, with environmental conditions, and even from patient to patient. This has further contributed to the development of *in vivo* measurement techniques. Suction is the the most common. While the suction devices have definitely helped acquiring more personalized parameters, much work remains in this area. The main gaps in this setting are that the material parameters from suction measurements are not directly available. Given the complex loading scenario *in vivo*, analytical approximations are inaccurate. Classical inverse finite elements, on the other extreme, are ill-posed and time and resource intensive. We show a Bayesian framework for calibration of material properties that relies on surrogate models created through machine learning. Our approach thus leads to the inherent uncertainty of material behavior, used prior information, and is computationally efficient. We further show how different openings of the suction device and loading conditions can be used to maximize information and improve calibration. Further work in this are is the acquisition of patient data and improvement of the constitutive models considering other effects beyond hyperelastic behavior, such as viscoelastic effects.

The state of pre-stress has also been documented, starting with the seminal work of Langer in the nineteenth century who measured residual deformation in cadavers. The state of pre-stress is often changed in reconstructive surgery in the technique of

tissue expansion. Skin grows in response to tissue expansion. This biological adaptation introduced a new type of uncertainty. The mechanobiology of skin growth is still poorly understood. In this dissertation we show first how to characterize the mechanics of skin growth with continuum mechanics on an animal model of tissue expansion. The method relies on MVS and isogeometric analysis. We showed that, following the framework of finite growth - the multiplicative split of the deformation gradient into growth and elastic contributions - we can describe skin adaptation to chronic hyper-stretch induced by the tissue expansion process. This work showed, on the other hand, the importance of the uncertainty analysis not just considering mechanical properties but also biological behavior. In order to do model calibration with this noisy data we developed a multi-fidelity surrogate model framework that incorporates the different sources of uncertainty, biological and mechanical. This work has thus settled the methodology and initial data for skin growth models. Much work remains to be done in this area. Certainly more animal data is needed before extending this tool to the clinical setting. More work on calibration of the computational model is also needed and underway using the tools developed in this dissertation.

The last portion of the dissertation addresses directly the computational modeling of the reconstructive surgery step. We showed first the effect of uncertainty in mechanical behavior and simple geometric quantities on the stress profiles from idealized flap designs. We studied the mechanics of advancement, transposition and rotation flaps in flat geometries. This setting allowed us to dissect the distinctive features of these flap designs, and the effect of material behavior uncertainty. To do so, we once again posed the problem within a Bayesian framework witht he help of machine learning tools to deal with the computational cost. We found that the most sensitive parameter for the design of the flap is the direction of anisotropy and offered recommendations for surgeons based on our analysis of flap biomechanics. Combining these techniques with patient-specific geometries, we further showed the variations in stress profiles in the patient geometries when the material properties are uncertain. Our analysis cemented the notion that predictive models have to account

for mechanical behavior uncertainty and provide probabilities of stress rather than single predictions which may lead to erroneous conclusions about the stress profile for an individual. At the time of writing of this dissertation, the work on patient-specific rotation flaps is being considered in a clinical journal and thus shows the potential impact of our work in the clinical setting in the near future. More work is also needed in this area in the future. The current pipeline is still not automated and not robust compared to the idealized cases. Thus, one avenue of research would be to further develop the model generation algorithms leveraging our previous work. Lastly, an important limitation of restricting our attention to the biomechanics of reconstructive surgery is that we ignore the processes that take place immediately after surgery. The wound healing process following surgery is complicated and involves many other factors that just mechanical cues. For instance, blood flow and inflammation are also incredibly important in the subsequent healing progression after surgery, but we are not incorporating those aspects into out model. Therefore, perhaps the widest and most challenging avenue of research in the future would be to not just improve our recommendation of flap design based solely on mechanics, but to predict the final outcome.

In summary, this dissertation has improved our understanding of different reconstructive surgery techniques in terms of skin mechanics. In particular, we have shown the importance of considering the uncertainty of skin mechanical and biological response when designing reconstructive procedures in ideal and individual cases. We are confident that the tools and results presented are impacting medicine and will continue to do so as these technologies are developed further.

REFERENCES

REFERENCES

[1] T. Humphreys, "Cutaneous flaps," in Skin Cancer Management. Springer, 2009, pp. 153–178.

[2] L. C. Bartlett, "Pressure necrosis is the primary cause of wound dehiscence," Canadian Journal of Surgery, vol. 28, no. 1, pp. 27–30, 1985.

[3] G. C. Gurtner, R. H. Dauskardt, V. W. Wong, K. A. Bhatt, K. Wu, I. N. Vial, K. Padois, J. M. Korman, and M. T. Longaker, "Improving cutaneous scar formation by controlling the mechanical environment: large animal and phase i studies," Annals of surgery, vol. 254, no. 2, pp. 217–225, 2011.

[4] V. W. Wong, K. Levi, S. Akaishi, G. Schultz, and R. H. Dauskardt, "Scar zones: Region-specific differences in skin tension may determine incisional scar formation," Plastic and Reconstructive Surgery, vol. 129, no. 6, pp. 1272–1276, 2012.

[5] R. Ogawa, K. Okai, F. Tokumura, K. Mori, Y. Ohmori, C. Huang, H. Hyakusoku, and S. Akaishi, "The relationship between skin stretching/contraction and pathologic scarring: The important role of mechanical forces in keloid generation," Wound Repair and Regeneration, vol. 20, no. 2, pp. 149–157, 2012.

[6] S. P. Paul, "The golden spiral flap: A new flap design that allows for closure of larger wounds under reduced tension - how studying nature's own design led to the development of a new surgical technique.(report)(brief article)," Frontiers in Surgery, vol. 3, 2016.

[7] A. K. Gosain, C. G. Zochowski, and W. Cortes, "Refinements of tissue expansion for pediatric forehead reconstruction: a 13-year experience," Plastic and reconstructive surgery, vol. 124, no. 5, pp. 1559–1570, 2009.

[8] S. P. Paul, J. Matulich, and N. Charlton, "A new skin tensiometer device: computational analyses to understand biodynamic excisional skin tension lines," Scientific reports, vol. 6, no. 1, pp. 1–5, 2016.

[9] J. D. Humphrey, Cardiovascular solid mechanics: cells, tissues, and organs. Springer Science & Business Media, 2013.

[10] R. Vandiver and A. Goriely, "Differential growth and residual stress in cylindrical elastic structures," Philosophical Transactions of the Royal Society A: Mathematical, Physical and Engineering Sciences, vol. 367, no. 1902, pp. 3607–3630, 2009.

[11] Y. Lanir, "Mechanisms of residual stress in soft tissues," Journal of biomechanical engineering, vol. 131, no. 4, 2009.

[12] M. K. Rausch, M. Genet, and J. D. Humphrey, "An augmented iterative method for identifying a stress-free reference configuration in image-based biomechanical modeling," Journal of Biomechanics, vol. 58, pp. 227–231, 2017.

[13] A. Buganza Tepole and A. K. Gosain, Constitutive Modelling of Skin Growth. Cham: Springer International Publishing, 2019, pp. 77–100.

[14] A. Buganza Tepole, A. K. Gosain, and E. Kuhl, "Computational modeling of skin: using stress profiles as predictor for tissue necrosis in reconstructive surgery," Computers & structures, vol. 143, pp. 32–39, 2014.

[15] E. Sifakis, J. Hellrung, J. Teran, A. Oliker, and C. Cutting, "Local flaps: A real-time finite element based solution to the plastic surgery defect puzzle," in Studies in Health Technology and Informatics, 2009.

[16] P. H. DeHoff and J. E. Key, "Application of the finite element analysis to determine forces and stresses in wound closing," Journal of Biomechanics, vol. 14, no. 8, pp. 549–554, 1981.

[17] A. Rajabi, A. T. Dolovich, and J. D. Johnston, "From the rhombic transposition flap toward z-plasty: an optimized design using the finite element method," Journal of biomechanics, vol. 48, no. 13, pp. 3672–3678, 2015.

[18] D. Remache, J. Chambert, J. Pauchot, and E. Jacquet, "Numerical analysis of the vy shaped advancement flap," Medical engineering & physics, vol. 37, no. 10, pp. 987–994, 2015.

[19] N. Mitchell, M., C. Cutting, B., T. King, W., A. Oliker, D., and E. Sifakis, D., "A real-time local flaps surgical simulator based on advances in computational algorithms for finite element models," Plastic and reconstructive surgery, vol. 137, no. 2, pp. 445e–452e, 2016.

[20] M. B. Rubin and S. R. Bodner, "A three-dimensional nonlinear model for dissipative response of soft tissue," International Journal of Solids and Structures, 2002.

[21] D. C. Schneider, T. M. Davidson, and A. M. Nahum, "In vitro biaxial stress-strain response of human skin," Archives of Otolaryngology, vol. 110, no. 5, pp. 329–333, 1984.

[22] W. A. Wan Abas, "Biaxial tension test of human skin in vivo," Bio-medical materials and engineering, vol. 4, no. 7, pp. 473–486, 1994.

[23] T. K. Tonge, L. S. Atlan, L. M. Voo, and T. D. Nguyen, "Full-field bulge test for planar anisotropic tissues: Part I-Experimental methods applied to human skin tissue," Acta Biomaterialia, vol. 9, no. 4, pp. 5913–5925, 2013.

[24] D. Batisse, R. Bazin, T. Baldeweck, B. Querleux, and J.-L. Lévêque, "Influence of age on the wrinkling capacities of skin," Skin Research and Technology, vol. 8, no. 3, pp. 148–154, 2002.

[25] A. Delalleau, G. Josse, J.-M. Lagarde, H. Zahouani, and J.-M. Bergheau, "Characterization of the mechanical properties of skin by inverse analysis combined with the indentation test," Journal of Biomechanics, vol. 39, no. 9, pp. 1603–1610, 2006.

[26] H. V. Tran, F. Charleux, M. Rachik, A. Ehrlacher, and M. C. Ho Ba Tho, "In vivo characterization of the mechanical properties of human skin derived from mri and indentation techniques," Computer methods in biomechanics and biomedical engineering, vol. 10, no. 6, pp. 401–407, 2007.

[27] J. Weickenmeier, M. Jabareen, and E. Mazza, "Suction based mechanical characterization of superficial facial soft tissues," Journal of biomechanics, vol. 48, no. 16, pp. 4279–4286, 2015.

[28] L. K. Smalls, R. Randall Wickett, and M. O. Visscher, "Effect of dermal thickness, tissue composition, and body site on skin biomechanical properties," Skin Research and Technology, 2006.

[29] C. Flynn, A. J. Taberner, P. M. F. Nielsen, and S. Fels, "Simulating the three-dimensional deformation of in vivo facial skin," Journal of the mechanical behavior of biomedical materials, vol. 28, pp. 484–494, 2013.

[30] M. Tschoi, E. A. Hoy, and M. S. Granick, "Skin Flaps," Surgical Clinics of North America, vol. 89, no. 3, pp. 643–658, 2009.

[31] R. M. Koch, M. H. Gross, F. R. Carls, D. F. von Buren, G. Fankhauser, and Y. I. H. Parish, "Simulating facial surgery using finite element models," in Proceedings of the ACM SIGGRAPH Conference on Computer Graphics, 1996, pp. 421–428.

[32] T. E. Rohrer and A. Bhatia, "Transposition Flaps in Cutaneous Surgery," Dermatologic surgery, vol. 31, pp. 1014–1023, 2005.

[33] A. Wittek, K. Miller, R. Kikinis, and S. K. Warfield, "Patient-specific model of brain deformation: Application to medical image registration," Journal of Biomechanics, vol. 40, no. 4, pp. 919–929, 2007.

[34] V. Luboz, M. Chabanas, P. Swider, and Y. Payan, "Orbital and maxillofacial computer aided surgery: patient-specific finite element models to predict surgical outcomes," Computer methods in biomechanics and biomedical engineering, vol. 8, no. 4, pp. 259–265, 2005.

[35] J. Paterno, I. N. Vial, V. W. Wong, K. C. Rustad, M. Sorkin, Y. Shi, K. A. Bhatt, H. Thangarajah, J. P. Glotzbach, and G. C. Gurtner, "Akt-mediated mechanotransduction in murine fibroblasts during hypertrophic scar formation," Wound Repair and Regeneration, vol. 19, no. 1, pp. 49–58, 2011.

[36] V. W. Wong, M. T. Longaker, and G. C. Gurtner, "Soft tissue mechanotransduction in wound healing and fibrosis," 2012.

[37] J. M. Benítez and F. J. Montáns, "The mechanical behavior of skin: Structures and models for the finite element analysis," Computers & Structures, vol. 190, pp. 75–107, 2017.

[38] H. Shimizu, Shimizu's textbook of dermatology. Hokkaido University, 2007.

[39] C. Griffiths, J. Barker, T. Bleiker, R. Chalmers, and D. Creamer, Rook's textbook of dermatology. John Wiley & Sons, 2016.

[40] F. Xu and T. Lu, Introduction to skin biothermomechanics and thermal pain. Springer, 2011.

[41] S. M. Maricich, S. A. Wellnitz, A. M. Nelson, D. R. Lesniak, G. J. Gerling, E. A. Lumpkin, and H. Y. Zoghbi, "Merkel cells are essential for light-touch responses," Science, vol. 324, no. 5934, pp. 1580–1582, 2009.

[42] K. Langer, "On the anatomy and physiology of the skin: I. the cleavability of the cutis," British Journal of Plastic Surgery, vol. 31, no. 1, pp. 3–8, 1978.

[43] C. H. Daly, "Biomechanical properties of dermis," Journal of Investigative Dermatology, vol. 79, no. 1, pp. 17–20, 1982.

[44] P. A. Payne, "Measurement of properties and function of skin," Clinical Physics and Physiological Measurement, vol. 12, no. 2, p. 105, 1991.

[45] J. W. Y. Jor, M. D. Parker, A. J. Taberner, M. P. Nash, and P. M. F. Nielsen, "Computational and experimental characterization of skin mechanics: identifying current challenges and future directions," Wiley Interdisciplinary Reviews: Systems Biology and Medicine, vol. 5, no. 5, pp. 539–556, 2013.

[46] S. Wiedersberg, C. S. Leopold, and R. H. Guy, "Bioavailability and bioequivalence of topical glucocorticoids," European Journal of Pharmaceutics and Biopharmaceutics, vol. 68, no. 3, pp. 453–466, 2008.

[47] F. Groeber, M. Holeiter, M. Hampel, S. Hinderer, and K. Schenke-Layland, "Skin tissue engineeringin vivo and in vitro applications," Advanced drug delivery reviews, vol. 63, no. 4-5, pp. 352–366, 2011.

[48] S. Baranoski, E. A. Ayello, M. Tomic-Canic, and J. Levine, "Skin: an essential organ," Wound Care Essentials: Practice Principles. Springhouse, PA: Lippincott, Williams & Wilkins, pp. 47–59, 2004.

[49] H. Alexander and T. H. Cook, "Accounting for natural tension in the mechanical testing of human skin," Journal of Investigative Dermatology, vol. 69, no. 3, 1977.

[50] Y. Lanir, "Skin mechanics," in Handbook of bioengineering. McGraw-Hill, 1987, pp. 11.11–11.25.

[51] A. N. Annaidh, K. Bruyère, M. Destrade, M. D. Gilchrist, and M. Otténio, "Characterization of the anisotropic mechanical properties of excised human skin," Journal of the mechanical behavior of biomedical materials, vol. 5, no. 1, pp. 139–148, 2012.

[52] K. Parsons, Human thermal environments: the effects of hot, moderate, and cold environments on human health, comfort, and performance. CRC press, 2014.

[53] M. J. Muoz, J. A. Bea, J. F. Rodrguez, I. Ochoa, J. Grasa, A. Prez Del Palomar, P. Zaragoza, R. Osta, and M. Doblar, "An experimental study of the mouse skin behaviour: Damage and inelastic aspects," Journal of Biomechanics, vol. 41, no. 1, pp. 93–99, 2008.

[54] R. C. Haut, "The effects of orientation and location on the strength of dorsal rat skin in high and low speed tensile failure experiments," Journal of biomechanical engineering, vol. 111, no. 2, pp. 136–140, 1989.

[55] G. Limbert, "Chapter 4: State-of-the-art constitutive models of skin biomechanics," in Computational biophysics of the skin (ed. B Querleux). Pan Stanford Publishing Pty Ltd, Singapore, 2014, pp. 95–131.

[56] D. R. Veronda and R. A. Westmann, "Mechanical characterization of skinfinite deformations," Journal of Biomechanics, vol. 3, no. 1, pp. 111–124, 1970.

[57] T. C. Gasser, R. W. Ogden, and G. A. Holzapfel, "Hyperelastic modelling of arterial layers with distributed collagen fibre orientations," Journal Of The Royal Society Interface, vol. 3, no. 6, pp. 15–35, 2006.

[58] G. A. Holzapfel and T. C. Gasser, "A viscoelastic model for fiber-reinforced composites at finite strains: Continuum basis, computational aspects and applications," Computer methods in applied mechanics and engineering, vol. 190, no. 34, pp. 4379–4403, 2001.

[59] G. A. Holzapfel, T. C. Gasser, and R. W. Ogden, "A new constitutive framework for arterial wall mechanics and a comparative study of material models," Journal of elasticity and the physical science of solids, vol. 61, no. 1-3, pp. 1–48, 2000.

[60] T. K. Tonge, L. M. Voo, and T. D. Nguyen, "Full-field bulge test for planar anisotropic tissues: Part II-A thin shell method for determining material parameters and comparison of two distributed fiber modeling approaches," Acta Biomaterialia, vol. 9, no. 4, pp. 5926–5942, 2013.

[61] C. Flynn, "Chapter 5: Fiber-matrix models of the dermis," in Computational biophysics of the skin (ed. B Querleux). Pan Stanford Publishing Pty Ltd, Singapore, 2014, pp. 133–159.

[62] H. H. Mitchell, T. S. Hamilton, F. R. Steggerda, and H. W. Bean, "The chemical composition of the adult human body and its bearing on the biochemistry of growth," Journal of Biological Chemistry, vol. 158, no. 3, pp. 625–637, 1945.

[63] Y. T. Lanir, "Constitutive equations for fibrous connective tissues," Journal of biomechanics, vol. 16, no. 1, pp. 1–12, 1983.

[64] P. A. Shoemaker, D. Schneider, M. C. Lee, and Y. C. Fung, "A constitutive model for two-dimensional soft tissues and its application to experimental data," Journal of Biomechanics, vol. 19, no. 9, pp. 695 – 702, 1986.

[65] J. E. Bischoff, E. M. Arruda, and K. Grosh, "A rheological network model for the continuum anisotropic and viscoelastic behavior of soft tissue," Biomechanics and modeling in mechanobiology, vol. 3, no. 1, pp. 56–65, 2004.

[66] E. Raposio and R. E. A. Nordström, "Biomechanical properties of scalp flaps and their correlations to reconstructive and aesthetic surgery procedures," Skin Research and Technology, vol. 4, no. 2, pp. 94–98, 1998.

[67] H. S. Ryu, Y. H. Joo, S. O. Kim, K. C. Park, and S. W. Youn, "Influence of age and regional differences on skin elasticity as measured by the cutometer®," Skin Research and Technology, vol. 14, no. 3, pp. 354–358, 2008.

[68] H. Ohshima, S. Kinoshita, M. Oyobikawa, M. Futagawa, H. Takiwaki, A. Ishiko, and H. Kanto, "Use of cutometer area parameters in evaluating age-related changes in the skin elasticity of the cheek," Skin Research and Technology, vol. 19, no. 1, pp. e238–e242, 2013.

[69] T. Hermanns-Lê, I. Uhoda, S. Smitz, and G. E. Piérard, "Skin tensile properties revisited during ageing. where now, where next?" Journal of Cosmetic Dermatology, vol. 3, no. 1, pp. 35–40, 2004.

[70] P. Elsner, D. Wilhelm, and H. I. Maibach, "Mechanical properties of human forearm and vulvar skin," British Journal of Dermatology, vol. 122, no. 5, pp. 607–614, 1990.

[71] K. S. Wu, W. W. van Osdol, and R. H. Dauskardt, "Mechanical properties of human stratum corneum: effects of temperature, hydration, and chemical treatment," Biomaterials, vol. 27, no. 5, pp. 785–795, 2006.

[72] M. Geerligs, L. Van Breemen, G. Peters, P. Ackermans, F. Baaijens, and C. Oomens, "In vitro indentation to determine the mechanical properties of epidermis," Journal of Biomechanics, vol. 44, no. 6, pp. 1176–1181, 2011.

[73] H. Zahouani, C. Pailler-Mattei, B. Sohm, R. Vargiolu, V. Cenizo, and R. Debret, "Characterization of the mechanical properties of a dermal equivalent compared with human skin in vivo by indentation and static friction tests," Skin research and technology, vol. 15, no. 1, pp. 68–76, 2009.

[74] C. Pailler-Mattei, S. Bec, and H. Zahouani, "In vivo measurements of the elastic mechanical properties of human skin by indentation tests," Medical engineering & physics, vol. 30, no. 5, pp. 599–606, 2008.

[75] F. M. Hendriks, D. Brokken, J. T. W. M. Van Eemeren, C. W. J. Oomens, F. P. T. Baaijens, and J. B. A. M. Horsten, "A numericalexperimental method to characterize the nonlinear mechanical behaviour of human skin," Skin Research and Technology, vol. 9, no. 3, pp. 274–283, 2003.

[76] R. B. Groves, S. A. Coulman, J. C. Birchall, and S. L. Evans, "An anisotropic, hyperelastic model for skin: experimental measurements, finite element modelling and identification of parameters for human and murine skin," Journal of the mechanical behavior of biomedical materials, vol. 18, pp. 167–180, 2013.

[77] A. I. Sakellarios, M. I. Papafaklis, P. Siogkas, L. S. Athanasiou, T. P. Exarchos, K. Stefanou, C. V. Bourantas, K. K. Naka, L. K. Michalis, O. Parodi, and D. I. Fotiadis, "Patient-specific computational modeling of subendothelial ldl accumulation in a stenosed right coronary artery: effect of hemodynamic and biological factors," American journal of physiology. Heart and circulatory physiology, vol. 304, no. 11, p. H1455, 2013.

[78] J. Ho, H. Von Holst, and S. Kleiven, "Automatic generation and validation of patient-specific finite element head models suitable for crashworthiness analysis," International Journal of Crashworthiness, vol. 14, no. 6, pp. 555–563, 2009.

[79] A. Krishnamurthy, C. T. Villongco, J. Chuang, L. R. Frank, V. Nigam, E. Belezzuoli, P. Stark, D. E. Krummen, S. Narayan, J. H. Omens, A. D. Mcculloch, and R. C. P. Kerckhoffs, "Patient-specific models of cardiac biomechanics," Journal of Computational Physics, vol. 244, pp. 4–21, 2013.

[80] A. M. Zöllner, A. Buganza Tepole, A. K. Gosain, and E. Kuhl, "Growing skin: tissue expansion in pediatric forehead reconstruction," Biomechanics and modeling in mechanobiology, vol. 11, no. 6, pp. 855–867, 2012.

[81] D. M. Espino, D. E. T. Shepherd, and D. W. L. Hukins, "Evaluation of a transient, simultaneous, arbitrary lagrange-euler based multi-physics method for simulating the mitral heart valve," Computer Methods in Biomechanics and Biomedical Engineering, vol. 17, no. 4, pp. 450–458, 2014.

[82] A. Schäfer, J. Weickenmeier, and E. Kuhl, "The interplay of biochemical and biomechanical degeneration in alzheimers disease," Computer Methods in Applied Mechanics and Engineering, vol. 352, pp. 369–388, 2019.

[83] A. Buganza Tepole, "Computational systems mechanobiology of wound healing," Computer Methods in Applied Mechanics and Engineering, vol. 314, pp. 46–70, 2017.

[84] M. Freutel, H. Schmidt, L. Drselen, A. Ignatius, and F. Galbusera, "Finite element modeling of soft tissues: Material models, tissue interaction and challenges," Clinical Biomechanics, vol. 29, no. 4, pp. 363–372, 2014.

[85] Y.-C. Fung, Biomechanics: mechanical properties of living tissues. Springer Science & Business Media, 2013.

[86] A. Hagemann, K. Rohr, H. S. Stiehl, U. Spetzger, and J. M. Gilsbach, "Biomechanical modeling of the human head for physically based, nonrigid image registration," IEEE Transactions on Medical Imaging, vol. 18, no. 10, pp. 875–884, 1999.

[87] G. M. Bydder, J. V. Hajnal, N. Saeed, and I. R. Young, "Registration and subtraction of serial mr images of the brain," Radiology, vol. 201, pp. 136–136, 1996.

[88] S. K. Warfield, F. Talos, A. Tei, A. Bharatha, A. Nabavi, M. Ferrant, P. McL. Black, F. A. Jolesz, and R. Kikinis, "Real-time registration of volumetric brain mri by biomechanical simulation of deformation during image guided neurosurgery," Computing and Visualization in Science, vol. 5, no. 1, pp. 3–11, 2002.

[89] G. Picinbono, H. Delingette, and N. Ayache, "Non-linear anisotropic elasticity for real-time surgery simulation," Graphical Models, vol. 65, no. 5, pp. 305–321, 2003.

[90] J. Berkley, G. Turkiyyah, D. Berg, M. Ganter, and S. Weghorst, "Real-time finite element modeling for surgery simulation: An application to virtual suturing," IEEE Transactions on visualization and computer graphics, vol. 10, no. 3, pp. 314–325, 2004.

[91] C.-H. Wong, F. Cui, B.-K. Tan, Z. Liu, H.-P. Lee, C. Lu, C.-L. Foo, and C. Song, "Nonlinear finite element simulations to elucidate the determinants of perforator patency in propeller flaps," Annals of Plastic Surgery, vol. 59, no. 6, pp. 672–678, 2007.

[92] H. W. Nienhuys and A. F. V. D. Stappen, "Supporting cuts and finite element deformation in interactive surgery simulation," 2001.

[93] M. Bucki, C. Lobos, and Y. Payan, "A fast and robust patient specific finite element mesh registration technique: Application to 60 clinical cases," Medical Image Analysis, vol. 14, no. 3, pp. 303–317, 2010.

[94] S. Morganti, M. Conti, M. Aiello, A. Valentini, A. Mazzola, A. Reali, and F. Auricchio, "Simulation of transcatheter aortic valve implantation through patient-specific finite element analysis: Two clinical cases," Journal of Biomechanics, vol. 47, no. 11, pp. 2547–2555, 2014.

[95] A. Horton, A. Wittek, G. R. Joldes, and K. Miller, "A meshless total lagrangian explicit dynamics algorithm for surgical simulation," International Journal for Numerical Methods in Biomedical Engineering, vol. 26, no. 8, pp. 977–998, 2010.

[96] Z. A. Taylor, M. Cheng, and S. Ourselin, "High-speed nonlinear finite element analysis for surgical simulation using graphics processing units," IEEE Transactions on Medical Imaging, vol. 27, no. 5, pp. 650–663, 2008.

[97] T. Lee, E. E. Vaca, J. K. Ledwon, H. Bae, J. M. Topczewska, S. Y. Turin, E. Kuhl, A. K. Gosain, and A. Buganza Tepole, "Improving tissue expansion protocols through computational modeling," Journal of the mechanical behavior of biomedical materials, vol. 82, pp. 224–234, 2018.

[98] T. Lee, I. Bilionis, and A. Buganza Tepole, "Propagation of uncertainty in the mechanical and biological response of growing tissues using multi-fidelity gaussian process regression," Computer Methods in Applied Mechanics and Engineering, vol. 359, p. 112724, 2020.

[99] T. Lee, S. Y. Turin, A. K. Gosain, and A. Buganza Tepole, "Multi-view stereo in the operating room allows prediction of healing complications in a patient-specific model of reconstructive surgery," Journal of Biomechanics, vol. 74, pp. 202–206, 2018.

[100] T. Lee, S. Y. Turin, A. K. Gosain, I. Bilionis, and A. Buganza Tepole, "Propagation of material behavior uncertainty in a nonlinear finite element model of reconstructive surgery," Biomechanics and Modeling in Mechanobiology, vol. 17, no. 6, pp. 1857–1873, 2018.

[101] T. Lee, A. K. Gosain, I. Bilionis, and A. Buganza Tepole, "Predicting the effect of aging and defect size on the stress profiles of skin from advancement, rotation and transposition flap surgeries," Journal of the Mechanics and Physics of Solids, vol. 125, pp. 572–590, 2019.

[102] J. Marcus, D. B. Horan, and J. K. Robinson, "Tissue expansion: past, present, and future," Journal of the American Academy of Dermatology, vol. 23, no. 5, pp. 813–825, 1990.

[103] C. G. Neumann, "The expansion of an area of skin by progressive distention of a subcutaneous balloon: Use of the method for securing skin for subtotal reconstruction of the ear," Plastic and reconstructive surgery, vol. 19, no. 2, pp. 124–130, 1957.

[104] B. Khalatbari and A. Bakhshaeekia, "Ten-year experience in face and neck unit reconstruction using tissue expanders," Burns, vol. 39, no. 3, pp. 522–527, 2013.

[105] C. Radovan, "Breast reconstruction after mastectomy using the temporary expander," Plastic and Reconstructive Surgery, vol. 69, no. 2, pp. 195–208, 1982.

[106] R. Rivera, J. LoGiudice, and A. K. Gosain, "Tissue expansion in pediatric patients," Clinics in plastic surgery, vol. 32, no. 1, pp. 35–44, 2005.

[107] R. E. De Filippo and A. Atala, "Stretch and growth: the molecular and physiologic influences of tissue expansion," Plastic and reconstructive surgery, vol. 109, no. 7, pp. 2450–2462, 2002.

[108] L. A. Taber, "Biomechanics of growth, remodeling, and morphogenesis," Applied mechanics reviews, vol. 48, no. 8, pp. 487–545, 1995.

[109] Y. Iwahira and Y. Maruyama, "Combined tissue expansion: clinical attempt to decrease pain and shorten placement time." Plastic and reconstructive surgery, vol. 91, no. 3, pp. 408–415, 1993.

[110] D. C. Pamplona, R. Q. Velloso, and H. N. Radwanski, "On skin expansion," Journal of the mechanical behavior of biomedical materials, vol. 29, pp. 655–662, 2014.

[111] J. G. Beauchene, M. M. Chambers, A. E. Peterson, and P. G. Scott, "Biochemical, biomechanical, and physical changes in the skin in an experimental animal model of therapeutic tissue expansion," Journal of Surgical Research, vol. 47, no. 6, pp. 507–514, 1989.

[112] C. A. VanderKolk, J. J. McCann, G. M. Mitchell, and B. M. O'Brien, "Changes in area and thickness of expanded and unexpanded axial pattern skin flaps in pigs," British journal of plastic surgery, vol. 41, no. 3, pp. 284–293, 1988.

[113] E. J. F. Timmenga, R. Schoorl, and P. J. Klopper, "Biomechanical and histomorphological changes in expanded rabbit skin," British journal of plastic surgery, vol. 43, no. 1, pp. 101–106, 1990.

[114] L. Camison, M. Bykowski, W. W. Lee, J. C. Carlson, J. Roosenboom, J. A. Goldstein, J. E. Losee, and S. M. Weinberg, "Validation of the Vectra H1 portable three-dimensional photogrammetry system for facial imaging," Sep 2017.

[115] A. Buganza Tepole, M. Gart, C. A. Purnell, A. K. Gosain, and E. Kuhl, "Multiview stereo analysis reveals anisotropy of prestrain, deformation, and growth in living skin," Biomechanics and modeling in mechanobiology, vol. 14, no. 5, pp. 1007–1019, 2015.

[116] A. Buganza Tepole, M. Gart, C. A. Purnell, A. K. Gosain, and E. Kuhl, "The Incompatibility of Living Systems: Characterizing Growth-Induced Incompatibilities in Expanded Skin," Annals of Biomedical Engineering, vol. 44, no. 5, pp. 1734–1752, 2016.

[117] A. Buganza Tepole, E. E. Vaca, C. A. Purnell, M. Gart, J. McGrath, E. Kuhl, and A. K. Gosain, "Quantification of strain in a porcine model of skin expansion using multi-view stereo and isogeometric kinematics," JoVE (Journal of Visualized Experiments), no. 122, p. e55052, 2017.

[118] G. Limbert, "Mathematical and computational modelling of skin biophysics: a review," Proceedings of the Royal Society A: Mathematical, Physical and Engineering Sciences, vol. 473, no. 2203, p. 20170257, 2017.

[119] M. F. Leyva-Mendivil, A. Page, N. W. Bressloff, and G. Limbert, "A mechanistic insight into the mechanical role of the stratum corneum during stretching and compression of the skin," Journal of the mechanical behavior of biomedical materials, vol. 49, pp. 197–219, 2015.

[120] M. F. Leyva-Mendivil, J. Lengiewicz, A. Page, N. W. Bressloff, and G. Limbert, "Skin microstructure is a key contributor to its friction behaviour," Tribology Letters, vol. 65, no. 1, p. 12, 2017.

[121] T. J. R. Hughes, J. A. Cottrell, and Y. Bazilevs, "Isogeometric analysis: Cad, finite elements, nurbs, exact geometry and mesh refinement," Computer methods in applied mechanics and engineering, vol. 194, no. 39-41, pp. 4135–4195, 2005.

[122] A. Buganza Tepole, H. Kabaria, K.-U. Bletzinger, and E. Kuhl, "Isogeometric kirchhoff–love shell formulations for biological membranes," Computer methods in applied mechanics and engineering, vol. 293, pp. 328–347, 2015.

[123] E. K. Rodriguez, A. Hoger, and A. D. McCulloch, "Stress-dependent finite growth in soft elastic tissues," Journal of Biomechanics, vol. 27, no. 4, pp. 455–467, 1994.

[124] E. Kuhl, "Growing matter: A review of growth in living systems," Journal of the Mechanical Behavior of Biomedical Materials, vol. 29, pp. 529–543, 2014.

[125] L. Chen, N. Nguyen-Thanh, H. Nguyen-Xuan, T. Rabczuk, S. P. A. Bordas, and G. Limbert, "Explicit finite deformation analysis of isogeometric membranes," Computer Methods in Applied Mechanics and Engineering, vol. 277, pp. 104–130, 2014.

[126] L. A. Taber and S. Chabert, "Theoretical and experimental study of growth and remodeling in the developing heart," Biomechanics and modeling in mechanobiology, vol. 1, no. 1, pp. 29–43, 2002.

[127] M. K. Rausch and E. Kuhl, "On the effect of prestrain and residual stress in thin biological membranes," Journal of the Mechanics and Physics of Solids, vol. 61, no. 9, pp. 1955–1969, 2013.

[128] J. Schindelin, I. Arganda-Carreras, E. Frise, V. Kaynig, M. Longair, T. Pietzsch, S. Preibisch, C. Rueden, S. Saalfeld, B. Schmid, J.-Y. Tinevez, D. J. White, V. Hartenstein, K. Eliceiri, P. Tomancak, and A. Cardona, "Fiji: an open-source platform for biological-image analysis," Nature methods, vol. 9, no. 7, pp. 676–682, 2012.

[129] R. Rezakhaniha, A. Agianniotis, J. T. C. Schrauwen, A. Griffa, D. Sage, C. V. C. Bouten, F. N. Van De Vosse, M. Unser, and N. Stergiopulos, "Experimental investigation of collagen waviness and orientation in the arterial adventitia using confocal laser scanning microscopy," Biomechanics and modeling in mechanobiology, vol. 11, no. 3-4, pp. 461–473, 2012.

[130] S. Y. Turin, J. K. Ledwon, H. Bae, A. Buganza Tepole, J. Topczewska, and A. K. Gosain, "Digital analysis yields more reliable and accurate measures of dermal and epidermal thickness in histologically processed specimens compared to traditional methods," Experimental dermatology, vol. 27, no. 6, pp. 687–690, 2018.

[131] A. Buganza Tepole, C. Joseph Ploch, J. Wong, A. K. Gosain, and E. Kuhl, "Growing skin: A computational model for skin expansion in reconstructive surgery," Journal of the Mechanics and Physics of Solids, vol. 59, no. 10, pp. 2177–2190, 2011.

[132] M. Yang, Q. Li, L. Sheng, H. Li, R. Weng, and T. Zan, "Bone marrow–derived mesenchymal stem cells transplantation accelerates tissue expansion by promoting skin regeneration during expansion," Annals of surgery, vol. 253, no. 1, pp. 202–209, 2011.

[133] Y.-j. Zeng, C.-q. Xu, J. Yang, G.-c. Sun, and X.-h. Xu, "Biomechanical comparison between conventional and rapid expansion of skin," British journal of plastic surgery, vol. 56, no. 7, pp. 660–666, 2003.

[134] V. W. Wong, S. Akaishi, M. T. Longaker, and G. C. Gurtner, "Pushing back: wound mechanotransduction in repair and regeneration," Journal of Investigative Dermatology, vol. 131, no. 11, pp. 2186–2196, 2011.

[135] C. A. Derderian, N. Bastidas, O. Z. Lerman, K. A. Bhatt, S.-E. Lin, J. Voss, J. W. Holmes, J. P. Levine, and G. C. Gurtner, "Mechanical strain alters gene expression in an in vitro model of hypertrophic scarring," Annals of plastic surgery, vol. 55, no. 1, pp. 69–75, 2005.

[136] F. H. Silver, L. M. Siperko, and G. P. Seehra, "Mechanobiology of force transduction in dermal tissue," Skin Research and Technology, vol. 9, no. 1, pp. 3–23, 2003.

[137] C. Jiang, L. Shao, Q. Wang, and Y. Dong, "Repetitive mechanical stretching modulates transforming growth factor-β induced collagen synthesis and apoptosis in human patellar tendon fibroblasts," Biochemistry and Cell Biology, vol. 90, no. 5, pp. 667–674, 2012.

[138] J. H. C. Wang and B. P. Thampatty, "An introductory review of cell mechanobiology," Biomechanics and modeling in mechanobiology, vol. 5, no. 1, pp. 1–16, 2006.

[139] E. Fuchs and S. Raghavan, "Getting under the skin of epidermal morphogenesis," Nature Reviews Genetics, vol. 3, no. 3, pp. 199–209, 2002.

[140] J. H.-C. Wang, B. P. Thampatty, J.-S. Lin, and H.-J. Im, "Mechanoregulation of gene expression in fibroblasts," Gene, vol. 391, no. 1-2, pp. 1–15, 2007.

[141] J. C. Alex, T. K. Bhattacharyya, G. Smyrniotis, K. O'Grady, R. J. Konior, and D. M. Toriumi, "A histologic analysis of three-dimensional versus two-dimensional tissue expansion in the porcine model," The Laryngoscope, vol. 111, no. 1, pp. 36–43, 2001.

[142] E. D. Austad, K. A. Pasyk, K. D. McClatchey, and G. W. Cherry, "Histomorphologic evaluation of guinea pig skin and soft tissue after controlled tissue expansion." Plastic and reconstructive surgery, vol. 70, no. 6, pp. 704–710, 1982.

[143] P. E. Johnson, D. A. Kernahan, and B. S. Bauer, "Dermal and epidermal response to soft-tissue expansion in the pig." Plastic and reconstructive surgery, vol. 81, no. 3, pp. 390–397, 1988.

[144] T. Yasui, Y. Takahashi, M. Ito, S. Fukushima, and T. Araki, "Ex vivo and in vivo second-harmonic-generation imaging of dermal collagen fiber in skin: comparison of imaging characteristics between mode-locked cr: forsterite and ti: sapphire lasers," Applied optics, vol. 48, no. 10, pp. D88–D95, 2009.

[145] S. Göktepe, O. J. Abilez, K. K. Parker, and E. Kuhl, "A multiscale model for eccentric and concentric cardiac growth through sarcomerogenesis," Journal of theoretical biology, vol. 265, no. 3, pp. 433–442, 2010.

[146] S. Göktepe, O. J. Abilez, and E. Kuhl, "A generic approach towards finite growth with examples of athlete's heart, cardiac dilation, and cardiac wall thickening," Journal of the Mechanics and Physics of Solids, vol. 58, no. 10, pp. 1661–1680, 2010.

[147] M. Eskandari and E. Kuhl, "Systems biology and mechanics of growth," Wiley Interdisciplinary Reviews: Systems Biology and Medicine, vol. 7, no. 6, pp. 401–412, 2015.

[148] D. Ambrosi, G. A. Ateshian, E. M. Arruda, S. C. Cowin, J. Dumais, A. Goriely, G. A. Holzapfel, J. D. Humphrey, R. Kemkemer, E. Kuhl, J. E. Olberding, L. A. Taber, and K. Garikipati, "Perspectives on biological growth and remodeling," Journal of the Mechanics and Physics of Solids, vol. 59, no. 4, pp. 863–883, 2011.

[149] L. C. Lee, G. S. Kassab, and J. M. Guccione, "Mathematical modeling of cardiac growth and remodeling," Wiley Interdisciplinary Reviews: Systems Biology and Medicine, vol. 8, no. 3, pp. 211–226, 2016.

[150] P. J. A. Oomen, M. A. Holland, C. V. C. Bouten, E. Kuhl, and S. Loerakker, "Growth and remodeling play opposing roles during postnatal human heart valve development," Scientific reports, vol. 8, no. 1, p. 1235, 2018.

[151] M. Holland, S. Budday, A. Goriely, and E. Kuhl, "Symmetry breaking in wrinkling patterns: Gyri are universally thicker than sulci," Physical review letters, vol. 121, no. 22, p. 228002, 2018.

[152] M. K. Rausch and E. Kuhl, "On the mechanics of growing thin biological membranes," Journal of the Mechanics and Physics of Solids, vol. 63, pp. 128–140, 2014.

[153] V. Alastrue, M. Martinez, and M. Doblare, "Modelling adaptative volumetric finite growth in patient-specific residually stressed arteries," Journal of Biomechanics, vol. 41, no. 8, pp. 1773–1781, 2008.

[154] D. Klepach, L. C. Lee, J. F. Wenk, M. B. Ratcliffe, T. I. Zohdi, J. L. Navia, G. S. Kassab, E. Kuhl, and J. M. Guccione, "Growth and remodeling of the left ventricle: a case study of myocardial infarction and surgical ventricular restoration," Mechanics research communications, vol. 42, pp. 134–141, 2012.

[155] R. Chabiniok, V. Y. Wang, M. Hadjicharalambous, L. Asner, J. Lee, M. Sermesant, E. Kuhl, A. A. Young, P. Moireau, M. P. Nash, D. Chapelle, and D. A. Nordsletten, "Multiphysics and multiscale modelling, data–model fusion and integration of organ physiology in the clinic: ventricular cardiac mechanics," Interface focus, vol. 6, no. 2, p. 20150083, 2016.

[156] M. Latorre and F. J. Montáns, "Experimental data reduction for hyperelasticity," Computers & Structures, 2018.

[157] F. S. Costabal, K. Matsuno, J. Yao, P. Perdikaris, and E. Kuhl, "Machine learning in drug development: Characterizing the effect of 30 drugs on the qt interval using gaussian process regression, sensitivity analysis, and uncertainty quantification," Computer Methods in Applied Mechanics and Engineering, vol. 348, pp. 313–333, 2019.

[158] S. Madireddy, B. Sista, and K. Vemaganti, "A bayesian approach to selecting hyperelastic constitutive models of soft tissue," Computer Methods in Applied Mechanics and Engineering, vol. 291, pp. 102–122, 2015.

[159] F. S. Costabal, J. S. Choy, K. L. Sack, J. M. Guccione, G. S. Kassab, and E. Kuhl, "Multiscale characterization of heart failure," Acta biomaterialia, vol. 86, pp. 66–76, 2019.

[160] M. Peirlinck, F. S. Costabal, K. L. Sack, J. S. Choy, G. S. Kassab, J. M. Guccione, M. De Beule, P. Segers, and E. Kuhl, "Using machine learning to characterize heart failure across the scales," Biomechanics and modeling in mechanobiology, pp. 1–15, 2019.

[161] C. D. Cantwell, Y. Mohamied, K. N. Tzortzis, S. Garasto, C. Houston, R. A. Chowdhury, F. S. Ng, A. A. Bharath, and N. S. Peters, "Rethinking multiscale cardiac electrophysiology with machine learning and predictive modelling," Computers in biology and medicine, vol. 104, pp. 339–351, 2019.

[162] L. A. Mihai, T. E. Woolley, and A. Goriely, "Stochastic isotropic hyperelastic materials: constitutive calibration and model selection," Proceedings of the Royal Society A: Mathematical, Physical and Engineering Sciences, vol. 474, no. 2211, p. 20170858, 2018.

[163] B. Kouchmeshky and N. Zabaras, "Microstructure model reduction and uncertainty quantification in multiscale deformation processes," Computational Materials Science, vol. 48, no. 2, pp. 213–227, 2010.

[164] B. A. Le, J. Yvonnet, and Q.-C. He, "Computational homogenization of nonlinear elastic materials using neural networks," International Journal for Numerical Methods in Engineering, vol. 104, no. 12, pp. 1061–1084, 2015.

[165] L. Parussini, D. Venturi, P. Perdikaris, and G. E. Karniadakis, "Multi-fidelity gaussian process regression for prediction of random fields," Journal of Computational Physics, vol. 336, pp. 36–50, 2017.

[166] P. Perdikaris, M. Raissi, A. Damianou, N. Lawrence, and G. E. Karniadakis, "Nonlinear information fusion algorithms for data-efficient multi-fidelity modelling," Proceedings of the Royal Society A: Mathematical, Physical and Engineering Sciences, vol. 473, no. 2198, p. 20160751, 2017.

[167] F. Sahli Costabal, J. Yao, and E. Kuhl, "Predicting drug-induced arrhythmias by multiscale modeling," International journal for numerical methods in biomedical engineering, vol. 34, no. 5, p. e2964, 2018.

[168] P. Perdikaris and G. E. Karniadakis, "Model inversion via multi-fidelity bayesian optimization: a new paradigm for parameter estimation in haemodynamics, and beyond," Journal of The Royal Society Interface, vol. 13, no. 118, p. 20151107, 2016.

[169] N.-V. Nguyen, S.-M. Choi, W.-S. Kim, J.-W. Lee, S. Kim, D. Neufeld, and Y.-H. Byun, "Multidisciplinary unmanned combat air vehicle system design using multi-fidelity model," Aerospace Science and Technology, vol. 26, no. 1, pp. 200–210, 2013.

[170] C. M. Witzenburg and J. W. Holmes, "Predicting the time course of ventricular dilation and thickening using a rapid compartmental model," Journal of cardiovascular translational research, vol. 11, no. 2, pp. 109–122, 2018.

[171] B. Peherstorfer, K. Willcox, and M. Gunzburger, "Survey of multifidelity methods in uncertainty propagation, inference, and optimization," SIAM Review, vol. 60, no. 3, pp. 550–591, 2018.

[172] S. Madireddy, B. Sista, and K. Vemaganti, "Bayesian calibration of hyperelastic constitutive models of soft tissue," Journal of the mechanical behavior of biomedical materials, vol. 59, pp. 108–127, 2016.

[173] S. Sankaran and A. L. Marsden, "A stochastic collocation method for uncertainty quantification and propagation in cardiovascular simulations," Journal of biomechanical engineering, vol. 133, no. 3, p. 031001, 2011.

[174] C. M. Witzenburg and J. W. Holmes, "A comparison of phenomenologic growth laws for myocardial hypertrophy," Journal of Elasticity, vol. 129, no. 1-2, pp. 257–281, 2017.

[175] A. M. Zöllner, M. A. Holland, K. S. Honda, A. K. Gosain, and E. Kuhl, "Growth on demand: reviewing the mechanobiology of stretched skin," Journal of the mechanical behavior of biomedical materials, vol. 28, pp. 495–509, 2013.

[176] A. Buganza Tepole, A. K. Gosain, and E. Kuhl, "Stretching skin: The physiological limit and beyond," International journal of non-linear mechanics, vol. 47, no. 8, pp. 938–949, 2012.

[177] C. A. Purnell, M. S. Gart, A. Buganza Tepole, J. P. Tomaszewski, J. M. Topczewska, E. Kuhl, and A. K. Gosain, "Determining the differential effects of stretch and growth in tissue-expanded skin: Combining isogeometric analysis and continuum mechanics in a porcine model," Dermatologic Surgery, vol. 44, no. 1, pp. 48–52, 2018.

[178] J. W. Y. Jor, M. P. Nash, P. M. F. Nielsen, and P. J. Hunter, "Estimating material parameters of a structurally based constitutive relation for skin mechanics," Biomechanics and modeling in mechanobiology, vol. 10, no. 5, pp. 767–778, 2011.

[179] D. Laiacona, J. M. Cohen, K. Coulon, Z. W. Lipsky, C. Maiorana, R. Boltyanskiy, E. R. Dufresne, and G. K. German, "Non-invasive in vivo quantification of human skin tension lines," Acta biomaterialia, vol. 88, pp. 141–148, 2019.

[180] A. N. Annaidh, K. Bruyere, M. Destrade, M. D. Gilchrist, C. Maurini, M. Otténio, and G. Saccomandi, "Automated estimation of collagen fibre dispersion in the dermis and its contribution to the anisotropic behaviour of skin," Annals of biomedical engineering, vol. 40, no. 8, pp. 1666–1678, 2012.

[181] M. Pensalfini, J. Weickenmeier, M. Rominger, R. Santoprete, O. Distler, and E. Mazza, "Location-specific mechanical response and morphology of facial soft tissues," Journal of the mechanical behavior of biomedical materials, vol. 78, pp. 108–115, 2018.

[182] C. H. Daly and G. F. Odland, "Age-related changes in the mechanical properties of human skin," The Journal of Investigative Dermatology, vol. 73, no. 1, pp. 84–87, 1979.

[183] G. Limbert, M. A. Masen, D. Pond, H. K. Graham, M. J. Sherratt, R. Jobanputra, and A. McBride, "Biotribology of the ageing skinwhy we should care," Biotribology, 2019.

[184] S. Luebberding, N. Krueger, and M. Kerscher, "Mechanical properties of human skin in vivo: a comparative evaluation in 300 men and women," Skin Research and Technology, vol. 20, no. 2, pp. 127–135, 2014.

[185] N. Krueger, S. Luebberding, M. Oltmer, M. Streker, and M. Kerscher, "Age-related changes in skin mechanical properties: a quantitative evaluation of 120 female subjects," Skin research and technology, vol. 17, no. 2, pp. 141–148, 2011.

[186] V. Prot, B. Skallerud, and G. A. Holzapfel, "Transversely isotropic membrane shells with application to mitral valve mechanics. constitutive modelling and finite element implementation," International journal for numerical methods in engineering, vol. 71, no. 8, pp. 987–1008, 2007.

[187] C. M. Bishop, Pattern recognition and machine learning, ser. Information science and statistics. New York: Springer, 2006.

[188] R. Gramacy and H. Lee, "Cases for the nugget in modeling computer experiments," Statistics and Computing, vol. 22, no. 3, pp. 713–722, 2012.

[189] R. J. Adler, The geometry of random fields. SIAM, 2010.

[190] M. C. Kennedy and A. O'Hagan, "Predicting the output from a complex computer code when fast approximations are available," Biometrika, vol. 87, no. 1, pp. 1–13, 2000.

[191] L. Le Gratiet and J. Garnier, "Recursive co-kriging model for design of computer experiments with multiple levels of fidelity," International Journal for Uncertainty Quantification, vol. 4, no. 5, 2014.

[192] S. Koziel and L. Leifsson, "Multi-level cfd-based airfoil shape optimization with automated low-fidelity model selection," Procedia Computer Science, vol. 18, pp. 889–898, 2013.

[193] M. G. Hutchison, E. R. Unger, W. H. Mason, B. Grossman, and R. T. Haftka, "Variable-complexity aerodynamic optimization of a high-speed civil transport wing," Journal of Aircraft, vol. 31, no. 1, pp. 110–116, 1994.

[194] M. G. Turner, J. A. Reed, R. Ryder, and J. P. Veres, "Multi-fidelity simulation of a turbofan engine with results zoomed into mini-maps for a zero-d cycle simulation," in ASME Turbo Expo 2004: Power for Land, Sea, and Air. American Society of Mechanical Engineers, 2004, pp. 219–230.

[195] GPy, "GPy: A gaussian process framework in python," http://github.com/SheffieldML/GPy, since 2012.

[196] A. Buganza Tepole, M. Gart, A. K. Gosain, and E. Kuhl, "Characterization of living skin using multi-view stereo and isogeometric analysis," Acta biomaterialia, vol. 10, no. 11, pp. 4822–4831, 2014.

[197] I. M. Sobol, "Global sensitivity indices for nonlinear mathematical models and their monte carlo estimates," Mathematics and computers in simulation, vol. 55, no. 1-3, pp. 271–280, 2001.

[198] J. D. Herman and W. Usher, "Salib: An open-source python library for sensitivity analysis," J. Open Source Software, vol. 2, no. 9, p. 97, 2017.

[199] T. Homma and A. Saltelli, "Importance measures in global sensitivity analysis of nonlinear models," Reliability Engineering & System Safety, vol. 52, no. 1, pp. 1–17, 1996.

[200] A. Saltelli, "Making best use of model evaluations to compute sensitivity indices," Computer physics communications, vol. 145, no. 2, pp. 280–297, 2002.

[201] M. Eskandari, W. G. Kuschner, and E. Kuhl, "Patient-specific airway wall remodeling in chronic lung disease," Annals of biomedical engineering, vol. 43, no. 10, pp. 2538–2551, 2015.

[202] S. Sankaran, J. D. Humphrey, and A. L. Marsden, "An efficient framework for optimization and parameter sensitivity analysis in arterial growth and remodeling computations," Computer methods in applied mechanics and engineering, vol. 256, pp. 200–210, 2013.

[203] H. Janssen, "Monte-carlo based uncertainty analysis: Sampling efficiency and sampling convergence," Reliability Engineering & System Safety, vol. 109, pp. 123–132, 2013.

[204] A. Bozkurt, A. Groger, D. Odey, F. Vogeler, A. Piatkowski, P. Fuchs, and N. Pallua, "Retrospective analysis of tissue expansion in reconstructive burn surgery: evaluation of complication rates," Burns, vol. 34, no. 8, pp. 1113–1118, 2008.

[205] J. A. van Aalst, T. McCurry, and J. Wagner, "Reconstructive considerations in the surgical management of melanoma," Surgical Clinics, vol. 83, no. 1, pp. 187–230, 2003.

[206] R. N. Vaishnav and J. Vossoughi, "Residual stress and strain in aortic segments," Journal of biomechanics, vol. 20, no. 3, pp. 235–239, 1987.

[207] Y.-C. Fung, "Stress, strain, growth, and remodeling of living organisms," in Theoretical, Experimental, and Numerical Contributions to the Mechanics of Fluids and Solids. Springer, 1995, pp. 469–482.

[208] C.-J. Chuong and Y.-C. Fung, "Residual stress in arteries," in Frontiers in biomechanics. Springer, 1986, pp. 117–129.

[209] M. K. Rausch, W. Bothe, J.-P. E. Kvitting, J. C. Swanson, N. B. Ingels, D. C. Miller, and E. Kuhl, "Characterization of mitral valve annular dynamics in the beating heart," Annals of biomedical engineering, vol. 39, no. 6, pp. 1690–1702, 2011.

[210] J. H. Omens and Y.-C. Fung, "Residual strain in rat left ventricle." Circulation research, vol. 66, no. 1, pp. 37–45, 1990.

[211] M. Genet, M. Rausch, L. C. Lee, S. Choy, X. Zhao, G. S. Kassab, S. Kozerke, J. M. Guccione, and E. Kuhl, "Heterogeneous growth-induced prestrain in the heart," Journal of Biomechanics, vol. 48, no. 10, pp. 2080–2089, 2015.

[212] Y.-C. Fung and S. Q. Liu, "Change of residual strains in arteries due to hypertrophy caused by aortic constriction." Circulation Research, vol. 65, no. 5, pp. 1340–1349, 1989.

[213] L. A. Taber and J. D. Humphrey, "Stress-modulated growth, residual stress, and vascular heterogeneity," Journal of biomechanical engineering, vol. 123, no. 6, p. 528, 2001.

[214] V. A. Lubarda, "Constitutive theories based on the multiplicative decomposition of deformation gradient: Thermoelasticity, elastoplasticity, and biomechanics," Applied Mechanics Reviews, vol. 57, no. 2, pp. 95–108, 2004.

[215] E. H. Lee, "Elastic-plastic deformation at finite strains," Journal of Applied Mechanics, Transactions ASME, vol. 36, no. 1, pp. 1–6, 1969.

[216] L. A. Taber and D. W. Eggers, "Theoretical study of stress-modulated growth in the aorta," Journal of theoretical biology, vol. 180, no. 4, pp. 343–357, 1996.

[217] G. Himpel, E. Kuhl, A. Menzel, and P. Steinmann, "Computational modelling of isotropic multiplicative growth," Cmes-Computer Modeling In Engineering and Sciences, vol. 8, no. 2, pp. 119–134, 2005.

[218] J. Lubliner, Plasticity theory. Courier Corporation, 2008.

[219] R. Skalak, S. Zargaryan, R. K. Jain, P. A. Netti, and A. Hoger, "Compatibility and the genesis of residual stress by volumetric growth," Journal of mathematical biology, vol. 34, no. 8, pp. 889–914, 1996.

[220] P. Steinmann, Geometrical Foundations of Continuum Mechanics, 1st ed., ser. Lecture Notes in Applied Mathematics and Mechanics, 2. Springer, Berlin, Heidelberg, 2015.

[221] P. J. Withers and H. K. D. H. Bhadeshia, "Residual stress. part 2–nature and origins," Materials science and technology, vol. 17, no. 4, pp. 366–375, 2001.

[222] R. De Wit, "A view of the relation between the continuum theory of lattice defects and non-euclidean geometry in the linear approximation," International Journal of Engineering Science, vol. 19, no. 12, pp. 1475–1506, 1981.

[223] J. P. Hirth, J. Lothe, and T. Mura, "Theory of dislocations," 1983.

[224] D. E. Hurtado and M. Ortiz, "Finite element analysis of geometrically necessary dislocations in crystal plasticity," International Journal for Numerical Methods in Engineering, vol. 93, no. 1, pp. 66–79, 2013.

[225] A. Menzel and P. Steinmann, "On the continuum formulation of higher gradient plasticity for single and polycrystals," Journal of the Mechanics and Physics of Solids, vol. 48, no. 8, pp. 1777–1796, 2000.

[226] J. D. Clayton, D. J. Bammann, and D. L. McDowell, "A geometric framework for the kinematics of crystals with defects," Philosophical Magazine, vol. 85, no. 33-35, pp. 3983–4010, 2005.

[227] M. Miri and N. Rivier, "Continuum elasticity with topological defects, including dislocations and extra-matter," Journal of Physics A: Mathematical and General, vol. 35, no. 7, p. 1727, 2002.

[228] G. Tomassetti, T. Cohen, and R. Abeyaratne, "Steady accretion of an elastic body on a hard spherical surface and the notion of a four-dimensional reference space," Journal of the Mechanics and Physics of Solids, vol. 96, pp. 333–352, 2016.

[229] R. Abi-Akl and T. Cohen, "Surface growth on a deformable spherical substrate," Mechanics Research Communications, vol. 103, 2020.

[230] J. D. Humphrey and K. R. Rajagopal, "A constrained mixture model for growth and remodeling of soft tissues," Mathematical models and methods in applied sciences, vol. 12, no. 03, pp. 407–430, 2002.

[231] E. Kröner, "Allgemeine kontinuumstheorie der versetzungen und eigenspannungen," Archive for Rational Mechanics and Analysis, vol. 4, no. 1, p. 273, 1959.

[232] P. Cermelli and M. E. Gurtin, "On the characterization of geometrically necessary dislocations in finite plasticity," Journal of the Mechanics and Physics of Solids, vol. 49, no. 7, pp. 1539–1568, 2001.

[233] K. Kondo, "On the geometrical and physical foundations of the theory of yielding," in Proceedings of 2nd Japan National Congress on Applied Mechanics, vol. 2, 1952, pp. 41–47.

[234] J. F. Nye, "Some geometrical relations in dislocated crystals," Acta metallurgica, vol. 1, no. 2, pp. 153–162, 1953.

[235] K. Kondo, "Non-riemannian geometry of imperfect crystals from a macroscopic viewpoint," in Memoirs of the unifying study of the basic problems in engineering science by means of geometry. Division DI, Gakujutsu Bunken Fukyo-Kai, 1955, vol. 1, pp. 6–17.

[236] A. Menzel and E. Kuhl, "Frontiers in growth and remodeling," Mechanics research communications, vol. 42, pp. 1–14, 2012.

[237] E. Kuhl, A. Menzel, and P. Steinmann, "Computational modeling of growth," Computational Mechanics, vol. 32, no. 1-2, pp. 71–88, 2003.

[238] P. Steinmann, "Views on multiplicative elastoplasticity and the continuum theory of dislocations," International Journal of Engineering Science, vol. 34, no. 15, pp. 1717–1735, 1996.

[239] K. Garikipati, "The kinematics of biological growth," Applied Mechanics Reviews, vol. 62, no. 3, 2009.

[240] D. Ambrosi and F. Mollica, "On the mechanics of a growing tumor," International journal of engineering science, vol. 40, no. 12, pp. 1297–1316, 2002.

[241] P. Ciarletta, "Buckling instability in growing tumor spheroids," Physical review letters, vol. 110, no. 15, p. 158102, 2013.

[242] A. A. Maradudin, "Screw dislocations and discrete elastic theory," Journal of Physics and Chemistry of Solids, vol. 9, no. 1, pp. 1–20, 1959.

[243] J. Weickenmeier, E. Kuhl, and A. Goriely, "Multiphysics of prionlike diseases: Progression and atrophy," Physical review letters, vol. 121, no. 15, p. 158101, 2018.

[244] P. M. Thompson, K. M. Hayashi, G. de Zubicaray, A. L. Janke, S. E. Rose, J. Semple, D. Herman, M. S. Hong, S. S. Dittmer, D. M. Doddrell, and A. W. Toga, "Dynamics of gray matter loss in alzheimer's disease," Journal Of Neuroscience, vol. 23, no. 3, pp. 994–1005, 2003.

[245] K. A. Pasyk, L. C. Argenta, and C. Hassett, "Quantitative analysis of the thickness of human skin and subcutaneous tissue following controlled expansion with a silicone implant." Plastic and reconstructive surgery, vol. 81, no. 4, pp. 516–523, 1988.

[246] A. K. Gosain, T. D. Santoro, D. L. Larson, and R. P. Gingrass, "Giant congenital nevi: a 20-year experience and an algorithm for their management." Plastic and reconstructive surgery, vol. 108, no. 3, pp. 622–636, 2001.

[247] K. M. Wisdom, S. L. Delp, and E. Kuhl, "Use it or lose it: multiscale skeletal muscle adaptation to mechanical stimuli," Biomechanics and modeling in mechanobiology, vol. 14, no. 2, pp. 195–215, 2015.

[248] A. M. Zöllner, O. J. Abilez, M. Böl, and E. Kuhl, "Stretching skeletal muscle: chronic muscle lengthening through sarcomerogenesis," PloS one, vol. 7, no. 10, 2012.

[249] D. Bray, "Axonal growth in response to experimentally applied mechanical tension," Developmental biology, vol. 102, no. 2, pp. 379–389, 1984.

[250] M. A. Holland, K. E. Miller, and E. Kuhl, "Emerging brain morphologies from axonal elongation," Annals of biomedical engineering, vol. 43, no. 7, pp. 1640–1653, 2015.

[251] E. Kuhl and P. Steinmann, "On spatial and material settings of thermo-hyperelastodynamics for open systems," Acta Mechanica, vol. 160, no. 3-4, pp. 179–217, 2003.

[252] E. Kuhl and P. Steinmann, "Computational modeling of healing: an application of the material force method," Biomechanics and Modeling in Mechanobiology, vol. 2, no. 4, pp. 187–203, 2004.

[253] E. Kuhl and P. Steinmann, "Mass- and volume-specific views on thermodynamics for open systems," Proceedings: Mathematical, Physical and Engineering Sciences, vol. 459, no. 2038, pp. 2547–2568, 2003.

[254] I. A. BROWN, "A scanning electron microscope study of the effects of uniaxial tension on human skin," British Journal of Dermatology, vol. 89, no. 4, pp. 383–393, 1973.

[255] G. E. Piérard and C. M. Lapière, "Microanatomy of the dermis in relation to relaxed skin tension lines and langer's lines." The American journal of dermatopathology, vol. 9, no. 3, pp. 219–224, 1987.

[256] M. Epstein and G. A. Maugin, "Thermomechanics of volumetric growth in uniform bodies," International Journal of Plasticity, vol. 16, no. 7-8, pp. 951–978, 2000.

[257] V. A. Lubarda and A. Hoger, "On the mechanics of solids with a growing mass," International journal of solids and structures, vol. 39, no. 18, pp. 4627–4664, 2002.

[258] M. K. Rausch, A. Dam, S. Göktepe, O. J. Abilez, and E. Kuhl, "Computational modeling of growth: systemic and pulmonary hypertension in the heart," Biomechanics and modeling in mechanobiology, vol. 10, no. 6, pp. 799–811, 2011.

[259] M. A. Holland, "Hitchhiker's guide to abaqus," May 7, 2018.

[260] G. B. Stokin and L. S. B. Goldstein, "Axonal transport and alzheimer's disease," Annual Review of Biochemistry, vol. 75, no. 1, pp. 607–627, 2006.

[261] S. H. Kwon, J. Padmanabhan, and G. C. Gurtner, "Chapter 14 - mechanobiology of skin diseases and wound healing," in Mechanobiology in Health and Disease, S. W. Verbruggen, Ed. Academic Press, 2018, pp. 415 – 448.

[262] M. A. Holland, B. Li, X. Q. Feng, and E. Kuhl, "Instabilities of soft films on compliant substrates," Journal of the Mechanics and Physics of Solids, vol. 98, pp. 350–365, 2017.

[263] S. Budday, P. Steinmann, and E. Kuhl, "The role of mechanics during brain development," Journal of the Mechanics and Physics of Solids, vol. 72, pp. 75–92, 2014.

[264] S. Budday, S. Andres, B. Walter, P. Steinmann, and E. Kuhl, "Wrinkling instabilities in soft bilayered systems," Philosophical Transactions of the Royal Society A: Mathematical, Physical and Engineering Sciences, vol. 375, no. 2093, p. 20160163, 2017.

[265] Y.-C. Fung, "What are the residual stresses doing in our blood vessels?" Annals of biomedical engineering, vol. 19, no. 3, pp. 237–249, 1991.

[266] J. A. McGrath and J. Uitto, "Anatomy and organization of human skin," in Rook's Textbook of Dermatology: Eighth Edition. Wiley-Blackwell, 2010, vol. 1, pp. 34–86.

[267] V. W. Wong, J. Paterno, M. Sorkin, J. P. Glotzbach, K. Levi, M. Januszyk, K. C. Rustad, M. T. Longaker, and G. C. Gurtner, "Mechanical force prolongs acute inflammation via t-cell-dependent pathways during scar formation," The FASEB Journal, vol. 25, no. 12, pp. 4498–4510, 2011.

[268] V. W. Wong, K. C. Rustad, S. Akaishi, M. Sorkin, J. P. Glotzbach, M. Januszyk, E. R. Nelson, K. Levi, J. Paterno, I. N. Vial, A. A. Kuang, M. T. Longaker, and G. C. Gurtner, "Focal adhesion kinase links mechanical force to skin fibrosis via inflammatory signaling," Nature medicine, vol. 18, no. 1, p. 148, 2012.

[269] K. C. Rustad, V. W. Wong, and G. C. Gurtner, "The role of focal adhesion complexes in fibroblast mechanotransduction during scar formation," Differentiation, vol. 86, no. 3, pp. 87–91, 2013.

[270] L. J. Draaijers, Y. A. M. Botman, F. R. H. Tempelman, R. W. Kreis, E. Middelkoop, and P. P. M. van Zuijlen, "Skin elasticity meter or subjective evaluation in scars: a reliability assessment," Burns, vol. 30, no. 2, pp. 109–114, 2004.

[271] H. Dobrev, "Use of cutometer to assess epidermal hydration," Skin research and technology, vol. 6, no. 4, pp. 239–244, 2000.

[272] M. Kauer, V. Vuskovic, J. Dual, G. Szekely, and M. Bajka, "Inverse finite element characterization of soft tissues," vol. 2208. Springer Verlag, 2001, pp. 128–136.

[273] G. G. Barbarino, M. Jabareen, and E. Mazza, "Experimental and numerical study on the mechanical behavior of the superficial layers of the face," Skin Research and Technology, vol. 17, no. 4, pp. 434–444, 2011.

[274] I. Bilionis and N. Zabaras, "Solution of inverse problems with limited forward solver evaluations: a bayesian perspective," Inverse Problems, vol. 30, no. 1, p. 015004, 2013.

[275] S. Razavi, B. A. Tolson, and D. H. Burn, "Review of surrogate modeling in water resources," Water Resources Research, vol. 48, no. 7, 2012.

[276] J. Salvatier, T. V. Wiecki, and C. Fonnesbeck, "Probabilistic programming in python using pymc3," PeerJ Computer Science, vol. 2, p. e55, 2016.

[277] A. Kapoor, K. Grauman, R. Urtasun, and T. Darrell, "Active learning with gaussian processes for object categorization," in 2007 IEEE 11th International Conference on Computer Vision. IEEE, 2007, pp. 1–8.

[278] E. Pasolli and F. Melgani, "Gaussian process regression within an active learning scheme," in 2011 IEEE International Geoscience and Remote Sensing Symposium. IEEE, 2011, pp. 3574–3577.

[279] B. Guyuron, Plastic Surgery. Saunders-Elsevier, 2009.

[280] G. Slabaugh, R. Schafer, T. Malzbender, and B. Culbertson, "A survey of methods for volumetric scene reconstruction from photographs," in Volume Graphics 2001. Springer, 2001, pp. 81–100.

[281] P. Metzler, Y. Sun, W. Zemann, A. Bartella, M. Lehner, J. A. Obwegeser, A. L. Kruse-Gujer, and H.-T. Lübbers, "Validity of the 3d vectra photogrammetric surface imaging system for cranio-maxillofacial anthropometric measurements," Oral and maxillofacial surgery, vol. 18, no. 3, pp. 297–304, 2014.

[282] C. Strecha, W. von Hansen, L. Van Gool, P. Fua, and U. Thoennessen, "On benchmarking camera calibration and multi-view stereo for high resolution imagery," in 2008 IEEE Conference on Computer Vision and Pattern Recognition, 2008, pp. 1–8.

[283] Y. Furukawa and J. Ponce, "Accurate, dense, and robust multiview stereopsis," IEEE Transactions on Pattern Analysis and Machine Intelligence, vol. 32, no. 8, pp. 1362–1376, 2010.

[284] S. Pieper, M. Halle, and R. Kikinis, "3D Slicer," 2004 2nd IEEE International Symposium on Biomedical Imaging: Nano to Macro (IEEE Cat No. 04EX821), vol. 2, pp. 632–635, 2004.

[285] S. M. Garn, S. Selby, and R. Young, "Scalp thickness and the fat-loss theory of balding," A. M. A. Archives of Dermatology and Syphilology, vol. 70, no. 5, pp. 601–608, 1954.

[286] H. T. Cox, "The cleavage lines of the skin," The British Journal of Surgery, vol. 29, no. 114, pp. 234–240, 1941.

[287] A. Buganza Tepole, J. P. Steinberg, E. Kuhl, and A. K. Gosain, "Application of finite element modeling to optimize flap design with tissue expansion." Plastic and reconstructive surgery, vol. 134, no. 4, pp. 785–92, 2014.

[288] V. H. Hiep, R. Keriven, P. Labatut, and J. P. Pons, "Towards high-resolution large-scale multi-view stereo," in 2009 IEEE Conference on Computer Vision and Pattern Recognition, 2009.

[289] C. Deroy, M. Destrade, A. Mc Alinden, and A. Ni Annaidh, "Non-invasive evaluation of skin tension lines with elastic waves," Skin Research and Technology, vol. 23, no. 3, pp. 326–335, 2017.

[290] H. Seo, S. J. Kim, F. Cordier, J. Choi, and K. Hong, "Estimating dynamic skin tension lines in vivo using 3D scans," in CAD Computer Aided Design, vol. 45, no. 2, 2013, pp. 551–555.

[291] S. Aarabi, M. T. Longaker, and G. C. Gurtner, "Hypertrophic scar formation following burns and trauma: new approaches to treatment," PLoS medicine, vol. 4, no. 9, p. e234, 2007.

[292] C. K. Sen, G. M. Gordillo, S. Roy, R. Kirsner, L. Lambert, T. K. Hunt, F. Gottrup, G. C. Gurtner, and M. T. Longaker, "Human skin wounds: a major and snowballing threat to public health and the economy," Wound repair and regeneration, vol. 17, no. 6, pp. 763–771, 2009.

[293] H. W. Rogers, M. A. Weinstock, S. R. Feldman, and B. M. Coldiron, "Incidence estimate of nonmelanoma skin cancer (keratinocyte carcinomas) in the us population, 2012," JAMA dermatology, vol. 151, no. 10, pp. 1081–1086, 2015.

[294] M. M. Loesch, A.-K. Somani, M. M. Kingsley, J. B. Travers, and D. F. Spandau, "Skin resurfacing procedures: new and emerging options," Clinical, cosmetic and investigational dermatology, vol. 7, p. 231, 2014.

[295] V. Madan, J. T. Lear, and R.-M. Szeimies, "Non-melanoma skin cancer," The Lancet, vol. 375, no. 9715, pp. 673–685, 2010.

[296] A. Drobyshev, K. Kurakin, N. Drobysheva, and E. Merzhvinskaya, "Evaluation of soft tissue changes in orthognathic surgery by means of cbct superimposed surfaces," International Journal of Oral and Maxillofacial Surgery, vol. 40, no. 10, p. 1082, 2011.

[297] C.-M. Chen, S. Lai, H.-E. Lee, K.-K. Chen, and K.-J. Hsu, "Soft-tissue profile changes after orthognathic surgery of mandibular prognathism," The Kaohsiung Journal of Medical Sciences, vol. 28, no. 4, pp. 216–219, 2012.

[298] N. Abe, S. Kuroda, M. Furutani, and E. Tanaka, "Data-based prediction of soft tissue changes after orthognathic surgery: clinical assessment of new simulation software," International journal of oral and maxillofacial surgery, vol. 44, no. 1, pp. 90–96, 2015.

[299] L.-J. Lo, J.-L. Weng, C.-T. Ho, and H.-H. Lin, "Three-dimensional region-based study on the relationship between soft and hard tissue changes after orthognathic surgery in patients with prognathism.(research article)(report)," PLoS ONE, vol. 13, no. 8, p. e0200589, 2018.

[300] S. M. Seitz, B. Curless, J. Diebel, D. Scharstein, and R. Szeliski, "A comparison and evaluation of multi-view stereo reconstruction algorithms," in 2006 IEEE computer society conference on computer vision and pattern recognition (CVPR'06), vol. 1. IEEE, 2006, pp. 519–528.

[301] Y. Lanir and Y.-C. Fung, "Two-dimensional mechanical properties of rabbit skinii. experimental results," Journal of Biomechanics, vol. 7, no. 2, pp. 171–182, 1974.

[302] P. Tong and Y.-C. Fung, "The stress-strain relationship for the skin," Journal of Biomechanics, vol. 9, no. 10, pp. 649–657, 1976.

[303] B. Müller, J. Elrod, M. Pensalfini, R. Hopf, O. Distler, C. Schiestl, and E. Mazza, "A novel ultra-light suction device for mechanical characterization of skin," PloS one, vol. 13, no. 8, p. e0201440, 2018.

[304] J. LoGiudice and A. K. Gosain, "Pediatric tissue expansion: indications and complications," pp. 866–872, 2003.

[305] C. Flynn, "Finite element models of wound closure," Journal of Tissue Viability, vol. 19, no. 4, pp. 137–149, 2010.

[306] A. B. Cua, K.-P. Wilhelm, and H. I. Maibach, "Elastic properties of human skin: relation to age, sex, and anatomical region," Archives of Dermatological Research, vol. 282, no. 5, pp. 283–288, 1990.

[307] C. E. Rasmussen and C. K. I. Williams, Gaussian processes for machine learning. MIT press Cambridge, 2006, vol. 1.

[308] R. R. Richardson, M. A. Osborne, and D. A. Howey, "Gaussian process regression for forecasting battery state of health," Journal of Power Sources, vol. 357, pp. 209–219, 2017.

[309] X. Wu, T. Kozlowski, and H. Meidani, "Kriging-based inverse uncertainty quantification of nuclear fuel performance code bison fission gas release model using time series measurement data," Reliability Engineering & System Safety, vol. 169, pp. 422–436, 2018.

[310] I. Bilionis, E. M. Constantinescu, and M. Anitescu, "Data-driven model for solar irradiation based on satellite observations," Solar Energy, vol. 110, pp. 22–38, 2014.

[311] A. I. J. Forrester and A. J. Keane, "Recent advances in surrogate-based optimization," Progress in Aerospace Sciences, vol. 45, no. 1, pp. 50–79, 2009.

[312] D. Higdon, J. Gattiker, B. Williams, and M. Rightley, "Computer model calibration using high-dimensional output," Journal of the American Statistical Association, vol. 103, no. 482, pp. 570–583, 2008.

[313] R. Tripathy, I. Bilionis, and M. Gonzalez, "Gaussian processes with built-in dimensionality reduction: Applications to high-dimensional uncertainty propagation," Journal of Computational Physics, vol. 321, pp. 191–223, 2016.

[314] G. Limbert and M. Taylor, "On the constitutive modeling of biological soft connective tissues: a general theoretical framework and explicit forms of the tensors of elasticity for strongly anisotropic continuum fiber-reinforced composites at finite strain," International Journal of Solids and Structures, vol. 39, no. 8, pp. 2343–2358, 2002.

[315] V. Alastrué, P. Sáez, M. Martínez, and M. Doblaré, "On the use of the bingham statistical distribution in microsphere-based constitutive models for arterial tissue," Mechanics Research Communications, vol. 37, no. 8, pp. 700–706, 2010.

[316] P. Cignoni, M. Callieri, M. Corsini, M. Dellepiane, F. Ganovelli, and G. Ranzuglia, "MeshLab: an Open-Source Mesh Processing Tool," in Eurographics Italian Chapter Conference. The Eurographics Association, 2008, pp. 129–136.

[317] M. D. McKay, R. J. Beckman, and W. J. Conover, "A comparison of three methods for selecting values of input variables in the analysis of output from a computer code," Technometrics, vol. 42, no. 1, pp. 55–61, 2000.

[318] Q. Du and J. E. Fowler, "Hyperspectral image compression using JPEG2000 and principal component analysis," Geoscience and Remote Sensing Letters, IEEE, vol. 4, no. 2, pp. 201–205, 2007.

[319] I. Bilionis and N. Zabaras, "Multi-output local gaussian process regression: Applications to uncertainty quantification," Journal of Computational Physics, vol. 231, no. 17, pp. 5718–5746, 2012.

[320] I. Bilionis, N. Zabaras, B. A. Konomi, and G. Lin, "Multi-output separable gaussian process: Towards an efficient, fully bayesian paradigm for uncertainty quantification," Journal of Computational Physics, vol. 241, pp. 212–239, 2013.

[321] T. Beeler, "Passive spatiotemporal geometry reconstruction of human faces at high fidelity," IEEE computer graphics and applications, vol. 35, no. 3, pp. 82–90, 2015.

[322] W.-C. Ma, A. Jones, J.-Y. Chiang, T. Hawkins, S. Frederiksen, P. Peers, M. Vukovic, M. Ouhyoung, and P. Debevec, "Facial performance synthesis using deformation-driven polynomial displacement maps," ACM Transactions on Graphics (TOG), vol. 27, no. 5, p. 121, 2008.

[323] N. Mitchell, C. Cutting, and E. Sifakis, "GRIDiron: an interactive authoring and cognitive training foundation for reconstructive plastic surgery procedures," ACM Transactions on Graphics (TOG), vol. 34, no. 4, pp. 1–12, 2015.

[324] J. Weickenmeier, C. A. M. Butler, P. G. Young, A. Goriely, and E. Kuhl, "The mechanics of decompressive craniectomy: Personalized simulations," Computer Methods in Applied Mechanics and Engineering, vol. 314, pp. 180–195, 2017.

[325] M. C. Kennedy and A. O'Hagan, "Bayesian calibration of computer models," Journal of the Royal Statistical Society: Series B (Statistical Methodology), vol. 63, no. 3, pp. 425–464, 2001.

[326] N. G. Norman, J. F. McGuire, S. Dyson, and D. Chark, "Nonmelanoma skin cancer of the head and neck ii: surgical treatment and reconstruction," American journal of otolaryngology, vol. 30, no. 3, pp. 181–192, 2009.

[327] J. S. Moyer, S. Rudy, P. S. Boonstra, C. Kraft, S. B. Chinn, S. R. Baker, J. L. Schwartz, C. K. Bichakjian, D. Fullen, A. B. Durham, L. Lowe, and T. M. Johnson, "Efficacy of staged excision with permanent section margin control for cutaneous head and neck melanoma," JAMA dermatology, vol. 153, no. 3, pp. 282–288, 2017.

[328] R. L. Siegel, K. D. Miller, and A. Jemal, "Cancer statistics, 2015," CA: a cancer journal for clinicians, vol. 65, no. 1, pp. 5–29, 2015.

[329] K. G. Patel and J. M. Sykes, "Concepts in local flap design and classification," Operative Techniques in Otolaryngology-Head and Neck Surgery, vol. 22, no. 1, pp. 13–23, 2011.

[330] P. J. Buchanan, T. A. Kung, and P. S. Cederna, "Evidence-based medicine: wound closure," Plastic and reconstructive surgery, vol. 138, no. 3S, pp. 257S–270S, 2016.

[331] S. Niroomandi, I. Alfaro, E. Cueto, and F. Chinesta, "Accounting for large deformations in real-time simulations of soft tissues based on reduced-order models," Computer Methods and Programs in Biomedicine, vol. 105, no. 1, pp. 1–12, 2012.

[332] N. V. Queipo, R. T. Haftka, W. Shyy, T. Goel, R. Vaidyanathan, and P. K. Tucker, "Surrogate-based analysis and optimization," Progress in aerospace sciences, vol. 41, no. 1, pp. 1–28, 2005.

[333] G. D. Dockery and M. E. Crawford, Flap classification and survival factors. Elsevier Ltd, 2012, pp. 143–149.

[334] C. Flynn, A. Taberner, and P. Nielsen, "Modeling the mechanical response of in vivo human skin under a rich set of deformations," Annals of biomedical engineering, vol. 39, no. 7, pp. 1935–1946, 2011.

[335] S. Atkinson and N. Zabaras, "Structured bayesian gaussian process latent variable model: Applications to data-driven dimensionality reduction and high-dimensional inversion," Journal of Computational Physics, vol. 383, pp. 166–195, 2019.

[336] G. A. Holzapfel and R. W. Ogden, "Constitutive modelling of arteries," in Proceedings of the Royal Society of London A: Mathematical, Physical and Engineering Sciences, vol. 466, no. 2118. The Royal Society, 2010, pp. 1551–1597.

[337] A. Menzel and T. Waffenschmidt, "A microsphere-based remodelling formulation for anisotropic biological tissues," Philosophical Transactions of the Royal Society of London A: Mathematical, Physical and Engineering Sciences, vol. 367, no. 1902, pp. 3499–3523, 2009.

[338] H. Hori, G. Moretti, A. Rebora, and F. Crovato, "The thickness of human scalp: normal and bald," Journal of Investigative Dermatology, vol. 58, no. 6, pp. 396–399, 1972.

[339] A. F. Bower, Applied mechanics of solids. CRC press, 2009.

[340] A. E. Ehret, K. Bircher, A. Stracuzzi, V. Marina, M. Zündel, and E. Mazza, "Inverse poroelasticity as a fundamental mechanism in biomechanics and mechanobiology," Nature communications, vol. 8, no. 1, p. 1002, 2017.

[341] R. Ababou, A. C. Bagtzoglou, and E. F. Wood, "On the condition number of covariance matrices in kriging, estimation, and simulation of random fields," Mathematical Geology, vol. 26, no. 1, pp. 99–133, 1994.

[342] D. E. Gormley, "A brief analysis of the burow's wedge/triangle principle," The Journal of dermatologic surgery and oncology, vol. 11, no. 2, pp. 121–123, 1985.

[343] G. H. Teichert and K. Garikipati, "Machine learning materials physics: Surrogate optimization and multi-fidelity algorithms predict precipitate morphology in an alternative to phase field dynamics," Computer Methods in Applied Mechanics and Engineering, vol. 344, pp. 666–693, 2019.

[344] N. Kumaraswamy, H. Khatam, G. P. Reece, M. C. Fingeret, M. K. Markey, and K. Ravi-Chandar, "Mechanical response of human female breast skin under uniaxial stretching," Journal of the mechanical behavior of biomedical materials, vol. 74, pp. 164–175, 2017.

[345] A. F. Borges, "Relaxed skin tension lines (rstl) versus other skin lines." Plastic and reconstructive surgery, vol. 73, no. 1, pp. 144–150, 1984.

[346] B. J. Wilhelmi, S. J. Blackwell, and L. G. Phillips, "Langer's lines: to use or not to use," 1999.

[347] G. G. Walmsley, Z. N. Maan, V. W. Wong, D. Duscher, M. S. Hu, E. R. Zielins, T. Wearda, E. Muhonen, A. Mcardle, R. Tevlin, D. A. Atashroo, K. Senarath-Yapa, H. P. Lorenz, G. C. Gurtner, and M. T. Longaker, "Scarless wound healing: Chasing the holy grail," Plastic and Reconstructive Surgery, vol. 135, no. 3, pp. 907–917, 2015.

[348] E. Raposio, R. E. Nordström, and P. Santi, "Undermining of the scalp: quantitative effects." Plastic and reconstructive surgery, vol. 101, no. 5, pp. 1218–1222, 1998.

[349] J. E. Leedy, J. E. Janis, and R. J. Rohrich, "Reconstruction of acquired scalp defects: an algorithmic approach," Plastic and reconstructive surgery, vol. 116, no. 4, pp. 54e–72e, 2005.

[350] A. Maciel-Miranda, S. F. Morris, and G. G. Hallock, "Local flaps, including pedicled perforator flaps: anatomy, technique, and applications," Plastic and reconstructive surgery, vol. 131, no. 6, pp. 896e–911e, 2013.

[351] N. Gümüş and S. Yılmaz, "Management of scar contractures of the hand using z advancement rotation flap," Burns, vol. 39, no. 5, pp. 978–983, 2013.

[352] S. P. Paul and R. A. Norman, Clinical Cases in Skin Cancer Surgery and Treatment. Springer, 2016.

[353] E. Arpaci, S. Altun, N. M. Ertas, A. C. Uysal, and E. Inozu, "Omega (ω) advancement flap: a circular flap design for the aesthetic closure of circular skin defect," Aesthetic plastic surgery, vol. 41, no. 2, pp. 327–334, 2017.

[354] R. L. Barnhill, D. L. Bader, and T. J. Ryan, "A study of uniaxial tension on the superficial dermal microvasculature," Journal of investigative dermatology, vol. 82, no. 5, pp. 511–514, 1984.

[355] E. Lejeune, "Mechanical mnist: A benchmark dataset for mechanical metamodels," Extreme Mechanics Letters, p. 100659, 2020.

[356] G. C. Y. Peng, M. Alber, A. Buganza Tepole, W. R. Cannon, S. De, S. Dura-Bernal, K. Garikipati, G. Karniadakis, W. W. Lytton, P. Perdikaris, L. Petzold, and E. Kuhl, "Multiscale modeling meets machine learning: What can we learn?" Archives of Computational Methods in Engineering, pp. 1–21, 2020.

[357] K. Langer, "On the anatomy and physiology of the skin: II. skin tension (with 1 figure)," British Journal of Plastic Surgery, vol. 31, no. 2, pp. 93–106, 1978.

[358] R. Reihsner, B. Balogh, and E. J. Menzel, "Two-dimensional elastic properties of human skin in terms of an incremental model at the in vivo configuration," Medical engineering & physics, vol. 17, no. 4, pp. 304–313, 1995.

[359] C. H. M. Thorne, Grabb and Smith's plastic surgery, 7th ed. Lippincott, Williams & Wilkins, 2014.

[360] W. D. Meador, G. P. Sugerman, H. M. Story, A. W. Seifert, M. R. Bersi, A. Buganza Tepole, and M. K. Rausch, "The regional-dependent biaxial behavior of young and aged mouse skin: A detailed histomechanical characterization, residual strain analysis, and constitutive model," Acta Biomaterialia, vol. 101, pp. 403–413, 2020.

[361] C. Flynn and B. A. O. McCormack, "Simulating the wrinkling and aging of skin with a multi-layer finite element model," Journal of biomechanics, vol. 43, no. 3, pp. 442–448, 2010.

[362] R. B. Groves, S. Coulman, J. C. Birchall, and S. L. Evans, "Quantifying the mechanical properties of human skin to optimise future microneedle device design," Computer methods in biomechanics and biomedical engineering, vol. 15, no. 1, pp. 73–82, 2012.

[363] P. Lakhani, K. K. Dwivedi, and N. Kumar, "Directional dependent variation in mechanical properties of planar anisotropic porcine skin tissue," Journal of the Mechanical Behavior of Biomedical Materials, vol. 104, p. 103693, 2020.

[364] R. L. Keeney and H. Raiffa, Decisions with Multiple Objectives: Preferences and Value Trade-Offs. Cambridge University Press, 1993.

[365] Y. Shi and R. Eberhart, "A modified particle swarm optimizer," in 1998 IEEE international conference on evolutionary computation proceedings. IEEE world congress on computational intelligence (Cat. No. 98TH8360). IEEE, 1998, pp. 69–73.

[366] A. Wahlsten, M. Pensalfini, A. Stracuzzi, G. Restivo, R. Hopf, and E. Mazza, "On the compressibility and poroelasticity of human and murine skin," Biomechanics and modeling in mechanobiology, vol. 18, no. 4, pp. 1079–1093, 2019.

[367] N. Pittar, T. Winter, L. Falland-Cheung, D. Tong, and J. Waddell, "Scalp simulation–a novel approach to site-specific biomechanical modeling of the skin," Journal of the mechanical behavior of biomedical materials, vol. 77, pp. 308–313, 2018.

VITA

VITA

Taeksang Lee was born on May 2, 1989, in Suwon, South Korea, and grew up in Anyang. He completed Bachelor and Master degree of Mechanical Engineering at Sungkyunkwan University in 2014 and 2016, respectively. During his undergraduate study, he had gone obligatory military service for about 2 years. He was advised and mentored by Prof. Moon Ki Kim for Master degree, and he received Outstanding Thesis Award at Sungkyunkwan University in 2016.

Taeksang moved to United States to pursue doctoral degree of Mechanical Engineering at Purdue University in 2016, and he has been advised and mentored by Prof. Adrian Buganza Tepole since last 4 years. As a research assistant, Taeksang has worked on computational biomechanics to improve reconstructive surgery, and as a teaching assistant, he taught Introduction to Finite Element Analysis for undergraduates for 3 semesters. Since starting research in South Korea and USA, he has published 7 peer-reviewed journal papers as a leading author and a few more manuscripts are in revision. He received KSEA/KOSEN Best Poster Award at UKC 2019 and has been awarded 2020 KSEA-KUSCO Scholarship.